Computer Simulation of Radiation Damage in Hexagonal Close-Packed Metals

This thesis is submitted in accordance with the requirements of the University of Liverpool for the degree of Doctor of Philosophy by

Stephen John Wooding

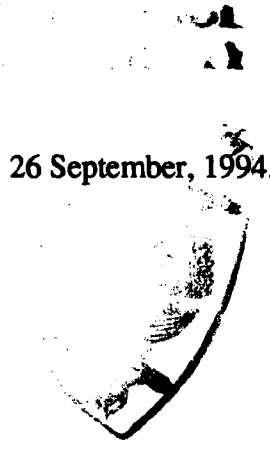

26 September, 1994.

Department of Materials Science & Engineering,
University of Liverpool,
P.O. Box 147,
Liverpool,
L69 3BX.

To my father, who taught me to question, and to my mother, from whom I learned that it is only through hard work that answers are found.

"...Of making many books there is no end, and much study wearies the body."

Ecclesiastes 12:12.

Abstract

Two HCP metals, titanium and zirconium, have been modelled using molecular dynamics and recently developed many-body potentials. These two metals have similar lattice parameters, $^{c}/_{a}$ ratios, melting temperatures, elastic and dislocation properties and, more importantly, responses to radiation damage (Griffith 1988, 1989 & 1991, Hood 1988 & 1993), but differ by nearly a factor of two in atomic mass, thereby allowing the direct investigation of the effect of mass on radiation damage in the HCP system. Using the MOLDY code, successfully modified for the HCP structure, these two models were rigorously investigated with respect to their point defect properties, displacement threshold energy response, and cascade processes. A marked preference for interstitial sites within the basal plane was found, in accordance with previous static studies on HCP metals. The displacement threshold energy showed a complex dependence on orientation within the HCP structure, but at higher energies this effect was swamped by structural disruptions during cascade development. The effect of mass was exhibited as a proportional increase in the mean displacement threshold energy, which carries over into cascade generation.

Cascade morphology was seen to undergo a transition at energies of ~1 keV, associated with the onset of true cascade conditions. This transition was reflected most markedly in the relaxation time for the recombination phase beyond the cascade peak, and explanation is presented for the transition in terms of ballistic, energetic and temporal effects. The dissimilarities between the two models were found to be mainly attributable to the mass difference. The condition of the cascade core at the peak was seen to be close to that of a liquid, with some discrepancies which indicate a lack of true melting, and an absence of the vacancy clustering often associated with a molten cascade core. The approximation of liquid-like structure was supported by the isotropy of the cascade-induced atomic mixing, despite the preference for basal-plane movement in the solid state. In agreement with modelling of other metals, the defect production efficiency for true cascade conditions was well below the NRT estimate, and an empirical relationship between final Frenkel-pair numbers and PKA energy is presented. SIA clustering occurred to a similar extent in both models, and small clusters were highly mobile and confined to single $<11\bar{2}0>$ rows in the basal planes. The implications of these findings for microstructural evolution are discussed, along with comparisons of the results with other systems.

Contents

Index

Acknowledgements

The author wishes to thank Prof. D.J. Bacon for his supervision and advice, in conjunction with Dr W.J. Phythian of AEA Technology (Harwell). Computing facilities at Manchester Computing Centre were funded by a Computational Initiative Grant from the EPSRC who, together with AEA Technology (Harwell), provided the author with a gratefully acknowledged CASE studentship.

Thanks (in no particular order) to Andy, Liz, Gao and Victor, the other members of the Radation Damage Group, who provided advice, discussion, and the odd bit of conversational relief when needed. Many thanks also to Alan, Pam, Tracey and Penny for lunchtime gaming, proper coffee and the occasional wet weekend.

Last, but by no means least, immeasurable thanks to Linda, for her continual support and selflessness during the last four years, and without whom this work would not have been possible.

I

Introductory Remarks and Thesis Overview

1.1 Introduction.

The study of damage caused to materials in radioactive environments has its roots in the nuclear power generation industry and was brought about by a need to understand effects seen in reactor core components over time, such as bulk shape changes, embrittlement and generally shorter life-spans than those expected. These deviations from originally intended forms and properties could have disastrous effects, such as fuel rods expanding and inhibiting the flow of core coolants, or pressure vessels becoming brittle over time and rupturing with catastrophic consequences. Hence the science of radiation damage was born. Since then, however, the area of applicability of such study has grown as technology has advanced, and now covers such subjects as ion-beam implantation within the semiconductor industry, ion and electron-beam milling and surface modification of materials, and even reaches as far as the field of space exploration with the presence of cosmic radiation and other atomic particles not present in terrestrial applications by virtue of the shielding effect of the earth's atmosphere.

Particle-based radiation damage occurs, in its basic form, as a disruption to the atomic structure of a material. An energetic particle, be it a neutron within a reactor core, an electron in a high-voltage microscope or even a whole atomic nucleus with its core electrons in the case of ion-beam applications, enters the material structure and eventually collides with one of the constituent atoms. How deep this particle penetrates depends on many parameters, including its mass, speed and charge and the structure and mass of the atoms of the target - ions will only penetrate a few nanometres whereas neutrons can travel several centimetres before a collision takes place. In this collision the incident particle will give up some of its energy, possibly causing the atom struck to move from its site and strike others, so leading to an avalanche of displacements as the initial energy of the incident particle is dissipated in a displacement 'cascade'. In some cases, the incident particle may still have sufficient

energy to continue further and produce several more displacement cascades before eventually coming to rest. The majority of the disturbed atoms will return to either their original locations, or closer sites made vacant by other displaced atoms, within a short space of time, invariably less than a few picoseconds ($^1/_{1,000,000,000,000}$th of a second). However, if the disruption to the structure of the material is great enough, some atoms may be ejected too far away from any empty sites to recombine and hence remain trapped as self-interstitial atoms (SIAs), leaving behind permanent vacancies in the atomic structure of the material. These point defects often cluster together forming 'dislocations' - discontinuities in the normally regular array of atoms. As might be expected, it is these defects which accumulate over time and cause the observed detrimental changes in reactor core component properties via phenomena such as 'irradiation creep', whereby a component elongates under its own weight due to defect diffusion, 'void swelling', caused by vacant sites agglomerating into microscopic cavities within the material, and grain-boundary embrittlement by the accumulation of SIAs and nuclear reaction products such as hydrogen. In semiconductors radiation damage can be quite severe, producing amorphous regions in an otherwise crystalline solid.

This study is concerned with the formation of displacement cascades and the defects they generate in one class of metals - those with the hexagonal-close-packed (HCP) structure. Most attention to date has been directed at the cubic metals such as iron and copper since both are widely used engineering and structural metals, iron in particular in the form of steels is utilised extensively in the nuclear power industry for pressure vessels, core structural elements and as part of the fuel cladding. Though less widely used, the HCP metals have an important role in engineering by virtue of their high strengths, elastic properties and in many cases excellent corrosion resistance. Zirconium in particular has a prominent application in PWR (Pressurised Water Reactors) environments as the major element in Zircaloy, a fuel-cladding alloy, and magnesium, another HCP metal is the primary constituent of the Magnox reactor fuel-

cladding alloy. Two metals in particular form the basis of this study, these being titanium, widely used in the aerospace industry and space programme because of its low weight and high specific strength and elastic properties, and zirconium which, as mentioned above, is used within the reactor core. In the past HCP metals have proved difficult to successfully model due to the lower symmetry of the structure and its associated effects on the macroscopic and microscopic scales. However, computing power has increased rapidly since the study of radiation damage first began, along with the complexity of the codes and equations governing the behaviour of model atoms, and therefore the spotlight has become increasingly focused on the more 'unusual' systems such as the HCP metals and even binary alloys.

An understanding of the mechanisms behind cascade evolution and the effects of structure and other parameters on the development and subsequent recombination of a cascade event, including the extent and form of the remaining defects, is vital if advances are to be made in improving component performance, and hence safety, in radiation-rich environments. The limitations in spatial and temporal scale of experimental observation mean that computer modelling is the only 'real' way to further knowledge in this field, and this work is intended to extend the awareness and understanding of that subject to include the HCP metals. The present investigation is the first to be reported of the simulation of cascade processes in such metals.

- § -

1.2 Thesis Overview.

The remainder of this thesis is laid out as follows:

Chapter 2 will review the initial ideas and development of the theory of radiation damage and summarise the present state of the subject. A summary of the information available from experimental observation via various techniques is also presented. Following that, the various methods of computer simulation are also outlined, and the results of the more pertinent studies detailed. In the final section, the issues which are, as yet, still not completely understood are listed.

Chapter 3 contains the details of the computer model used in this study, first summarising the available formalisms for the interatomic potential. The chosen potentials for this work are then described, along with the modifications made en route to ensure their suitability for this area of study. The code for the simulations is then briefly summarised, including its various modes of operation.

Chapters 4 and 5 follow on and present the results of static and low-energy simulations of the two model metals, Ti and Zr, as a necessary and important foundation for the higher energy cascade simulations. In chapter 4 a detailed review of past studies of point defects in HCP metals is presented and the resultant properties of point defects in the model metals in this work are described and compared. The implications of these results for cascade development and the final defect configurations are discussed. Chapter 5 deals with dynamic events at low energies where small numbers of displacements are generated which yield only one defect - the 'threshold' regime - and the results of an extensive study into the effect of the HCP structure on the directional dependence of the 'threshold displacement energy' are presented. The possible implications of these data are also discussed with respect to higher energy events.

The results of the full cascade simulations are presented in chapters 6 and 7. Chapter 6 contains the results and discussion associated with the formation and evolution processes within the cascade, and chapter 7 focusses on the final state of the cascade, i.e. the numbers and configurations of the SIAs and vacancies remaining as permanent modifications to the structure, since it is these which will directly affect the bulk properties of whatever component contains them.

A final summary and the conclusions of this study are given in chapter 8, and recommendations for further work are also listed.

- § -

II

Radiation Damage and Displacement Cascades

2.1 Introduction.

The study of radiation and the damage to materials exposed to it is by no means new, having a history of at least four decades. During that time many ideas and theories on the details and processes involved have been forwarded and modified, and are still being honed to achieve greater accuracy in calculation and better explanation of experimental and theoretical study. In this chapter the early ideas and descriptions of radiation damage will be reviewed, along with more recent experimental evidence of damage processes, and the use of computer simulation to model these processes will be discussed. The issues to be addressed in this work will also be outlined.

- § -

2.2 Early Theory of Radiation Damage.

It was originally thought that radiation damage occurred as a series of isolated point displacements forming single, well separated Frenkel pairs (vacancy-interstitial pairs) (Seitz 1952). However, as summarised by Olander (1976), an analytical investigation by Brinkman (1954) showed that the theoretical mean free path of any atom displaced with energy approaching several tens of keV was of the order of the atomic spacing, so every atom in the path of the primary knock-on atom (PKA) would be struck, and probably displaced. Based on this, his description of the form of the 'displacement cascade', or 'displacement spike' as originally put forward, was not a collection of isolated Frenkel defects, but rather a compact vacancy-rich core, the depleted zone, surrounded by a shell of displaced interstitials. From this model he also concluded that the core would be highly disordered due to the large amounts of energy deposited in such a small region by the high concentration of atomic collisions, and therefore could be regarded as having melted. His schematic diagram of a displacement cascade

is shown in fig. 2.1, and he further postulated that this vacancy-rich core could collapse to form a dislocation loop which would remain after the energy of the spike had dissipated.

One phenomena that Brinkman had overlooked, later proposed by Silsbee (1957), was that of focusing. This occurs when an atomic collision takes place in a close-packed row in the crystal, though not necessarily exactly parallel to it, and propagates a further series of collisions which become focused along the row, i.e. the angle of strike between each successive collision and the close-packed line reduces (fig 2.2). It should be noted that in this model the atoms are dislodged from their original site, collide with a neighbour and return to the same site. This Silsbee termed a 'focuson'. His calculations proved that there existed a critical set of values for the energy of the first collision and the inter-atom spacing within which this focusing would occur, and showed that this process was favoured at low energies. His mechanism provided a method of rapid energy removal from the core of a displacement cascade in the form of phonons, or lattice vibrations.

Soon afterwards Seeger (1958) proposed a very similar mechanism which this time involved each of the atoms in the chain leaving their original site, colliding with a neighbour as before, but this time permanently displacing that neighbour and settling on that neighbour's site instead of the site from which it originally came. This 'replacement-collision sequence' (RCS) not only provided a mechanism by which energy could be removed from the cascade core, but also mass since, when the energy of the original strike had been dissipated to the surrounding lattice by each successive collision in the sequence, the final atom in the chain would not have sufficient energy to displace its neighbour, becoming trapped away from the cascade nucleus to form an interstitial. This also lent support to Brinkman's idea of the interstitial mantle around the depleted zone. However, Seeger's overall interpretation of the actual form of the displacement spike differs from Brinkman's, as can be seen

in fig 2.3. His idea was that, rather than a central hole surrounded by ejected matter produced by an 'explosion' as Brinkman supposed, the cascade consisted of a series of inter-dependent collisions with much less disruption to the lattice, and with the possible formation of amorphous regions in areas of most disorder.

All these original ideas about the shape, configuration and final state of a displacement cascade were just that; ideas and theories. Being only qualitative, the next step was for experiments to be performed to provide quantitative results.

- § -

2.3 Experimental Evidence for Radiation Damage.

To provide some evidence for the early ideas about radiation damage and cascades, experiments were performed, and indeed still are at present. Sometimes complex in nature, with the results often requiring intricate analysis, these experiments helped provide support for the initial theories on the shape and morphology of particle-induced damage, and where differences were found, new ideas and theories were formed to account for these. In this section a sample of work is discussed, along with the most important conclusions drawn from these works.

2.3.1 Irradiation Sources.

In order to produce radiation damage in experimental specimens several sources have been used by various workers. These fall into three broad categories, defined by the nature of the irradiating particles as mentioned in chapter 1, i.e. electrons, neutrons and ions. Electron irradiation has the advantage of being easy to generate using an

electron microscope, and the samples can be observed in situ as the damage takes place. Fast neutron irradiation is only produced by nuclear-power reactors, and therefore such sources are very limited in availability, and quite difficult to control, whereas for ion irradiation, although requiring specialised equipment to undertake, sources are quite widely available. Usually materials are irradiated with self-ions or noble gas ions, although other heavier elements are sometimes used.

i) Electron Irradiation: When an electron collides with a lattice atom, the maximum amount of kinetic energy it can transfer to the atom with which it collides is given by (Thompson 1969)

$$E_{max} = \frac{2E_e(E_e + 2m_e c^2)}{Mc^2} \qquad (2.1)$$

where E_e is the electron energy, m_e is the electron mass, M is the mass of the target atom and c is the speed of light, as relativistic effects must be included for high-energy electrons. However, this equation yields results that indicate that, even for relatively light metals, electron radiation is unlikely to impart sufficient energy to any target atoms to produce extensive damage. For example, a 1 MeV electron can only pass on a maximum of 90.6 eV when colliding with a Ti atom (atomic mass 47.9 amu). This is within the displacement threshold regime, and therefore electron irradiation in a HVEM (High Voltage Electron Microscope) is useful for studying low-energy displacement events in many metals as will be discussed in chapter 5, but not for generating large displacement cascades.

ii) Neutron Irradiation: For a neutron colliding with an atom, the maximum amount of energy transferred in a head-on collision is given as

$$E_{max} = \frac{4E_n M m_n}{(M + m_n)^2} \qquad (2.2)$$

where E_n is the energy of the neutron and m_n is its mass. This gives a maximum PKA energy in Ti of 80.8 keV for a 1 MeV neutron, much higher than the case for an electron of the same initial kinetic energy, which makes neutrons a suitable source for cascade generation. However, since fast neutrons are only generated in a nuclear reactor, their use is limited by reactor availability and cost. There are other factors which make the use of neutrons unfavourable, such as the inability to control the energy spectrum to any fine degree, and the fact that neutron-irradiated specimens can become contaminated with radioactive fission products during irradiation. One other important factor is that neutrons have a low collision cross-section in most materials, and therefore require large specimens of the order of several cm in order to ensure that cascade formation takes place. In spite of this, some neutron-based experiments have been carried out, some of which will be referred to in later sections.

iii) Ion Irradiation: This is the most widely used technique for forming radiation damage and displacement cascades. The maximum energy available for the PKA in this case can be derived by substituting the mass of the incident ion for m_n in equation 2.2, and the energy of the ion for E_n. This yields the result that an ion can pass on up to 100% of its energy if the ion and the target are the same mass and the collision is head-on.

Ion sources have several advantages over the two others, including wide availability, the controllability of the energy and dose rates of the ions as well as the temperature of the target material, a wide variety of source masses, and the absence of the radioactive contamination associated with neutron irradiation.

Since the duration of a single displacement cascade event is of the order of less than a picosecond (10^{-12} s), experiments can only provide 'before and after' pictures of radiation damage, and cannot provide absolute data on the processes involved in the development of a cascade. Rather, data gleaned from the arrangement, numbers and

distribution of defects after irradiation is extrapolated in order to provide some insight into the evolution of the damage state.

2.3.2 Observation Methods

Several techniques are used to examine the damage produced by irradiation, including electrical resistivity and magnetic property measurements, FIEM (Field Ion Emission Microscopy) and TEM (Transmission Electron Microscopy).

i) Electrical and Magnetic Property Changes: A perfect metal has a particular set of electrical and magnetic properties, and the introduction of defects into a lattice can dramatically change these. Vacancies and SIAs hinder the flow of electrons through a metal and hence increase the resistivity such that

$$\Delta\rho = \sum_j c^j \rho_F^j \qquad (2.3)$$

where $\Delta\rho$ is the residual resistivity, c^j is the concentration of defects of type j (be they vacancies, SIAs, or clusters of either), and $\rho_F{}^j$ is the resistivity contribution of unit concentration of those defects. Measuring the changes in resistivity of a sample irradiated at low temperature as temperature is increased therefore gives indication of the movement and annihilation of various defect types, as shown by Vialaret et al. (1975) for Zr irradiated with neutrons at 24 K. Fig. 2.4 shows the resultant annealing curve. The general form of an annealing curve shows five stages, each linked with a particular defect type and configuration, with some stages consisting of several sub-stages.

Stage I is attributed to recombination of single point defects via SIA movement, and in the case of Zr is split into six sub-stages. I_A - I_C are linked to the recombination of

Frenkel pairs along different lattice directions ('correlated recombination'). I_D is associated with the recombination of a vacancy and SIA separated by more that the normal recombination distance (again, correlated recombination), and stages I_E and I_F arise from the annihilation of vacancies with SIAs not originally from those sites (uncorrelated recombination). Stage II is said to be due to the longer range migration of SIAs and SIAs escaping from the stress fields of traps such as solutes and grain boundaries, and interstitial loops may form and grow. During stage III vacancies become mobile, and begin to migrate, recombining with SIAs and interstitial loops, and also forming clusters or becoming trapped at sinks. Stage IV is characterised by the growth of vacancy loops to a size which becomes visible in the TEM, and stage V denotes the final evaporation of vacancy clusters and the annihilation of these vacancies with interstitial clusters to leave a recovered crystal.

It should be pointed out that the above description constitutes what has become known as the 'one-interstitial' model. An alternative, the 'two-interstitial' model, exists which differs slightly in the interpretation of stages I_E - IV, linking stage I_E with the mobility of a metastable interstitial configuration and shifting all subsequent stages along, so that stage II is due to longer range vacancy-SIA recombination, stage III is due to migration of the stable SIA and clustering, and vacancies are not mobile until stage IV. Vialaret et al. favour the former model, whereas others (Frank & Seeger 1987, Frank 1988) favour the latter.

Although the process of recovery gives no real data on the cascade processes, observation of the different stages of annealing can shed light on the types of defects generated by differing radiation sources. For example, fig 2.5, taken from the review by Zinkle and Singh (1993), shows the stage I sub-stages in copper after electron and neutron irradiation. For the electron case, five sub-stages are clearly present, indicating the presence and later annihilation of closely correlated Frenkel pairs as well as vacancy-SIA pairs separated by larger distances. In the neutron-irradiated

case, the only stage clearly present is I_D, linked to the uncorrelated recombination of vacancies with SIAs from other sites. The conclusion, based on this and other experiments (again, see Zinkle & Singh, 1993) was that, since electrons give rise to PKAs with lower energies than those created by neutrons, as PKA energy increases, the amount of closely-correlated defects reduces because of the increase in disorder created during the cascade and subsequent cooling. Thus the measurement of one particular bulk property can be used to deduce something about the manner in which cascades develop under different conditions.

The magnetic properties of materials are also affected by defects, in particular ordered alloys such as Ni_3Mn, in which atoms of each species have a specific number of neighbours of each type; this number changes when disordering occurs. Using these changes Kirk et al. (1977, 1978 & 1982) determined the disordering effects of RCSs brought about by thermal and fast neutron irradiation, generating PKAs of around 450 eV and 20 keV respectively. By comparison with computer simulation (which will be discussed in the next section), and from another independent study (Schwartz & Schwartz, 1978), they concluded that the low energy cascades yielded between 112 and 150 replacements per cascade, contained in only a few RCSs. The higher energy cascades did not seem to yield any significant (i.e. detectable) RCSs at all, again indicating a difference in low and high energy cascade development.

ii) FIEM Studies: Since the original proposal by Seeger of the RCS as a means of ejecting matter from the core of a cascade, several experiments have been devised to measure the lengths of RCSs in several materials. In one set Beavan et al. (1971) and Wei & Seidman (1981) irradiated atomically sharp tungsten needles with Au^+, W^+ and Cr^+ ions of various energies at 10 K, at which SIAs in W were known to be immobile (Wilson et al. 1975 & 1980). By using the FIEM to dismantle the needle tip atom by atom and recording the output, subsequent computer analysis of the results gave a 3-D map of the needle tip and showed that the vacancies produced were indeed

concentrated in a small region, surrounded by a mantle of interstitials. The assumption was that any interstitials created by the irradiation were the result of RCSs, which would be marked by a vacancy at one end and an interstitial at the other. Using the fact that RCSs propagate along close-packed rows, each interstitial could be linked to a vacancy and the RCS length measured. In the case of W at 10 K, this turned out to be 16 ± 12 nm, or 59 ± 46 replacements. However, several problems affect these measurements, including the fraction of interstitial detection at only 10% of the total generated, and the loss of up to 50% of the generated interstitials to the needle surface where they would be undetected, and so the length of longer RCSs would be undetermined. Even so, these results showed that the cascades created had at least the shape and form predicted by the early theories.

iii) TEM Studies: The TEM is by far the most widely used instrument to study radiation damage, both in its capacity to observe the strain fields around defect clusters, and as a lattice imaging tool to visualise the disordering effects of cascades in ordered alloys.

Many experiments have been conducted on a variety of metals over the last two decades or so to investigate the dependence of cascade development and subsequent collapse on material parameters. These include samples taken from neutron, electron and ion irradiated material. TEM samples are most commonly of the form of electrochemically thinned 3 mm discs, which may be cut from neutron-irradiated bulk samples, or prepared beforehand and then irradiated in a dedicated facility, where dose rates, temperature, ion mass and even ion charge can be carefully controlled. Pre-thinned samples can also be used in high-voltage TEM for the investigation of electron irradiation, or even irradiated in specialised facilities within the TEM specimen chamber for direct observation of damage. Though a large base of results from neutron-based experiments exists, which yield large dislocation loops and networks, these are at high doses and covering a wide spectrum of incident particle energies. Since this work is primarily concerned with cascades processes at low

doses, only some of the more prominent and conclusive works using ion and electrons will be referred to here, as a full report on all of these would be beyond the scope of this report.

Collapsed loops, the results of displacement cascades, appear in the TEM under different diffraction conditions as black-white images produced by their strain fields. These can then be analysed to deduce certain loop characteristics, e.g. Burgers vector, size and habit plane (Eyre et al. 1977). From a knowledge of the depth of the loops in the TEM sample, measured by stereo pair analysis, and the form of the black-white contrast images, their nature (i.e. vacancy or interstitial) can also be determined. One element that should be noted is that for thin-foil experiments the surfaces of the specimen act as sinks for interstitials, which are quite mobile even at low temperatures, and so are not observed either as SIAs or loops in the majority of this kind of work.

Any sample can be irradiated under a variety of conditions, the most important of which are temperature, ion energy and ion dose. The dose, the number of ions striking the sample per unit area during the irradiation, is taken as the theoretical maximum for the number of cascades which can be formed, N_c, assuming each ion causes one cascade. By measuring, using photographic techniques, the number of dislocation loops per unit area, N_L, and again assuming each loop is the collapsed vacancy-rich core of a cascade, the 'defect yield' Y (Merkle 1966) can be determined as N_L/N_c. The distribution of loop diameters can also be measured, and the mean diameter determined. From this, the number of vacancies N_v^{expt} contained in a loop of mean diameter can be calculated, along with the theoretical estimate of the total number of vacancies produced by single cascade N_v^{th} - this is calculated using the Norgett, Robinson & Torrens (1975) theory summarised later. The 'collapse efficiency' ε is then the ratio N_v^{expt}/N_v^{th}. Having defined these two cascade parameters, a third, the 'defect retention efficiency' (DRE) is calculated as the product of Y and ε, representing the total fraction of vacancies generated that are retained in visible collapsed loops.

English & Jenkins (1987) and Phythian et al. (1991) have summarised the findings of a large base of experiments and studies on a wide range of metals, predominantly cubic in the former review (Cu, Ag, Ni, Mo, Fe and Cu_3Au, but also HCP Ru) and entirely HCP in the latter (including Ti, Co, Re, Ru and Mg). Vacancy loops are formed in many metals irrespective of the temperature at which irradiation was carried out, i.e. Y was non-zero. Since vacancies are not mobile at temperature around a few tens of K, at which some irradiations were performed, the deduction is that the collapse of the vacancy-rich core must occur athermally at some point during the cascade process. This must be during the 'thermal spike', a phase after the initial displacement spike has reached its maximum size and the PKA energy has been distributed among the moving atoms. Furthermore, all the displaced atoms begin to recombine with vacant sites, so releasing energy (described in more detail in section 2.5). Y generally increases with irradiation temperature, indicating an increased ability for collapse at higher temperatures, possibly due to a longer thermal spike lifetime. Furthermore, the mean diameter of the loops produced do not change significantly with irradiation temperature for constant ion energy and mass, suggesting the presence of some sort of directed motion of vacancies towards the cascade core. This has given rise to several contrasting theories for possible mechanisms for this phenomenon which will be discussed in greater detail in section 2.5. The FCC, BCC and HCP metals all generally follow the above trends. However, in an attempt to better clarify the dependence of Y, ε and the DRE on material-specific parameters, Phythian et al. (1991) investigated their links to quantities such as melting temperature T_m, the degree of electron-phonon coupling θ_D (a measure of the ability of the electrons in the metal to be excited by lattice vibrations and thus remove thermal energy from the cascade), the energy density of the cascade, and the temperature of the cascade core, all of which influence the length of the thermal spike, and hence the time available for vacancy migration to form a loop. They found that there seemed to be no real dependence of Y, ε or DRE on any single parameter, and concluded that the observed differences between metals must have a more complex dependence on combinations of material parameters. More recently, however, Robertson et al.

(1993) have suggested, based on a quite extensive set of experimental results encompassing a variety of target metals, irradiating ions and energies, that Y is seen to be correlated to the energy density of the cascade and to θ_D in materials with a strong degree of electron-phonon coupling. For those materials with little electronic coupling, the dependence on other parameters such as melting temperature and stacking fault energy becomes more significant, but not in any obvious or simple manner, as suggested by Phythian et al.

By making use of the disordering effects of irradiation damage on ordered alloys, ion irradiated Cu_3Au thin foil specimens were observed by Jenkins et al. (1976) using the {110} superlattice spots. This enabled them to image the disordered zones in the foils caused by the cascades, and most of the zones observed contained dislocation loops - the collapsed vacancy-rich cores as predicted by Brinkman. As ion energy was increased, the disordered zones became larger and more irregular in shape. Although it was thought that RCSs would not generate enough disorder to be observable, Jenkins and Wilkens (1976) did observe short 'tubes' of disordering in their specimens which could be interpreted as evidence of RCS formation.

Nonetheless, the basic findings of such TEM studies concur with the initial theories: that cascade size increases with ion energy, and the cascades may collapse independently of ambient temperature to form vacancy loops. The length of the thermal spike phase may have an effect on this, such that the shorter the thermal spike, the less time available for vacancy diffusion. The major failings of this type of experiment is that no measurements are made of the interstitial components of the damage, or of very small vacancy clusters and loops, although the vacancy component is the most important in the role of void swelling.

Despite the wealth of information gleaned from irradiation experiments, they also fail on one other main point in that cascade processes cannot be observed directly. Since cascade events only last for a few ps, however, no experiment could hope to observe

them as they occur, and so computer-based models have been developed to simulate these damage processes.

- § -

2.4 Computer Modelling.

Although models of radiation damage have existed for over three decades, co-existing with experiments, their use has been severely limited by computing power, enabling only small micro-crystals and very low PKA energies to be simulated at first, whilst experimental work was conducted with ion energies over three orders of magnitude greater, and therefore the connection between the two was somewhat thin in their infancy. More recently however, models approaching experimental energies are beginning to be constructed, narrowing the gap a great deal. In this section, the origins of computer simulation will be explored, and the spinoffs of the early work, often still in use, will be described.

2.4.1 The Beginnings of Dynamic Simulation.

Computer simulation of radiation damage has its roots in the pioneering work at the Brookhaven Laboratories in the 1960s, with the work of Gibson et al. (1960). Their techniques and assessment of what was required to successfully model a real metal have been little modified over the last thirty years or so and, even though computing power was small by today's standards, the code they developed was quite complex even when compared to the codes in use at present.

Their work concentrated on lower energy events, particularly just above the threshold

displacement energy (generally of the order of tens of eVs, though some calculations were carried out at up to 400 eV), and their model was set up to represent metallic FCC copper. They used a Born-Mayer two-body potential of the form

$$V(r) = Be^{-\beta r} \qquad (2.4)$$

where B and β are fitting constants. (Potentials are discussed in more detail in chapter 3). It should be noted that this potential is always positive i.e. repulsive, and has no cohesive component, and therefore required the addition of an external force, detailed later, to stop the model atoms dissociating. The actual number of atoms used in their model micro-crystals was between 500 and 1000.

Having given a selected atom a predetermined amount of energy in a particular direction, their code used the classical Newtonian equations of motion to calculate the forces, positions, velocities and accelerations of all the atoms in the crystallite many times over throughout a single simulation. To save on computer time they also included a routine to calculate the optimal size of timestep, the amount of time between recalculations of the forces etc., depending on the energy of the atoms in the previous step. The greater the forces and velocities of the atoms, the smaller the time step down to some minimum. However, a maximum time step was also be set as even at low energies the atoms still behave as a series of coupled oscillators with an associated frequency, and the time step must be smaller than the period of these oscillations.

In order to account for the presence of a continuous medium around the tiny crystal they were generating, and to provide some cohesive force to counteract the repulsive nature of the Born-Mayer potential, an additional force was applied to the atoms on the surface of the block in the form of two elements: a spring, or elastic, force proportional to the displacement of the surface atom to account for the resistance of

bulk material to slow or static deformation, and a viscous force proportional to the atom's velocity to reflect the material's opposition to rapid deformation. The sizes of both elements were chosen carefully to allow efficient absorption of any displacements or shock-waves reaching the crystal boundaries whilst minimising any reflections which could have adverse effects on the results. Unfortunately a compromise had to be reached it setting these parameters as there is a peak frequency at which such forces absorb, becoming less efficient either side of that peak. This additional force also had the effect of mimicking, to some small extent, the cohesive effect of the electrons in the metal.

Their results and conclusions were wide-ranging and quite substantial, providing further backing for the proposed energy transfer mechanisms of Silsbee and Seeger, the focuson and RCS. Though they found that the vacancies which remained after the cascade were in a relatively compact central region, the volume was by no means amorphous as Seeger had suggested and far from the huge void of Brinkman's model. The interstitial mantle was not as dense as Brinkman predicted either, but rather consisted of a small number of SIAs separated from their associated vacancy by a few lattice parameters or more, and was often quite diffuse. The simulation results gave the impression that the real situation lay somewhere between these two main ideas.

Gibson et al. also investigated the effect of the lattice structure of the metal on the displacement threshold energy, completed later (Vineyard & Gibson 1961), and this was repeated for α-iron (Erginsoy, Vineyard & Englert 1964). In addition they noticed that, even though many atoms might be displaced during the cascade, only a very small number remained as permanent defects, and those that recombined released energy, sustaining the thermal spike and thus producing a residue of heat localised in the area of the cascade which took much longer to dissipate than the lifetime of the displacement events.

As stated earlier, this work was ground-breaking, and was one of the first sets of full 'molecular dynamics' (MD) calculations, proving that computers were feasible tools for both helping to understand the mechanisms of radiation damage in a qualitative manner and providing quantitative data to help refine the theoretical models of real metals.

Since these beginnings in the 1960s the power of computers has increased by several magnitudes in both speed and capacity, with events of energies over 10 keV being simulated in blocks of a quarter of a million atoms or more, with initial crystal temperatures greater than the 0 K that was common in the early years of computer modelling. During the last thirty years or so several different conventions have arisen for the simulation of dynamic events, and two techniques cover the greater majority of these.

2.4.2 The Binary Collision Approximation.

This model arises from several simplifications, and is quite widely used (Beeler 1966, Robinson & Torrens 1974, Caro et al. 1990, Heinish & Singh 1992). In this model the cascade is assumed to develop as a series of two-body collisions governed by conservation of momentum equations. Atoms are displaced from their sites and added to the cascade if, in a collision, they receive energy greater than some critical value E_{crit}, and in displacement loose their binding energy E_b to the surrounding lattice. Atoms are stopped, and removed from the cascade if their energy falls below E_{crit}. (Note that E_{crit} is generally only a few eV and is the energy require to temporarily displace an atom - it is not the same as E_d, the threshold displacement energy, which is the energy required to permanently displace an atom and create a Frenkel pair.) In the simplest form of the BCA, moving atoms are assumed only to interact with

stationary ones, and only if they approach within some set interaction distance, beyond which the two atoms in question are unaware of one another. These assumptions give rise to quite a simple model which can be used to simulate large numbers of cascades at much higher energies (up to several hundred keV) than is possible with 'true' MD models.

The BCA-based codes are especially good at throwing light on high-energy dynamic processes, but ignore such parameters as thermal lattice vibrations and many-body effects, with some even ignoring lattice structure (e.g. TRIM, Ziegler et al. 1985). Because of the exclusion of temperature and time, BCA codes have several failings to do with the thermal spike and subsequent cooling phases of the cascade event, which are now known to be crucial in defect production by cascades. However, in recent work Caro et al. (1990) proposed a set of heat equations to help correctly model this portion of the cascade which gave good results in comparison to MD codes. Examples of BCA codes include MARLOWE (Robinson & Torrens 1974) and CASCADE (Beeler & Besco 1964). A major drawback of these programs with respect to analysis of cascade phase durations is the lack of any recognition of real time during the simulations. This situation was addressed by Fukumura et al. (1991), who modified the MARLOWE code by adding several equations to sum the time between successive collisions of one particle, the time being derived from the kinetic energy of that particle and the distance between collisions.

2.4.3 'True' Molecular Dynamics.

This technique is now becoming increasingly widely used, and is little different in essence from the form used by Gibson et al. Using the classical equations of motion, MD codes repeatedly calculate the space-time trajectories of all the atoms in a model crystal using an interaction potential derived from and fitted to the material's lattice

dimensions and bulk properties.

By definition this methodology is more complex than the BCA, requiring the rapid solving of many thousands of vector equations for position, velocity and force for each division of time. The potentials used are also often complex in order to accurately model their namesake material, with these complexities requiring much greater amounts of computer time and capacity than the BCA formalism. Thus the limits of crystal size and PKA energy that can be simulated fall short of those of the BCA codes. Since MD codes are time-based, unlike the BCA approach, and can also satisfactorily simulate lattice vibrations up to temperatures in excess of the melting point of the material modelled, they therefore provide an inherently more accurate picture of cascade processes than the BCA which, by its very name, is an approximation.

The most widely used examples of full MD codes are MOLDY (MOLecular DYnamics) and its derivatives, developed at the Daresbury Laboratory (Heyes & Smith 1987), and at the Harwell Laboratories as MOLDY6 (Finnis 1988) and used at the Lawrence Livermore Laboratories as MOLDYCASK (Diaz de la Rubia & Guinan 1990). There now exist numerous variants on the original code to model a variety of lattice structures, mostly FCC and BCC to date including pure Cu (Foreman et al. 1992) and Fe (Calder & Bacon 1993), ordered alloys (Ni_3Al, Diaz de la Rubia et al. 1994, Gao & Bacon 1993) and disordered alloys (Cu-Au, Deng & Bacon 1994), and one descendant of this code is used in this study, modified to model the HCP metals.

One other simulation technique used, discussed in more detail in chapter 4, is that of 'static' simulation which, although not used to model the cascade stage of damage, is of wide application in the realm of the post-cascade state and is used to good effect in the treatment of vacancy and interstitial clusters, stacking faults and surfaces with respect to energies, configurations and stability.

- § -

2.5 The Displacement Cascade.

As a result of all the simulations to date and deductions from experimental work the displacement cascade as an event has been spilt into several phases, each with its own set of characteristics and predominating effects.

(i) The Initial Strike: This takes place when an incident particle, whether neutron, electron, or ion, enters the metal and strikes an atom, passing on energy greater than E_d in that collision and thus dislodging it. If the energy imparted in this collision is great enough, this atom can displace another, as can the primary particle, and an avalanche of displacements can occur.

(ii) The Collisional Phase, or Displacement Spike: This phase is characterised by the increasing number of atoms displaced from their sites, each colliding with their neighbours, though occasionally an atom may 'channel' and travel quite far from its original site before striking another atom. The energy of the initial strike is spread over an increasingly larger region by interactions and collisions until the distribution has become so diffuse that no atom has energy great enough to cause other displacements, the mean free path of any moving atoms has shrunk to less that the nearest-neighbour separation, and therefore no more displacements take place. This phase typically lasts a few tenths of a picosecond depending on the PKA energy.

(iii) The Relaxation Phase, or Thermal Spike: Once the cascade has reached its maximum volume at the end of the collisional phase, displaced atoms then begin to recombine with close vacancies, releasing energy as they do so. This means that even

though the number of defects is reducing, the temperature at the cascade core may still be rising. However, as the number of defects nears its final value, the temperature begins to fall, but may still exhibit 'hot-spots' localised around remaining defects, giving them sufficient energy to migrate to form clusters or annihilate with those of opposite type.

(iv) The Final Defect State: Sometimes referred to as the 'primary defect state', this is reached a few ps after the initial strike, though this time depends again on the energy of the PKA. Some vacancies and interstitials will remain, unable to recombine with each other, and unable to move very far during the time when the temperature generated by the cascade finally dissipates into the surrounding lattice. In general, the vacancies lie near the centre of the regions of most disorder, often forming discs which can collapse to form vacancy dislocation loops which can be observed in a TEM as described previously. The interstitials tend to be situated near the edge of the cascade envelope, often in small clusters.

However, even though the cascade phases are well defined, there are still numerous questions about the processes occurring within each of these phases, and the relationship of these processes to the size and duration of each phase.

- § -

2.6 Questions to be Addressed.

There are several main issues which are still not fully understood, despite the wealth of experimental and simulation data produced so far. Possible trends have been identified within the cubic systems, though very little work has been done on the HCP metals. It is hoped that this work will help to clarify the relevance of these

tendencies to the HCP metals, and identify and possibly explain the similarities and differences which exist.

2.6.1 Vacancy-Interstitial Separation.

One of the questions which has not yet been answered in a completely satisfactory manner is that of exactly how matter is ejected from the cascade core. It was originally thought that RCS events were primarily responsible for this, and much work was done on counting the number of replacements in sequences found in experimental and simulated results (Bullough 1992), as already mentioned. Several other mechanisms have also been proposed, some involving the outward movement of interstitials, and others the inward migration of the vacancies.

One idea regarding SIAs is that they are produced by a shock-wave phenomenon which, as the cascade expands and disorders during the collisional phase, causes atoms on the periphery to be ballistically ejected outwards and, as the cascade collapses, they cluster together in the elevated temperatures of the thermal spike and are left trapped (English et al. 1992). One variant of this is interstitial loop 'punching' which results from several neighbouring and parallel RCSs travelling out of the cascade core together, and forming an interstitial loop at their end (Diaz de la Rubia & Phythian 1992).

On the vacancy side, there are two main theories as to why the core collapses to form a vacancy loop as observed in experiment. One, proposed by Protasov & Chudinov (1982), was that, during the thermal spike phase, vacancies were able to migrate up the thermal gradients in the cascade core towards its hot centre, thereby forming a loop which remained until the thermal spike had dissipated. However, Averback and Seidman (1987) hypothesised that the cascade core melted, not unreasonable

considering the amount of energy concentrated in such a small region, and that the vacancies were 'swept' towards the centre of the cascade as the liquid core resolidified radially inwards, again giving rise to a vacancy loop. Kapinos and Bacon (1993) have also recently put forward a model which includes the equalisation of pressure within the molten core and this, coupled with the high thermal gradients present, allows the vacancies to be swept into the centre to form a loop. However, these explanations assume the melting of the cascade core region.

2.6.2 Cascade Core Melting.

Ever since Brinkman's first sketches of cascade cores, there has been debate as to whether the core of a cascade becomes liquid or remains solid during the collisional and thermal spike phases. From simulation, temperatures in excess of the melting temperature of the model have been recorded, and radial distribution analysis of the spatial arrangement of the atoms in the core have yielded curves close to, but not exactly, that of a liquid (Diaz de la Rubia et al. 1989, Foreman et al. 1992, Calder & Bacon 1993). However, descriptions of this region vary, and include super-heated solids, cavitated quasi-liquids and true molten metals. What is apparent from these works is that the atomic density within the cascade region is reduced to 80 - 85% of the density of the surrounding bulk solid, again in line with the early ideas. This issue is still subject to much discussion, with some favouring the melting idea on the basis of core collapse and loop formation, and others the superheated solid or quasi-liquid analogy on the grounds that a 'true' liquid cannot be formed within the confines of the temporal and spatial dimensions of a cascade core. Whatever the interpretation the cascade core structure has implications for ion mixing, something of importance when considering alloys, particularly the ordered ones. This also has bearing on the formation radiation-induced phase changes, analogous to temperature-induced phase changes, in some metals.

2.6.3 Cascade Efficiency

The efficiency of a displacement cascade is not the same as the DRE mentioned previously, but is a measure of the ability of a material to produce and retain defects in any configuration, not just in dislocation loops, in a single cascade created by a PKA of known energy. This parameter is of major relevance to the long-term microstructural evolution of radiation-damaged materials, and has long been based on the NRT formula (Norgett, Robinson & Torrens 1975)

$$N_F = k\frac{E_{dam}}{2E_d} \qquad (2.5)$$

where N_F is the final number of Frenkel pairs, E_{dam} is the proportion of the PKA energy available for displacements (which can be less than E_{pka} due to electronic losses), E_d is the displacement threshold energy per atom, and k is the cascade efficiency factor. This expression is a modification of the Kinchin & Pease (1955) hard-sphere approximation, and the inclusion of k allows for the fact that atoms do not scatter by hard-sphere interactions. Originally k was estimated by Norgett et al. to be 0.8, except at very low energies where E_d becomes increasingly directionally dependent. Even at higher PKA energies, this expression is greatly affected by the value of E_d used, and it is therefore important to measure E_d correctly.

In computer simulation studies of displacement cascades in various cubic metals (Foreman et al. 1992, Diaz de la Rubia & Phythian 1992, Calder & Bacon 1993) a dependence of k on PKA energy has been observed by rearranging equation 2.5 with respect to k and calculating an effective efficiency from the final number of Frenkel pairs produced in simulated cascades. An example k-curve is shown in fig. 2.6 for computer simulations in α-iron. In all the studies the effective k starts at the NRT

estimate of ~0.8 at PKA energies of the order of 100 eV, and then drops quite sharply to 30-40% of its initial value at E_{pka} between 500 eV and 2 keV depending on the simulated metal. The efficiency then decreases more slowly as PKA energy increases. This has been interpreted as a change in cascade structure at energies of the order of 1 keV from an open, RCS-dependent form below this energy, to a dense, highly disordered structure above it. The form of the k-curve appears to have no crystal-structure dependence within the cubic metals, though the energy of the 'knee' varies from metal to metal. Also calculated in the above studies was the efficiency factor for single and di-interstitials only, as it is assumed that these smaller defects are more mobile that larger clusters, and can therefore migrate from the cascade site into the bulk . As shown in fig. 2.6, the k-curve for the single and di-interstitials follows the k-curve for all defects until the 'knee', where is falls below as larger SIA clusters are formed at higher PKA energies, again indicating a change in dominating cascade processes at energies around 1-2 keV. It is important to investigate to what extent this effect is present in the HCP metals, as it has direct bearing on the numbers of defects remaining for post-cascade processes, particularly in light of the lower symmetry of the HCP system and its possible effects on defect behaviour.

2.6.4 Defect Clustering

The importance of single and clustered defects has already been stated, but one issue still under scrutiny is the mechanisms by which these clusters form, particularly among the SIAs. Possible mechanisms for vacancy clustering have already been outlined in sections 2.6.1 and 2.6.2 with respect to Frenkel pair separation and core melting. Vacancy clustering is thought to take place during the thermal spike since, at temperatures below stage III annealing (or stage IV depending on the preferred model) after a cascade, thermal vacancy diffusion is not possible. However, SIAs are mobile at much lower temperatures, and may either be formed at the end of the

collisional phase, as with loop punching, or during the elevated temperatures of the thermal spike, or even afterwards by thermal diffusion. Differences have been observed between SIA cluster sizes in simulations of BCC iron and FCC copper, with iron exhibiting a lesser degree of larger (e.g. tri- and tetra-interstitial) cluster formation at lower PKA energies (Calder & Bacon 1993). The dependence of clustering on PKA energy is also borne out by the observation that SIAs produced by RCSs in lower energy cascades were well separated from one another and little clustering occurred, whereas at higher PKA energies beyond the knee in the k-curve, collective RCSs and ballistic effects sometimes led to SIAs within a few nearest-neighbour distances which subsequently reorganised into small clusters during the thermal spike, thus explaining the 'split' in the total and small-cluster k-curves referred to in the previous section. Depending on which clustering mechanisms predominate, small mobile clusters of defects may be produced which can then migrate to surfaces and sinks such as grain boundaries and precipitates, or larger, sessile clusters formed which are unable to move, and this also has great bearing on the post-cascade evolution of microstructure. Again, the differences in symmetry between the cubic and hexagonal lattices may have direct consequences with respect to the above effects, and the orientations preferable for cluster formation and movement.

2.6.5 Structural Dependence

As mentioned in the above sections, by far the greater majority of cascade simulation has been conducted on the cubic metals, and very little attention has been directed towards the other significant systems, specifically the HCP class. Much groundwork has been done with respect to the energetics, configurations and volume effects of point and extended defects with static simulation (see reviews and studies by Bacon 1988, Johnson 1991 and Mercer-Calder 1992), but no work of real significance

exists on dynamic events. Within the cubic system, no real dependence of general qualitative cascade effects on crystal structure has been found, though specific quantitative parameters are material dependent. It was therefore intended in this work to provide a foundation study within the HCP system to explore the similarities and differences between two quite different classes of metals in all aspects of cascade mechanisms.

- § -

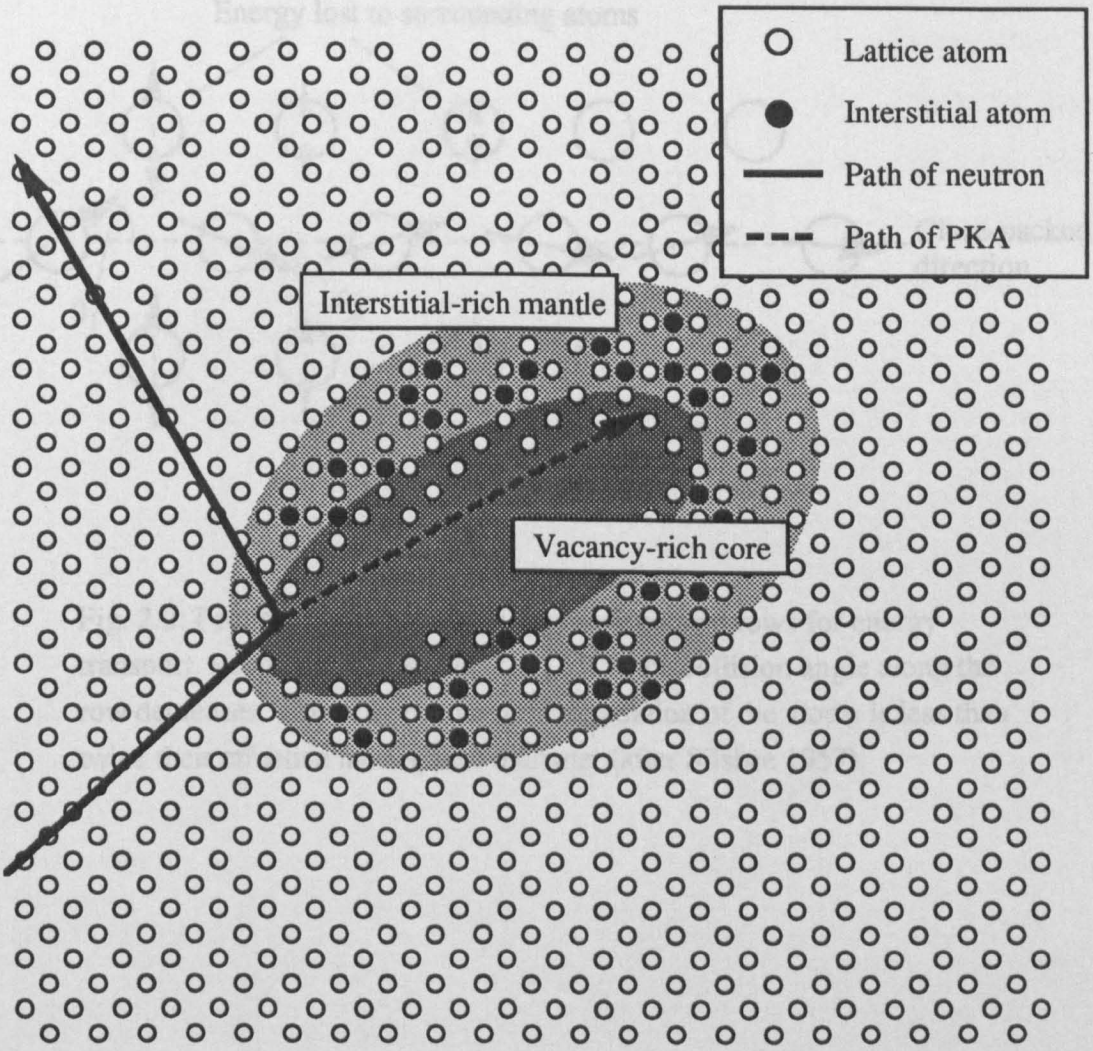

Fig. 2.1: Qualitative schematic of a displacement spike (after Brinkman 1954).

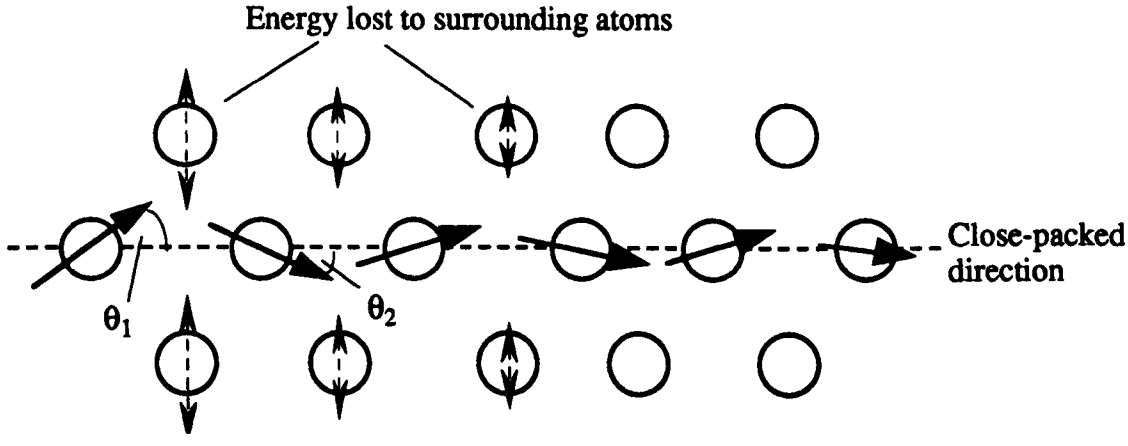

Fig. 2.2: Focusing of collisions along close packed rows for energy transport. Focusing occurs if $\theta_n < \theta_{n-1}$, i.e. the collision angle along the row decreases. This only occurs if the separation of the atoms is less than twice their effective hard-sphere diameter (after Silsbee 1957).

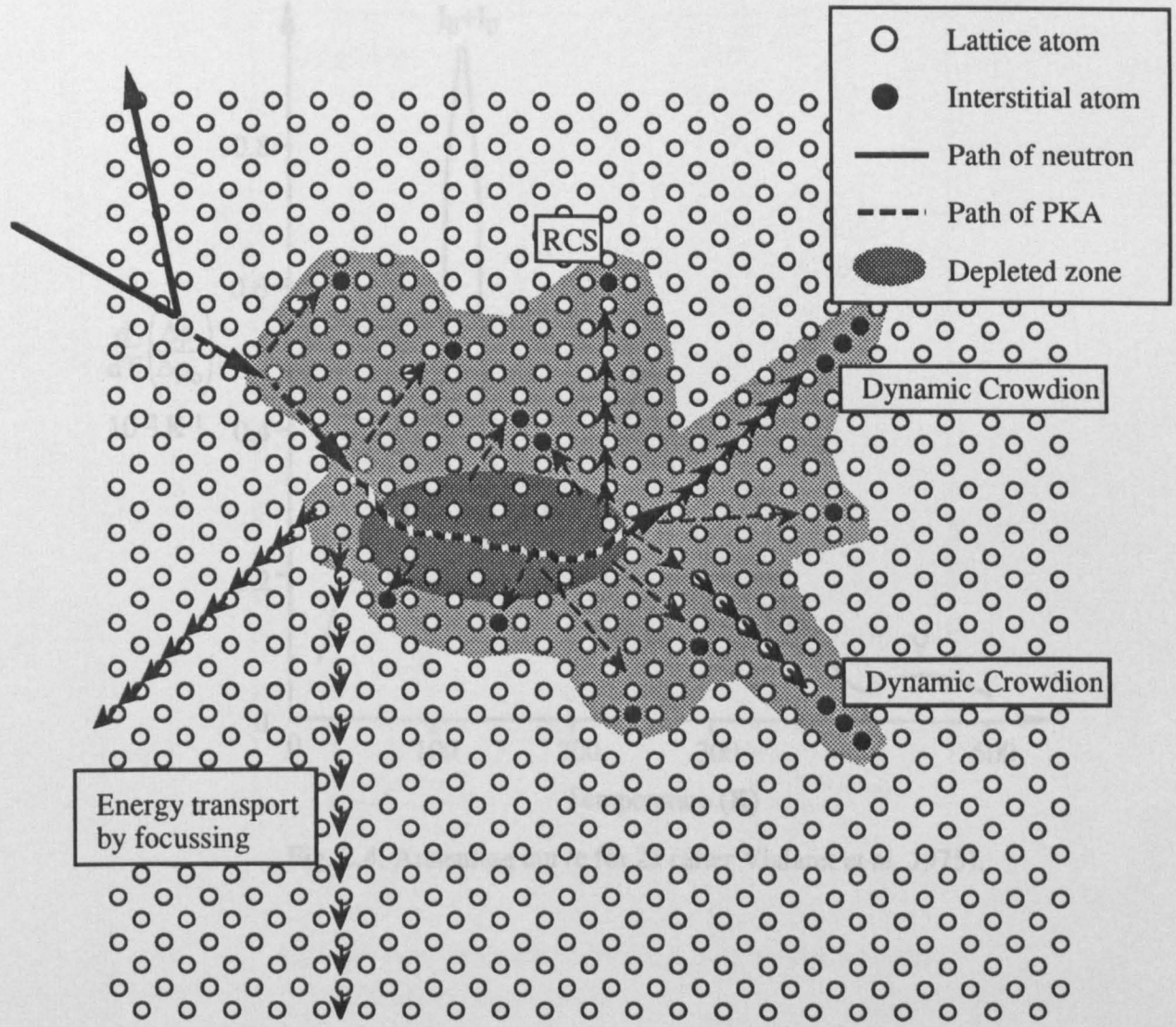

Fig. 2.3: Later version of the displacement spike, including mass and energy transport mechanisms (after Seeger 1958).

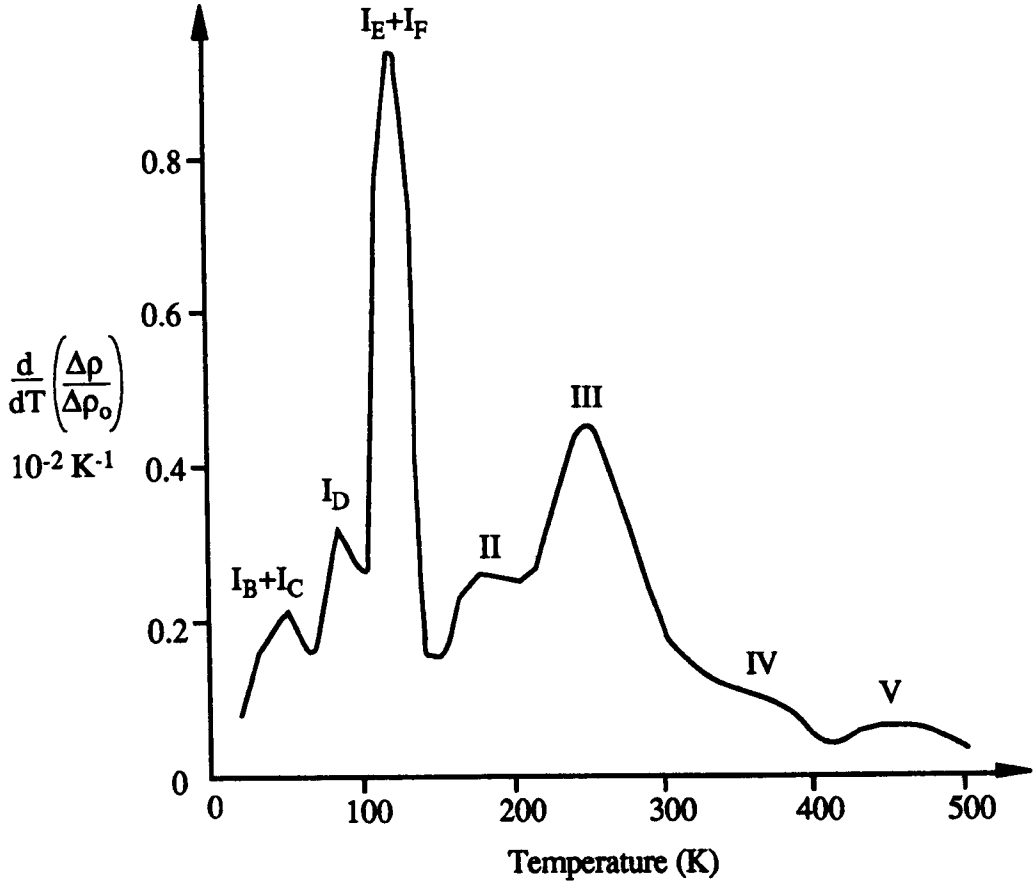

Fig. 2.4: Annealing curve for Zr (after Vialaret et al. 1975).

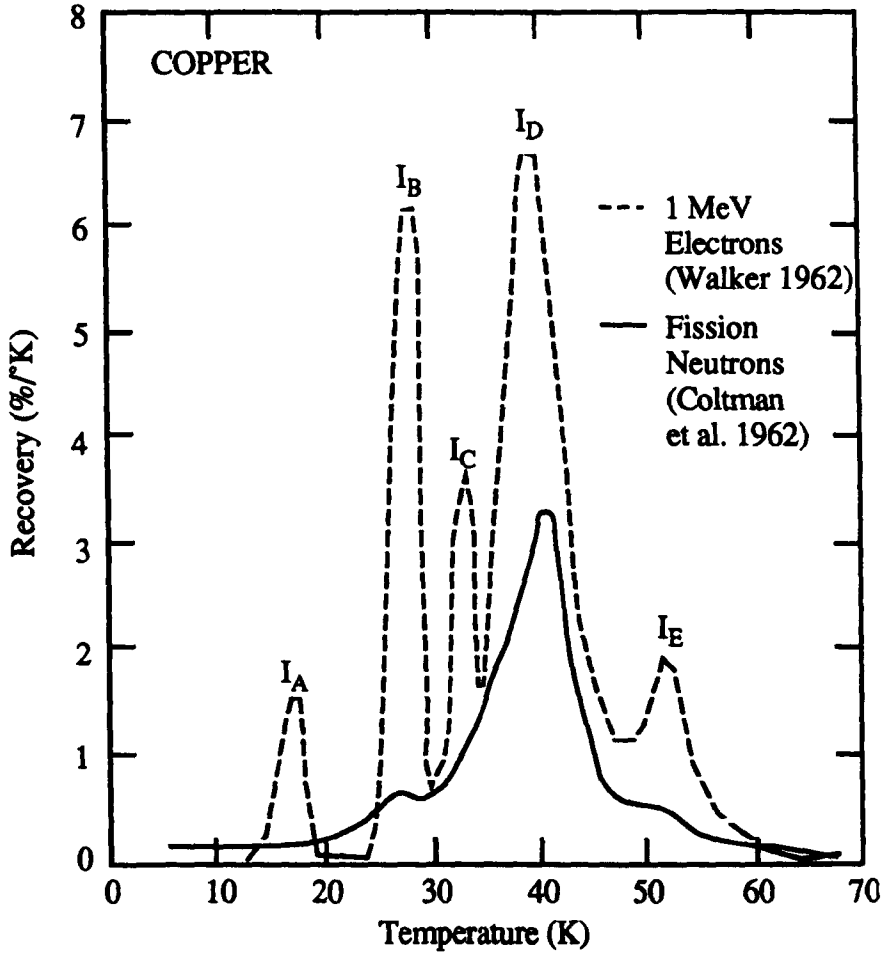

Fig. 2.5: Annealing curve for Cu after irradiation at 4 K (after Zinkle & Singh 1993).

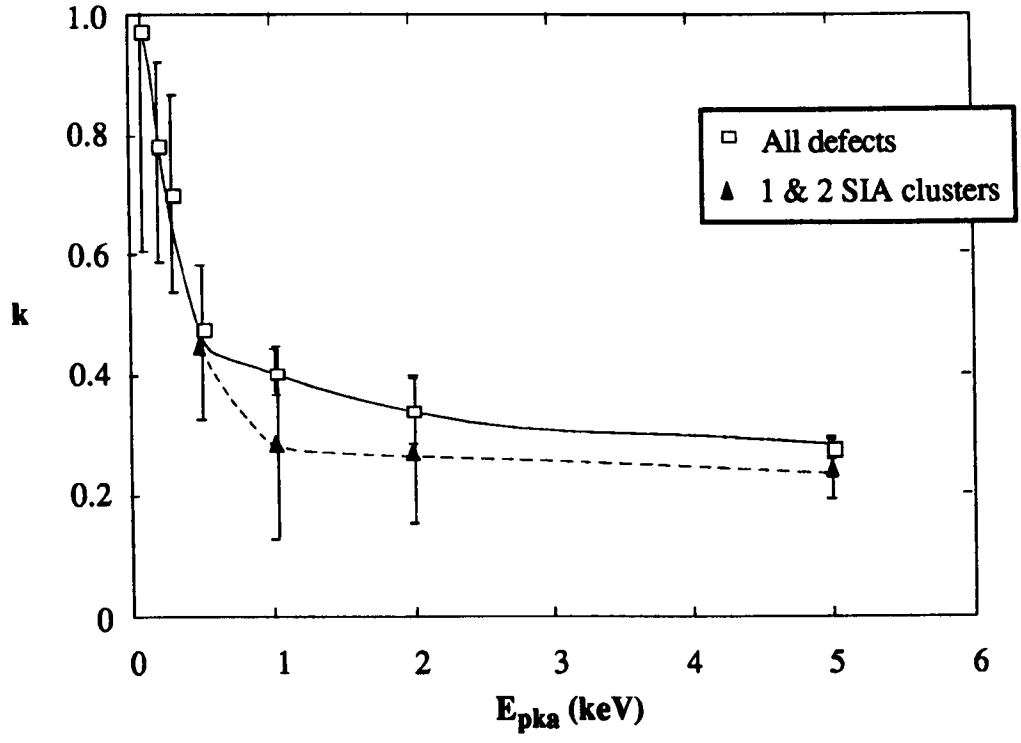

Fig. 2.6: Cascade efficiency factor k vs. PKA energy for MD simulations of BCC iron at 100 K (after Calder & Bacon 1993). The error bars denote the standard deviation from the mean.

III

The Computer Model

3.1 Introduction.

Any attempt to simulate a material of any kind, not just metals, requires the presence of several basic elements: a structural geometry to govern the spatial relationship of the atoms or molecules to one another, a set of expressions to govern their interactions and a computer code to perform the calculations.

In this chapter the origins of interatomic potentials will be briefly discussed, and the different models and approaches within the field will be made apparent. The form of the potentials used in this work will then be discussed in more detail, along with the modifications and enhancements made to them en-route. The code used to perform the simulations will also be described, and the general methods used throughout the modelling will be introduced.

- § -

3.2 Potentials in General.

The forces governing the interactions of atoms in the solid state have been the subject of much study for many years. Probably the most widely known approximation to such atom-atom interactions is the Lenard-Jones (LJ) potential (1924),

$$V(r)=\frac{V_0}{(n-m)}\left\{m\left(\frac{r_0}{r}\right)^n-n\left(\frac{r_0}{r}\right)^m\right\} \qquad (3.1)$$

where n and m are integers (usually taken to be 12 and 6 respectively), V_0 is the minimum value of the potential at r_0, and r is the actual inter-atom separation at which the value of the potential is to be calculated. The form of this equation is shown schematically in fig. 3.1. The form of the LJ potential is typical of many pair potentials, which at separations less than r_0 have a negative gradient and are therefore

repulsive in this region, since force is proportional to the gradient of a potential: this models the Coulomb repulsion of the ion cores. At separations greater than r_0 the gradient is positive, and hence the force is attractive to mirror the sharing of electrons in ionic materials. For separations equal to r_0 there is no force as the gradient is zero, giving r_0 as the equilibrium separation of two atoms isolated from the rest of the universe. In order to account for the energy of a solid block of many atoms, a sum has to be taken of all the interactions of each atom with every other atom present. This gives

$$E_{tot} = \sum_{i=1}^{n} \sum_{j=i+1}^{n} V(r_{ij}) \qquad (3.2)$$

where E_{tot} is the total energy of a block containing n atoms, and $V(r_{ij})$ is the potential between the ith and jth atom, separated by a distance r_{ij}. Thus the cohesive energy per atom of a crystal described by this potential is given as

$$E_c = \frac{E_{tot}}{n} \qquad (3.3)$$

Since these simple beginnings, the complexity of the equations used to model material behaviour has increased dramatically, particularly over the last few decades. Models do now exist which make use of first-principles derivations involving density-functional theory, but the resulting expressions for the interatomic forces, although not impossible to solve, are quite complex and unwieldy (Finnis 1992). With present levels of computational speed and power, simulations using these methods are severely limited in size, often to only a few atoms and, even though they give accurate predictions, their use is therefore somewhat restricted. Approximations have therefore been made in an attempt to yield equations simple enough to be of extensive computational application, but encompassing most of the requirements for constructing a model which is a good parallel of reality. Those which are in

widespread use are discussed further, and can be broadly divided into two main categories.

3.2.1 Pairwise or Two-body Potentials.

So called because they only take into account the actions of two atoms on one another in a solid, and sum these interactions over all atoms present, these potentials, of which the Lenard-Jones is one (see Bacon 1988 for a review of HCP potentials), are limited in that they ignore the cohesive effect of the electrons in the metal. In so doing, they can only give indication of the general qualitative properties of HCP metals, such as the effects of the lower symmetry of the HCP lattice on defects and stacking faults.

Another deficiency in this class of potentials is that the cohesive energy E_c and the unrelaxed vacancy formation energy E_f^v are equal as a result of the equational form. Whilst this is approximately true for some noble gas solids, metals in general have $E_f^v \approx {}^1/_3\, E_c$. Thus if the potential yields a correct value of E_c, E_f^v is too large, and if the potential parameters are adjusted to give a correct value for E_f^v, then E_c becomes too small. Also inherent in this framework is the Cauchy relationship for the elastic constants of the model metal such that $C_{12} = C_{44}$ in the cubic metals and $C_{13} = C_{44}$ in the HCP case, though some 'non-equilibrium' pair potentials break these conditions by the addition of an external pressure applied to the surfaces of a model crystal (Bacon 1988).

3.2.2 Many-body or N-body Potentials.

By adding a second term to the pair-wise eqn. 3.1 to account for the effect of the

electron 'gas', the presence of the valence and conduction bands can included without having to resort to elaborate first-principles derivations of the actual band energetics (Ackland, Finnis & Vitek 1988). Within this class of potentials there are several sub-divisions based on the the initial assumptions and approximations used to derive the pair and many-body terms of the potential.

Finnis and Sinclair (1984) approached the problem by considering the effect of electron bands spreading as atoms are added together to form a solid. The pair term of their potential was entirely repulsive in nature to reflect the electrostatic interactions of the ion cores of the constituent atoms, whilst their second term accounted for the cohesive effect of the electrons, in particular those in the d-band.

Daw and Baskes (1984) took a slightly different approach and considered the energetics of embedding a single atom in a metallic solid: the 'embedded atom method' (EAM). They assumed this solid to consist of a homogeneous electron gas, a valid approximation since the arrangement of the metallic ions in the lattice would be effectively screened by the 'free' electrons and therefore not noticed by the atom to be embedded. Hence their pair-wise interaction term is, as in the FS model, purely repulsive to model the ion-ion interactions, and the second term reflects the embedding energy required to plant an atom at its site. This second term is negative and depends on the local density of electrons around a particular atom.

Others have considered the constituent atoms and electrons together to form a continuous medium in the 'effective medium' model (Norskov & Lang 1981), and the 'local volume' model (Voter & Chen 1987). Additional approaches include the 'glue' model, in which the effect of the electrons is approximated to an extra 'adhesive' which contributes to the binding of the atoms (Ercolessi, Tosatti & Parinello 1986).

Different though the starting points for each model may be, all contain three basic

elements: a pair-wise interaction term representing ion-ion repulsion, an n-body term to account for the presence of the electrons, and an embedding function to reflect the energy gained by placing an atom within such an electron gas. It is the FS approach which is used in this work, and this is now described in more detail.

3.2.3 The Finnis-Sinclair Formalism.

Using the FS formalism, the total energy of some atom i in a solid is given as

$$E_i = \frac{1}{2}\sum_j V(r_{ij}) - f(\rho_i) \qquad (3.4)$$

where index j runs over the neighbours of atom i, r_{ij} is the separation of the atoms i and j, $V(r_{ij})$ is a pairwise potential energy at that separation and $f(\rho_i)$ is the embedding function. ρ_i is the total many-body contribution representing the local electron density, and is a function of the position of the surrounding ions, given by

$$\rho_i = \sum_j \phi(r_{ij}) \qquad (3.5)$$

where $\phi(r_{ij})$ is the many-body contribution between atoms i and j .

In this model V(r) is completely repulsive, i.e. positive, from tight-binding theory, and $\phi(r)$ is attractive, i.e. negative, to account for the cohesive effect of the valence electrons. The embedding function f(x) has been shown to be a square room term by ab-initio calculations (Robertson et al. 1993), within the second moment approximation, i.e.

$$f(\rho_i) = \sqrt{\rho_i} \qquad (3.6)$$

The simplicity of this approach is that V(r) and $\phi(r)$ are both pair-wise functions,

though their actual mathematical forms can differ quite radically from one model to another. However, they generally include parameters fitted to known physical properties of the metals under study, such as lattice parameters, cohesive, vacancy formation and stacking fault energies and elastic constants. Using this pattern many materials have been simulated, particularly with reference to the properties of defects such as grain boundaries, point defects, dislocations and stacking faults. More recently, higher energy events such as displacement cascades have begun to be investigated using these inherently more complex and more compute-intensive potentials.

3.2.4 HCP-Specific Potentials.

Attention has so far been primarily concentrated on the cubic metals, such as copper, gold and iron, for which much experimental data as regards material properties is available, and because of the relatively simple nature and symmetry of the cubic lattice. More recently however, the HCP metals have come under study. These have several added problems over the cubic metals in that they have five independent elastic constants as opposed to three for FCC and BCC metals, and have two separate lattice parameters instead of one, this being due to the lower symmetry of the hexagonal lattice.

Earlier attempts using pair potentials (See Bacon 1988 for a full review) achieved the HCP structure by taking a potential which yields a stable FCC lattice, and inserting a repeated intrinsic stacking fault every third plane to change the FCC ABCABCABC... {111} stacking sequence to the HCP ABABABAB... [0001] stacking sequence. If the potential parameters are then 'tweaked' so the energy of the FCC intrinsic stacking fault of this type becomes negative, then the HCP structure becomes favourable, and if positive then the FCC lattice is preferred. However, using this method highlights

two more failings of pair potentials in that all the HCP crystals so produced have a $^{c}/_{a}$ ratio very close to the ideal value of $\sqrt{(^{8}/_{3})}$, not what is observed in most real HCP metals (Pearson 1967), and the stacking fault energies for such models are quite small in comparison to reality (Bacon 1988).

More recently much better attempts have been made using the many-body formalism (Igarashi, Khanatha & Vitek 1991, Oh & Johnson 1989) which give good fits to most of the physical parameters, and have been used mainly in static investigations. However in the case of Igarashi et al. the potentials they developed were highly oscillatory in nature in both the ion-ion interaction and n-body terms and, when used for point defect simulation, it was found that such potentials had excessively high interstitial formation energies (Mercer-Calder 1992). The oscillations in the two terms also caused problems with stability in the presence of defects. The Oh & Johnson potentials were of a relatively long range, which made more widespread application impractical as computing time increases dramatically with the range of the potential used (Kulp et al. 1992). However, the $^{c}/_{a}$ ratios produced by these potentials are far more consistent with real metals and this factor is important in the formation and migration of point defects and clusters, which will be discussed in chapter 4.

Of the many potentials investigated in the Mercer-Calder (1992) study, the most favourable potential overall with respect to stability, point defects and clusters, and good agreement with the material parameters for its namesake metal was developed by Ackland (1992) to model α-Ti. Since then he has applied his technique to produce another potential of similar form for α-Zr (Ackland et al. 1994). As these two potentials form the basis of the work performed here, they are now described in more detail, together with the modifications made to them.

- § -

3.3 The Ackland Potentials.

Ackland began his parametrisation from a similar point to that mentioned previously with reference to the pair potentials - that of using the similarity of a faulted FCC {111} stacking sequence and the ideal HCP (0001) sequence. Indeed the radial distribution of the nearest eighteen neighbours to any atom in the FCC lattice is identical to that of an ideal HCP metal, though the atom positions are not the same. However, Ackland extended the range of his potential slightly beyond this to take in the next two neighbours - those at separation c from the origin - and, since their contribution is quite weak as they are in the 3rd-nearest-neighbour shell, treated them as a perturbation rather than a full stacking fault. In his parametrisation, Ackland used the following elastic constant equalities:

$$2C_{66} = C_{11} - C_{12} \tag{3.7}$$

$$C_{33} + C_{13} = C_{11} + C_{12} \tag{3.8}$$

$$C_{12} + C_{44} = C_{13} + C_{66} \tag{3.9}$$

Equation 3.7 is true of any lattice possessing hexagonal symmetry. Equations 3.8 and 3.9 result from his short-range approximation and are not specifically related to the HCP structure, as they apply to the ideal $^{c}/_{a}$ ratio HCP and FCC structures as long as only the first eighteen neighbour interactions are included. However, this was in fact a valid approach since from experimental data (listed by Ackland 1992) many HCP metals obey equations 3.8 and 3.9 to within a few percent. There are exceptions, as with most approximations, due to large $^{c}/_{a}$ ratios, and magnetic and binding effects in some HCP metals, such as Zn, Co, Cd and Be.

Ackland fitted his potentials to only three elastic constants (calculated from experimentally determined values for Ti and Zr), consistent with his approximation, and to E_c and E_f^v. By extending the range of the potential to include the third-nearest-

neighbours, thus breaking the equalities 3.8 and 3.9, and by setting a net attraction at this separation to ensue that the FCC {111} intrinsic stacking fault energy was negative, i.e. preferable, he produced a model with a $^{c}/_{a}$ ratio a great deal less than ideal in comparison to the attempts with pair potentials discussed above. The so-called 'inner' elastic constants, which are present due to the diatomic basis of the HCP structure, were ignored in the fitting, but the resulting values for the HCP elastic constants (now five as a result of extending the potential range, not the three used in the original parametrisation) agreed well with experimentally measured values in which these inner distortion effects are included.

The Ackland models use the FS formalism for calculating the total energy for each atom (equations 3.4, 3.5 & 3.6), with V(r) and ϕ(r) being cubic splines of the form

$$V(r_{ij}) = \sum_{k=1}^{n} a_k (r_k - r_{ij})^3 h(r_k - r_{ij}) \qquad (3.10)$$

$$\phi(r_{ij}) = \sum_{k=1}^{m} A_k (R_k - r_{ij})^3 h(R_k - r_{ij}) \qquad (3.11)$$

A_k and a_k are fitting constants, R_k and r_k the knot points of the two splines, and n and m are the number of knot points in each term (for the Ackland potentials n=6 and m=2, though for Zr n was increased to 7 for reasons explained later). h(x) is a simple step function such that h(x)=1 if x>0, and h(x)=0 if x≤0, which means that as r_{ij} decreases, the number of cubic splines active in each equation increases up to a maximum. The values of these parameters are given in table 3.1 for both the Ti and Zr potentials. The equational form of the potentials is arbitrary, and the choice of cubic splines was simply to ensure automatic continuity in the first and second derivatives.

One problem with the Ackland parameters as supplied is that, due to his parametrisation method, they were cast with reference to an FCC lattice, so all values

of a_k and A_k (with units of eV and eV^2 per FCC lattice parameter cubed respectively) had to be scaled to reflect the fact that the HCP basal lattice parameter is equivalent to the FCC nearest neighbour distance in the ideal case, which is $^1/_{\sqrt{2}}$ times the FCC lattice parameter. Thus a_k and A_k were scaled by a factor of $2\sqrt{2}$, and all values of r_k and R_k scaled by $\sqrt{2}$ to give units of eV/a_0^3 and eV^2/a_0 respectively. A small correction factor (<0.5 %) had to be applied to all the potential parameters before calculation to give the correct lattice dimensions and a stable lattice at 0 K, simply because the FCC lattice parameters Ackland fitted to and the HCP basal lattice parameters used in this work were not exactly a factor of $\sqrt{2}$ different. The values given in table 3.1 have been scaled as described, and are the values actually used in all the simulations detailed in this work. Table 3.2 gives the values of E_c, E_f^v, the I_2 stacking fault energy (...ABABCACA...) and elastic constants obtained from these are seen to agree to within a few percent or so of those given by the potential, thus showing that the perturbation approximation Ackland made in his fitting was valid.

Originally these potentials were intended for use in simulating static properties such as point defects, stacking faults and surface reconstructions, which they do to good effect (Ackland 1992, Ackland et al. 1994). This meant that attention was concentrated in the area of low energy interactions and atomic displacements much less than the equilibrium atom separation. However, for this project, in which high-energy collision events and atomic displacements around defect clusters were envisaged, interactions well inside the normal nearest-neighbour spacing were required, and therefore the potentials had to accurately predict atomic behaviour in this regime in order to be of use. This was tackled in two ways, as outlined below.

3.3.1 Verification of the P-V Response

Changes in local atomic volume, and hence local pressure, are brought about by the

production of defects, particularly SIAs, and radial pressure waves can be generated during the collisional phase of a displacement cascade. It is therefore important that any models used to investigate these matters give good representations of the 'true' response to pressure and volume changes, and it is also a convenient way of checking the validity of a model, as pressure-volume (P-V) data can be quite accurately obtained by experimental measurement. Two independent sets of 'experimental' data were used for verification of the theoretical P-V response given by the two potentials.

From the theory of Rose et al. (1984), it was shown that all solid metals follow, to a very good approximation, the same empirical equation of state, which depends on several material parameters such that

$$P(\Omega) = 3B\left\{\frac{\left(\frac{\Omega}{\Omega_0}\right)^{\frac{1}{3}} - 1}{\left(\frac{\Omega}{\Omega_0}\right)^{\frac{1}{3}}}\right\} e^{-a^*}\left(1 - 0.15a^* + 0.05a^{*2}\right) \qquad (3.12)$$

where $P(\Omega)$ is the pressure at a given atomic volume Ω, B is the bulk modulus, Ω_0 is the equilibrium atomic volume, and a^* is given by

$$a^* = \frac{r_{wse}\left\{\left(\frac{\Omega}{\Omega_0}\right)^{\frac{1}{3}} - 1\right\}}{L} \qquad (3.13)$$

in which r_{wse} is the equilibrium radius of the Weigner-Seitz cell, and L is given as

$$L = \left(\frac{E_c}{12\pi B r_{wse}}\right) \qquad (3.14)$$

where E_c is the cohesive energy. Using the values given in table 3.4 for these parameters, the P-V response of the Ti and Zr potentials was determined.

This second set of measurements was taken from ballistic experiments (Kinslow 1970) in which the metal under consideration was subjected in bulk form to high velocity impacts from a ballistically fired flat plate, and the velocity of the impacting plate and resultant shock-wave in the solid were measured, and the P-V response determined.

To compare these two sets of data with the potentials, the HAIN FORTRAN code (Bacon & Martin 1981) was employed. This uses the potential form and parameters and the lattice structure to determine the lattice parameters, elastic constants, Ω, E_c and E_f^v for a given pressure P. Given a trial set of lattice parameters, the code calculates the elastic constants and internal stress matrix, applying a lattice strain to offset the applied external pressure iteratively, until the internal stresses are removed. Using this program, the P-V response of the Ti and Zr Ackland potentials was determined. It was found that in as-supplied form the Ackland Zr potential gave too shallow a P-V curve at high pressures, and so the 7th term in the V(r) equation was added for this work to shift the original P-V response to more closely match the other data sources, particularly the experimental data.

The results of the HAIN code, along with the Rose-Ferrante theoretical predictions and Kinslow's experimental results are shown in figs. 3.2(a) and (b) for Ti and Zr respectively, with the pressure normalised to units of kT_m/Ω_0 (Boltzmann's constant times melting temperature per equilibrium atomic volume) for the sake of comparison. In both cases the potentials fit extremely well to the experimental data, but differ from the Rose-Ferrante predictions by around 10% in the volume response for a given pressure. Another feature of these two potentials is that, although fitted to two different metals with differing properties, their P-V curves follow each other very closely in these normalised units. This is, however, to be expected given the similarity of their properties in equation 3.12 when expressed in normalised units of

kT_m and Ω_0. Once the effectiveness of the P-V curve for each potential had been established, one further modification was necessary.

3.3.2 Addition of the Biersack-Ziegler Universal Potential.

Due to the origins of the two potentials lying in the field of statics, little attention had been given to the modelling of high energy events, during which atoms may be forced to approach within small fractions of their equilibrium separation a_0. As a result of this both the Ti and Zr potentials proved too soft at separations less than $\sim^1/_3\ a_0$, and during preliminary simulations atoms with sufficient energy were able to 'pass through' one another without V(r) going to infinity. To rectify this, the universal potential of Biersack & Ziegler (1982) was spliced into the inner core of the Ackland potential, replacing the Ackland pair-potential. This 'universal' potential has been tested against many other empirically fitted and theoretical potentials, and was deemed to be the best of its kind in one quite exhaustive study (O'Connor and Biersack 1986) in which it is compared to over one hundred other potentials. It has also been widely used to good effect by workers using the BCA-based models (TRIM, MARLOWE) mentioned in the previous chapter.

The universal potential is essentially a screened-Coulomb repulsion term which is of the form

$$V(r_{ij}) = \frac{Z_1 Z_2 e^2}{4\pi\varepsilon_0 r_{ij}} \varphi\left(\frac{r_{ij}}{a_{scr}}\right) \qquad (3.15)$$

where Z_1 and Z_2 are the atomic numbers of the two atoms involved, e is the electronic charge, ε_0 is the permitivity of free space, and the screening length a_{scr} is given by

$$a_{scr} = \frac{0.8853 a_{bohr}}{\left(\sqrt{Z_1} + \sqrt{Z_2}\right)^{\frac{2}{3}}} \qquad (3.16)$$

in which a_{bohr} is the Bohr radius, and is equal to 0.529 Å. $\varphi(x)$ is an exponential function such that

$$\varphi(x) = \sum_{k=1}^{4} C_k e^{-(B_k x)} \qquad (3.17)$$

The values of B_k and C_k, which are dimensionless, are listed in table 3.3.

In order to ensure continuity in the pair interaction term, and its first derivative, a four-term exponential curve was fitted in between the universal and Ackland potentials, such that

$$V(r_{ij}) = F_0 e^{(F_1 + F_2 r_{ij} + F_3 r_{ij}^2 + F_4 r_{ij}^3)} \qquad (3.18)$$

The values of F_n are listed in table 3.5. Great care had to be taken in choosing appropriate points to cross from one potential to another to ensure that the region in which the exponential operated was relatively small, and that the Ackland potential was still effective for small deformations and volume changes for which it was intended, and has been shown to give good results (Ackland 1992). The cross-over points were also adjusted carefully to give as best a continuity as possible in the second derivative of the pair interaction term. Given in table 3.6 are the cross-over points for both the Ti and Zr composite potentials, the form of which is shown in figs. 3.3(a) and (b). As a general observation it can be seen that the universal potential is effective at separations less than $\sim^1/_3\ a_0$, and the Ackland potential at separations greater than $\sim^2/_3\ a_0$ in both cases, with the exponential fitting curve active between these two values. The values of V(r) at these points are also listed in table 3.5, and are of significance in the calculation of displacement threshold energy, which will be discussed in chapter 5. The many-body term $\phi(r)$ was left unchanged and becomes negligible in comparison to V(r) at small values of r.

- § -

3.4 Simulation Methodology and the MOLDY Code.

The MOLDY code, as introduced in the previous chapter and originally used for the cubic metals, has been modified to allow modelling of the HCP metals. The Ackland potentials have been incorporated directly into the relevant routines within MOLDY in their equational form, and a breakdown of the MOLDY program, and the modifications are given in appendix A.

Essentially MOLDY models an arrangement of interacting points in space, keeping a time-based record of the positions, velocities, accelerations and rates of change of acceleration of all the 'atoms' in the model. Initially, the atoms are situated at lattice points which describe the HCP structure, and their cartesian coordinates are constrained to fall between -0.5 and +0.5 in the x, y and z directions, forming a cuboid simulation 'block', for reasons of simplicity and to allow the physical dimensions of the simulation block to vary with time via the Lagrangian equations of motion (Andersen 1980, Parinello & Rahman 1980) - these are stored elsewhere as a 3 x 3 'box' matrix, and the absolute coordinates of each atom can then be calculated by multiplying its position vector by the box matrix. This gives rise to flexible boundary conditions, allowing thermal expansion and contraction as exists in reality, and bulk dimensional changes due to point defects. The boundaries in the present version of MOLDY are also 'periodic', i.e. in order to provide a continuous medium around the block, it is simply repeated at each face as shown in fig. 3.4, so atoms on opposite block faces react with one another. This has the disadvantage of requiring large enough box dimensions so that any events modelled do not affect their own development by self-interaction, e.g. a cascade developing to a size which is larger than the box in one or more directions. However, the main advantage of this kind of

method is the absence of any additional layers of atoms at the block surfaces to simulate a continuous medium which would take up valuable computing time. Although MOLDY is quite versatile and is able to apply constant pressure to the block boundaries, in this work no pressure is used since the potentials employed are of the equilibrium variety, and are therefore stable.

Atomic interactions are calculated using a potential to determine the net force on each atom as a result of the rest, and hence by Newtonian mechanics their accelerations. The equations of motion of each atom are calculated over finite 'real' slices of time known as time-steps, and since the late 1980's the use of a Gear 4-value predictor-corrector algorithm (Berendsen & Van Gunsteren 1986) has been incorporated which allows the time-step, referred to as Δt, to vary in size according to the largest predicted atomic energies and movements within the next time-step, shortening the time-step as the strength of the interatomic forces increases, e.g. during the collisional phase of a cascade, and lengthening it as interactions become much weaker, e.g. during the final damage state of a cascade when only point defects and small clusters are present. (A highly detailed account of the various methods for changing the size of the time-step and predicting the progress of the atoms is given by Eckstein, 1991.) This also prevents atoms with large velocities passing through others because the time-step is too large, i.e. they could move 'through' a neighbouring atom when the distance they move within that time-step is calculated. The lower limit for the size of the time-step is usually chosen so that the fastest atom does not move more than 5 - 10% of the interatomic distance at the maximum predicted energy (in this case Δt_{min} is set at 0.01 fs), and the upper limit set to around one tenth of the atomic vibrational period. (Here Δt_{max} is 0.01 ps, a general approximation for most metals.)

In order to use time efficiently when calculating the forces on the atoms, instead of summing the interactions of each atom in the block with all others, only the atoms within a certain cut-off distance of each other are used. Early versions of MOLDY

accomplished this by keeping a neighbour list, essentially a short list for each atom in the block containing the indices of all the other atoms nearer than this cut-off distance. However, though this did reduce the amount of time spent in force calculation, the neighbour lists require constant updating every few time-steps, and calculation time scales as the square of the number of atoms in the block, i.e. $t_{calc} \propto N^2$. A more efficient method, originally described by Fincham and Heyes (1985), is the now widely used 'link-cell' method. In this the simulation block is split into smaller sub-blocks or cells of dimension such that an integral number of cells exists along each block side, but the size of the cell is as close to, but not less than, the range of the potential being used. Each cell has a linked list of the atoms which lie within it, reducing the number of lists required from one per atom to one per cell. During force calculations, only interactions between atoms within the 26 neighbouring link-cells are considered. This can be a little uneconomic, as all the atoms within the cells are taken into account irrespective of their actual separation, but the benefits of this system far outweigh this small disadvantage. The link-cell contents and their lists are updated every time-step, which scales as N, and not N^2 thus becoming much more efficient for large blocks. Since then Heyes & Smith (1987) have produced the vectorised link-cell method for the newer generation of vector-processor computers which can handle repetitive calculations very rapidly, but require careful programming to make the most of their advantages.

There now follows a description of the several 'modes' in which MOLDY may be used for modelling.

3.4.1 Equilibration.

Before any dynamic event modelling can take place, a block of atoms must be generated in thermal equilibrium as would exist in reality. Each atom is given a

random velocity in a random direction, scaled such that the mean temperature given by the kinetic energy of the atoms is equal to the required block temperature. In order to remove any small 'pockets' of large temperature deviation from that required, a block is allowed to 'equilibrate' for around 1000 time-steps (~10 ps), time for ~100 lattice vibrations, and this allows the phonons to come to thermal equilibrium throughout the block, producing an approximately Maxwellian energy distribution about the intended kinetic temperature. By changing the equilibration time of a block, the atomic positions also change slightly with thermal vibration, though the block is still at the same temperature, and this allows statistical variation when modelling dynamic events.

3.4.2 Dynamic Simulation.

Once a block has been equilibrated, a cascade is started by choosing an atom near the centre of the block to be the PKA, and setting its energy and direction of motion to a chosen value. As a general rule of thumb, found empirically during cascade simulation in Cu (Foreman et al. 1991), the block should contain a number of atoms such that $N \geq 16\ E_{pka}$ in order to contain the cascade produced. The simulation is then started and a cascade develops, with MOLDY checking the atom positions every time step and marking any atoms which are more than some search distance r_{srch} from a perfect lattice site as an interstitial. It should be noted that these atoms are not 'true' interstitials, only displaced atoms and, as will be described later, one SIA may give rise to two or three displaced atoms in the immediate vicinity. Lattice sites which have no atom within r_{srch} are flagged as vacancies, though again they are not true vacancies. The value used for r_{srch} is somewhat arbitrary, and varies from study to study, with values of 0.25 a_0 in use for FCC metals (Foreman et al. 1991), 0.30 a_0 for BCC Fe (Calder and Bacon 1993) and 0.32 a_0 in this work, and is generally chosen to be small enough to make the presence of 'real' interstitials apparent, but

large enough not to cause flagging of atoms moving by thermal vibration, or too many of those displaced in the vicinity of a SIA. For example Calder and Bacon (1993) chose the value of 0.30 a_0 in order to show both symmetrically displaced atoms in the BCC <110> dumbbell, but none of the other surrounding atoms which will have also moved smaller amounts as a result of the presence of the dumbbell. The search sphere has a volume of ~0.2 Ω_0 in most cases. (For FCC its volume is 0.26 Ω_0, 0.23 Ω_0 for BCC and 0.19 Ω_0 for HCP.)

During simulation, MOLDY keeps a record of cumulative time, the number of vacancies and interstitials present (these are, or should be, equal and give the parameter N_d, the number of displaced atoms) and the total potential and kinetic energy in the block, as well as the temperature and atomic volume at each time-step. These parameters allow the determination of the evolution of each phase of the cascade as N_d initially increases to a maximum (N_{peak}), then falls to its final value (N_f) at the end of the cascade and into the primary damage state. This takes between 5 and 10 ps (up to 1000 or more time-steps) depending on the shape of the cascade and the PKA energy. The coordinates of all flagged vacancies and interstitials can also stored at regular intervals, usually every five or ten time-steps, for later viewing using packages such as MacAtoms™, Ball-and-Stick™ and Atom-TV™, which give a visual representation of the cascade as it develops. Every few hundred time-steps all the coordinates and thermodynamic data for every atom in the block can be recorded for subsequent analysis in terms of radial pair distribution functions, mixing parameters and temperature distributions, all of which serve to give insight into cascade processes and evolution.

3.4.3 Static Simulation.

Although MOLDY was designed with dynamic modelling in mind, so-called static

modelling can also be undertaken. Static-specific codes, such as XLITE, simulate blocks of atoms without temperature, i.e. at 0 K, and attempt to remove all forces throughout the block by iterative movement of the atoms. Point defects and small clusters can be investigated using static simulation with respect to stability, volume and energetic effects, and MOLDY can also be used to do this by constantly 'quenching' the simulation block every time-step after the insertion of a defect. This quenching is done by checking the velocities and accelerations of all the atoms, and reducing the velocity, by some fixed fraction, of any atom whose net velocity and acceleration are in opposite directions, i.e. any atom which is moving but slowing down is slowed further, or stopped completely. This means that atoms only move in small steps as they would in any static-specific code. Note that cascades cannot be simulated in this manner, only non-mobile defects, and this process is used in the work conveyed in the next chapter to compare the results of a previous static study using the Ackland α-Ti potential to those from MOLDY using the same potential.

Throughout the remaining chapters, the finer details of the modelling procedures used in each stage of the work, such as block sizes, PKA directions, methods of analysis and any modifications to these methods, will be given but the basic methods remain the same as those described above.

- § -

Table 3.1: List of parameters for the Ackland Ti and Zr n-body potentials, modified as discussed in section 3.2.

Parameter	Ackland Ti potential	Ackland Zr potential
a_0 (Å)	2.966	3.249
c/a	1.592	1.595
a_1 (eV/a_0^3)	-20.513919	-21.003326
a_2 (eV/a_0^3)	29.0005774	30.055536
a_3 (eV/a_0^3)	-7.818214	-7.526378
a_4 (eV/a_0^3)	-3.735130	-0.470275
a_5 (eV/a_0^3)	26.770918	23.603433
a_6 (eV/a_0^3)	12.905300	50.064913
a_7 (eV/a_0^3)	-	251.381704
r_1 (a_0)	1.716143	1.716385
r_2 (a_0)	1.688009	1.688247
r_3 (a_0)	1.575475	1.603835
r_4 (a_0)	1.336341	1.336529
r_5 (a_0)	1.125339	1.125498
r_6 (a_0)	0.994669	0.984811
r_7 (a_0)	-	0.886330
A_1 (eV^2/a_0^3)	14.297431	17.341328
A_2 (eV^2/a_0^3)	-14.392773	-0.305449
R_1 (a_0)	1.716143	1.716385
R_2 (a_0)	1.477008	1.477216

Table 3.2: Values of various physical parameters for α-Ti and α-Zr given by the Ackland potentials (SFE = stacking fault energy).

Parameter	Ti	Zr
E_c (eV)	4.853	6.250
E_f^v (eV)	1.450	1.786
V_f^v (Ω_0)	0.804	0.726
I_2 SFE (eV/a_0^2)	0.0387	0.0371‡
C_{11} ($eV/Å^3$)	1.052 (1.099)	0.932 (0.970)
C_{12} ($eV/Å^3$)	0.612 (0.542)	0.544 (0.420)
C_{13} ($eV/Å^3$)	0.475 (0.426)	0.436 (0.403)
C_{33} ($eV/Å^3$)	1.355 (1.189)	1.090 (1.077)
C_{44} ($eV/Å^3$)	0.321 (0.317)	0.221 (0.227)

The values for the elastic constants have been determined using the HAIN code, also used to determine the P-V response of the potentials. The numbers in brackets are the experimental values for the same parameters (Ackland 1992, Ackland et al. 1994)

‡ The I_2 stacking fault has recently been found to have positive energy, but proved to be unstable in the α-Zr potential, preferring to restack when relaxed.

Table 3.3: Biersack-Ziegler Universal potential parameters.

k	B_k	C_k
1	3.2000	0.1818
2	0.9423	0.5099
3	0.4029	0.2802
4	0.2016	0.0282

Table 3.4: Parameters used in the Rose et al. P-V calculations.

Parameter	Ti	Zr
E_c (eV)	4.86	6.25
B (GPa)	109.7	97.3
r_{wse} (Å)	1.62	1.77

Table 3.5: Parameters for the Exponential fitting curve.

Parameter	Ti	Zr
F_0 (eV)	1.00	1.00
F_1	8.8245	13.4037
F_2 (Å^{-1})	-4.0652	-12.2190
F_3 (Å^{-2})	-0.4919	5.0261
F_4 (Å^{-3})	0.3019	-0.8435

Table 3.6: Fitting points for the Composite potential.

	Ti r (Å)	Zr r (Å)
Biersack/Exp. crossover.	1.10 (64.1 eV)	1.20 (92.0 eV)
Exp/Ackland crossover.	2.09 (25.4 eV)	2.55 (2.6 eV)

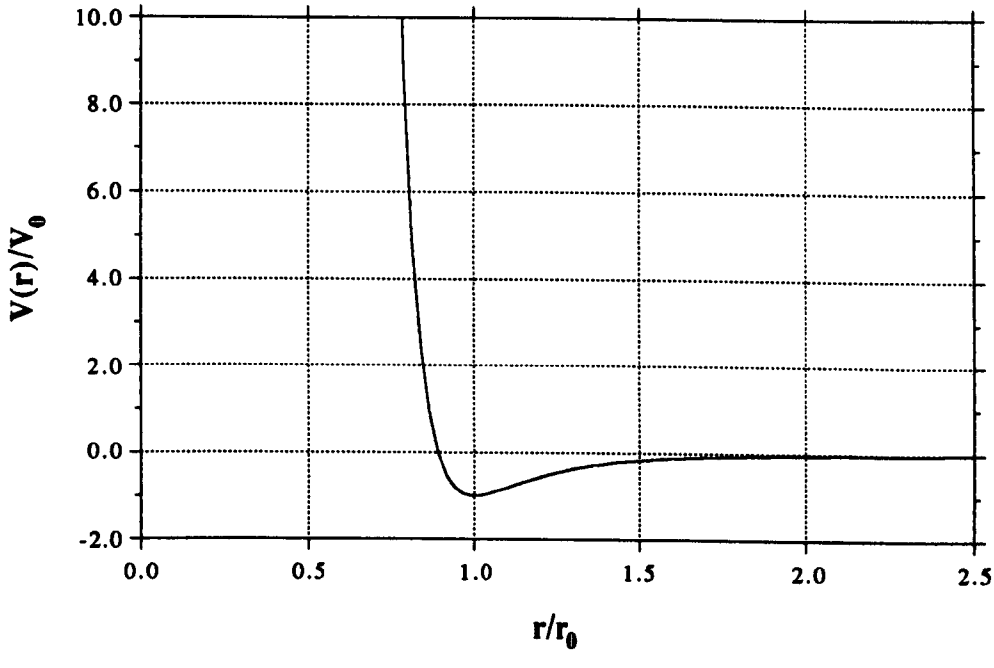

Fig. 3.1: Plot of the Lenard-Jones pair potential with normalised units.

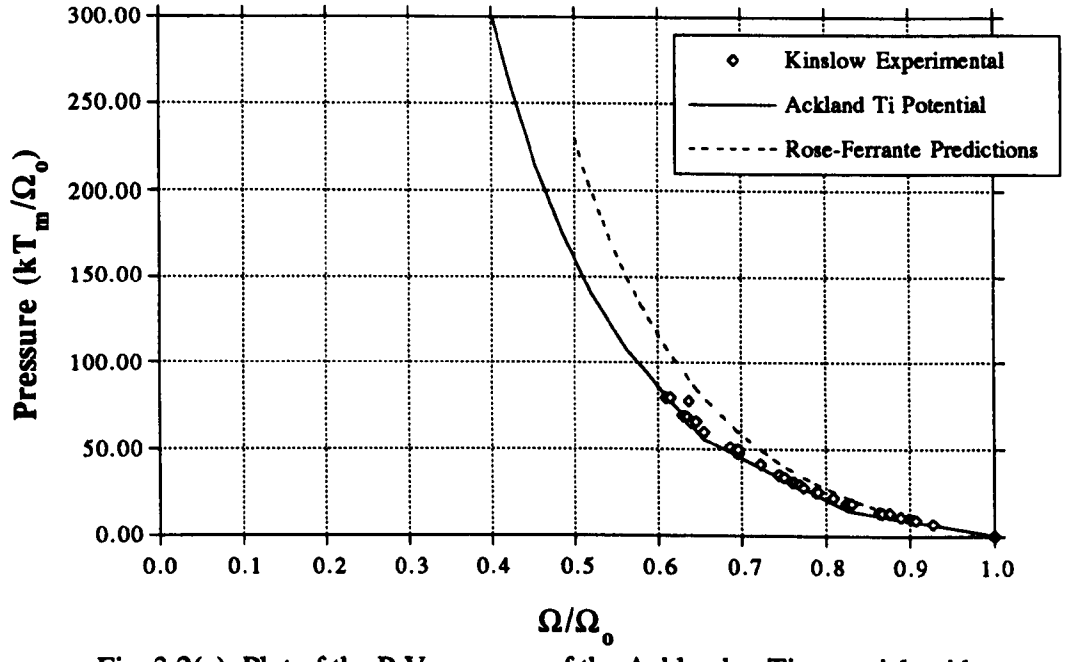

Fig. 3.2(a): Plot of the P-V response of the Ackland α-Ti potential, with Kinslow's experimental data and the Rose-Ferrante theoretical predictions. (kT_m = 0.169 eV, Ω_0 = 17.98 Å^3)

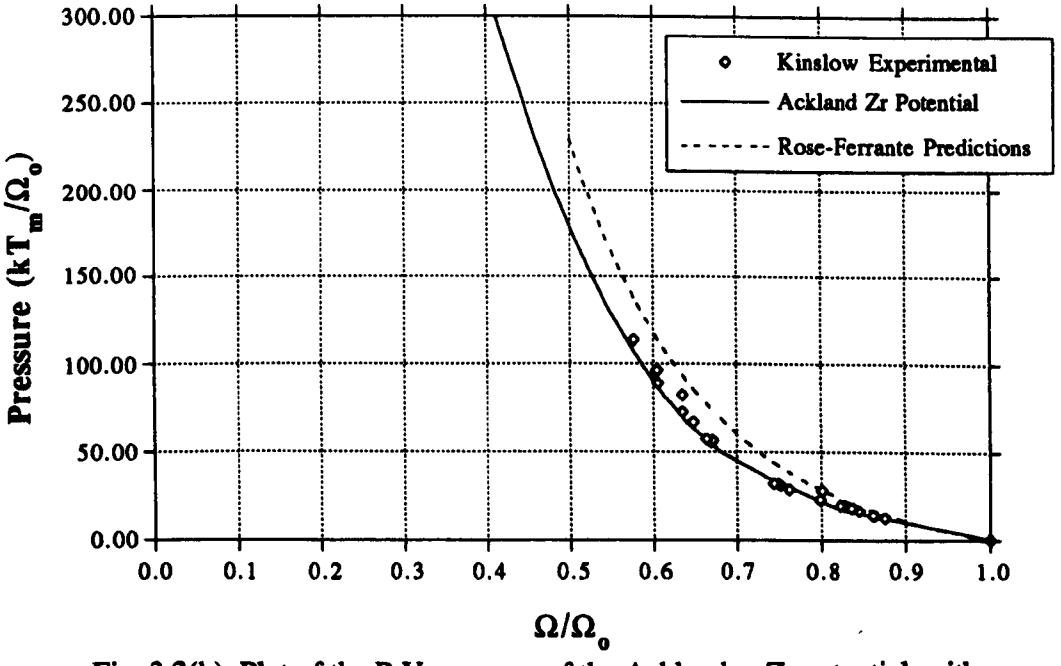

Fig. 3.2(b): Plot of the P-V response of the Ackland α-Zr potential, with Kinslow's experimental data and the Rose-Ferrante theoretical predictions. (kT_m = 0.174 eV, Ω_0 = 23.69 Å^3)

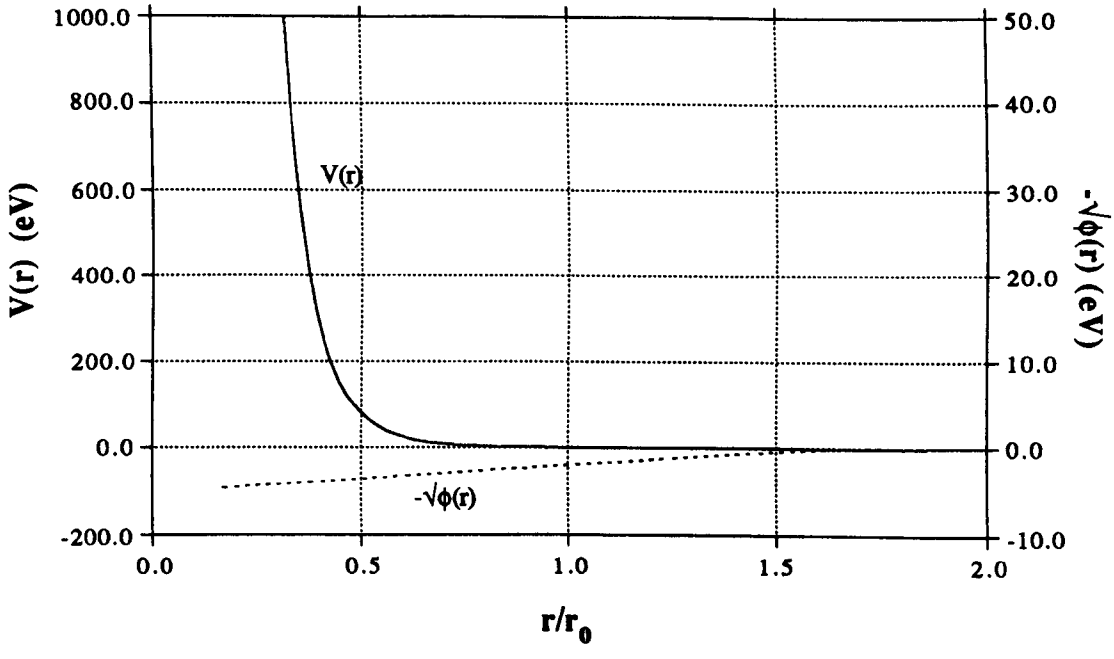

Fig. 3.3(a): Plot of the pair and many-body terms of the Ackland α-Ti potential.

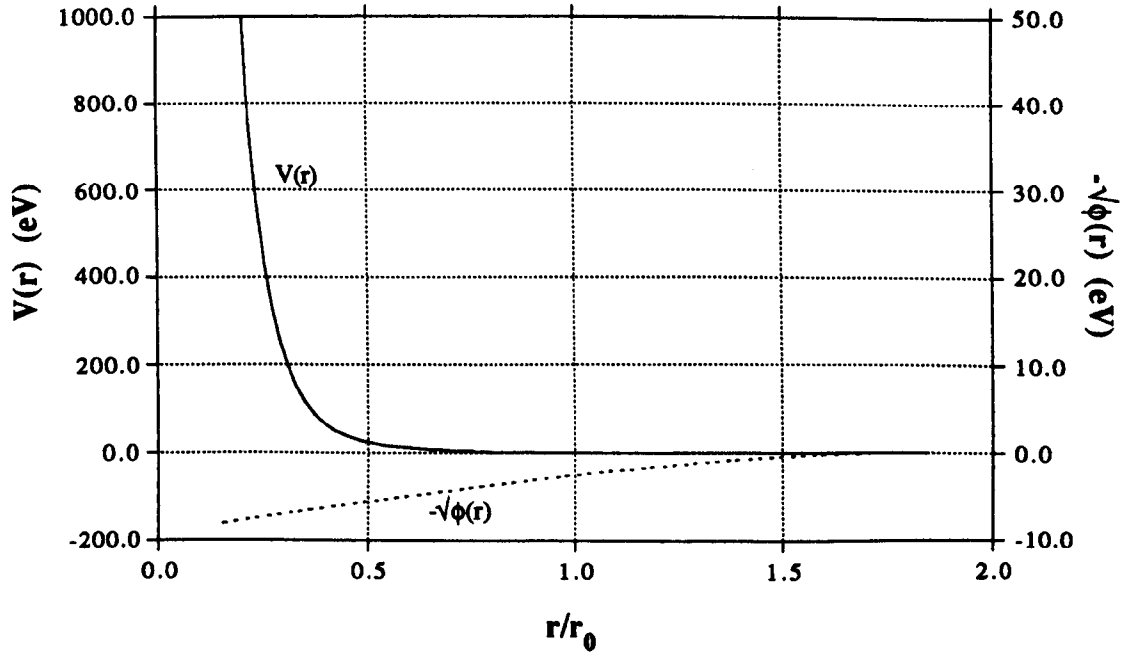

Fig. 3.3(b): Plot of the pair and many-body terms of the Ackland α-Zr potential.

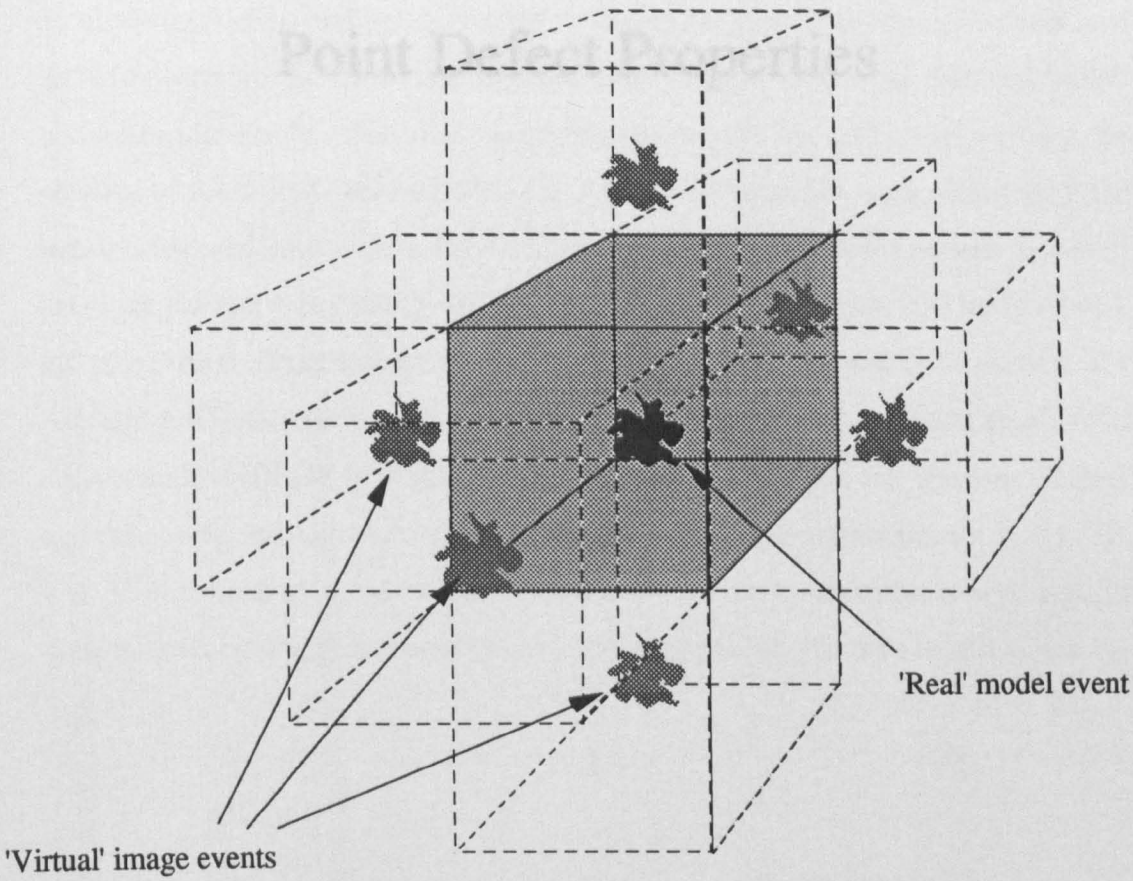

Fig. 3.4: Schematic of simulation 'block' with image blocks, and hence events, created by periodic boundary conditions. For simplicity, not all the image blocks are shown, as there are 26 in all which completely surround the central 'real' block.

IV

Point Defect Properties

4.1 Introduction.

Although this work is primarily concerned with dynamic cascade processes, the end product of a cascade is usually many point defects in the form of single and clustered vacancies and SIAs, and thus an understanding of the properties of point defects is of great importance. There has been a good deal of study of single and clustered defects within the last few decades using computer modelling. In line with other workers, the notation of Johnson & Beeler (1981) for the eight different SIA sites within the HCP lattice is adopted, as shown in fig.4.1. In the following sections the general results of previous studies using pair potentials and many-body potentials will be reviewed, including the findings associated with the Ackland potentials used in this work. The Ackland α-Ti and α-Zr potentials have been reinvestigated with regard to single point defects using MOLDY in a 'quasi-static' fashion as outlined in the previous chapter, and the results are compared with calculations for the same quantities using XLITE. The implications of these results with respect to stable, metastable and unstable defects, defect mobility and possible preferential migration will then be discussed.

- § -

4.2 The Simulation of Point Defects, Past and Present.

The technique generally used to simulate point defects and determine their formation volumes and energies is quite simple. A simulation block of N atoms is set up within whatever computer model is chosen, and the total energy E_p of the perfect crystal, along with the associated total volume V_p, calculated. The cohesive energy $E_c = E_p/N$, as in equation 3.3, and the volume per atom $\Omega_0 = V_p/N$. The defect(s) are then added, and the system allowed to 'relax', or come to equilibrium again. This may be by the 'conjugate-gradients' method, as used in the XLITE code, or by reaching a

total configuration of interatomic force equilibrium via MD, these two situations being essentially identical but arrived at by differing methods. The new total energy E_{rd} of the relaxed crystal containing the defects, and the volume V_{rd}, can then be determined.

Generally two main quantities are quoted in the literature to indicate the stability of point defects: the formation energy E_f and the formation volume V_f. Both are determined quite simply from parameters within the computer model used. The formation energy is given as

$$E_f^{n(i/v)} = E_{rd} - E_p \pm nE_c \qquad (4.1)$$

where n is the number of defects in the cluster, either SIAs (i) or vacancies (v). The formation volume is given, in units of Ω_0, by

$$V_f^{n(i/v)} = \frac{V_{rd} - V_p}{\Omega_0} \mp n \qquad (4.2)$$

The addition of nE_c in E_f and the subtraction of n in V_f accounts for the apparent moving of atoms from the surface of the block to the interior when interstitials are formed, and similarly the subtraction of nE_c in E_f and the addition of n in V_f accounts for the removal of atoms from the centre of the block and their addition to the surface when vacancies are created. However, equation 4.2 assumes the use of a model with flexible boundary conditions, such as exist in MOLDY. For constant volume models such as XLITE, other methods based on the expression

$$V_f = -\frac{\Omega}{B}\left(\frac{dE_f}{d\Omega}\right) \qquad (4.3)$$

where B is the bulk modulus and Ω the atomic volume, must be used by calculating E_f for a range of values of Ω, plotting the results on a graph and inputting the gradient into the above expression as the differential (Finnis & Sanchdev 1976, Harder &

Bacon 1986, Mercer-Calder 1992).

Modelling undertaken so far in this area can conveniently be divided into two sections, as in the previous chapter. based on the nature of the interatomic potential used. However, an exhaustive commentary on all investigations made into these matters is beyond the scope of this report, so reference will be made to several comprehensive reviews of this kind of work.

4.2.1 Pair Potential Modelling.

The history of pair-potential based simulation of point defects is quite long and various potentials have been proposed and modified. However, the agreement in the results these models give is quite remarkable. The Mercer-Calder (1992) study included a detailed examination of a variety of pair-potentials which all give $^{c}/_{a}$ close to, or equal to, ideal, and the results are summarised in table 4.1(a). The most common stable SIA was the BO, as it also is in the Johnson (1991) study. There were two exceptions to this, giving the T interstitial as the most stable, but in both of these cases the same equational form for the potential was used, and this was highly oscillatory in nature and had quite hard repulsive forces between second and third neighbours, thus favouring an out-of-basal-plane site. The predictions for the metastable interstitial are more varied, with different models giving the C, T and S sites as possibilities. As the metastable interstitial is though to account for the last substage in stage I annealing, and the stable SIA for stage III in the two-interstitial model, this C-T-S region of metastability would provide a route for isotropic SIA diffusion is the early stages of annealing. Bacon (1988) also concurred with the BO as the stable interstitial, suggesting the C site as the most probable metastable position, as did Frank (1988). Frank also correlated the results used in his review to experimental data and theories of low temperature annealing and, based on the two-

interstitial model, concluded that the metastable C interstitial was responsible for stage I_E annealing in α-Zr (see section 2.3.2 and fig. 2.4), migrating in a (quasi) one-dimensional manner, and that the stable BO interstitial became mobile in stage III, migrating isotropically. Frank also drew a direct analogy with the cubic metals as they also exhibit this same metastable interstitial, one-dimensional migration during the final stage I sub-stages, and the isotropic migration of the stable SIA during stage III annealing. However, Frank suggested that this was only the case for HCP metals with a $^c/_a$ ratio ≤ ideal. Extrapolating the data used in his review, he proposed that in metals with $^c/_a$ ratio ≥ ideal, the S interstitial was the most likely candidate for the stable site, with the C and BO as metastable interstitials. He also proposed a possible migration route for the S interstitial, again moving quasi-one-dimensionally out of the basal plane.

The pair-potential models therefore give several proposals for the stable interstitial in HCP metals, and the general consensus falls to the BO for metals with $^c/_a$ ratio ≤ ideal, with the C as the metastable site. Several possible migration routes have been suggested, but opinion varies on this and includes BO → BC → BT → BC → BO from Johnson (1991) and BO → BS → BO (Johnson & Beeler 1981, Bacon 1988), both basal migration routes, BO → BS → C → BS → BO for migration between adjacent basal planes (Bacon 1988), and movement between the C, T and S sites in varying combinations (Frank 1988, Johnson 1991) for non-basal migration.

However, as was stated in the previous chapter, pair-potential-based models suffer from two main problems: the $^c/_a$ ratio is always very close to ideal, and the vacancy formation and cohesive energies are linked in such away as to always make one quite inaccurate if the other is correct. Recent work by Oh & Johnson (1989) suggests that the value of the $^c/_a$ ratio may play a very important role in the preferred stable sites, and Johnson (1991) indicated that the addition of many-body interactions would also affect this.

4.2.2 Many-body Potential Modelling.

The investigation by Oh & Johnson (1989) was made using a Zr model with EAM-derived potentials. They found a range of $^{c}/_{a}$ ratios, between 1.580 and 1.625, over which the HCP structure was stable, i.e. E_c was highest for the HCP structure than any other. For $^{c}/_{a} < 1.580$ the BCC structure became more favourable, with the FCC lattice stable for $^{c}/_{a} > 1.625$. They then chose the two values of $^{c}/_{a}$ at either end of this stability region, both less than ideal, (the latter only slightly) to construct two models. They found that for the lower $^{c}/_{a}$ ratio the BO site was the stable interstitial, with the C as the metastable interstitial. The larger $^{c}/_{a}$ ratio gave the C interstitial as stable and the O as metastable, and hence they concluded that as the $^{c}/_{a}$ ratio is decreased from ideal, basal defects increase in stability. Igarashi et al. (1991) also developed a range of potentials covering eight HCP metals including Ti and Zr. Using the F-S formalism, their results suggested that the C interstitial was the stable interstitial, with the exceptions of the Zn and Zr models in which the O site was the most stable. The results for Zn are not surprising, as Zn has a $^{c}/_{a}$ ratio a good deal greater than ideal. However, for these two exceptions the C site was the first metastable interstitial with the O site as metastable for the rest of their models. The results of the Igarashi et al. study are, however, subject to some concern since, as can be seen from table 4.1(b), the defect formation energies in some of their models are much higher than expected in comparison to other models and, as pointed out in the previous chapter, their potentials can be unstable in the presence of defects.

Johnson (1991) investigated the effects of many-body forces on the stability of SIAs, comparing the results from his EAM model with those of Johnson & Beeler (1981) for α-Ti. In both the pair-wise and n-body models, the BO interstitial was the most stable, with the major difference between the two models being the possible migration

routes of defects. In his previous pair-potential model, an isotropic migration path was possible, but the many-body model gave a basal preference to migration, as described in the previous section.

4.2.3 Present MD Results.

Mercer-Calder's study (1992) also included the Ackland (1992) α-Ti potential used in this work. However, it was felt necessary to reinvestigate these properties for both the α-Ti and new α-Zr potentials using the MOLDY code, rather than the older XLITE code used in the original testing. A small block of 1960 atoms (10 x 14 x 14 planes) was set up in MOLDY at 0 K with continuous heat removal, as detailed in section 3.4, and allowed to come to equilibrium with each defect in turn placed near the centre of the block.

The results, shown in tables 4.2(a) and (b) for α-Ti and α-Zr respectively, give indication that in both cases basal defects are favoured due to the lower formation energy of these interstitials, and their stability when compared to the non-basal forms. Indeed, in both models the O and T sites are unstable, reconfiguring to basal defects, and, perhaps surprisingly, the BT interstitial is also unstable, moving to the BO site on relaxation. For the Ti model the BS and BC configurations have extremely close formation energies with the BS being the slightly more favourable and, from cascade simulation at temperature discussed in later chapters, these two states appear to be degenerate. The BO interstitial has a formation energy quite close to the BS and BC. In the case of Zr, however, it is the BC which has the lower formation energy, and the BO, whilst still having a formation energy quite close to the other two stable basal forms, is not as relatively stable as in the Ti model. Also stable in both models is the S or c-axis split configuration, having a formation energy much greater than all the others, but which, although stable in static simulation, collapses onto the basal plane

given a small amount of thermal energy.

One noticeable difference between the two models is that for Zr the C (crowdion) interstitial is stable, which is not the case for Ti where it reconfigures to the BS form. This is thought to be due to the slightly higher $^{c}/_{a}$ ratio in Zr, being 1.595 as opposed to 1.592 in Ti, which gives slightly more room for an extra atom to sit in the <$\bar{2}$203> rows.

For Ti, all the values for V_f^i are small and negative, indicating that the change in volume caused by adding an interstitial is $<\Omega_0$, whereas in Zr the formation volumes are small and positive which means that the volume change due to an interstitial is $>\Omega_0$. From this we can deduce that the Zr potential, relatively speaking, is harder at small volume changes than the Ti case.

Comparison with the results from the XLITE code mentioned above shows some small differences in the formation energies of the defects, with the XLITE routines yielding slightly larger interstitial formation energies, e.g. E_f^i for the BC configuration is 3.24 eV in the Mercer-Calder study for the Ti potential, whereas using MOLDY the result is 3.09 eV for the same form. However, the stable configurations resulting from both codes are qualitatively identical, given that in that study the BS form was not explicitly modelled. This small discrepancy in formation energies is due to the differing boundary conditions in the two codes used. As previously stated, MOLDY has flexible boundary, constant pressure conditions (in all cases in this work, this pressure is zero) which allows the bulk expansion of the simulation block when a SIA is added or, similarly, a bulk contraction when atoms are removed to create vacancies, and the modelling of thermal expansion is also possible. The XLITE routines, on the other hand, use constant volume conditions at zero temperature, which allows the build up of internal pressures. Without bulk dimensional changes to alleviate the lattice distortions which cause this, defects

therefore have a slightly higher formation energy in the XLITE model, despite the use of an identical interatomic potential. This also accounts for the difference in formation volumes of similar defects on the two models, e.g. for the BC interstitial again, V_f^i = -0.03 Ω_0 in MOLDY, but is calculated as -0.11 Ω_0 using XLITE, and this comes about because MOLDY allows the local strains to be shared throughout the whole lattice by a slight block expansion, whereas XLITE hinders relaxation around the interstitial by the lack of bulk volume change, and hence concentrates the strain energy in a smaller local volume around the interstitial. The same is true in the case of vacancies, with MOLDY calculating V_f^v = 0.80 Ω_0 and E_f^v = 1.43 eV and XLITE yielding values of 0.76 Ω_0 and 1.45 eV respectively, again indicating a hinderance in relaxation around the defect in XLITE since the formation volume is slightly less and the formation energy slightly higher.

Qualitatively speaking, therefore, the final outcome of these two methods is the same, and the indication is that the MOLDY code, although designed with temperature and dynamic events in mind, also gives excellent indication of static properties such as those discussed here.

- § -

4.3 Discussion and Implications.

In terms of the two-interstitial model, the results in tables 4.3(a) and (b) indicate that, in the Ackland α-Ti and α-Zr models used in this work, the BS and BC interstitials are essentially identical in formation energy and, being degenerate, are the stable interstitial sites. In the Ti model, the BO interstitial is very close in stability to the BS and BC forms, but for Zr is almost identical in formation energy to the C interstitial. The suggestion is therefore the BO and C are the first and second metastable

interstitials. What is clearly apparent is the very close stability of the basal defects in both potentials compared to non-basal configurations, providing for strongly preferential migration within the basal planes, most likely via a BS → BC → BS route. However, at higher energies migration between planes could take place along the BC/BS → C → BS/BC route. These points on migration are qualitatively borne out in very recent work by Mikhin et al. (1994) in which a long-range pseudo-potential is used to investigate two models for Zr with differing $^{c}/_{a}$ ratios (similar to the Oh & Johnson study, 1989). In their model the BO site was stable, with the BS site metastable for $^{c}/_{a}$ = 1.580, and the C site metastable with $^{c}/_{a}$ = 1.625. They investigated the migration of vacancies and interstitials in these two models, and found that the lowest-energy migration route for interstitials was along the <11$\bar{2}$0> directions (i.e. in the basal plane) via the BO → BS → BO route, with an associated migration energy of only 0.03 eV. The out-of plane migration energy along the <$\bar{2}$203> directions (BO → C → BO) was 0.2 eV, indicating a strong preference for basal plane migration, although their routes are slightly different to that proposed in this work. They also simulated di-interstitials, again concentrating on migration, and found that they too preferred to migrate along the <11$\bar{2}$0> directions in the basal plane by alternate SIA 'shuffling' along neighbouring rows. This point has great implications for the mobility of multiple-SIA clusters during the post-cascade damage state and, if these are as mobile as the Mikhin et al. work suggests, can greatly increase the point defect production bias.

As far as clusters are concerned, no specific investigation was conducted in this work, but the Mercer-Calder study covered clusters of SIAs from two to nine in number, which were extensively modelled in a variety of configurations. The conclusions were that in the HCP metals, di-interstitials form preferentially in the basal planes, taking the form of two BS/BC interstitials in neighbouring close-packed rows, in agreement with Mikhin et al., and clusters of three or more will, in the majority of cases, form perfect prism plane loops, with Burgers vector $\mathbf{b}=^{1}/_{3}$<11$\bar{2}$0>.

That is not to say that no other configurations are possible, as many others were stable in the aforementioned study.

With respect to vacancies, most workers have found that single vacancy migration is approximately isotropic. Di-vacancy formation depends on the $^{c}/_{a}$ ratio, with the out-of-plane configuration slightly more preferable for $^{c}/_{a} \leq$ ideal. Di-vacancy migration slightly favours out-of-plane motion, as shown by Mikhin et al., due to the difference in symmetry encountered if migration is attempted in the basal plane because of the tetrahedral and octahedral regions of the lattice.

In summary then, for the Ackland potentials used in this work, the BS and BC sites are favoured as the most stable SIA sites. Others expected to occur as a result of displacement cascades include the BO and C interstitials, though in dynamic simulation these may reconfigure to the more stable states. The implications, based on the results of MD 'quasi-static' modelling in this work, and the simulations of other workers, is that SIAs are highly mobile within the basal planes in the HCP metals with small migration energies in comparison to vacancies, whose migration may be regarded as isotropic. Also implied is the high in-plane mobility of small SIA clusters by the 'crowdion' mechanism of Mikhin et al. Woo (1988, 1991) has already indicated that this fundamental 'diffusion anisotropy difference' (DAD) for vacancies and SIAs in HCP metals may dominate over the 'elastic interaction difference' (EID) of sinks with differing types of point defect, providing another mechanism for increased defect production biasing in the HCP metals.

- § -

Table 4.1(a): Summary of stable and first metastable SIA sites and energies for existing pair potentials (after Mercer-Calder 1992).

Model	Stable Interstitial	E_f (eV)	Metastable Interstitial	E_f (eV)
Mg [1]	T	1.25	O	-
Mg [2a]	BO	1.84	T	1.87
Mg [2b]	BO	1.37	S	1.43
Co [3]	T	3.19	BO_A*	3.20
Co [4]	BO	4.54	C	4.72
Ti [5]	BO	4.32	T	4.59
Zr [6]	BO	3.83	C	4.01
Zr [2a]	BO	4.55	T	4.70
Zr [2b]	BO	4.20	S	4.31

1. Tomé, Monti & Savino (1979) 2. Monti et al. (1991). (a): strongly repulsive. (b): weakly repulsive
3. Oh & Johnson (1988) 4. Foster et al. (1987) 5. Johnson & Beeler (1981) 6. Fuse (1985)

* The BO_A interstitial lies between the BC and BO sites, but does not share a site with another displaced atom, as in the case of the BS interstitial.

Table 4.1(b): Summary of stable and first metastable SIA sites and energies for existing many-body potentials (after Mercer-Calder 1992).

Model	Stable Interstitial	E_f (eV)	Metastable Interstitial	E_f (eV)
Mg [7]	C	2.02	O	2.08
Mg [8]	C	7.10	O	7.24
Co [8]	C	2.39	O	24.62
Ru [8]	C	27.30	O	27.57
Hf [8]	C	9.50	O	9.69
Be [8]	C	10.50	O	10.60
Zn [8]	O	1.98	C	2.20
Ti [7]	C	3.76	BO	3.79
Ti [8]	C	7.70	O	8.08
Zr [7]	C	4.52	O	4.62
Zr [8]	O	7.55	C	7.70
General [9]	BO	3.33	T	3.39

7. Oh & Johnson (1988) 8. Igarashi et al. (1991) 9. Johnson (1991)

Table 4.2(a). Point defect data for Ackland Ti Potential.

Initial defect	Final Defect	Formation Energy (eV)	Formation Volume (Ω_0)
Vacancy	Vacancy	1.43	0.80
BS	BS	3.07	-0.07
O	"	"	"
C	"	"	"
BC	BC	3.09	-0.03
BO	BO	3.11	-0.13
BT	"	"	"
T	"	"	"
S	S	3.65	-0.19

Table 4.2(b). Point defect data for Ackland Zr Potential.

Initial Defect	Final Defect	E_f (eV)	V_f (Ω_0)
Vacancy	Vacancy	1.79	0.74
BC	BC	3.76	0.33
BS	BS	3.76	0.35
T	"	"	"
BO	BO	3.97	0.30
BT	"	"	"
O	"	"	"
C	C	3.98	0.27
S	S	4.32	0.20

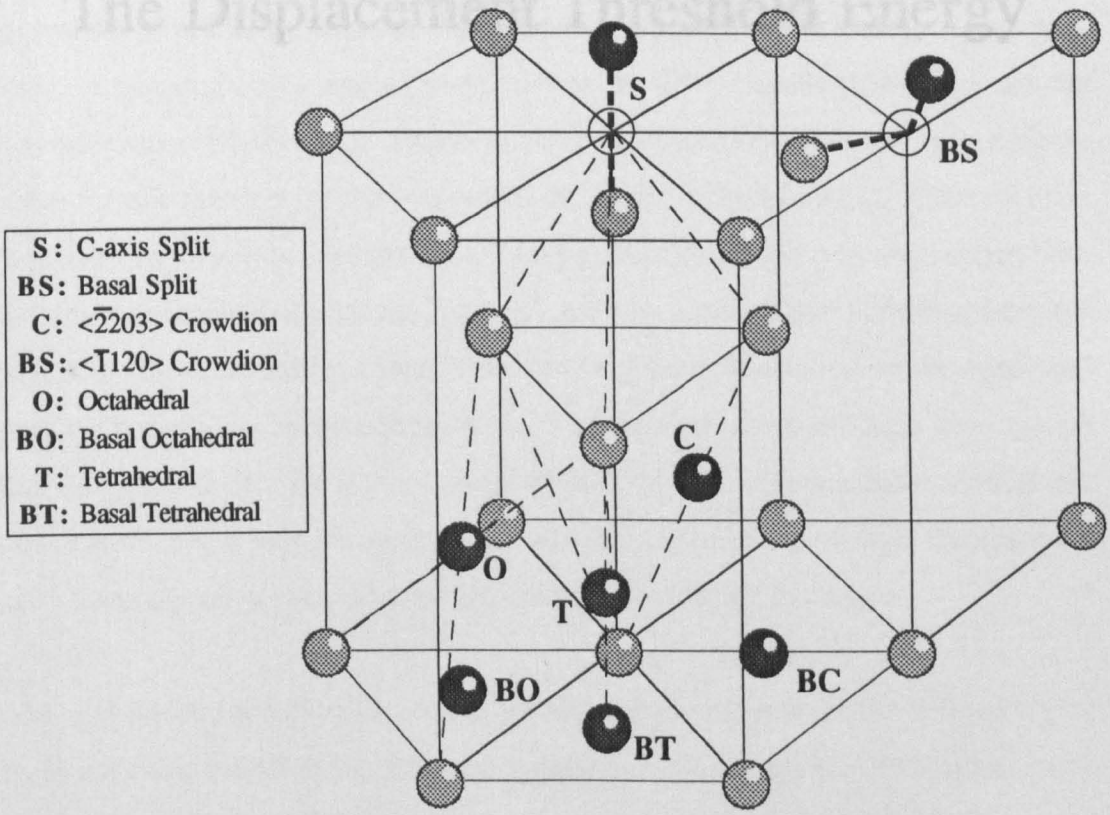

Fig. 4.1: Schematic of eight possible SIA sites in the HCP lattice (after Johnson & Beeler 1981)

V

The Displacement Threshold Energy

5.1 Introduction

The displacement threshold energy, or E_d, has been repeatedly referred to in the preceding chapters and, by way of reminder, is the amount of kinetic energy needed to be imparted to an atom to permanently displace it from its lattice site, thus generating a Frenkel pair. Its value is of paramount importance in damage theory with many other quantities depending on it, such as the NRT cascade efficiency k and the displacement cross-section σ. However, although E_d is often taken to have a single value for one material for the purpose of theory and calculations, E_d is directionally dependent in reality, i.e. the amount of energy needed to displace an atom depends on the direction in which the atom is 'pushed', and this is due to the local arrangement of atoms in the surrounding lattice. This has long been known to be the case, and mention has already been made in chapter 2 of the first computer-based investigation into this phenomenon by Erginsoy et al. (1964) for Cu. Experimental studies of this effect have been undertaken but, as will be explained later, are fraught with complications and as such are often limited in their accuracy and scope.

Although several computer simulation investigations have been conducted recently for E_d in the cubic metals using many-body potentials (English et al. 1992, Bacon et al. 1993, Gao & Bacon 1993), none as yet have been performed for the HCP metals - indeed, this work is the first of its kind. In the remainder of this chapter, the method of investigation, again using MOLDY, will be described and the results for both the α-Ti and α-Zr models will be given. As in chapter 4, the possible implications of these results for cascade development processes, such as major RCS directions, cascade mixing and morphology, and final defect mobility will be discussed.

- § -

5.2 Experimental Summary for HCP metals.

The primary method of causing threshold displacement events for experimental purposes is by high energy electron radiation, either in an electron accelerator, or a high voltage electron microscope (HVEM). In the former case, the sample resistivity is measured as radiation progresses with increasing electron energy (E_e), and the threshold energy is determined by extrapolating back to zero damage rate and using equation 2.1, with $E_d = E_{max}$. For HVEM the sample can be directly observed as the beam voltage is varied and the threshold energy determined when point defect clusters begin to appear. Again, E_d is determined using equation 2.1.

Each method has its own set of advantages and disadvantages. Accelerator-based experiments are conducted at low temperatures, usually ~8 K, which allows the detection of closely correlated single defect pairs. HVEM experiments are normally performed at room temperature which, since it is well above stage III annealing temperatures, allows the SIAs produced to cluster into extended defects visible in the microscope.

The measurement of the directional dependence of E_d requires knowledge of the crystallographic orientation of the specimens used. For electron accelerator experiments separate specimens, each of accurately known surface normal, are required. For HVEM accurate sample orientation can be accomplished by using extinction contours and Kikuchi lines, without the need for crystallographically specific specimens.

There are, however, two main problems common to both forms of experiment. First, since electron beams are scattered on entering a surface and by collision, the beam direction is not necessarily the direction of the PKA, particularly if any 'easy' displacement directions, i.e. those having a relatively low value of E_d, lie near to the

angle of incidence. In this case the 'true' value of the displacement threshold energy E_d' is calculated as

$$E_d' = E_d \cos^2 \theta \qquad (5.1)$$

where θ is the angle between the incident electron beam and the PKA recoil direction.

The second problem is the production of sub-threshold damage, and is not so easy to account for in calculation. This occurs because of low-mass impurities in the samples, which the electrons collide with and, since they are lighter than the normal metal atoms, displace at energies lower than the true displacement threshold. The impurity PKA then causes secondary displacement events with maximum energy determined by equation 2.2, substituting the mass of the impurity for m_n. As a result of this 'assistance' effect, the minimum electron energy needed to produce Frenkel pairs is reduced somewhat. Sub-threshold damage is also caused by the presence of other defects such as twin boundaries and dislocations which disrupt the continuity of the lattice and, in regions where the local density is reduced, can therefore decrease the amount of energy required to permanently displace an atom. Ascribing any damage to true or sub-threshold processes is accomplished by observation and annealing (Mitchell et al. 1975). If the damage is not generally concentrated along the extinction contours used to set up the sample, and can be removed by low temperature annealing processes, which are assisted by impurities, then the implication is that it is sub-threshold. Several experiments have been conducted to determine E_d and its orientation dependence for a variety of HCP metals, and the results are summarised in table 5.1. Fig. 5.1 shows some of the major crystallographic directions in the HCP lattice.

Zr has been the subject of much scrutiny, probably because of its applications within the nuclear power industry. Neely (1970) found, using an accelerator, that the minimum value of the displacement threshold energy, E_d^{min}, was 24 eV, with a mean

value of 28 eV. However, he did not determine the direction in which the minimum occurred. Biget et al. (1971), again with an accelerator-based experiment, found that after many measurements taken at increasing electron energy, the damage rate had a noticeably stepped profile, with the steps corresponding to values of E_d of 21, 30, 50 and 110 eV. These results were then taken by Kenik & Mitchell (1975) and, using an orientation function for Zn, they concluded that these steps corresponded to displacements along the <$\bar{1}2\bar{1}0$> directions at 21 eV, <$\bar{1}100$> at 30 eV and [0001] at 50 eV, and therefore E_d^{min} occurred along the <$\bar{1}2\bar{1}0$> directions. They found no orientation along which the value of 110 eV fitted satisfactorily. However, Griffith (1989), this time using HVEM disputed their findings on the basis of his measurements, finding E_d^{min} along the <$\bar{1}100$> and <$\bar{1}123$> directions, within experimental error. Griffith pointed out that Kenik & Mitchell had fitted the results of Biget et al. for Zr, a metal with $^c/_a$ < ideal, to an orientation relationship for Zn, a metal whose $^c/_a$ is > ideal. He did, however, also suggest the possibility that E_d decreased as temperature increased, since he conducted his experiments at 300 K and not 8 K as the previous workers had done.

Accelerator experiments performed by Maury et al. (1970, 1973) on Co gave values of E_d between 25 and 27 eV in the <$\bar{1}2\bar{1}0$> directions, 23 eV along <$\bar{2}203$>, and between 22 and 40 eV for the [0001] orientation. As can be seen from table 5.1, the HVEM results from Howe (1970) agreed quite well with these, giving an orientation of <$\bar{1}2\bar{1}0$> for E_d^{min}. The same dependence was found for Zn and Cd with accelerator-based study, as summarised by Vajda (1977). These last two metals are of the same period, with Cd almost twice the mass of Zn. The orientation dependence is similar, and an increase in E_d with mass is apparent. However, this does not seem to hold for metals from different periods, since the results for Co are similar to those for Cd, but the mass of Co is quite close to Zn. That said, however, the two metals that are the subject of this work, Ti and Zr, have a relationship similar to that of Zn and Cd, and therefore a similar mass dependence of E_d may be expected.

As can be seen from table 5.1, E_d^{min} occurs most commonly along the <$\bar{1}2\bar{1}0$> directions and, despite the variability of E_d between the metals in other directions such as [0001], the values of E_d for the <$\bar{1}2\bar{1}0$> directions are very close, falling within a ±3.5 eV envelope. The exception to this is Zn which, as noted before, has a $^c/_a$ ratio > ideal.

That the <$\bar{1}2\bar{1}0$> directions seem to be the lowest displacement threshold energy directions is, perhaps, to be expected since these are the close-packed rows in the HCP lattice along which RCSs travel, providing an efficient means of separating Frenkel pairs by relatively large distances and transporting energy. However, only a very limited number of orientations have been studied by experiment on HCP metals, all low-index crystallographic directions, and thus it would be mistaken to take these results as conclusive. Indeed, the maximum value of E_d found by Biget et al. in Zr was 110 eV, a result which no other experiments found along any low-index directions in any of the above metals. What is of note, however, is the relative similarity of the values of E_d^{min}, irrespective of direction, for all the metals listed in table 5.1, the exception again being Zn.

- § -

5.3 Molecular Dynamics Methodology.

In light of the fact that even for a single metal the experimental results are somewhat variable, and only a few orientations have been studied, a thorough investigation was conducted into E_d and its directional dependence using the MOLDY code. However, this analysis is made more complex than in the cubic systems by a point which seems to have been either overlooked or ignored in experiment, this being that directions of

similar indices are not necessarily identical as far as PKA processes are concerned. Fig 5.2 shows a schematic of a stereographic projection of the HCP unit triangle, which spans some 60°, not 30° as might first be thought from crystallography. Examination of fig 5.3 makes this clearer, with the bold encircled letters on figs. 5.2 and 5.3 corresponding to identical sections of the HCP lattice. Taking atom 1 as the PKA, planes C and C' lie at either side of the unit triangle. These are not equivalent for atom 1 because plane C cuts through the octahedral SIA site nearest to atom 1, whereas C' passes through the nearest tetrahedral site. The directions that mark the junction of these planes with the basal plane are [$\bar{1}$100] and [01$\bar{1}$0] respectively and, even though members of the <$\bar{1}$100> set, they are therefore not equivalent for displacements of atom 1. The <$\bar{1}$2$\bar{1}$0> directions, however, are all similar by virtue of mirror symmetry. Similarly the BO and BT sites lie in regions B and B' respectively.

A small block of 1960 atoms (10 x 14 x 14), the same size as was used to investigate the point defect properties, was set up at 0 K within MOLDY. An atom near the centre of the block was chosen to be the PKA, and given a selected amount of kinetic energy, generally 30 eV, in a designated direction. The dynamic events were then allowed to develop and the simulation run for around 200 time-steps (up to ~2 ps), by which time the damage created by the PKA had had time to recombine and either perfect crystal or a Frenkel pair remained. For directions in which RCSs were generated, it was necessary to change the shape of the block from approximately cubic to a flatter cuboid containing 5376 atoms (24 x 28 x 8) to prevent the RCS from crossing a block face, reentering and interacting with itself as a result of the periodic boundary conditions. Longer simulation times, up to 800 time-steps (~8 ps), were also required for these directions to let the RCS develop fully. If no defects had been produced at the end of the run, the PKA energy was increased, usually in steps of 5 eV, and the simulation repeated. Conversely, if one (or several) defects remained, the PKA energy was reduced by 5 eV and the run repeated. In this way E_d in the chosen direction could be 'bracketed' to within ±2.5 eV.

32 PKA directions around the edges of the two halves of the unit triangle, denoted by 'triangles' A-B-C and A-B'-C' in fig 5.2, were simulated for both the Ti and Zr models. Some 18 of the PKA directions were also repeated in Ti at 100 K in order to investigate the effect of temperature on E_d.

- § -

5.4 Results.

The results for the Ti and Zr models at 0 K are shown in figs 5.4(a) and (b) as plots of E_d versus angle around the two halves of the unit triangle. Figs. 5.5(a) and (b) show the Ti results for 0 and 100 K.

It is apparent from all the graphs that E_d has quite a complex directional dependence in both Ti and Zr, with values from 12.5 to 57.5 ± 2.5 eV for Ti, and 17.5 to 132.5 ± 2.5 eV for Zr. The only experimental investigation to show variability of this order is the Biget et al. (1971) study on Zr which yielded values between 21 and 110 eV. However, the direction for this highest value was, as mentioned before, not experimentally determined.

There is great similarity between the forms of the 0 K curves for the two metals (figs. 5.4 (a) and (b)), suggesting that the main contributor to the orientation dependence of E_d is the lattice itself. There is little difference between the B and B' regions for both models with the exception of one or two directions which will be discussed later. The most marked differences occur in the C and C' regions, with very similar form in both metals. With respect to temperature, figs. 5.5(a) and (b) show that generally it has little effect on E_d with, again, the exception of several directions within the B and

B' regions.

The underlying mechanisms for the variance of E_d with direction will now be considered with reference to the Ti model. Since the overall form of the E_d curves is very similar, most of the features of the Ti discussion will also apply to the Zr model. However, the differences between the two models will be pointed out and discussed, and the effect of mass and temperature considered.

- § -

5.5. Discussion.

5.5.1 Geometry or Structural Effects.

Throughout the following discussion, reference will be made to 'lenses', formed by nearest-neighbour atoms, which the PKA must traverse in order to produce a stable Frenkel pair. These are depicted in fig. 5.6 as L_1, L_3 and L_4, after Vajda (1977). The PKA is labelled as atom 1. Lens L_1, formed by atoms 2, 3, 6 and 5 is rectangular, and approximately twice the area of the other two triangular lenses, formed by atoms 3,4 and 6 (L_4) and 5, 6 and 7 (L_3). In an ideal HCP lattice, the two triangular lenses are of the same size, but for the two models used here, with $^c/_a$ ratio < ideal, L_3 is the larger of the two. It is evident that the closer to the centre of a lens the PKA attempts to cross, and the nearer to the lens normal its direction, the smaller the amount of movement required from the atoms at the lens vertices to let the PKA pass through, meaning a lesser degree of local distortion in the lattice, and hence a lower value of E_d for that direction. The same is true as lens size increases. However, it is not just the arrangement of these lenses that governs the shape of the E_d curves; the location of the atoms around this unit cell also play an important role in determining E_d, particularly

in the basal plane.

Beginning with the [0001] direction for Ti, the PKA passes through lens L_3. As it does so, atoms 5, 6 and 7 are displaced outwards slightly, but quickly move back onto their sites, effectively trapping the PKA and, since only a few atoms are displaced by relatively small distances, only a small amount of energy is required. Moving the PKA direction along the A line, the angle at which the PKA crosses L_3 and the distance from the lens centre increases, since atoms 5 and, particularly, 6 must be temporarily displaced further to allow the PKA to pass between them, and E_d is therefore increased. The PKA has enough energy remaining after doing this to cause additional displacements in the planes further above. The peak in E_d along the [$\bar{1}2\bar{1}3$] direction arises as a result of a combination of two collisions, one at a high angle to atom 6 in which a large amount of energy in lost, and a later head-on collision with an atom two planes up. In order to generate a defect far enough from the PKA site to prevent recombination, a relatively large amount of energy is needed, and a region of damage several planes deep results. The [$\bar{1}2\bar{1}2$] direction, a further 11° on, runs through fairly open space within the HCP lattice, with no atoms lying particularly close to the PKA path, and thus very few are displaced, reducing E_d. The [$\bar{2}4\bar{2}3$] and [$\bar{1}2\bar{1}1$] directions, though close to [$\bar{1}2\bar{1}2$], produce similar conditions to the [$\bar{1}2\bar{1}3$] direction in that both lead to a head-on collision with an atom two planes up. This can be thought of a passing through the L_3 lens at a high angle to the normal and close to one corner, therefore requiring a large amount of energy by producing a high number of temporarily displaced atoms in the planes above the PKA site. For the [$\bar{2}4\bar{2}1$] direction, the PKA does not actually pass through the plane above, but rather bounces off atom 6, displacing atoms in the planes above and below the original PKA site. Though these displacements are small, there are many and so E_d is large. Finally, at the end of the A line is the [$\bar{1}2\bar{1}0$] direction, lying in the basal plane. This is a close-packed direction, and produces an RCS of some 13 replacements. Other pairs of displaced atoms in the planes above and below are produced as the RCS passes,

associated with interactions with nearest-neighbours such as atom 6. It is one of these pairs that pins the final defect and, despite the fact that the energy required to produce an RCS in this direction is quite small, a larger amount is needed to provide sufficient separation of the Frenkel pair to prevent 'snap-back' of the RCS (also noted in cubic systems, Bacon et al. 1993) without producing an SIA.

Moving the PKA direction along side B towards [$\bar{2}3\bar{1}0$], atom 3 is struck and undergoes a series of focused collisions along the [$\bar{1}2\bar{1}0$] direction. There are several other atoms also displaced, increasing E_d. Further round, along the [$\bar{3}4\bar{1}0$] and [$\bar{5}6\bar{1}0$] directions, atom 3 is still made to recoil by the PKA, but the [$\bar{1}2\bar{1}0$] RCSs are shorter, and only half as many temporary displacements are produced and E_d is therefore low. For the [$\bar{1}100$] direction, four [$\bar{1}2\bar{1}0$] RCSs are produced, two at 90° to the PKA direction by atoms 2 and 3, and two at 30° by the atom directly in the PKA path. A set of frames depicting this cascade, produced from 'Ball & Stick™', are shown in fig 5.7. These RCSs are between 7 and 8 replacements in length, and the final defect is produced as they collapse. However, a moderately high energy is required to prevent complete recombination, so E_d is again increased.

As the PKA direction again rises towards [0001] along C, the PKA traverses lens L_1, which is larger than L_3 and rectangular. As explained previously, the energy required to cross this lens is small, producing E_d^{min} for the Ti model. However, lens L_3 is reentered near the [$\bar{1}102$] direction, and E_d rises again as its edge is crossed, due to atoms 5 and 6. E_d then falls as the PKA direction returns to [0001].

On moving along B' from [$\bar{1}2\bar{1}0$], the first two directions, [$\bar{1}3\bar{2}0$] and [$\bar{1}4\bar{3}0$], produce very similar cascades to their counterparts on side B. However, for [$\bar{1}6\bar{5}0$] E_d is much larger than at [$\bar{5}6\bar{1}0$]. The reason for this lies in the arrangement of atoms close to the PKA path. The [$\bar{1}6\bar{5}0$] direction, which is only 9° off [01$\bar{1}$0], runs very close to the basal tetrahedral site at the centre of the triangle formed by atoms 1, 3 and

4. At lower energies, the PKA is deflected away from this path and towards [$\bar{1}2\bar{1}0$] by the atoms directly above and below the BT site (atom 6 and its counterpart), producing a short RCS. In order for any lasting defects to be generated, the PKA energy must be sufficiently high to break through this barrier, and therefore a high E_d results. The [$5\bar{6}\bar{1}0$] direction, on the other hand, crosses the BO site in the centre of triangle 1-2-3 before encountering the BT site in the next unit cell and does not pass quite as near to it as the [$\bar{1}6\bar{5}0$] PKA, and hence a lower E_d ensues. The [$01\bar{1}0$] direction passes directly through the BT site, displacing atom 6 and its partner below, and, as in the [$\bar{1}100$], also produces 4 RCSs. These are shorter than for [$\bar{1}100$], containing between 5 and 7 replacements, but the peak number of displaced atoms is similar due to other displacements in the adjacent planes, and E_d is the same.

Rising out of the basal plane towards [0001] along C', the PKA path crosses lens L_4, one face of the 1-3-4-6 tetrahedron. Since this lens is smaller than L_3, more energy is needed, and thus more temporary displacements, to cause a permanent defect. Atom 6 also again plays an important role, as in the descent along A, and E_d increases to a peak at [$04\bar{4}3$], near the corner of L_4. E_d falls again along [$02\bar{2}3$], which corresponds to a head-on collision of the PKA with atom 6. This atom is ejected in almost the same direction as the PKA, and passes through the L_3 lens in the plane above before being trapped in the same manner as the [0001] case. This mechanism dominates as lens L_3 is encountered, and E_d remains constant up to the [0001] direction.

5.5.2 Mass Effects.

The processes behind the form of the E_d curve for Zr are much the same as for Ti, with very few differences between the two. The small differences that do exist have two possible causes, these being the slightly larger $^c/_a$ ratio of Zr (1.595 as opposed to 1.592 for Ti) and the slightly harder potential. The $^c/_a$ ratio difference means that

there is a little more space between the basal planes in the Zr model, and hence the distance between atoms in directions with a non-zero c-component is greater. However, this may be offset by the harder potential, which effectively increases the size of the atoms for any given interaction energy (or increases the interaction energy for a given separation). The effect of the BO and BT sites can again be seen in the B and B' regions, though a little more marked in the Zr model. The effect of mass is also obvious from figs 5.4(a) and (b), with E_d for most directions in Zr being generally around twice that in Ti. This was noted as a possibility in section 5.2 and has been seen in other studies, including comparisons between Ni and Al (Gao & Bacon 1993), which also have an approximately 2:1 mass and E_d ratio. Extrapolation of experimental data from Mitchell et al. (1975) for a variety FCC and BCC metals also showed a noticeable dependency of E_d on mass along some directions. However, despite this, E_d along the [$\bar{1}2\bar{1}0$] direction is identical in both metals at 0 K, having a value of 22.5 ± 2.5 eV, and the final Frenkel pair in the Zr model was also produced by an RCS of 13 replacements. This would seem to suggest some general minimum energy for displacements along the close-packed directions within the HCP system. Examination of the experimental results (except Zn for reasons explained earlier) in table 5.1 shows that this is possibly the case, with values of E_d along the <$\bar{1}2\bar{1}0$> directions between 21 and 27.5 eV.

5.5.3 Temperature Effects.

The effect of temperature, as shown for the Ti model in figs 5.5(a) and (b), is generally of little consequence to the displacement threshold energy. Fig 5.8 shows a series of frames for a cascade formed by a [$\bar{1}2\bar{1}3$] PKA at 100 K, a direction in which temperature has had little effect. As noted for the cubic metals (Calder & Bacon 1993), the thermal energy of the lattice serves to reduce E_d in directions falling at local maxima, and increase E_d for those which give local minima, also evident in the

comparison of the accelerator and HVEM results for Zr in table 5.1. The difference in E_d at the two temperatures studies here is, in most cases, between 0 and 10 eV. However, in directions in the basal plane, along sides B and B', there appear to be several anomalies. The value of E_d in the [$\bar{1}2\bar{1}0$] direction, lying at a local minimum on the 0 K curve, decreases further at 100 K rather than increasing. This is attributable to the thermal vibration of the lattice disrupting the replacement sequence and preventing its return, allowing a defect to be pinned as before, but for a shorter RCS length and hence a lower PKA energy. As discussed above, E_d for directions lying in the basal plane is highly sensitive to the arrangement of atoms in adjacent planes. With the addition of temperature, these atoms are no longer stationary or in regular array due to their thermal energy, and thus the distinction between the effects of the BO and BT sites becomes somewhat lessened. This thermal motion also causes the slight increase in E_d along the <$\bar{1}100$> type directions by disrupting the paths of the four outgoing RCSs and concentrating the temporary displacements in a smaller region. This allows recombination to occur and a slightly higher E_d is required to give sufficient separation for the final defect pair. The thermal energy of the lattice appears to have little, if any, effect on the values of E_d along sides C and C', indicating that the T and O sites may still play a part at higher PKA energies.

5.5.4 Other Correlations.

Throughout these simulations a strong correlation between N_{peak}, the peak number of atoms temporarily displaced during the cascade, and the value for E_d in that particular direction, as shown in figs 5.9(a) and (b) for Ti (again at 0 and 100 K) and Zr respectively. In this case a displaced atom is defined as one that is more than 0.27 a_0 from a lattice site, and not 0.32 a_0 as mentioned in section 3.42. This is simply because a small number of displacements were expected at near threshold energies, and a lower value of r_{srch} would make more displaced atoms 'visible', and make the

form of the final defect more apparent. However, at these relatively low energies, this small change in r_{srch} was found to have little effect on N_{peak}. In general then, the energy per displacement in a compact cascade at E_d is approximately 3 eV for Ti and 4.6 eV for Zr, whereas for cascades where the majority of displaced atoms are contained in focused collision sequences, this falls to near 1 eV for Ti and around 2.6 eV for Zr, with the exception of the [$\bar{1}$2$\bar{1}$0] direction where the single RCS generated has a length of 14 replacements, yielding around 1 eV per displacement when all other temporary displacements are included.

Also worthy of note are the final configurations of the SIAs produced. In the Ti model, the majority are of the BS variety, in agreement with the predictions of the static results in chapter 4. Indeed, only two of the Ti threshold simulations gave a different result, the metastable BO interstitial. For the Zr model the majority of SIAs remaining after threshold events were BC, again in accordance with the static results, and some were found in the BS and C forms.

- § -

5.6 Implications.

E_d has a far more complex directional dependence than experiment would seem to suggest, and is greatly affected by the local arrangement of atoms around the PKA. The most striking evidence for this is shown in the very different form of E_d for the C and C' regions of the unit triangle. Temperature generally appears to have little effect, save for the smoothing out of the E_d curves. Explanation is found for the one high measurement of Biget et al. of 110 eV for Zr in that several directions close to <$\bar{1}$2$\bar{1}$1> give $E_d \geq 100$ eV. However, for the most part, the experimental data referred to here do not mirror this wide range in values of E_d, and many values are close to

that measured for the <$\bar{1}2\bar{1}0$> directions. Since it is difficult in any electron-based experiment to ensure that the PKA is ejected in exactly the same direction as the incident electron, it is quite possible that many experimental measurements are, in fact, recording E_d for directions close to <$\bar{1}2\bar{1}0$> regardless of the initial beam orientation. This direction appears to be of importance over a range of HCP metals, with E_d having remarkably similar values for both the experimental data and simulation results, possibly suggesting the dominance of a simple collisional phenomenon. However, since displacement cascades at energies greater than threshold can greatly disrupt the lattice within the cascade core, the effects of any local structure may be swamped by the disordering effect of the cascade itself.

Correlating the results from this and the previous chapter, it is expected that cascades at higher energies will show preferential displacements within the basal planes due to the generally lower threshold displacement energy in directions lying in these planes and the lower formation energy for basal SIAs. These should be visible using the computer software mentioned in chapter 3. This is by no means implying that all, or even the majority of displacements will be in these directions, but rather that there should be a visible tendency for them to occur in the basal planes. This also implies that any intracascade atomic mixing will mirror this effect, manifesting itself as a discrepancy in the net distances atoms move in the basal and c-axis directions between their initial and final sites.

It is also expected that higher energy cascades will produce, for the most part, highly mobile SIAs lying in the basal planes, which may agglomerate into mobile small clusters. RCSs have been demonstrated here to be efficient, low energy producers of Frenkel pairs as predicted in initial theories (chapter 2), but displacements in other directions have also proved to produce defects at low energies, particularly for the Ti model, in which displacements through the L_1 lens have a slightly lower E_d than the principal <$\bar{1}2\bar{1}0$> RCS directions. However, since the NRT efficiency calculations

require a single value of E_d, these have been numerically calculated as the mean of the area integral under the E_d curves around the sides A-B-C-C'-B', giving $\bar{E}_d \approx 30$ eV for Ti and $\bar{E}_d \approx 55$ eV for Zr, though the separate means for each of the A, B, C, B' and C' regions vary by up to ±40% of these values. This, and the energy per displacement at the cascade peak calculated for the threshold events suggest that for a given PKA energy, N_{peak} for Ti should be approximately 1.5 - 2 times that for Zr.

- § -

Table 5.1: Summary of experimental results for the orientation dependence of E_d in several HCP metals. (E_d^{min} is underlined to show which direction it lies in.)

(All accelerator-based experiments were conducted at ≤8 K, and all HVEM studies at ~300 K)

Metal	Method	E_d (eV) <$\bar{1}2\bar{1}0$>	<$\bar{1}100$>	<$\bar{1}2\bar{1}3$>	<$\bar{2}203$>	[0001]	E_d^{min} (eV)
Zr	Accel.[1]	-	-	-	-	-	24 (28 mean)
	Accel.[2,3]	<u>21</u>	30	-	-	50	21(110 max)
	HVEM [4]	27.5	24.5	<u>24</u>	-	25.5	24
Co	Accel.[5]	25	-	-	-	<u>22</u>	22
	Accel.[6]	27	-	-	<u>23</u>	40	23
	HVEM [7]	<u>23</u>	30	-	-	33	23
Zn	Accel.[6]	<u>14</u>	-	-	25	19	14
	HVEM [8]	-	-	-	-	<u>15</u>	15
Cd	Accel.[6]	<u>21</u>	-	-	≥35	≥40	21

1. Neely (1970) 2. Biget et al. (1971) 3. Kenik & Mitchell (1975) 4. Griffith (1989)
5. Maury et al. (1970) 6. Vajda (1977) 7. Howe (1970) 8. Mitchell et al. (1975)

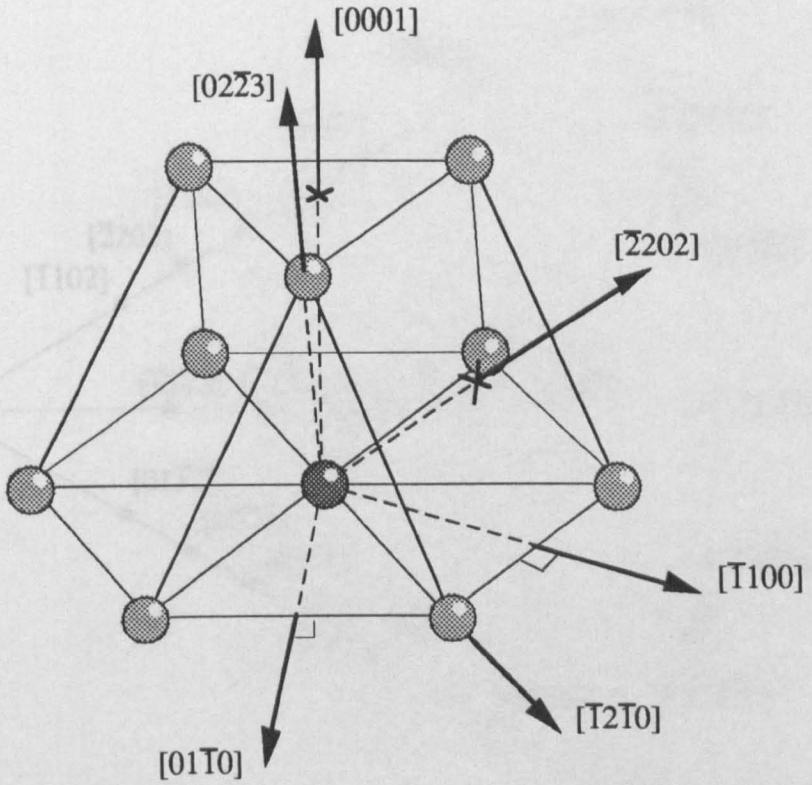

Fig. 5.1: Schematic of part of the HCP unit cell, showing major crystallographic directions.

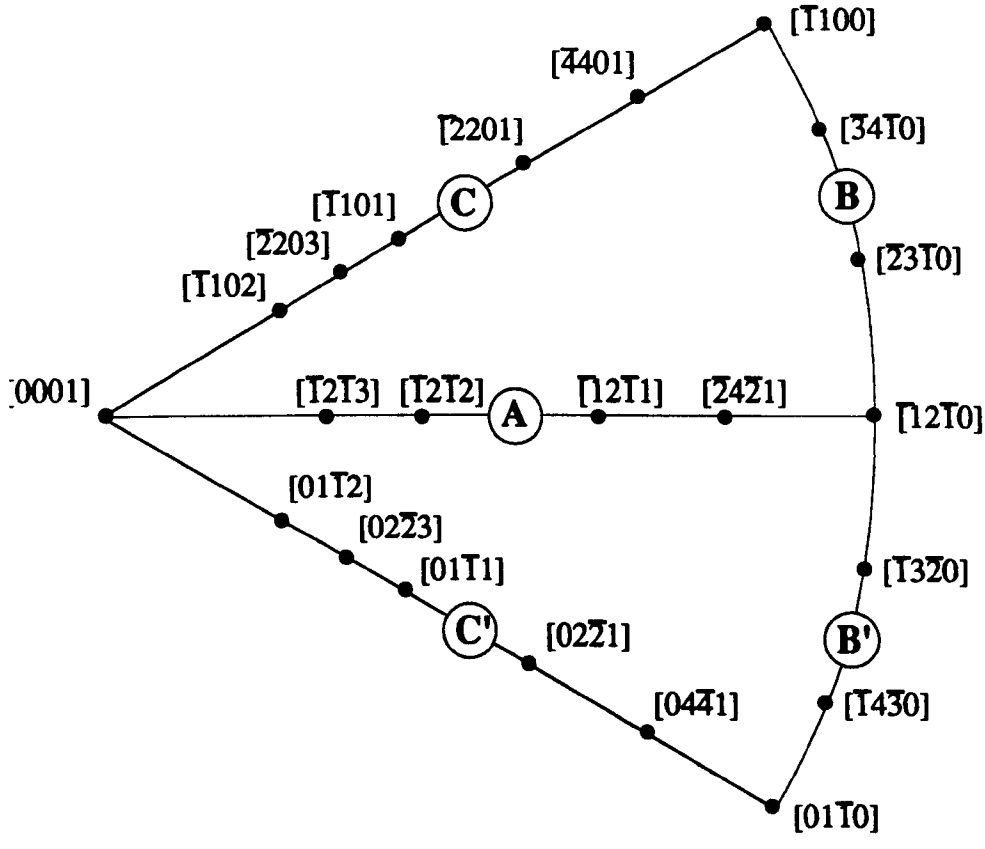

Fig. 5.2: [0001] stereographic projection of the HCP unit triangle, showing major crystallographic directions.

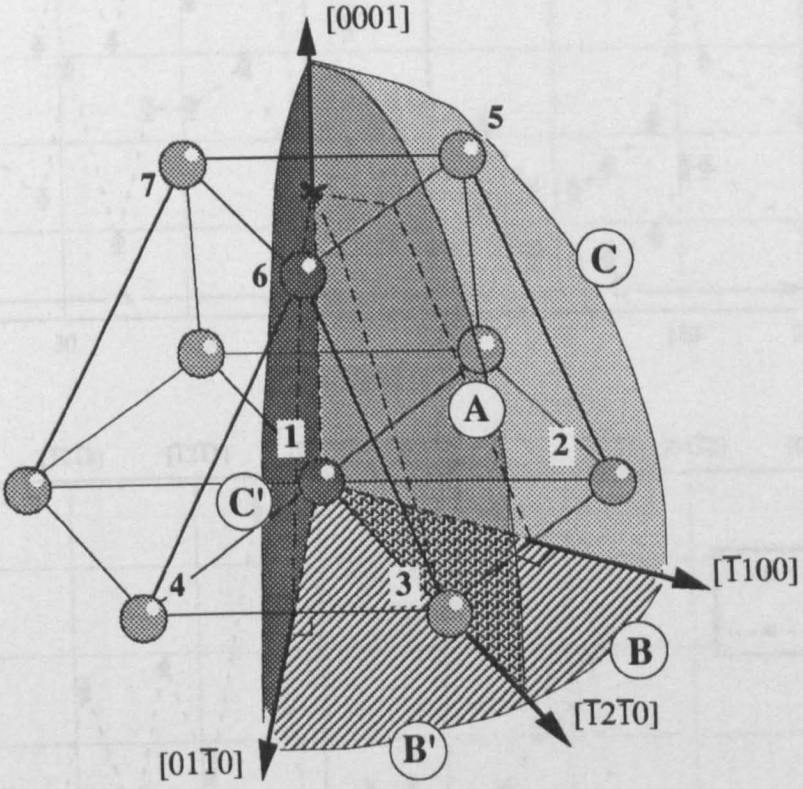

Fig. 5.3: Schematic of part of the HCP unit cell, showing boundary planes for the two halves of the unit triangle.

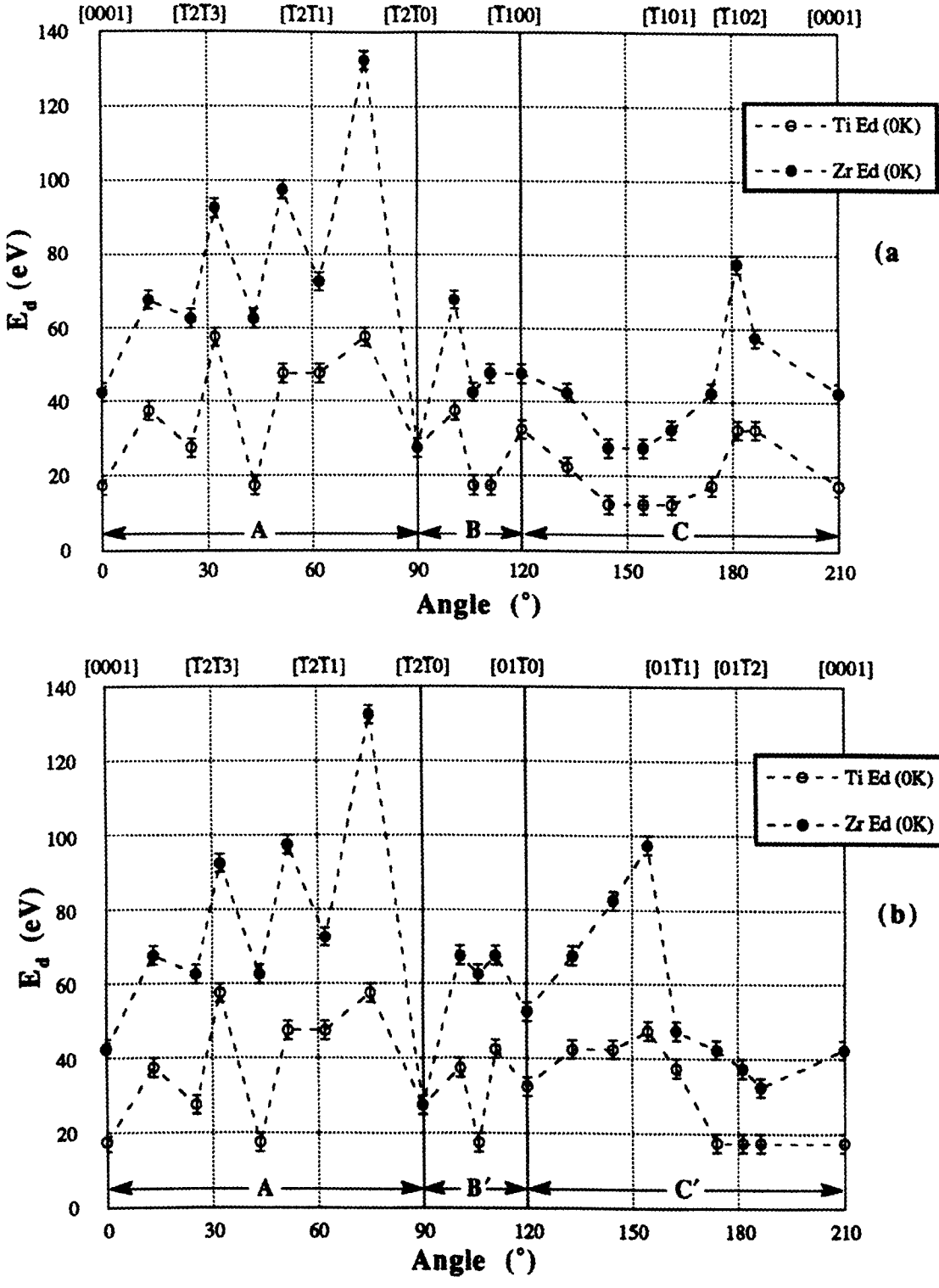

Figs. 5.4(a) & (b): Plots of displacement threshold energy at 0 K versus direction for the two halves of the unit triangle. Both the Ti and Zr data are shown for comparison.

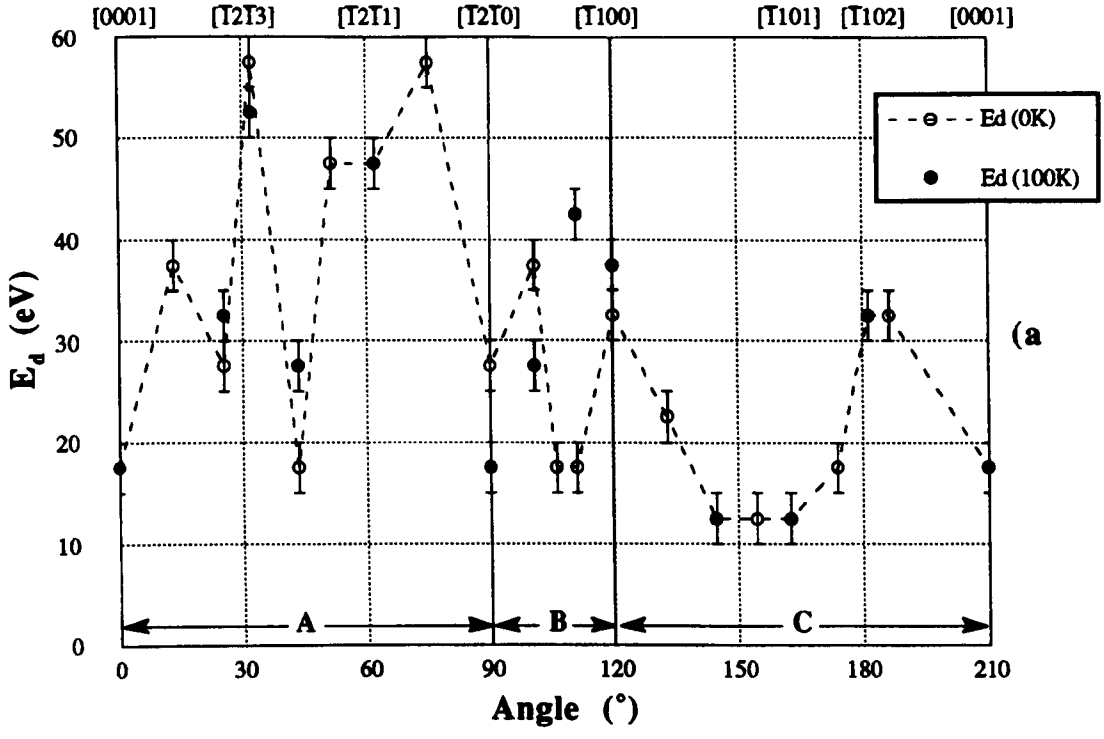

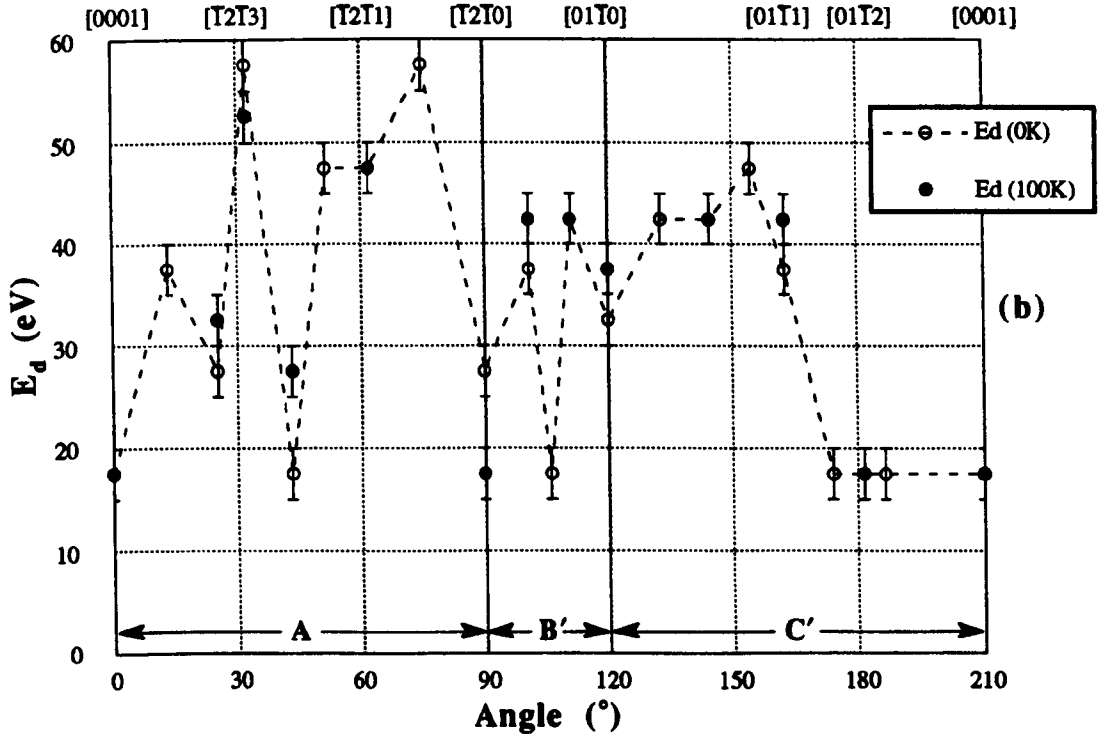

Figs. 5.5(a) & (b): Plots of displacement threshold energy versus direction at 0 K and 100 K for the Ti model.

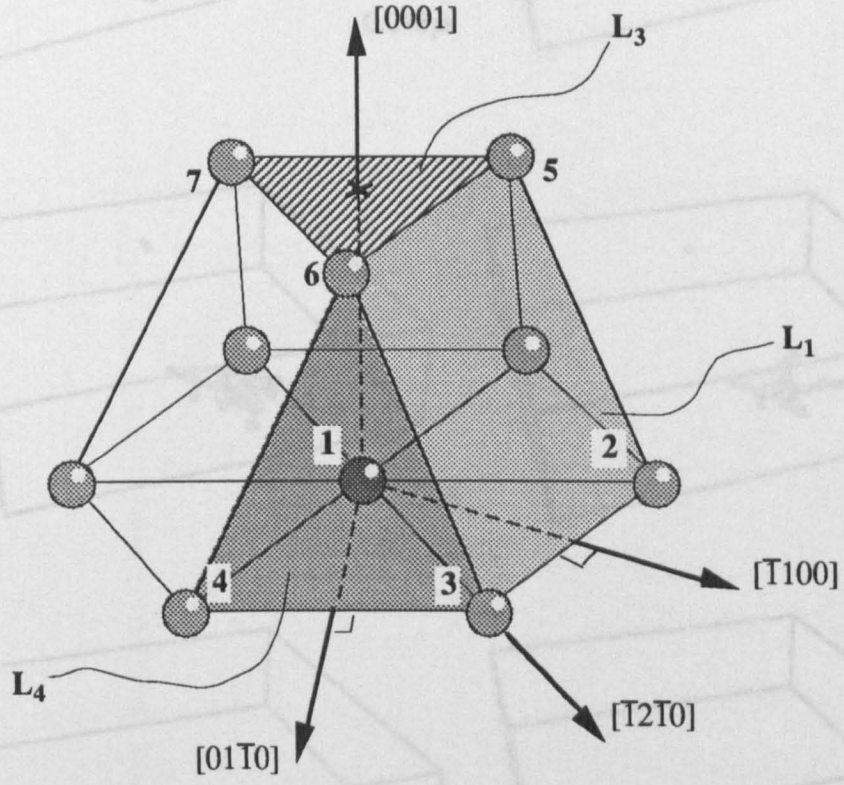

Fig. 5.6: Schematic of part of the HCP unit cell showing atom 'lenses', after Vajda (1977).

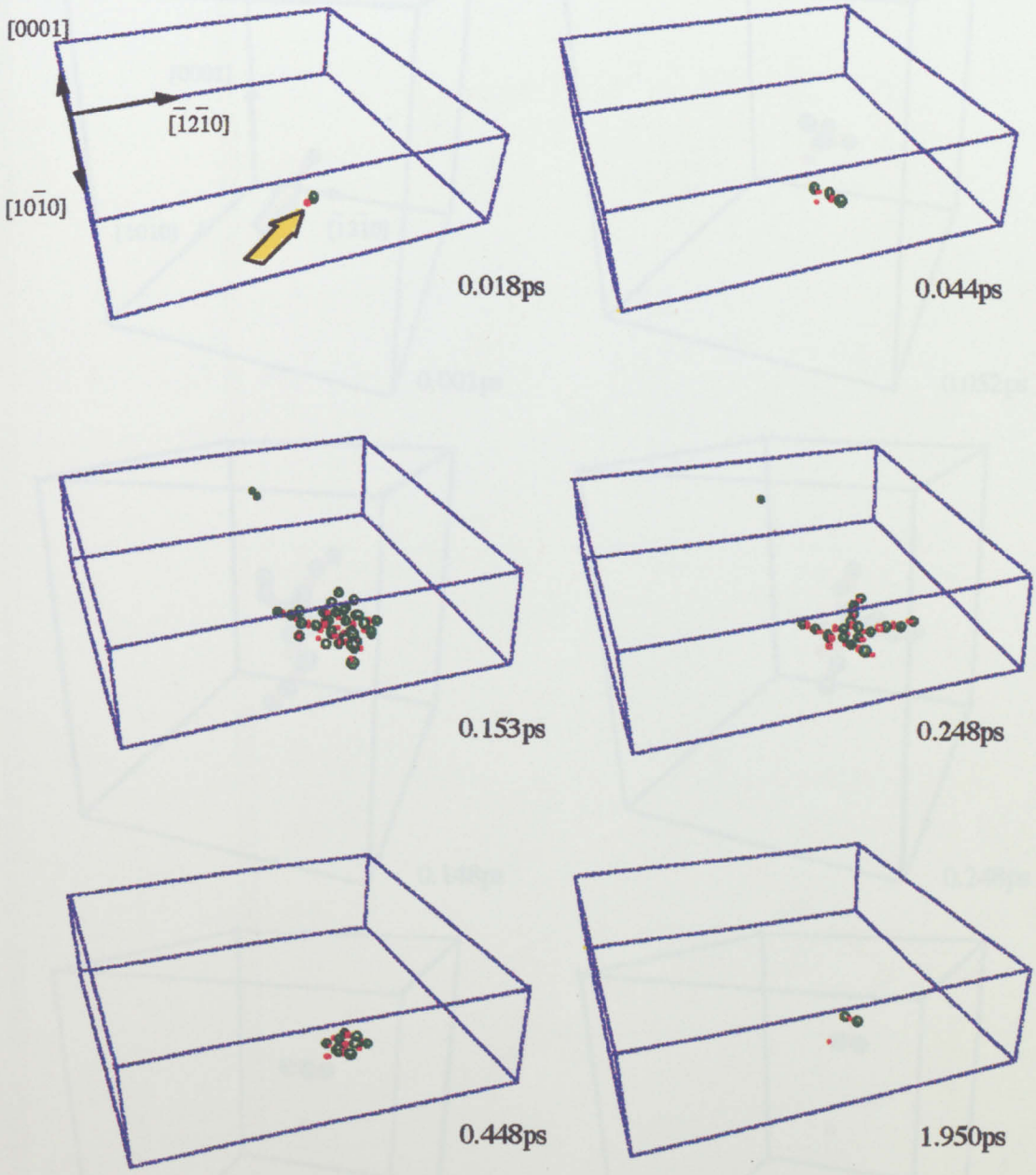

Fig. 5.7: Series of frames of a cascade generated by a [$\bar{1}$100] 35 eV PKA (shown by the arrow) at 0 K. Vacancies are shown as small, dark spheres, and the larger lighter spheres represent displaced atoms. Note that in the final frame, though two displaced atoms are visible, they constitute a single BS interstitial. Real time is shown for each frame.

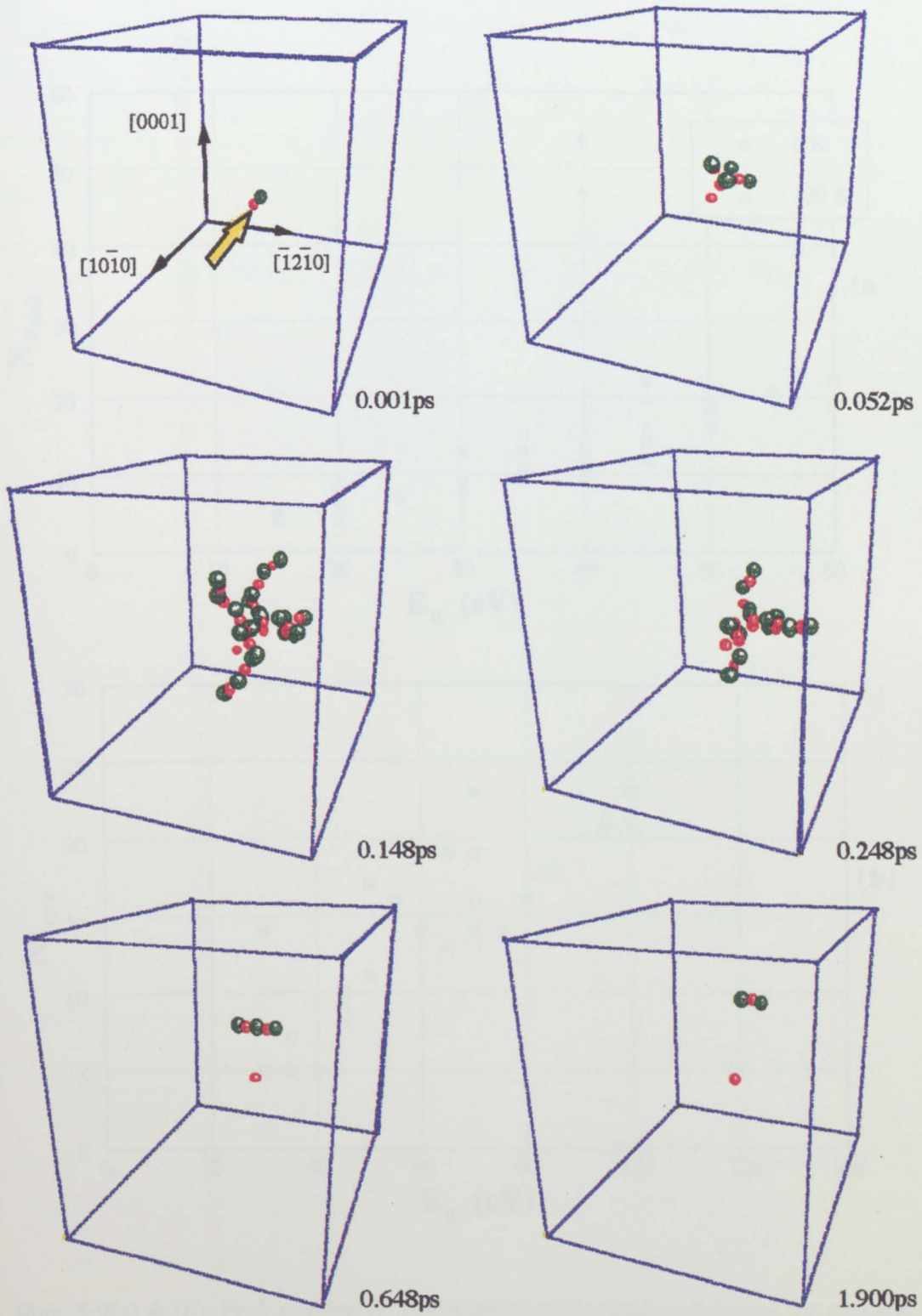

Fig. 5.8: Series of frames of a cascade generated by a [$\bar{1}$2$\bar{1}$3] 55 eV PKA (shown by the arrow) at 100 K. Again, note that the two displaced atoms in the final frame are a single BS interstitial.

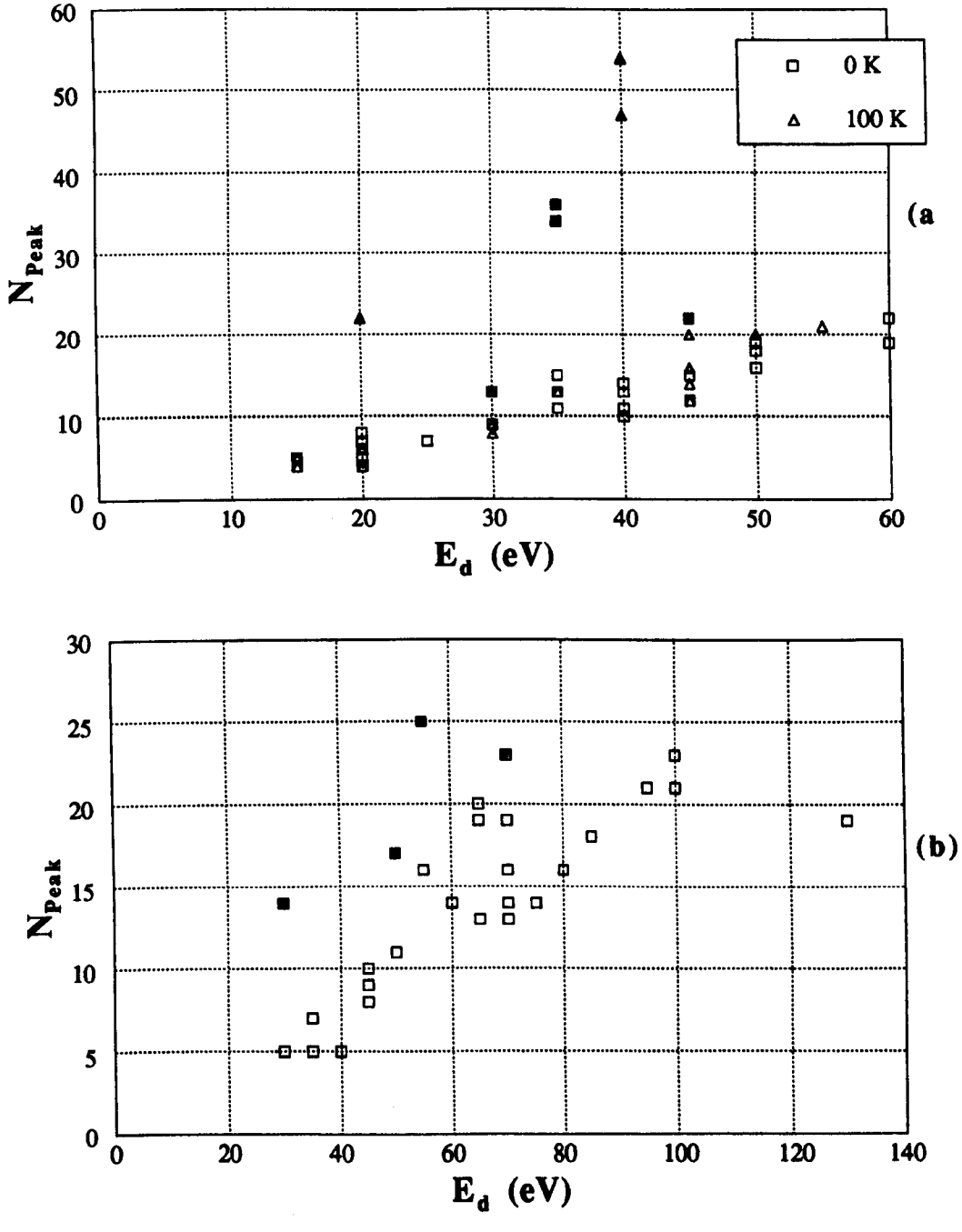

Figs. 5.9(a) & (b): Peak number of atoms temporarily displaced during the cascade versus displacement threshold energy for (a) Ti at 0 and 100 K, and (b) Zr at 0 K only. Filled boxes denote cascades dominated by focussed-collision sequences.

VI

Cascade Formation Processes

6.1 Introduction.

Having dealt with near-threshold phenomena in the previous chapter, and established the possibilities of several effects of the HCP structure on cascade formation at higher energies, the next two chapters will deal with displacement cascades created by PKAs with energy between 300 eV and 5 keV. In this chapter the results of the MD simulations of the these cascades will be detailed with respect to cascade formation processes, i.e. from initial recoil, and through the collisional and relaxation phases. No direct reference will be made to the configurations of SIAs and vacancies in this chapter, though details which are relevant to cascade formation and relaxation will be mentioned. Chapter 7 will deal with the final defect state, also known as the 'nascent' or 'primary damage' state. However, since the thermal spike encompasses the relaxation phase and continues into the primary damage state, there will be a small amount of overlap in discussion between the two chapters.

- § -

6.2 MD Methodology for Higher Energy Cascades.

In order to ascertain whether the crystal structure effects revealed in the previous chapter are still present at higher energies, four specific PKA directions have been chosen for cascade generation, rather than use the more common approach of random or single, high-index directions. The indices of the four recoil trajectories are $[\bar{5}7\bar{2}2]$, $[\bar{2}7\bar{5}2]$, $[\bar{2}3\bar{1}9]$ and $[\bar{1}3\bar{2}9]$, shown in fig 6.1 as D_1 to D_4. The first pair of directions are inclined at 16° to the basal plane, and pass quite closely above the O and T sites respectively, with the second pair lying at 18° to the c-axis. The second direction within each pair takes the PKA close to the nearest-neighbour atom at $^1/_3[02\bar{2}3]$, though not to a direct collision. These four directions are all of relatively high index,

this being a deliberate choice in order to avoid channelling from the first few collisions, and all lie within the two halves of the unit triangle, rather than on the boundaries.

The PKA energies used were specifically 300 eV, 500 eV, 1 keV, 2 keV and 5 keV, and the block sizes and number of simulations run at each energy are detailed in table 6.1 - a total of 36 cascades in Ti and 32 in Zr. All the simulations were carried out at a block temperature of 100 K to mimic thermal energy just above zero-point. Each block was equilibrated as described in chapter 3 for at least 1000 time-steps (~10 ps), to allow any long wavelength phonons or pockets of thermal energy formed as a result of the initially random atom velocities to come to equilibrium. For any PKA energies at which more than one simulation was performed with the same PKA direction, several blocks with different equilibration times were used to provide discrete initial conditions for each run.

By way of reminder, MOLDY as used in this work produces a variety of output data. At each documented time-step (usually every 5 or 10 time-steps), a snapshot of the cascade is made in the form of a list of spatial coordinates of all the displaced atoms and vacant sites, as defined in the preceding chapter, for use in the MacAtoms™, Ball & Stick™ and Atom-TV™ visualisation packages on the Apple Mac™ and Silicon Graphics Indigo machines, and this will be referred to as the 'TV file'. The real time, total number of vacant sites, total kinetic and potential energies and volume per atom are also recorded in the 'summary file' at these intervals to give time-dependent quantitative data, and every few hundred time-steps the coordinates of all the atoms in the block and all thermodynamic variables are dumped in a single 'atom file'. The size of this file, especially for large blocks, prohibits the retaining of more than a few of these for each cascade.

The results of the cascade simulations are presented in the subsequent sections of this

chapter, dealing first with those from observation of the TV files, i.e. the qualitative aspects deduced from the simulations and, following that, the quantitative data from the summary and atom files will be detailed and discussed.

- § -

6.3 Qualitative Results.

Since it would be impractical to show the temporal and spatial development of all the cascades simulated during the course of this study, several 'frames' at various times from a selection of cascades are presented in figs. 6.2(a) - (e) for Ti and 6.3(a) - (e) for Zr, one cascade at each value of E_{pka}. In each case at least four 'snapshots' are shown; one at t_{peak} when N_d has reached its maximum value N_{peak}, one labelled τ_d (this quantity will be described later, and has direct bearing on cascade evolution), one at time $t_{peak} + \tau_d$, when N_d has reached $^1/_e N_{peak}$ (i.e. 37 % of its maximum value), one frame near the end of the recombination phase, and one depicting the final defect state. These cascades were selected as being fairly typical of the form at that energy, though the variability in appearance and evolution of cascades at the same PKA energy, and even with the same initial PKA direction, implies the use of 'typical' in its broadest sense. Note that no discernible effect of PKA direction on cascade form was found at these energies, either in observation or measurement, in contradiction to the near-threshold effects in chapter 5. However, though the actual shape of the cascade seems to have no real dependence on initial PKA trajectory, one general observation from a variety of studies (Calder & Bacon 1993, Foreman et. al. 1992) including this is that the forward momentum of the PKA carries into and through the various cascade phases such that the regions of most disorder lie a short distance from the original PKA site in the general direction of the initial PKA path, and the SIAs remaining beyond the relaxation phase are often distributed further from the initial

PKA site than the vacancies again along the initial PKA trajectory. This effect is not simply quantifiable due to the large variety of final defect states produced, but is nonetheless apparent from the TV files.

Figs 6.5(a) - (e) show the same cascades as in figs. 6.2 and 6.3 at t_{peak} in the three orthogonal projections shown schematically in fig. 6.4. Cascades with the same value of E_{pka} in the Ti and Zr models are shown side by side for comparisons' sake, giving visual indication of the differences in cascade size between the two metals.

It was observed from plots such as these that in both models the cascade morphology changes with PKA energy. For E_{pka} below ~1 keV, the cascades have a quite 'open' and diffuse form, with a few long focused-collision sequences often occurring, though they do not always result in the production of a defect. At higher energies the cascades generally contain one, though sometimes several, discernible, compact regions of pronounced disorder at t_{peak}. This disordered material is surrounded by atoms displaced away from these regions, often in collective focused sequences, and therefore probably due to a shock-wave from the expanding cascade core. These regions are most obvious in the x and -y projections in figs. 6.5(a) - (e), since these show the basal planes edge-on, and any disordering effects are shown as visible disturbances to these otherwise flat planes. At energies of 2 - 5 keV in both models, individual cascades ranged from several small, dense regions of disorder surrounded by more open regions of displaced atoms and fairly short focused-collision sequences, to a single, large and highly disordered region with a mantle of radially displaced atoms. Figs. 6.5(d) shows both these forms for 2 keV cascades in the Ti and Zr models respectively. The former, more diffuse configuration exhibits a smaller peak number of displacements, shorter recombination phase and a higher final number of defects compared to the latter. In general, the greater part of the SIAs were generated at the boundaries of the highly disordered regions, with the vacant sites existing near their centres. Other single SIAs are formed by RCSs, and some clusters

by ballistic ejection mechanisms. However, in only a small number of cases was anything resembling vacancy loop formation seen and, as can be seen in the cascade pictures, both the SIA and vacancy distributions are quite scattered, especially at higher PKA energies.

Other features apparent from the visualisations are the greater number of atoms displaced at the cascade peak and the generally greater cascade volume for the Ti cascades and, from closer examination of the visual data, the higher number of defects remaining after the cascades in Ti, which will be discussed later.

In summary then, even the TV files alone yield important information on the general form of cascades in both metals and indicate the differences between them. Generally the PKA moves off its site and can traverse several lattice parameters before any other displacements become apparent. Eventually the PKA loses the majority of its kinetic energy in one or several collisions (see section 6.4.3) a small distance away from its original site and this distance increases with PKA energy. The cascade core then develops. Most cascades tend to have a very approximately ovoid shape, but their longer axis appears to have no dependence on initial PKA direction and is much more dependent of the multitude of displacements that follow. At low PKA energies, the core remains quite open and diffuse, but as E_{pka} increases so does the density of the core. On occasions though, at higher energy the PKA or one of the secondary recoil atoms can travel along open channels within the atomic structure. The 'channelled' atom can move relatively long distances before any significant collisions take place, so spreading the PKA energy over a larger volume in the crystal and creating a much more diffuse cascade, akin to those formed at lower values of E_{pka}. Sometimes two or more distinct regions of disorder, otherwise known as 'subcascades', are produced in this manner, though this was a rare occurrence in these simulations. Focused-collision sequences are often present and many extend from the cascade core but retract just before N_d reaches its peak, and in most cases leave no permanent defect. Beyond the

cascade peak, many atoms recombine rapidly with the sites from which they came. However, the regions of strong disorder identified above can remain visible for some time as displaced atoms recombine by diffusive mechanisms with other vacant sites, until finally only 'true' interstitials and vacancies remain in the primary damage state.

The following section deals with the results from the summary and atom files, and is subdivided according to the various aspects of cascade development, based on the nature of the data within each subsection.

- § -

6.4 Quantitative Results.

6.4.1 Ballistic Aspects.

Having observed that the number of displaced atoms increases rapidly to a maximum and then decreases at a slower rate to some final value, figs. 6.6(a) and (b) show the numerical variation of N_d with time and PKA energy for the for those cascades shown in figs. 6.2, 6.3 and 6.5. Figs. 6.7(a) and (b) show the range of N_d for all cascades simulated in the Ti and Zr models respectively. There is, particularly at the higher PKA energies, a wide envelope for N_d for cascades with the same initial value of E_{pka}, in accord with the variability of the visual results described in the previous section. The mean value of N_{peak}, as shown in fig. 6.8, increases with E_{pka} for both Ti and Zr, and is higher for Ti than Zr, again in agreement with the qualitative assessment based on observation in the preceding section. However, the relationship between these two quantities is not linear, and exhibits a shift in energy per displaced atom at the peak between PKA energies of around 1 - 2 keV. At $E_{pka} \leq 1$ keV, the

energy per displaced atom is ~2.05 eV for Ti and ~3.95 eV for Zr. Above this, it falls to ~1.35 eV/atom for Ti and ~2.15 eV/atom for Zr. These results are close to those reported in chapter 5 for the 'normal' and focused-collision dominated cascades respectively that are formed at threshold. This therefore indicates a marked change in the proportion of atomic displacements contained in focused sequences in cascades from a low proportion in the form of a few individual sequences at PKA energies below ~1 keV, to a higher fraction contained in collective displacements above this. This is also in agreement with the change in cascade formation and morphology observed from the TV files.

6.4.2 Temporal Aspects.

The variation of the mean value of t_{peak} is shown against PKA energy for the Ti and Zr models in fig. 6.9. Here t_{peak} for Ti is lower than for Zr at a given E_{pka}, showing the effect of mass, but both models show essentially the same form. Once more there is a transition at E_{pka} ~1 - 2 keV, which coincides with the shift in N_{peak} vs. E_{pka} described above. It again indicates a marked increase in the fraction of displaced atoms contained in multiple focused-collision sequences, and is such that although N_{peak} increases disproportionately with E_{pka}, t_{peak} actually undergoes a relative decrease in comparison, since the majority of the extra displacements require low energy. They are also such that they will recombine quickly beyond the peak. This effect has also been noted in other systems, including α-Fe and Ni_3Al (Calder & Bacon 1993, Gao & Bacon 1994).

It was noted by Calder & Bacon (1993) for a given E_{pka} that, once past t_{peak}, the number of displaced atoms initially decreases with time in an exponential fashion such that

$$\left(N_d - N_f\right) \propto exp\left(-\frac{t}{\tau_d}\right) \qquad (6.1)$$

where N_f is the final number of displaced atoms, and τ_d is the time from the peak for N_d to fall to 37% of its maximum value, as mentioned in section 6.3. Fig. 6.10 shows N_d against time for a Zr cascade with E_{pka} = 1 keV, and shows this effect clearly for a period of ~0.9 ps after the peak. This is attributable to the correlated athermal recombination with their original sites of atoms displaced by small distances, such as those contained in short focused-collision sequences or in the mantle of radially displaced atoms described above for the higher energy cascades. Beyond this time, displaced atoms undergo uncorrelated recombination with vacant sites by diffusive mechanisms during the remainder of the thermal spike as N_d nears its final value. The characteristic 'relaxation time' τ_d can be found from the gradient of the 'linear' region of this N_d vs. time curve, remembering that in fig. 6.10 N_d is plotted on a log axis. Similar plots for other energies in both metals were presented in figs. 6.6 (a) and (b). The dependence of τ_d on E_{pka} is shown in fig. 6.11 for both models, and again a transition at 1 keV is exhibited. This is most obvious and extremely abrupt for the Ti model, with a steady increase in τ_d up to ~0.57 ps at E_{pka} = 1 keV and little change thereafter, whereas for Zr the transition is more gradual but nevertheless present.

This sudden transition in the Ti model gives another indication of the change in cascade morphology that occurs with increasing E_{pka}. For PKA energies of up to 1 keV, the cascade form is quite open and diffuse as seen from the TV files. This is reflected in the τ_d curve as an increase in the relaxation time with E_{pka}, since this open form allows the recombination of the increasing number of displaced atoms by a process which looks similar to the collisional phase in reverse, i.e. one displaced atom, as it recombines, pushes another onto its site, and this continues until the cascade reaches its final state. As the cascade increases in size with PKA energy, τ_d reflects this. However, above 1 keV, 'true' cascade conditions, i.e. the existence of a definite and compact disordered cascade core, are established and, as described in section 6.4.1, a large proportion of the increasing number of displaced atoms are

those contained in short radial focused-collision sequences around the periphery of the core. These short low-energy sequences can collapse rapidly and with minimum interference with one another and, since they can also collapse simultaneously, the number of these sequences is almost irrelevant as far as τ_d is concerned. Therefore it is only the displaced atoms outside the cascade core which contribute significantly to τ_d. At these higher PKA energies, the displaced core atoms remain so for much longer than $t_{peak} + \tau_d$. Thus, above PKA energies of 1 keV, even though N_{peak} is still markedly increasing, τ_d for the Ti model increases only slightly with PKA energy.

For the Zr model this establishment of a true cascade is more progressive but, since the atomic mass of Zr is twice that of Ti and the energy per atom for focused-collision events is higher, the transition from a collection of closely-correlated displacements at low E_{pka} to true cascade conditions at high energies is expected to be slower. For α-Fe, for example (Calder & Bacon 1993), which is also heavier than Ti but lighter than Zr, the transition in τ_d occurs at around 2 keV, and it is therefore quite possible that a more marked shift in τ_d for Zr will occur at higher PKA energies than the 5 keV upper limit simulated in this study.

6.4.3 Energy Aspects.

At each documented time-step, the total kinetic and potential energies of the simulation block are recorded, and in all cases these exhibit a form with respect to time as shown in fig. 6.12 for a cascade in Zr with E_{pka} = 1 keV. Note that here the kinetic energy (KE) and potential energy (PE) per atom are displayed. Initially the block is in equilibrium at 100 K, and therefore all the atoms have only ~0.01 eV of kinetic energy corresponding to their thermal energy. Once the cascade is initiated, the PKA energy dominates the block KE and, as the cascade progresses, this reduces as disorder is created in collisions and thus the potential energy increases. The few sudden spikes in

the curves (drops in KE and increases in PE) during the first ~0.05 ps are due to the initial high-energy collisions during which the PKA loses the majority of its KE as it approaches very close to the target atoms, and hence the PE temporarily increases during these encounters. However, at ~0.1 ps there is a 'blip' in both the KE and PE, producing a local maximum in the KE curve (and a local minimum in PE) and therefore a temporary equilibrium between the two. This corresponds to a change in the distribution of energy from a few atoms possessing KE far in excess of thermal values (the results of the first few collision events) to a state where many more atoms have an energy distribution above $\bar{E}_d$ as the disordered cascade core starts to become established. Fig. 6.13 shows E_{max}, the maximum KE of any atom within the block, against time and it can be seen that, in this case, by ~0.13 ps no atom possesses KE greater than $\bar{E}_d$ (55 eV for Zr) even though the evolution time is only just over $^1/_4$ t_{peak}. By ~0.16 ps E_{max} is less than E_d^{min} (27.5 ± 2.5 eV for Zr) and therefore there is no longer sufficient KE available to initiate permanent displacement events. At t_{peak} (0.471 ps in this case) $E_{max} \approx 1.6$ eV, and therefore the assumption could be made that this is approximately the value of E_{crit}, the amount of energy required to temporarily displace an atom, as used in the BCA discussed in chapter 3. However, E_{crit} is dependent on the value of r_{srch} used to identify displaced atoms in MOLDY, and therefore should only be taken as an indication of the order of E_{crit} rather than an absolute. Even so, at this point E_{max} is ~0.55 eV less than the energy per atom required for focused-collision events in Zr, and can therefore be taken as a good indication of the maximum possible value of E_{crit}.

Also at t_{peak} the KE and PE curves reach equilibrium again, shown as a local minimum in KE and a maximum in PE, thus indicating the state of most structural disorder. This is analogous to a pendulum reaching the top of its swing. Beyond the peak the PE begins to reduce towards its final value, and the KE increases again as the displaced atoms move back either to their original positions or other empty sites. By the end of the relaxation phase the PE and KE settle around their new equilibrium

values. The energy of the PKA has been dissipated throughout the block, manifesting itself as a rise in the ambient kinetic temperature. Note that after a cascade the PE is always higher than the KE by an amount corresponding to the formation energy of the permanent defects created, minus the binding energy of any clusters which may have formed.

6.4.4 Cascade Core Structure.

One of the issues raised in section 2.6 was whether or not the core of a cascade actually melts and becomes liquid. This point is crucial to some models which explain the vacancy clustering seen in experiment, as outlined in chapter 2. However, the state of the cascade core is still quite difficult to ascertain, especially for cascades at PKA energies of less than 1 keV, since at these energies no truly discernible regions of high structural disorder exist and it would therefore be unfruitful to analyse the state of the central region of such cascades. Even at the upper limit of E_{pka} used in this work the variability of cascade form makes the use of any analytical techniques difficult. Despite this, there are a number of methods available which can give a good indication of the core state.

The radial pair distribution function g(r) has been calculated at various times for three of the higher energy cascades which were approximately spherical in shape, thus allowing the cascade core to be contained in a spherical region - one 5 keV cascade in Ti, and one 2 keV and one 5 keV cascade in Zr. This function is shown in figs. 6.14(a), (b) and (c) respectively. Note that the centre of the cascade core has been taken as the centre of gravity of the vacant sites, and the radius of the inner region over which g(r) was calculated was kept constant at 4 a_0, chosen to encompass the most disordered region of the cascade without including large amount of undisturbed material which could affect g(r). This inner sphere contains approximately 390 atoms

in an equilibrated block, which were then analysed with respect to all their neighbour atoms contained in a larger outer sphere of radius 7 a_0 (containing a further ~2500 atoms). The common features of these three g(r) plots are the rapid loss of solid-state order within a fraction of a ps, and the reaching of a highly disordered state at the cascade peak, as expected from the KE and PE plots in the previous section. However, this highly disordered state then persists for several ps before the peaks in g(r) which denote a crystalline solid then reappear. Fig. 6.14(d) shows g(r) for the Zr model at various temperatures from 0 K to 2800 K, and shows that the characteristic peaks which might be expected of a solid are blurred even at 600 K, and by 1500 K only four are discernible. At 2100 K (which was verified as a liquid by visual observation of the atomic positions in the block using AVS™) g(r) shows small peaks at radii of approximately a_0, $2a_0$ and $3a_0$, indicative of the liquid state. Comparison of fig. 6.14(d) with the three previous figs. shows that, at t_{peak}, g(r) most closely resembles that of a liquid.

The core kinetic temperature (i.e. the mean temperature per atom) with respect to time has also been calculated for these cascades as shown in fig 6.15. Note that in the initial stages of the cascade the core temperature calculations are artificially high due to the high PKA energy affecting the mean, and therefore the first temperature shown for each cascade is that at t_{peak}. The melting temperature (T_m) of pure Ti and Zr is 1960 K and 2120 K respectively, and T_m for the models used in this work have been estimated at 1410 ± 150 K and 2030 ± 160 K respectively by a derivative of the method employed by Kapinos & Bacon (1993) to investigate vacancy sweeping (see appendix B for more details). Whilst T_m for the Ti model is ~28% lower than the experimental value, T_m as calculated for the Zr model is in good agreement with experiment. The reason for the discrepancy in T_m between the Ti model and experiment has not been determined.

From both the g(r) and core temperature plots, it is apparent that the cascade core is

extremely disordered and very hot, with temperatures in excess of T_m for both the model and experiment, and the conclusion could be made that the core is therefore liquid. However, g(r) for the HCP structure, which has lower symmetry than the cubic systems, is quite sensitive to temperatures below T_m, as demonstrated in fig 6.14(d), and therefore a g(r) which may seem to suggest a liquid could also be derived from a very hot, highly disordered solid. This has been seen to be the case for α-Fe (Calder & Bacon 1993) in which g(r) resembles that of a super-heated solid rather that a true liquid. However, in work on Cu (Foreman et al. 1992), g(r) for the core of a 2 keV cascade was closer to that of a liquid.

The density of the cascade core may also be used to give indication of its state when compared to the density of the solid in equilibrium (ρ_0). For the 2 keV Zr cascade mentioned above, the core density is 0.83 ρ_0 at t_{peak} (derived from the ratio of number of atoms in the core sphere at the cascade peak to the number in the sphere in equilibrium at 100 K). For the 5 keV Zr cascade the core density has also fallen to 0.83 ρ_0, and is only 0.80 ρ_0 for the 5 keV Ti cascade. For a true liquid in equilibrium, the density is typically around 0.95 ρ_0 (Smithells Metals Reference Book), so these values are more consistent with those of a cavitated liquid. However, they could also be close to those of hot solid with a high concentration of vacancies.

Therefore, even based on this variety of data, the state of the cascade core cannot be definitely set as either a solid or a liquid. Whilst possessing the highly disordered form, density and temperature expected of a liquid, the same results could be derived from a super-heated, vacancy-rich solid. Given the extremely small temporal scale of the cascade and the submicroscopic size of the core, it also seems unlikely that a true liquid, with the characteristic Maxwell-Boltzmann distribution of velocities, could be established so rapidly and in such a confined volume despite the large energy densities involved. Therefore the best description of the cascade core state is a hot, highly disordered liquid-like solid or quasi-liquid.

The mean cascade volume at t_{peak} is shown in fig 6.16 for both models against E_{pka}. The cascade volume is taken to be the volume of an ovoid, centred on the centre of gravity of the vacant sites and of dimensions equal to the RMS distances of the vacancies from their centre of gravity in the x, y and z directions (r_x, r_y and r_z), such that the cascade volume V_{casc} is given as

$$V_{casc} = \frac{4}{3}\pi r_x r_y r_z \qquad (6.2)$$

Again a transition is evident at a PKA energy of around 1 keV, and is most prominent in the Ti model, even within the large error brought about by the relatively low number of samples at the higher energies. As was the case with τ_d previously in section 6.4.2, the shift is not so prominent in Zr but is nonetheless present. Once more this transition is linked to the change in cascade morphology at 1 keV and the associated increase in the proportion of atoms contained in the radially displaced mantle that surrounds the cascade core. However, the increase in the size of the disordered core also has its effect on V_{casc}, and the sudden growth in V_{casc} at 2 keV cannot be attributed solely to the presence of atoms displaced by a shockwave from the core.

- § -

6.5 Discussion and Summary.

6.5.1 The Collisional Phase.

The results from section 6.4.3 indicate that this phase divides conveniently into two substages characterised by the change in E_{max} with time. The 'blip' in the KE curve at

~0.1 ps corresponds closely to the point at which E_{max} falls below $\bar{E}_d$, and it is interesting to note that this time of 0.1-0.2 ps is that quoted by Diaz de la Rubia et al. (1989) as being the end of the collisional phase. Clearly, by consideration of the N_d plots in figs. 6.6 and 6.7, this is not the case. Rather, this point signifies the end of the permanent displacement stage of the collisional phase since, when E_{max} has fallen below E_d^{min} (which occurs at around 0.2 ps later for the cascade under consideration) no more permanent displacements can be initiated. Therefore in the rest of this discussion, the first substage of the collisional phase, from the initial impulse to the PKA up to the point at which E_{max} falls below E_d^{min}, will be referred to as the 'primary collisional phase', and the remainder of the collisional phase from that point to t_{peak} will be termed the 'secondary collisional phase'. The lengths of these two stages will be referred to as t_1 and t_2 and are such that $t_{peak} = t_1 + t_2$.

Data for E_{max} was only generated for the one Zr cascade detailed in section 6.4.3, so no direct comments on the effects of E_{pka} and mass on the lengths of the two collisional stages can be made. However, by extrapolation of the rest of the data in this chapter, their effects can be inferred.

Based on the change in cascade morphology with increasing PKA energy noted from both the TV files and quantitative data (t_{peak}, N_{peak}, τ_d), the ratio of t_1:t_2 could also be expected to be affected by this transition. At low energies the secondary collisional phase will dominate, since E_{pka} is closer to E_d, and the number of atoms and time required to dissipate the PKA energy is less, meaning fewer permanent displacements. As PKA energy is increased it is anticipated that the primary phase will become more prominent by virtue of the time taken to develop the dense and highly disordered hot cascade core in dispersing the PKA energy, and the fact that the majority of the temporary displacements in cascades at high PKA energies are contained in focused-collision sequenced which form readily and rapidly, and therefore require a comparatively short secondary phase. Note that the displacements

in the primary stage will not all be permanent since there is a distribution of KE values, some of which will be below E_d^{min}.

The transition from primary to secondary stage is not initially obvious from the TV files at low values of E_{pka}, but becomes more noticeable at the higher energies, particularly 5 keV and in the very compact cascades. The change is detected as the nature of the temporary displacements changes from seemingly random, uncorrelated trajectories during the primary stage to coordinated movement radially outwards from the most disordered zone during the secondary stage. This would also agree with the nature of these two stages as discussed above in that the primary stage contains the permanent displacements which require high disordering or large Frenkel pair separation, and the secondary stage consists only of temporary displacements such as exist in RCSs and focused-collision sequences.

By the end of the primary collisional phase the cascade core is established and visible, though the use of the term 'cascade core' is somewhat inapplicable at the lower PKA energies. From the TV files it is also seen that the bulk of the SIAs which remain after the recombination phase are left around the periphery of the core regions(s), even though more displacements are generated in the secondary stage. This again ties in with the nature of the two phases as described above.

6.5.2 The Cascade Peak.

The end of the secondary collisional phase is marked by the peak in the number of temporarily displaced atoms at time t_{peak}, and both N_{peak} and t_{peak} depend in a non-linear fashion on E_{pka} and mass (figs. 6.8 and 6.9). The mass dependence of N_{peak} on PKA energy can be attributed simply to the difference in $\bar{E}_d$, since the larger the displacement threshold energy the lower the number of atoms required to dissipate the

PKA energy, and hence N_{peak} reduces as mass increases. Note that, although there is a factor of almost two between $\bar{E}_d$ for the two models in this work, N_{peak} does not mirror this because many displacements will occur at energies less than $\bar{E}_d$ (though obviously above E_d^{min}) and the ratio of energy per displaced atom in the two metals is less than 2:1, as described in section 6.4.1. Therefore the ratio of values of N_{peak} for Ti and Zr is somewhat less than two.

Even though N_{peak} is reduced as mass increases, t_{peak} increases. This is due to the larger momentum and lower velocity of a heavier object than a lighter object with the same kinetic energy. In this case the objects are atoms, and a doubling of mass for the same KE results in an reduction in velocity of a factor of $1/\sqrt{2}$ (~0.707). However, the ratio of t_{peak} values for the two models is 1:1.22 (Ti:Zr), and not 1:1.41 as might be expected from the resulting ratio of velocities if the cascade dimensions were equal in both models. As pointed out above, cascade size reduces with mass and therefore the increase in time taken to reach peak cascade size is partially offset by this, thereby reducing the ratio of t_{peak} values for the two models in question.

As far as the structure of the cascade core is concerned, the issue is still somewhat open to contention. Given the data from the various analysis techniques as laid out in section 6.4.4 the core cannot be defined as either a true solid or liquid. Irrespective of the exact definition of the state of the core, it is such that the structural effects seen at near-threshold energies are swamped as the structure is disrupted, and hence no dependence of cascade form on PKA direction is seen.

6.5.3 The Relaxation Phase.

Beyond the cascade peak the number of displaced atoms reduces via two different mechanisms and, accordingly, the relaxation phase can also be split into two

substages, though both these stages are within the thermal spike. Initial recombinations are seen to be rapid and essentially athermal in nature and, in the lighter of the two model metals, almost independent of E_{pka} beyond 1 keV. As pointed out in section 6.3.2, they occur between displaced atoms and either their original sites or other neighbouring vacant sites, and the duration of this phase is characterised by the relaxation time τ_d. However, in this work, as in work on α-Fe (Calder & Bacon 1993), these relaxations can continue past τ_d, and therefore sometimes account for the majority of the recombinations which take place, not just the 63% reduction in N_d used to denote τ_d. At the end of this athermal stage only the disordered cascade core remains visible, though some SIAs may have been formed by RCSs and cooperative displacements further away from the core, and these also remain.

Beyond this time thermal processes dominate and displaced atoms recombine by diffusive mechanisms fuelled by the formation energy released by previous relaxation events. The thermal spike continues until this energy is lost by conduction into the surrounding lattice.

6.5.4 The Thermal Spike.

Although no direct quantification of this phase has been made, the length of the thermal spike can be approximately deduced from the core temperature plots in fig. 6.15. Defining the 'thermal relaxation time' τ_T in a similar manner to τ_d, the duration of the thermal spike can be estimated and is of the order of 3 - 5 ps and therefore τ_T is between five to ten times larger than τ_d for the same cascade. This is also in agreement with the work on α-Fe cited above.

The thermal spike persists beyond the final recombinations and, given that the

simulation method uses periodic boundary conditions, permanently raises the ambient block temperature. The change in temperature dependes on the energy deposited in the block by the PKA, such that

$$\Delta T = \frac{E_{pka}}{3k_B N} \tag{6.3}$$

where ΔT is the change in kinetic temperature per atom, k_B is Boltzmann's constant, and N is the total number of atoms in the block. This is half the energy available from the PKA, since there is approximate equipartition of the deposited energy between the PE and KE at the end of the cascade, as shown in section 6.4.3. This is because no conduction into a surrounding medium is accounted for. However, there is a small discrepancy between the temperature given by equation 6.3 and the actual block temperature due to energy losses as a result of the approximations made by the predictor-corrector equations. These approximations are caused by the time-step interval not being infinitesimally small, and equate to a loss of ~2 - 9 K per ps during the thermal spike in these simulations.(The magnitude of this loss depends on time-step size, block size and atomic mass - the larger the time-step or block, the greater the number of approximations made, and the lighter the mass, the more significant the approximations are, and hence the greater the energy loss).

- § -

Table 6.1: Details of cascades simulated for the Ti and Zr models, with PKA energy, number of simulations per direction and block size.

PKA Energy	Ti		Zr	
	Cascades per PKA Direction	Number of Atoms in Block	Cascades per PKA Direction	Number of Atoms in Block
300 eV	2	12480	2	12480
500 eV	2	21840	2	12480
1 keV	2	21840	2	12480
2 keV	2	46086	1	104832†
5 keV	1	104832	1	104832

† Initial simulations at 2 keV in a block of similar size to those in Ti produced several cascades which self-interacted across the box boundaries, and therefore block size had to be increased.

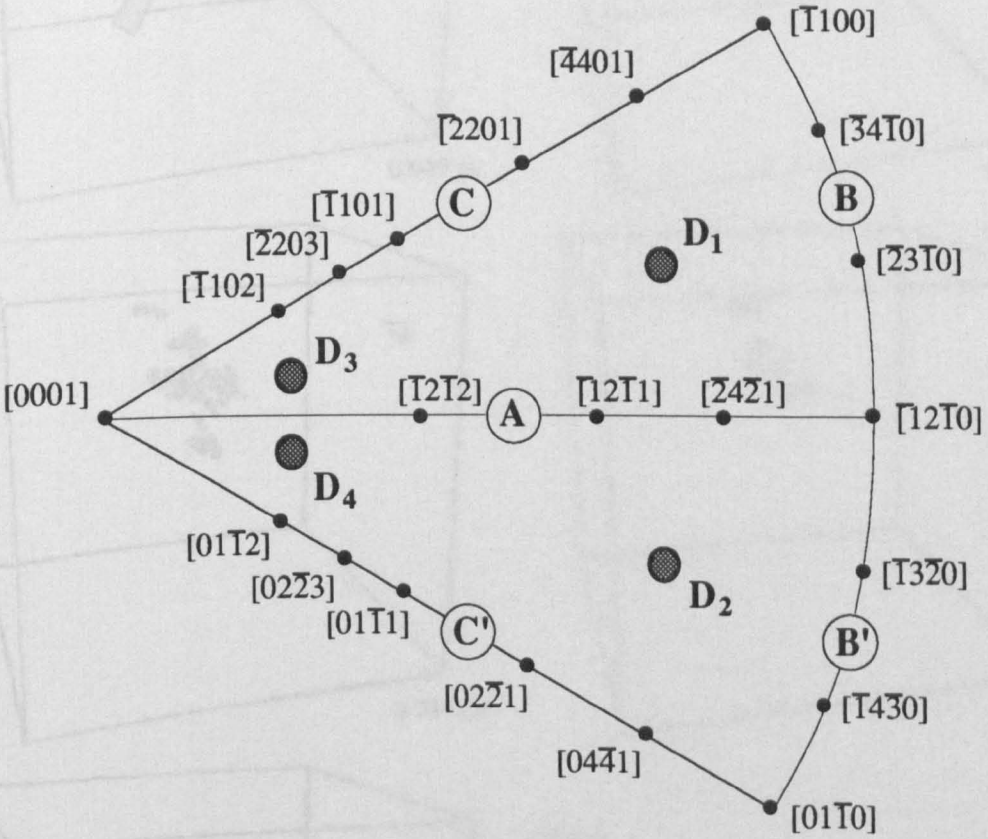

Fig. 6.1: Schematic of the HCP unit triangle, showing the four PKA directions used.

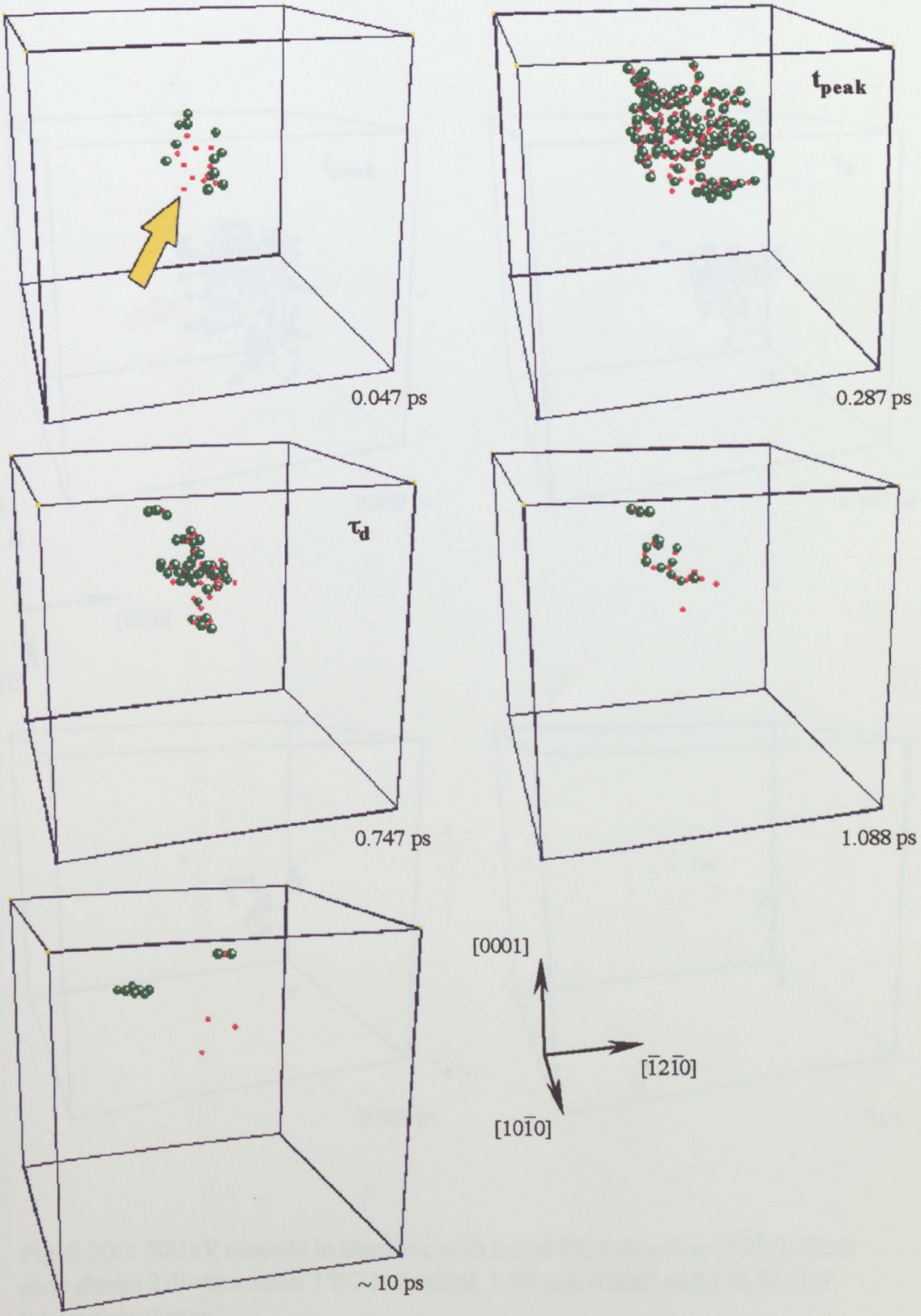

Fig. 6.2(a): 300 eV cascade in titanium, with initial PKA direction [$\bar{1}3\bar{2}9$]. Final state shows 3 single vacancies, 1 BC interstitial and 1 di-BC/BS interstitial cluster.

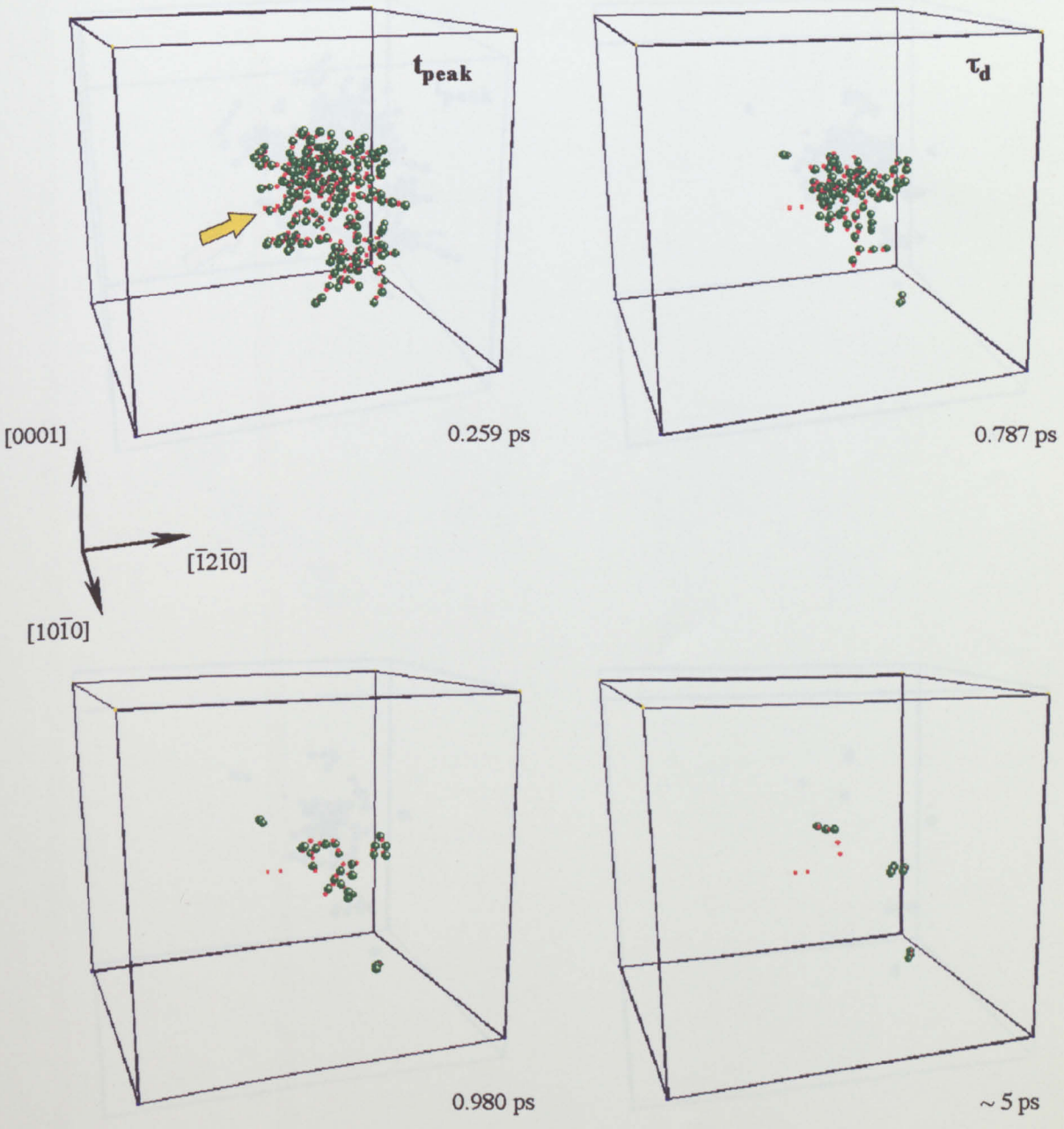

Fig. 6.2(b): 500 eV cascade in titanium, with initial PKA direction [$\bar{2}7\bar{5}2$]. Final state shows 2 di-vacancies, 1 BC interstitial, 1 BS interstitial, and 1 di-BC/BS interstitials cluster.

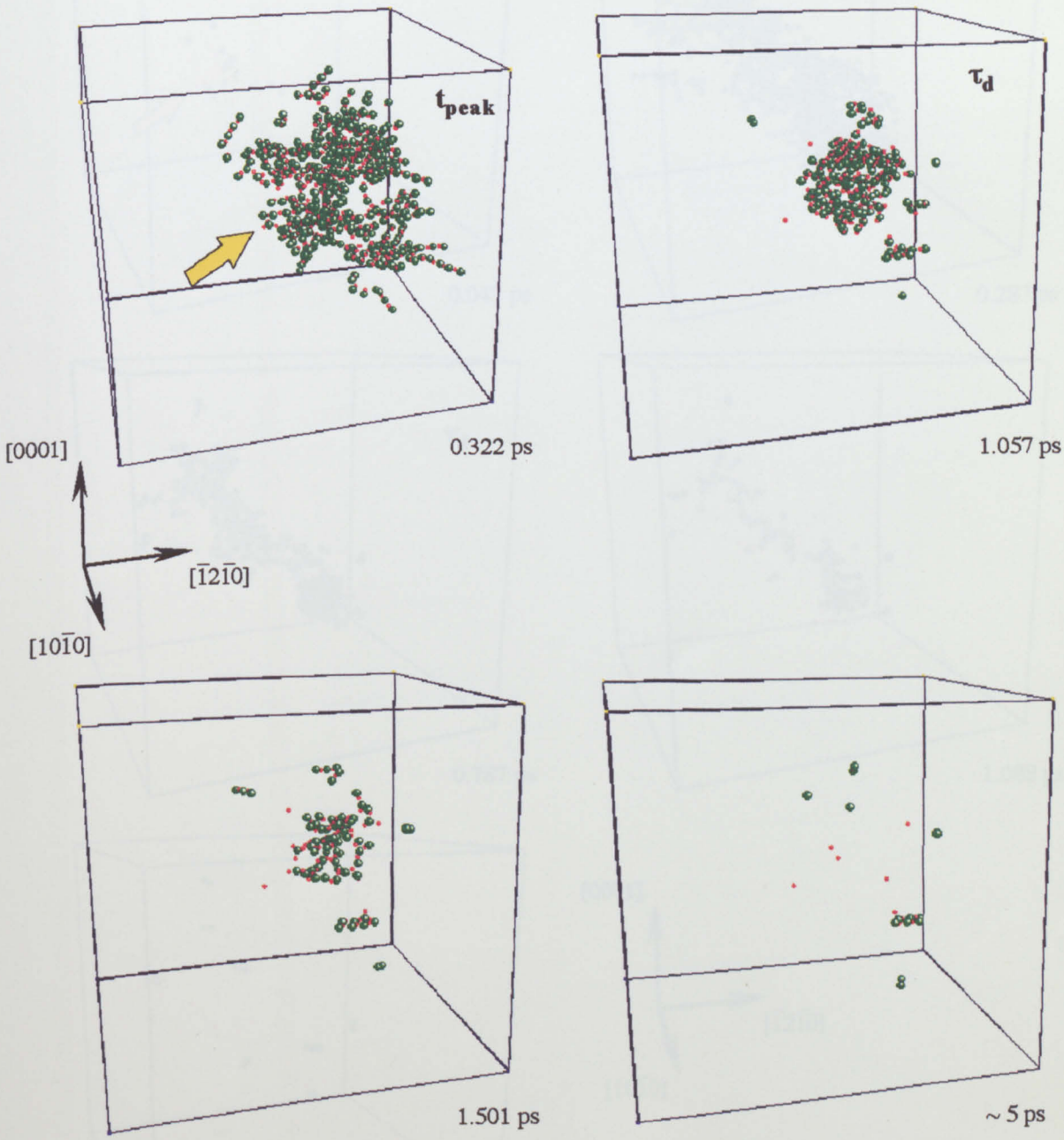

Fig. 6.2(c): 1 keV cascade in titanium, with initial PKA direction $[\bar{5}7\bar{2}2]$. Final state shows 3 single vacancies and 2 di-vacancies, 5 BS interstitials and 1 di-BC/BS interstitial cluster.

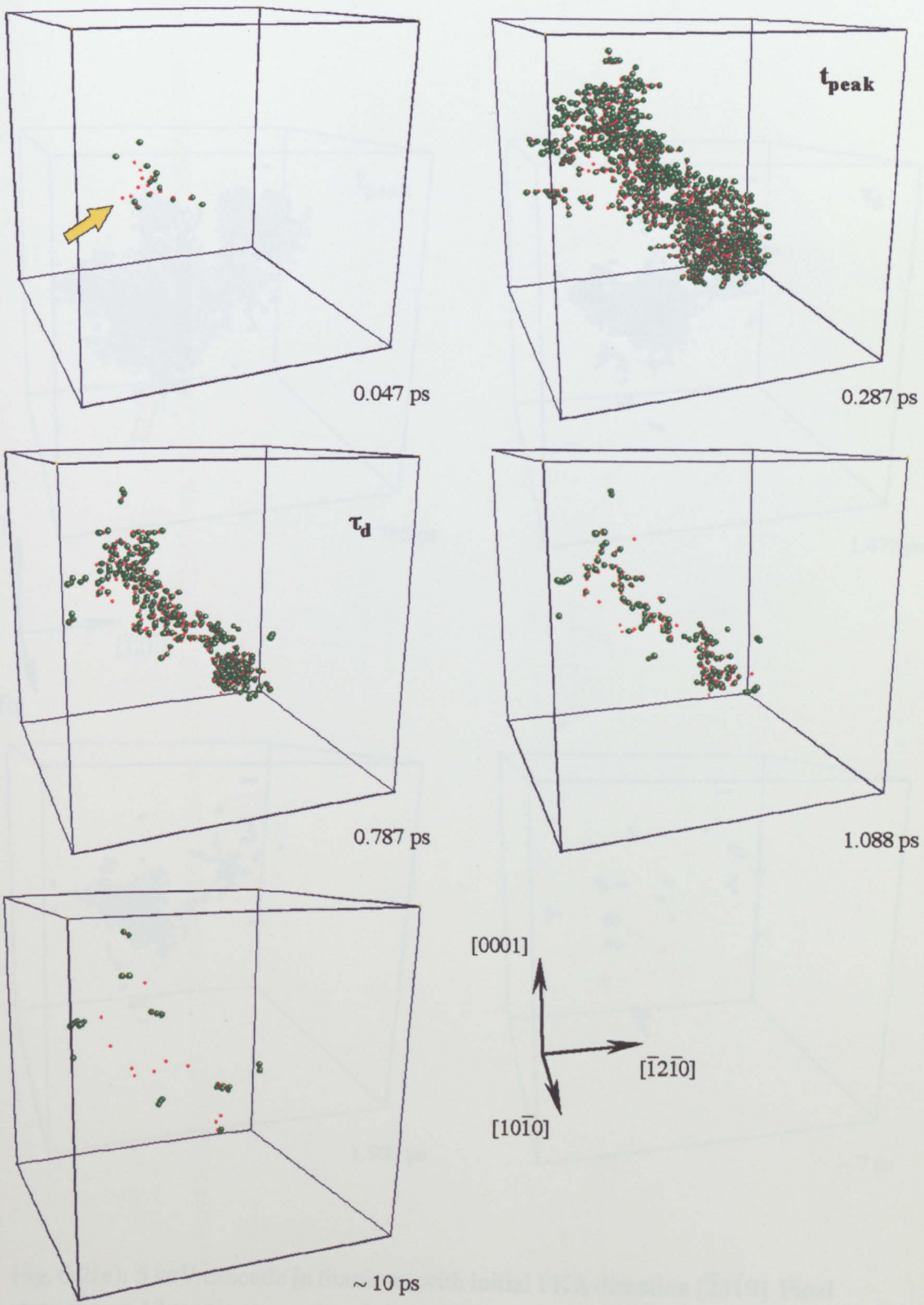

Fig. 6.2(d): 2 keV cascade in titanium, with initial PKA direction [$\bar{5}\bar{7}\bar{2}2$]. Final state shows 9 single vacancies and 1 di-vacancy, 2 BC, 4 BS and 1 C single interstitial, and 2 di-BC/BS interstitial clusters.

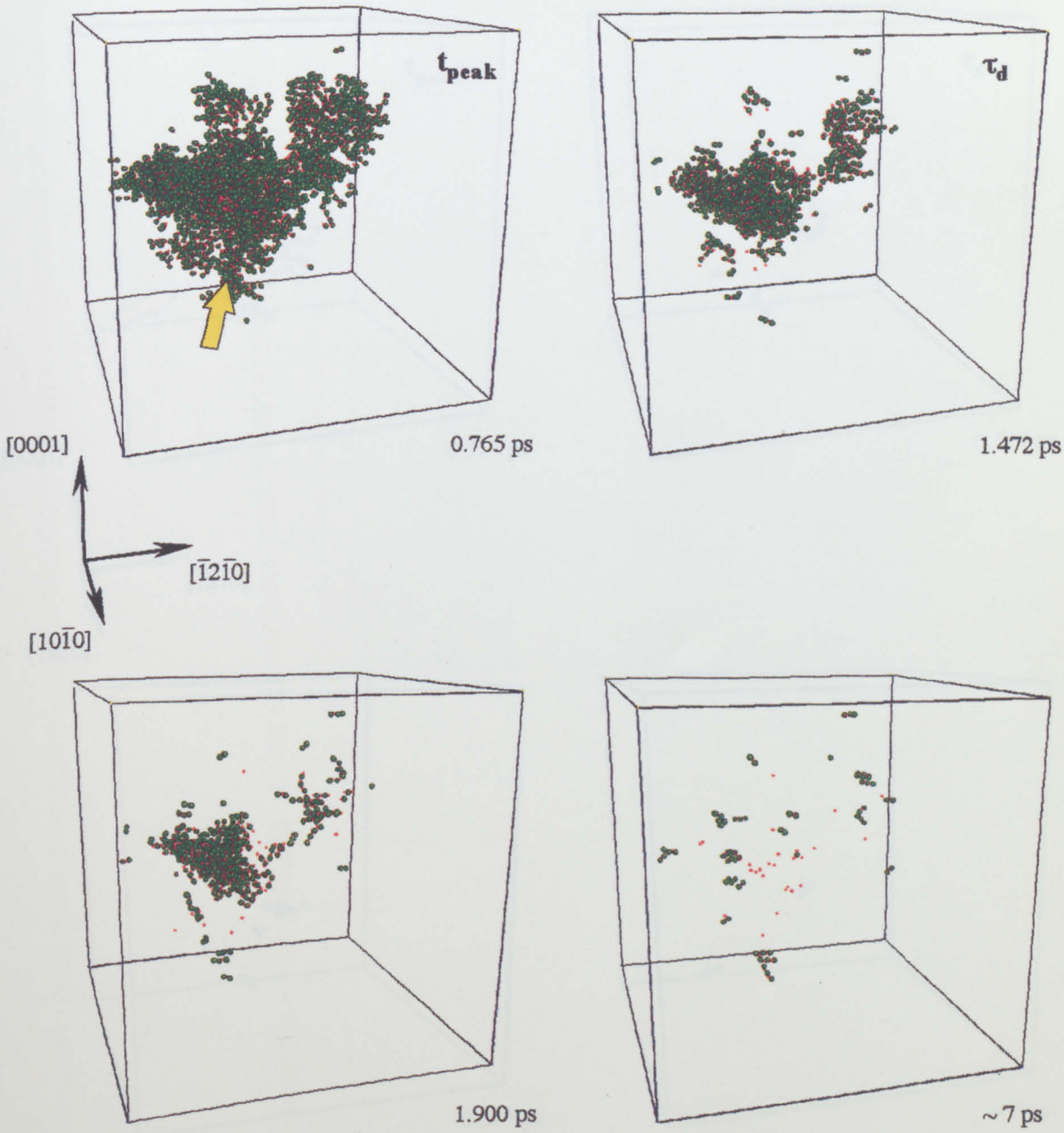

Fig. 6.2(e): 5 keV cascade in titanium, with initial PKA direction [$\bar{2}3\bar{1}9$]. Final state shows 12 single vacancies, 4 di-vacancies, 3 tri-vacancies, 1 BT, 5 BS, 3 BC and 2 C single interstitials, 1 di-BC/BS, 3 di-C, 2 tri-BC/BS and 1 tetra-BC/BS interstitial cluster.

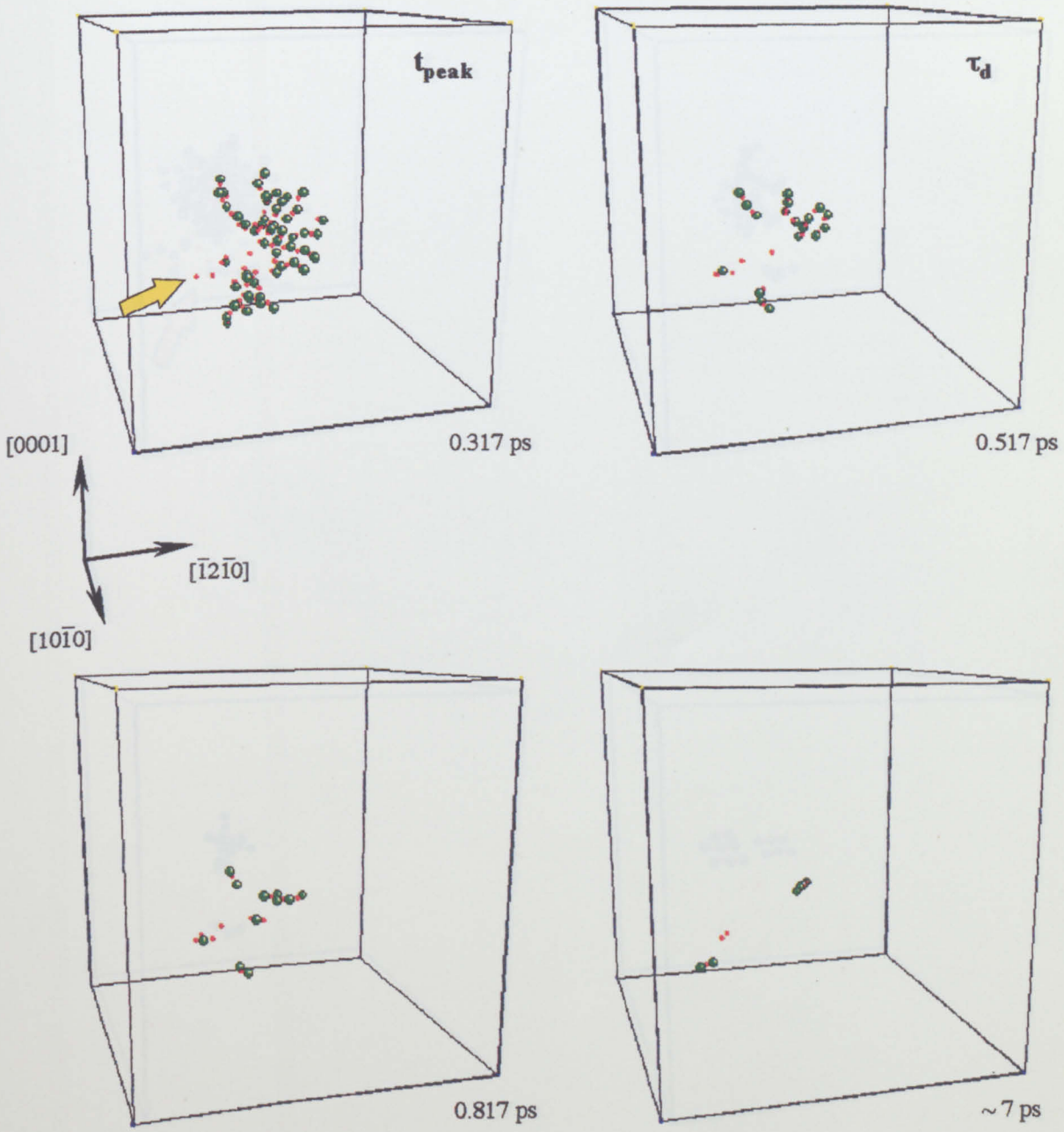

Fig. 6.3(a): 300 eV cascade in zirconium, with initial PKA direction [$\bar{2}7\bar{5}2$]. Final state shows 1 di-vacancy, and 1 BC and 1 BS interstitial.

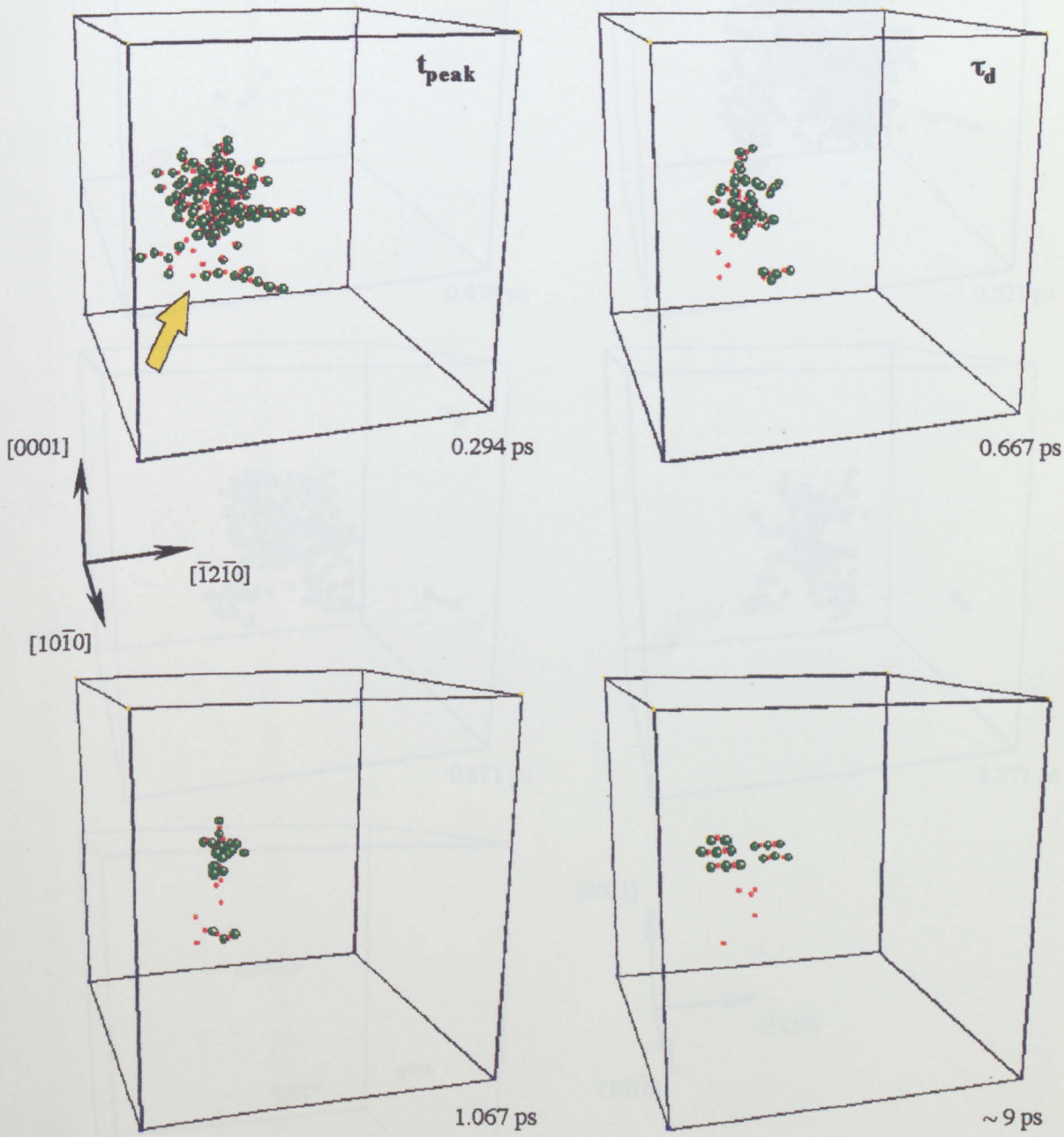

Fig. 6.3(b): 500 eV cascade in zirconium, with initial PKA direction [$\bar{1}3\bar{2}9$]. Final state shows 2 single vacancies and 1 tri-vacancy, 1 di-BC/BS and 1 tri-BC/BS interstitial cluster.

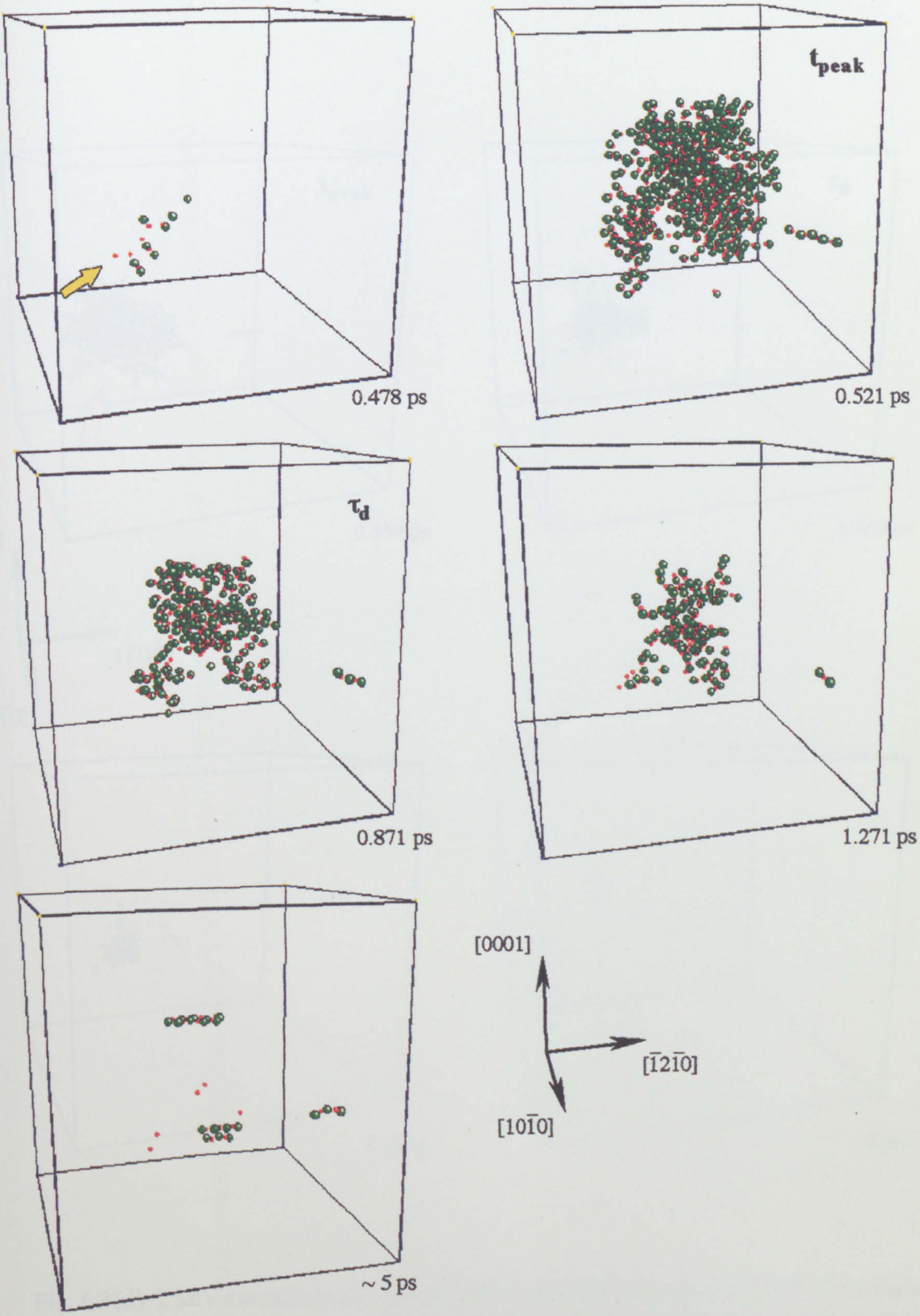

Fig. 6.3(c): 1 keV cascade in zirconium, with initial PKA direction [$\bar{5}\bar{7}22$]. Final state shows 3 single vacancies and 1 di-vacancy, 1 BC interstitial and 2 di-BC/BS interstitial clusters.

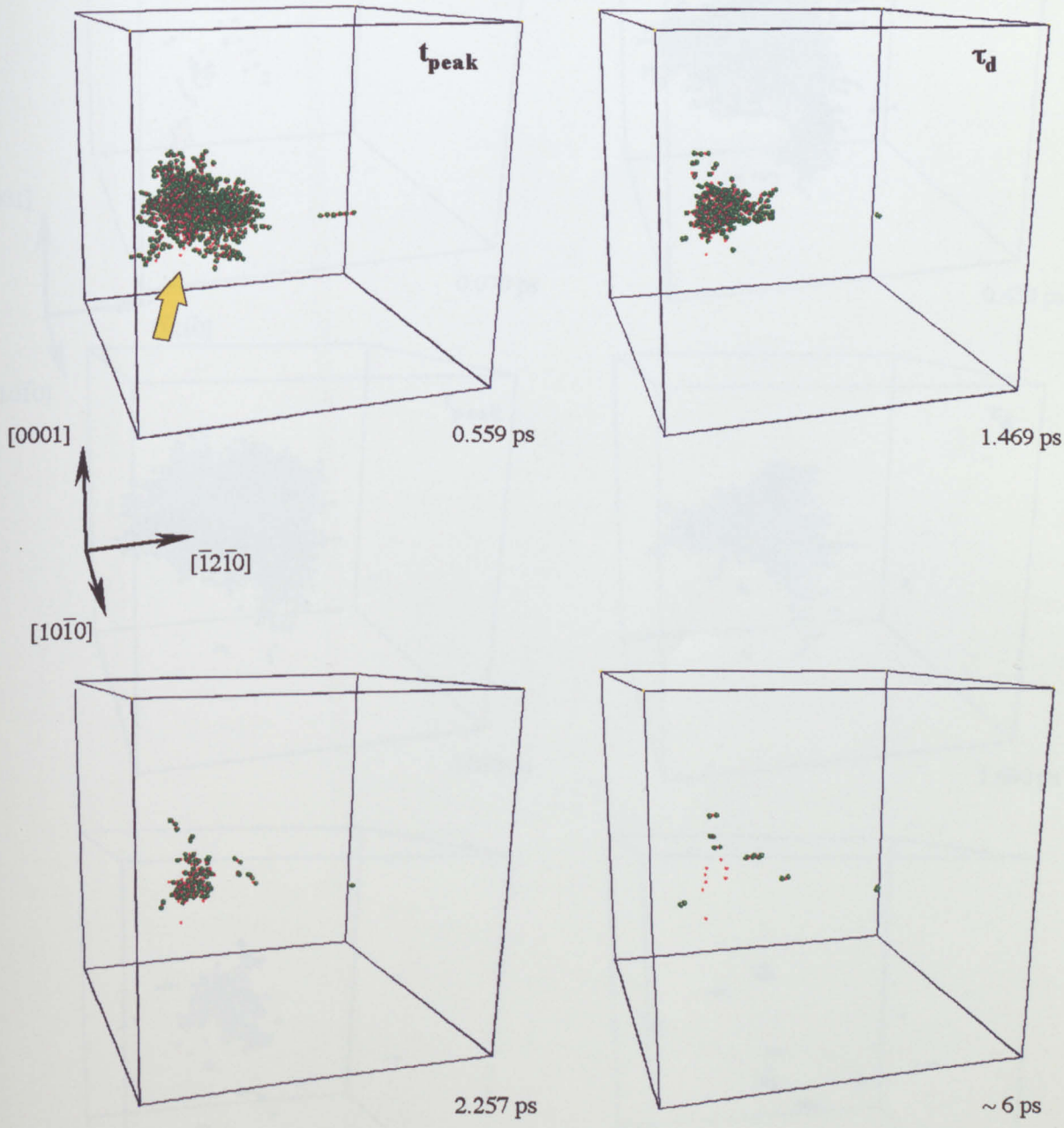

Fig. 6.3(d): 2 keV cascade in zirconium, with initial PKA direction [$\bar{2}3\bar{1}9$]. Final state shows 3 vacancies, 1 di-vacancy and 1 tri-vacancy, 6 BS interstitials and 1 di-BC/BS interstitial cluster.

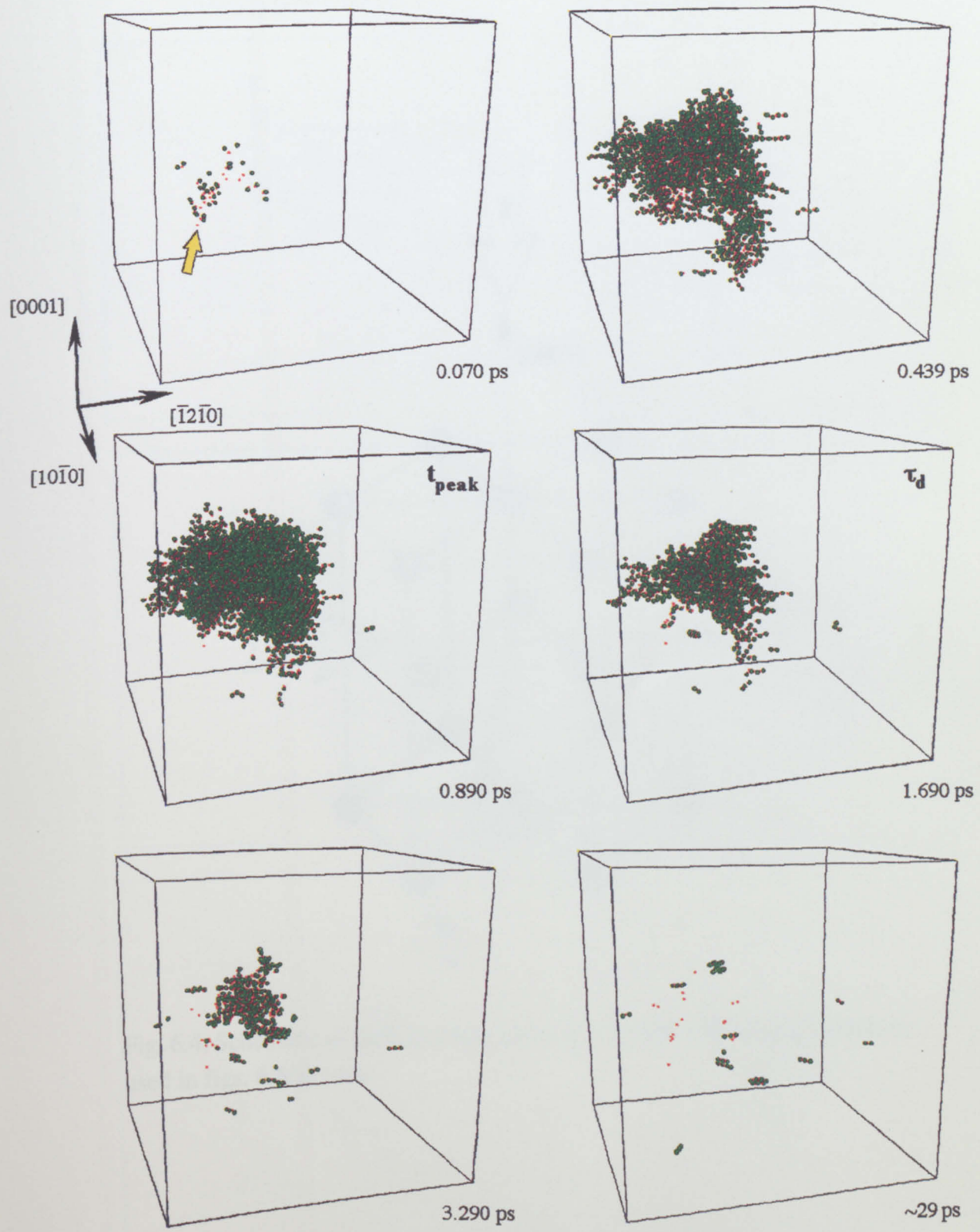

Fig. 6.3(e): 5 keV cascade in zirconium, with initial PKA direction [$\bar{2}3\bar{1}9$]. Final state shows 6 vacancies, 4 di-vacancies and 1 tetra-vacancy, 3 BS, 3 BC and 1 C single interstitial, 2 di-BC/BS, 1 tri-BC/BS and 1 tetra-BC/BS interstitial cluster.

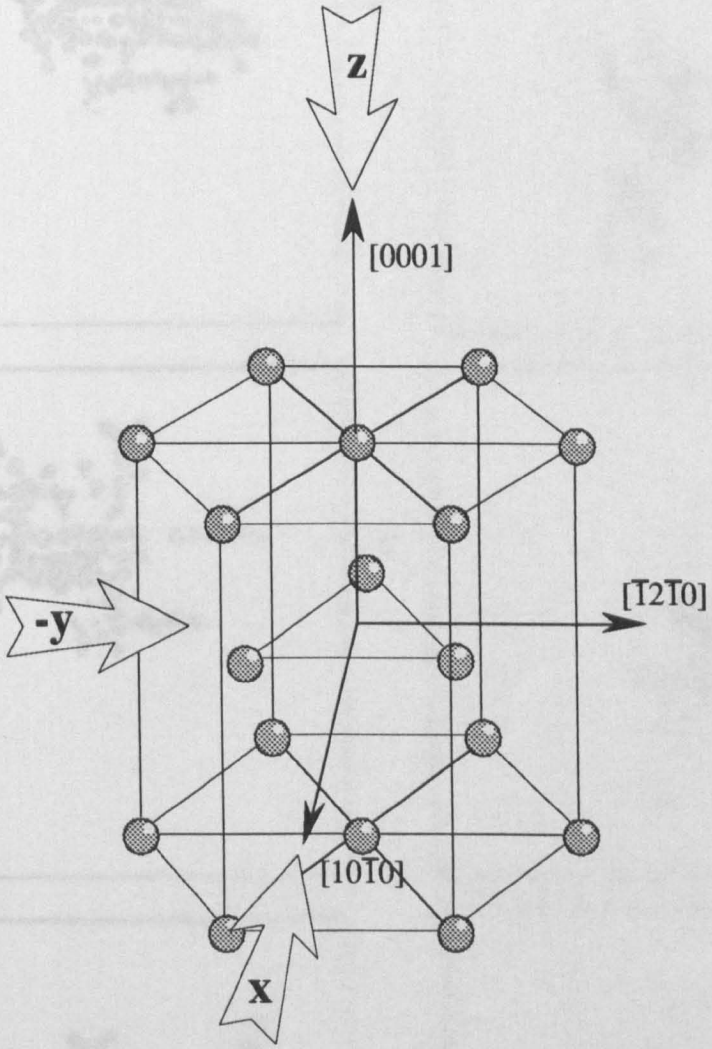

Fig. 6.4: Schematic of HCP structure showing x, -y and z viewing directions as used in figs. 6.5(a) - (e).

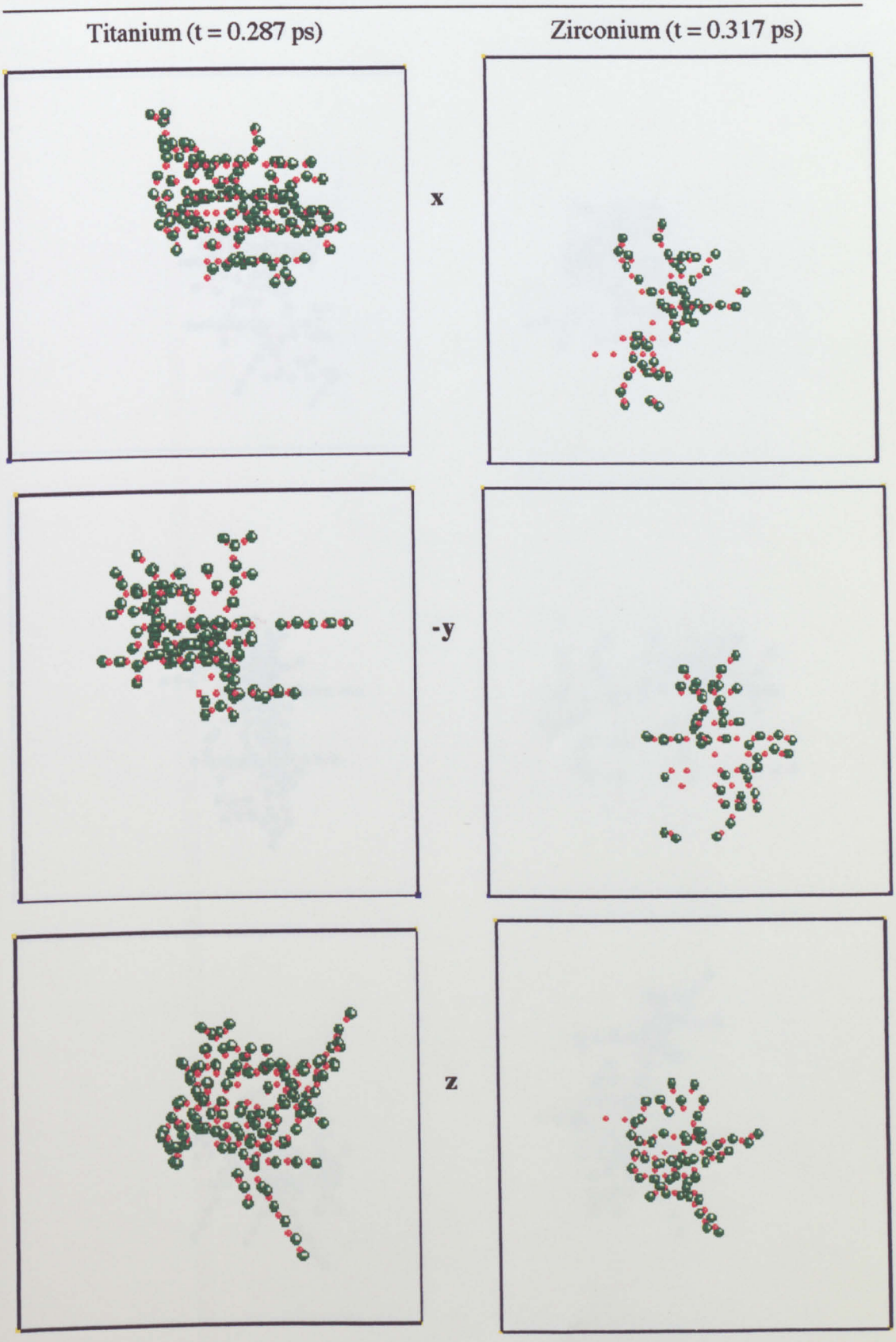

Fig. 6.5(a): 300 eV cascades in Ti and Zr at t_{peak}, showing projections along 3 orthogonal axes.

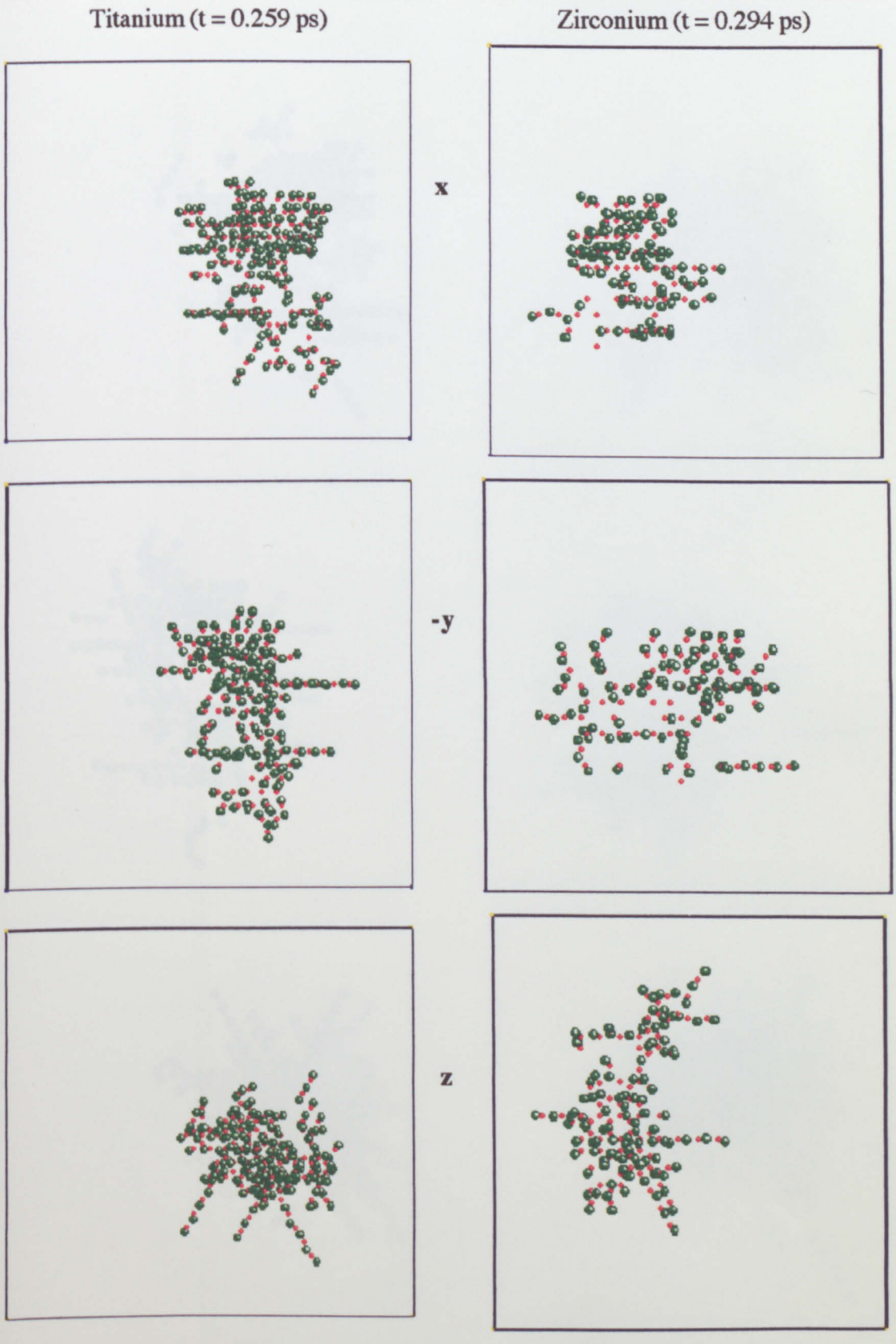

Fig. 6.5(b): 500 eV cascades in Ti and Zr at t_{peak}, showing projections along 3 orthogonal axes.

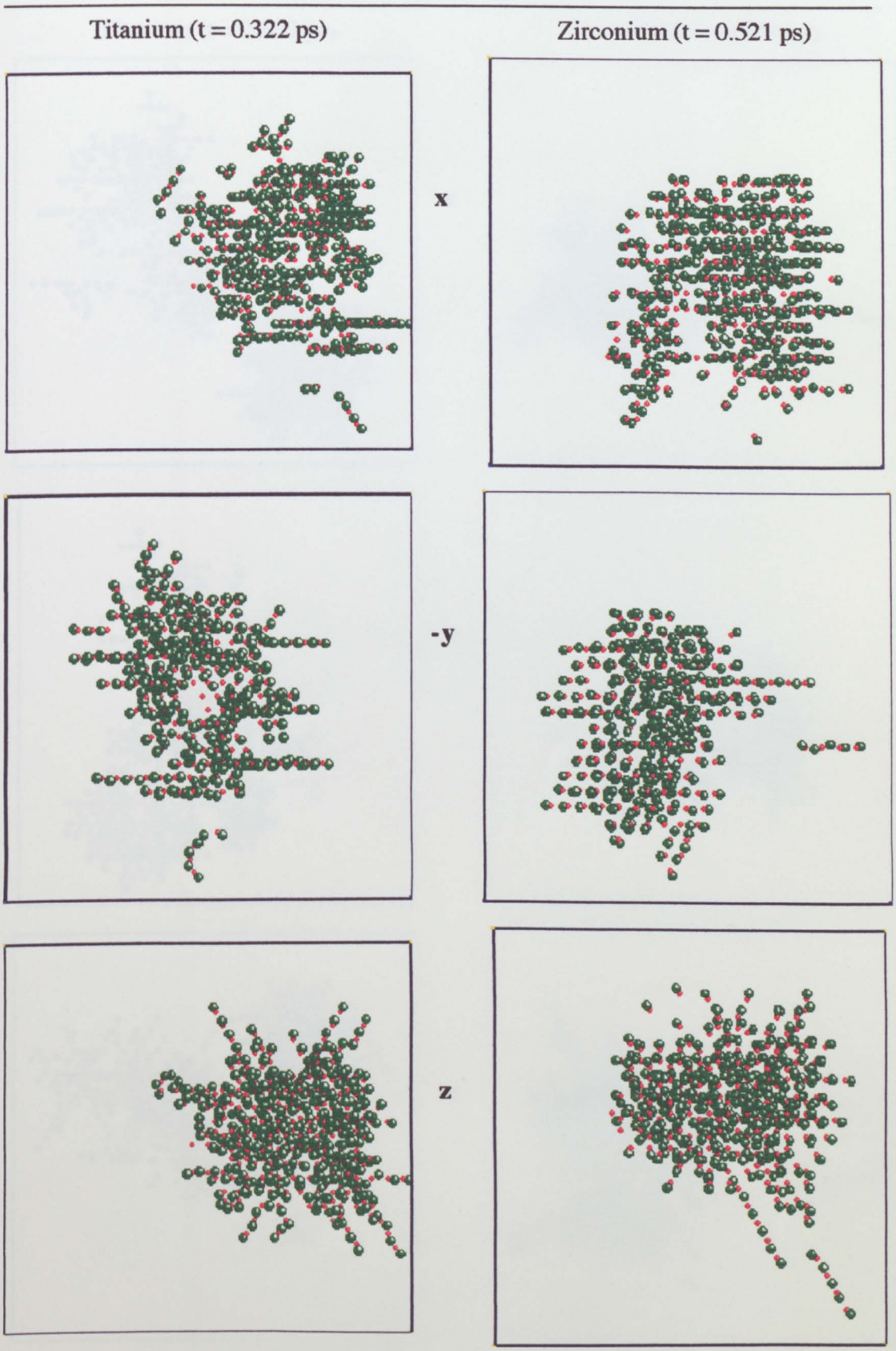

Fig. 6.5(c): 1 keV cascades in Ti and Zr at t_{peak}, showing projections along 3 orthogonal axes.

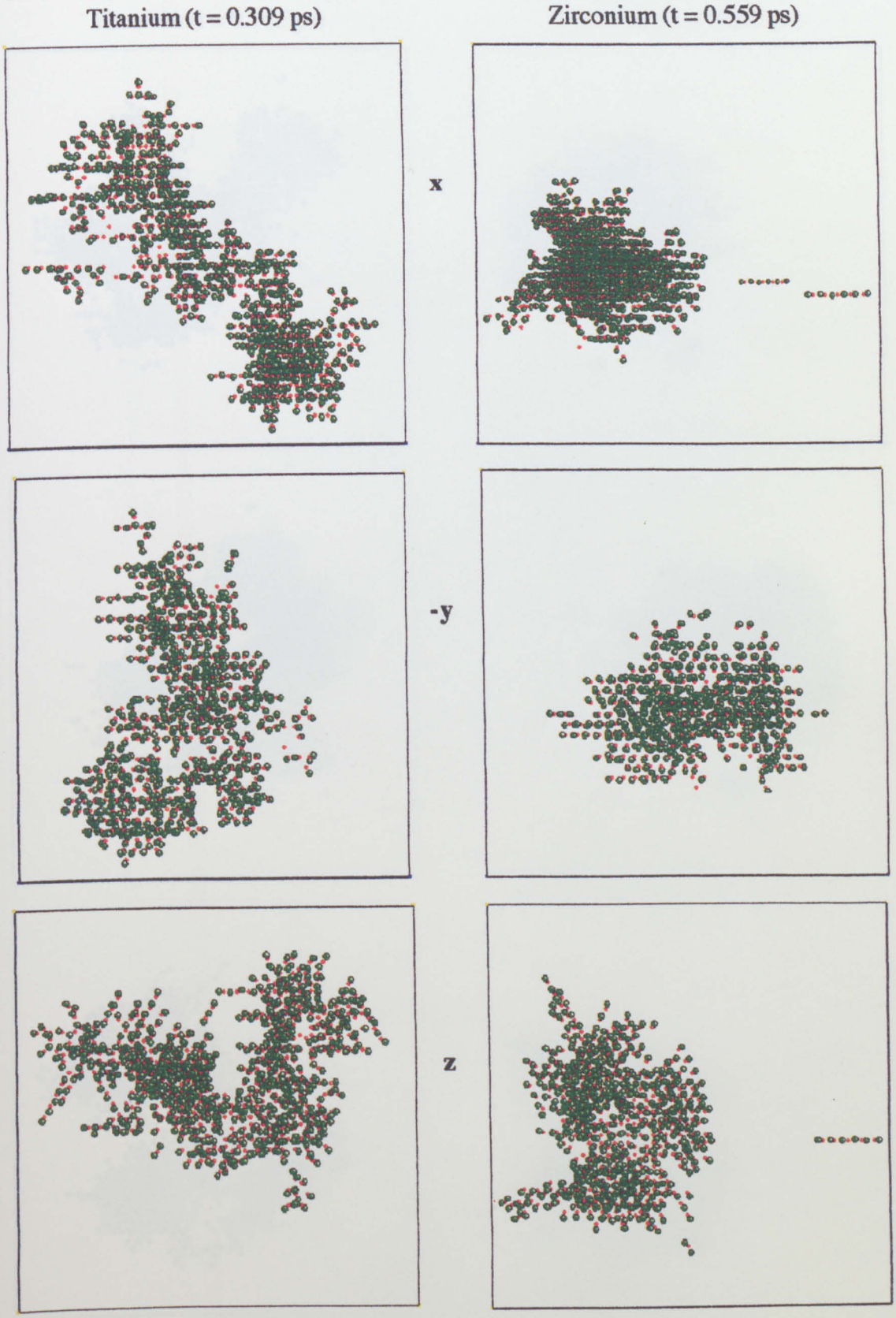

Fig. 6.5(d): 2 keV cascades in Ti and Zr at t_{peak}, showing projections along 3 orthogonal axes.

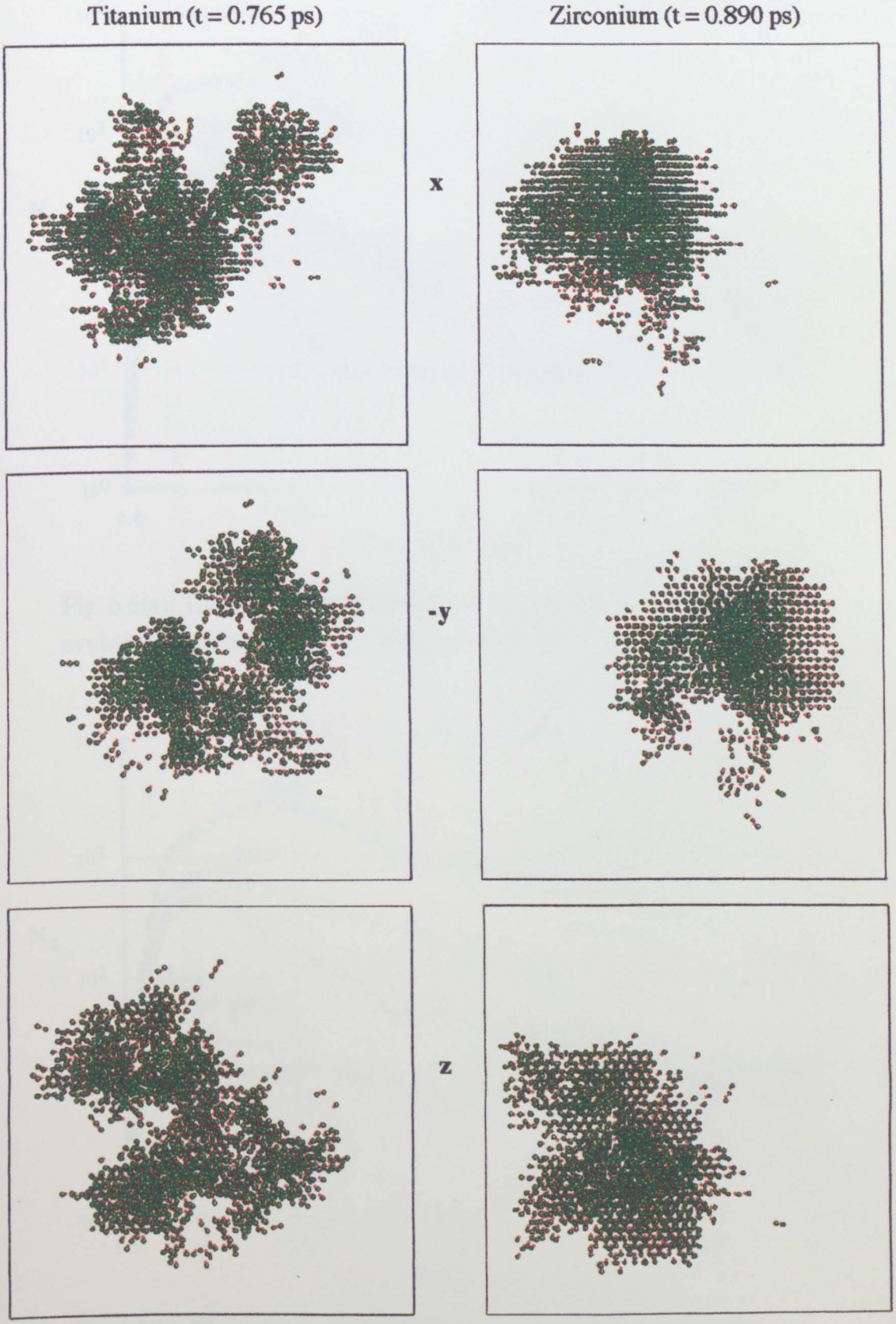

Fig. 6.5(e): 5 keV cascades in Ti and Zr at t_{peak}, showing projections along 3 orthogonal axes.

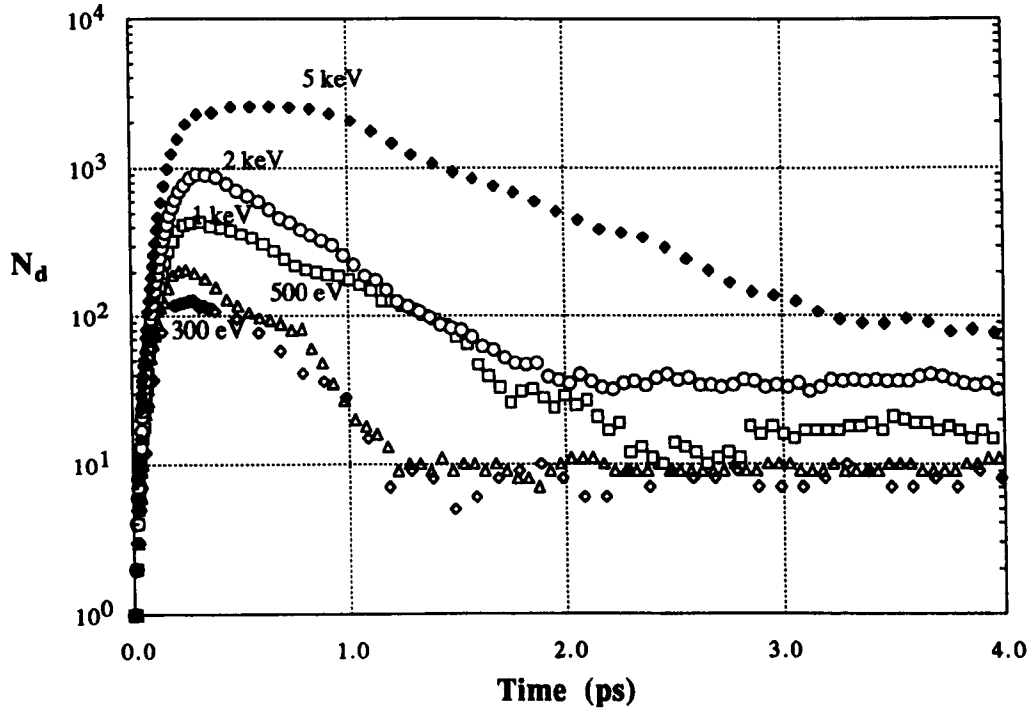

Fig. 6.6(a): The number of temporarily displaced atoms vs. cascade evolution time for one cascade at each value of PKA energy in titanium.

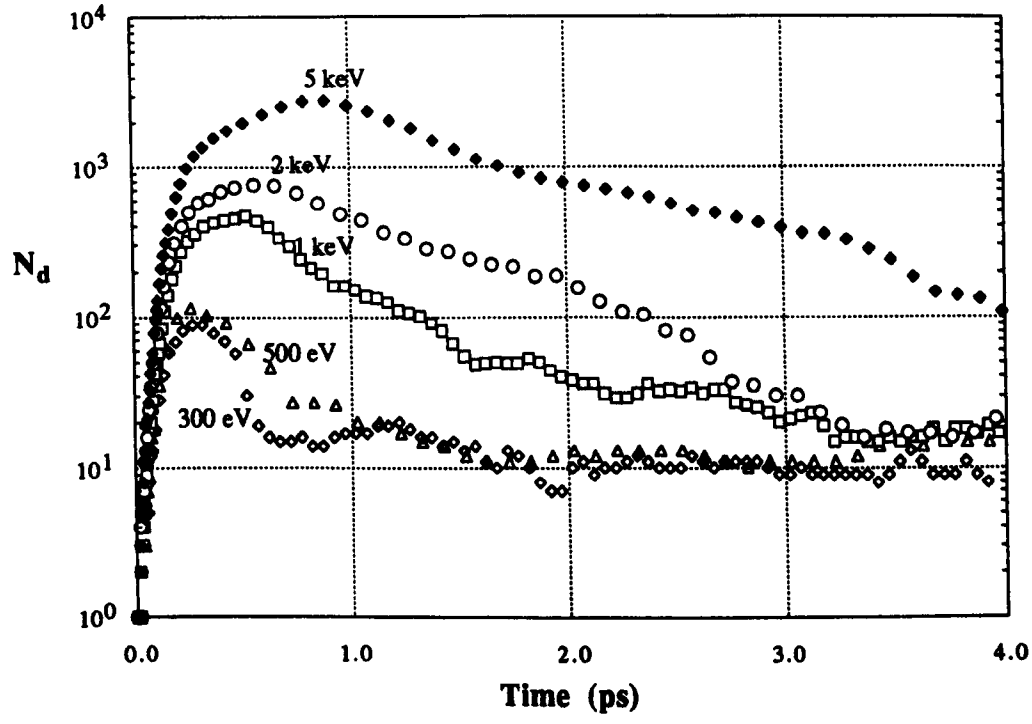

Fig. 6.6(b): The number of temporarily displaced atoms vs. cascade evolution time for one cascade at each value of PKA energy in zirconium.

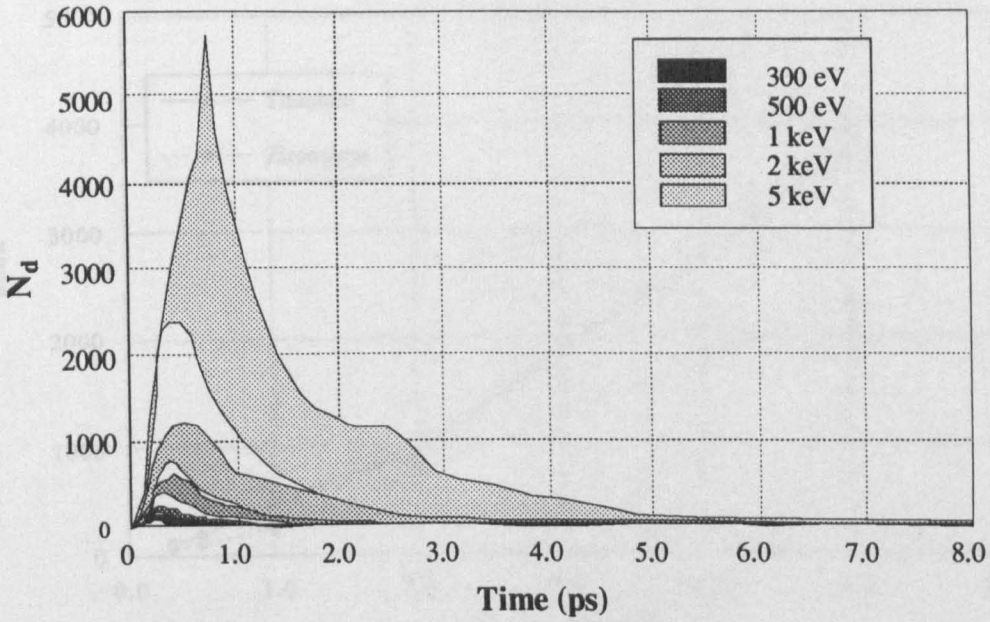

Fig. 6.7(a): The number of temporarily displaced atoms vs. cascade evolution time for all cascades in titanium.

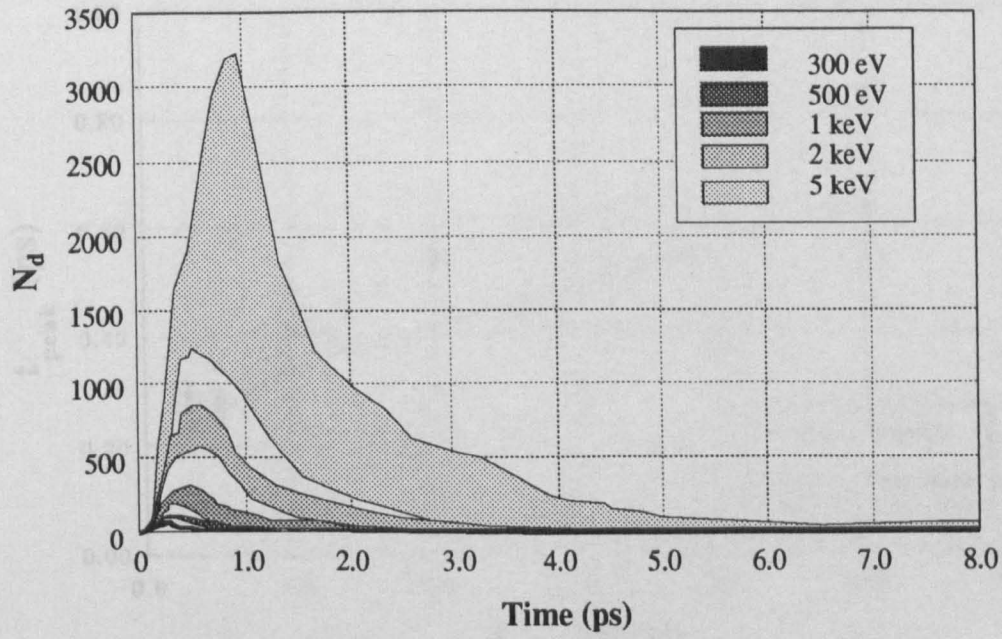

Fig. 6.7(b): The number of temporarily displaced atoms vs. cascade evolution time for all cascades in zirconium.

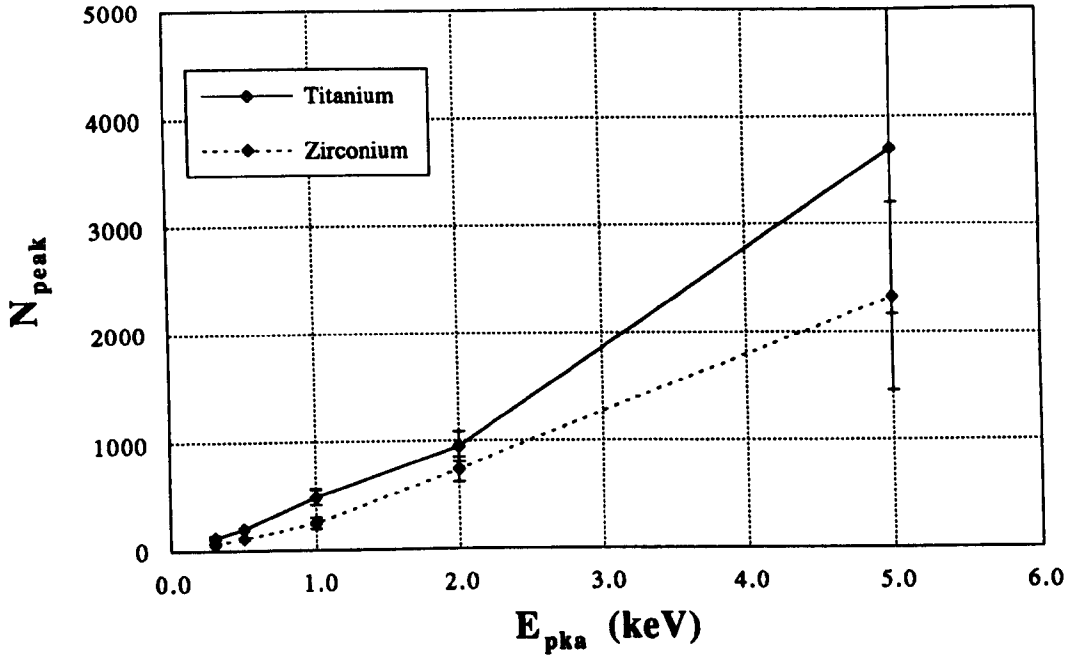

Fig. 6.8: Mean number of atoms temporarily displaced at the cascade peak vs. PKA energy for all cascades in both models. The error bars indicate the standard deviation from the mean.

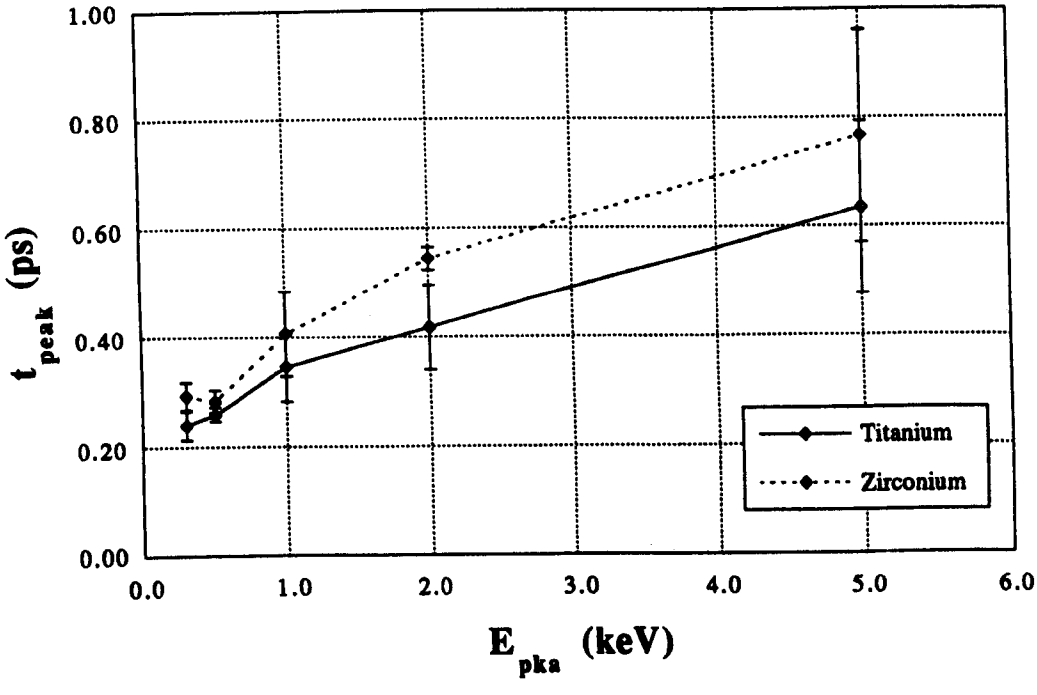

Fig. 6.9: Mean time to the cascade peak vs. PKA energy for all cascades in both models. The error bars indicate the standard deviation from the mean.

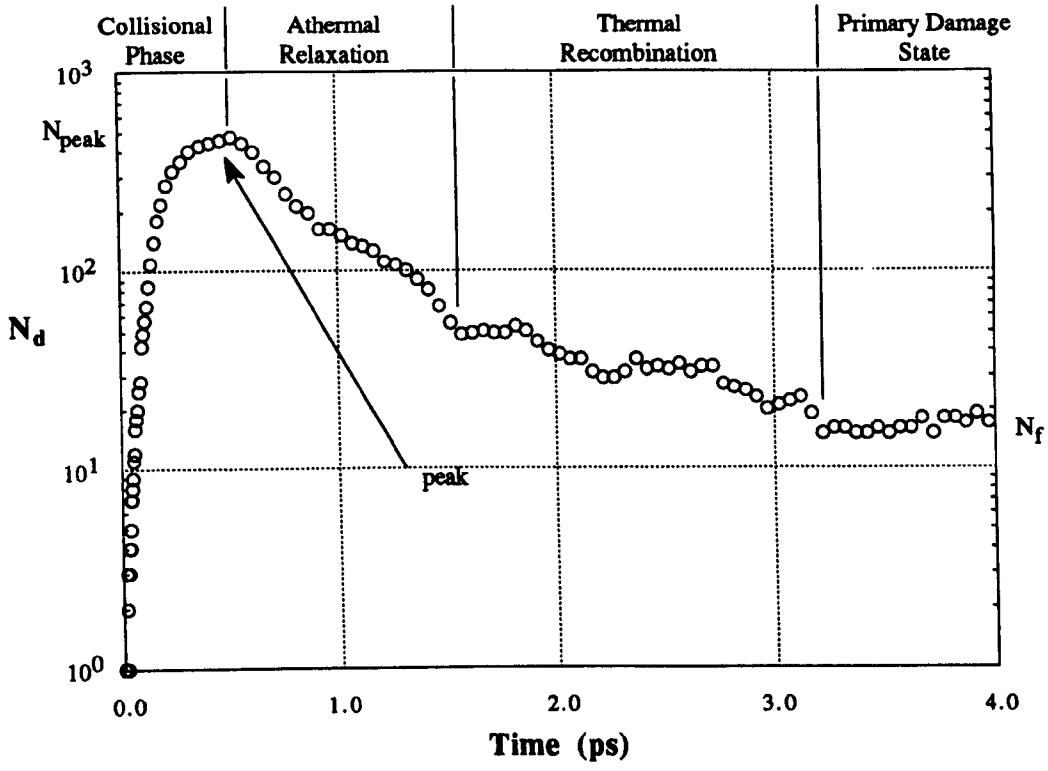

Fig. 6.10: Number of displaced atoms vs. evolution time for one 1 keV cascade in zirconium, showing the various cascade phases, including the exponential reduction in N_d just past the cascade peak.

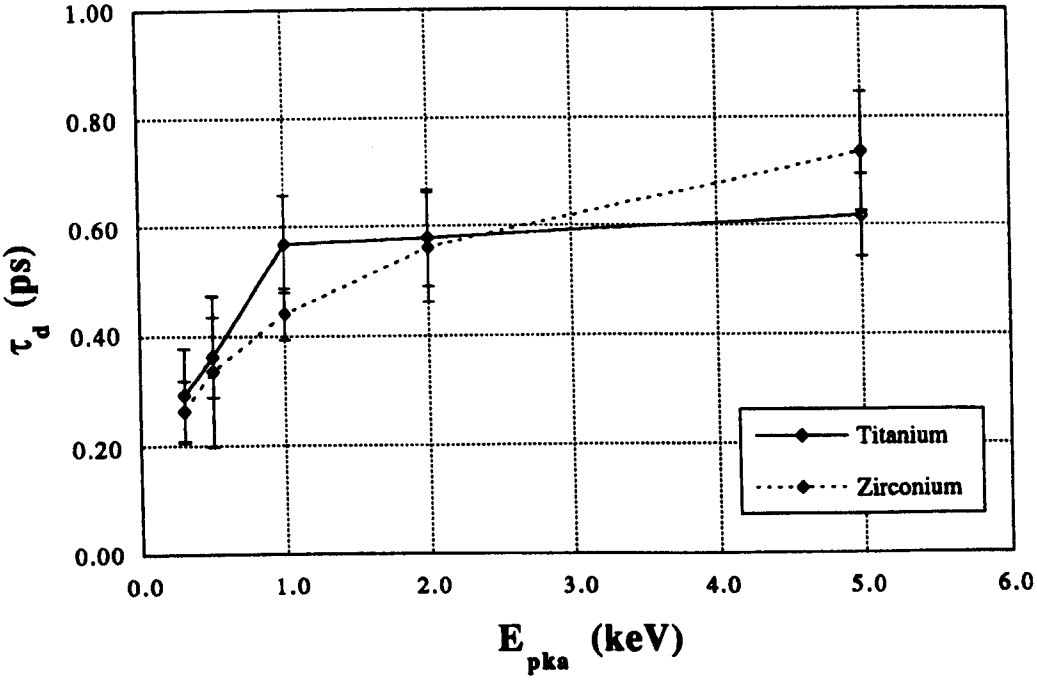

Fig. 6.11: Relaxation time vs. PKA energy for all cascades in both models. The error bars indicate the standard deviation from the mean.

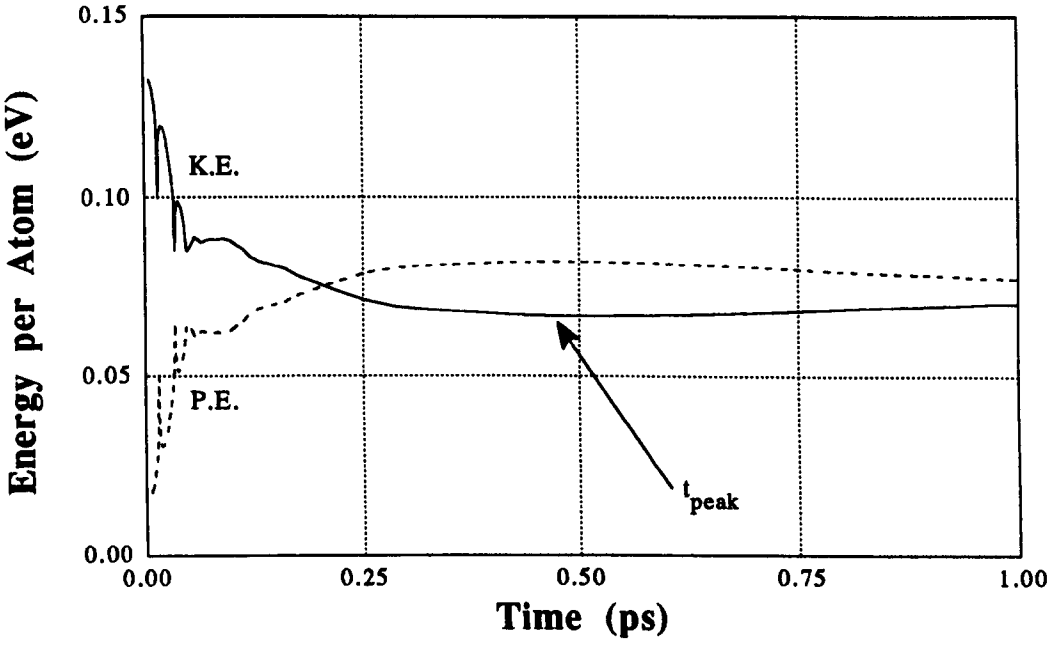

Fig. 6.12: Kinetic (K.E.) and potential energies (P.E) per atom vs. evolution time for a 1 keV cascade in zirconium.

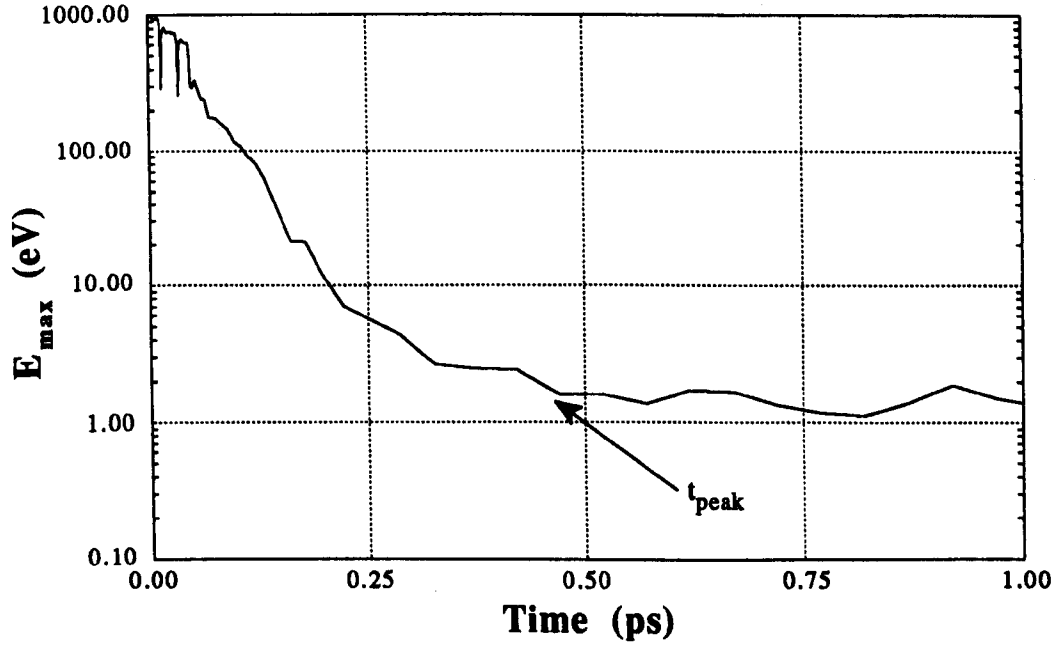

Fig. 6.13: Maximum kinetic energy E_{max} of any atom vs. evolution time in the above 1 keV zirconium cascade.

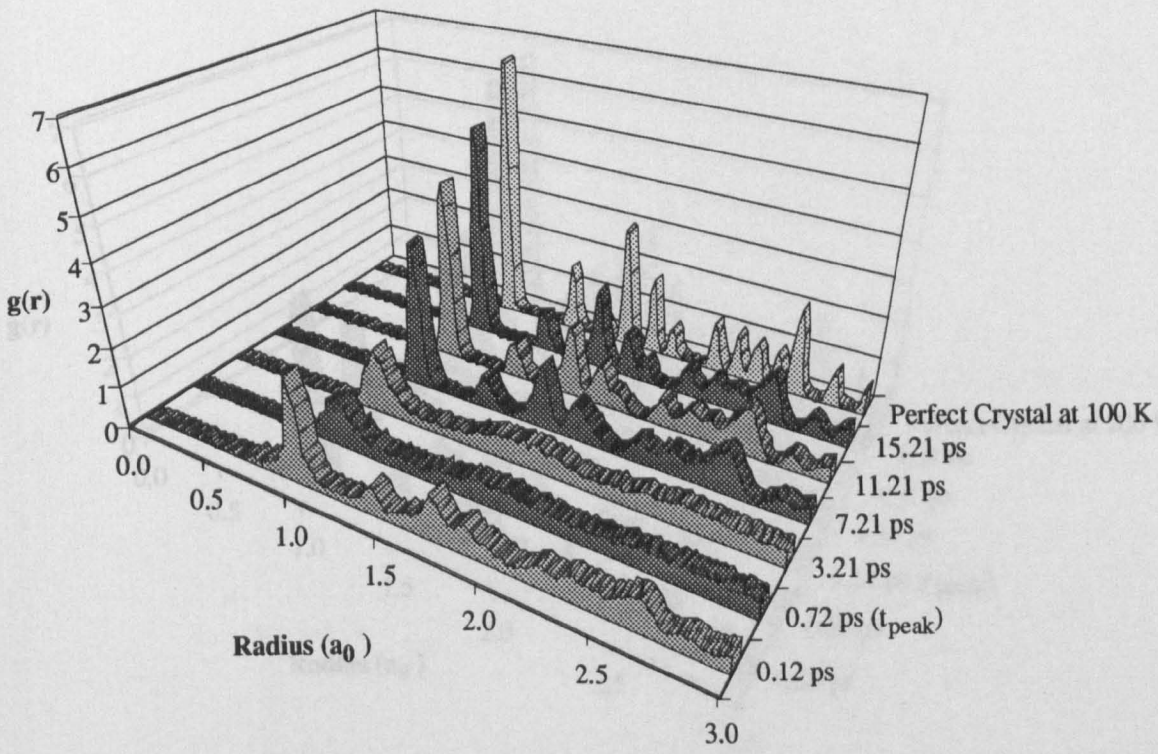

Fig. 6.14(a): The radial pair distribution function g(r) of the core of a 5 keV cascade in titanium at various times during its evolution. For reference purposes g(r) for a perfect crystal at 100 K is also shown.

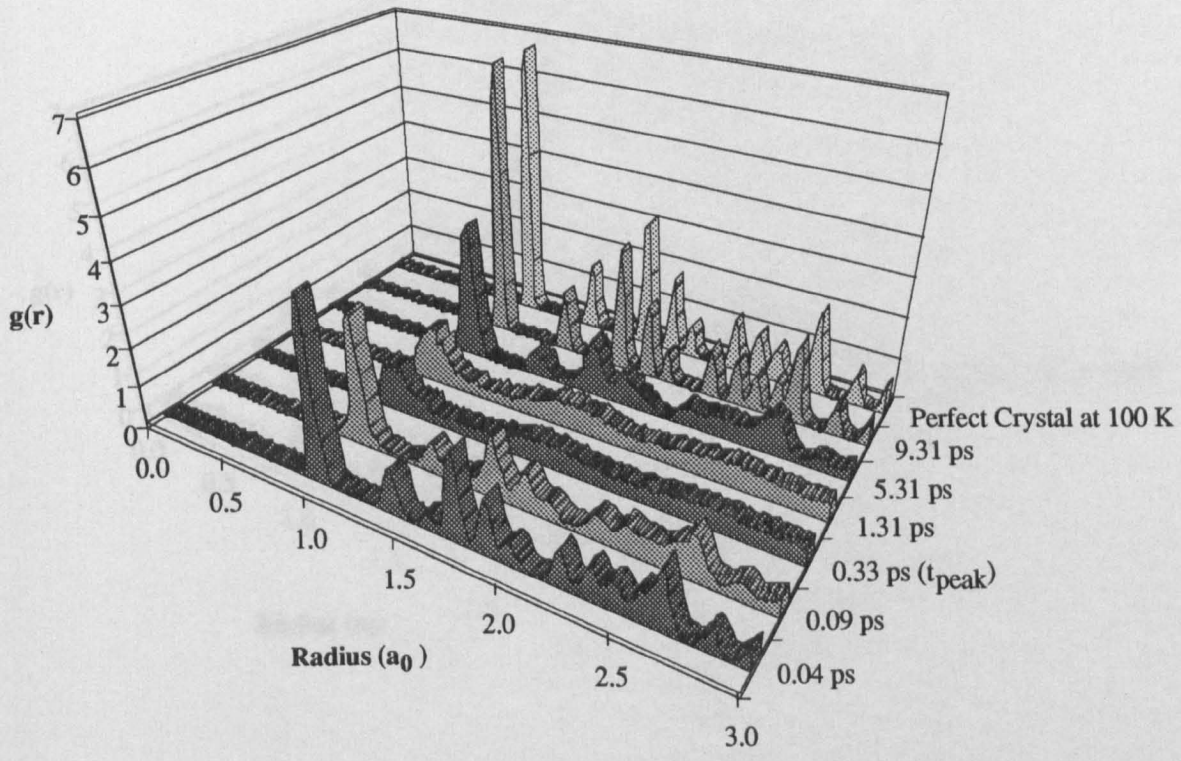

Fig. 6.14(b): The radial pair distribution function g(r) of the core of a 2 keV cascade in zirconium at various times during its evolution. For reference purposes g(r) for a perfect crystal at 100 K is also shown.

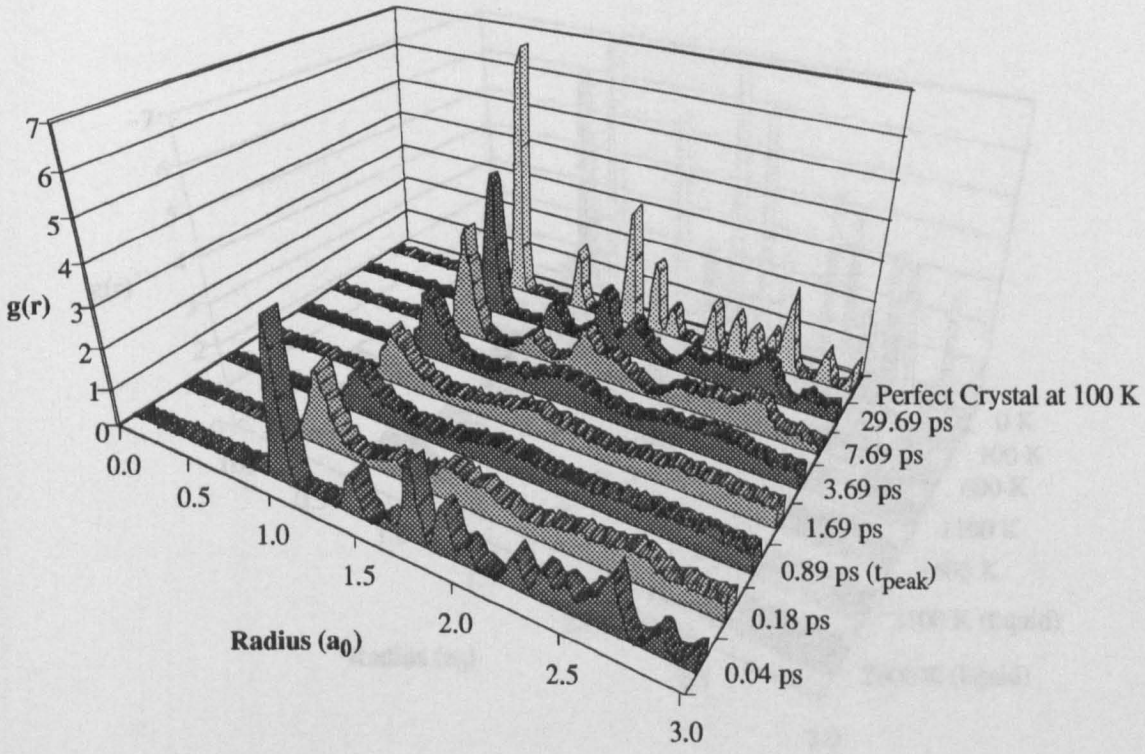

Fig. 6.14(c): The radial pair distribution function g(r) of the core of a 5 keV cascade in zirconium at various times during its evolution. For reference purposes g(r) for a perfect crystal at 100 K is also shown.

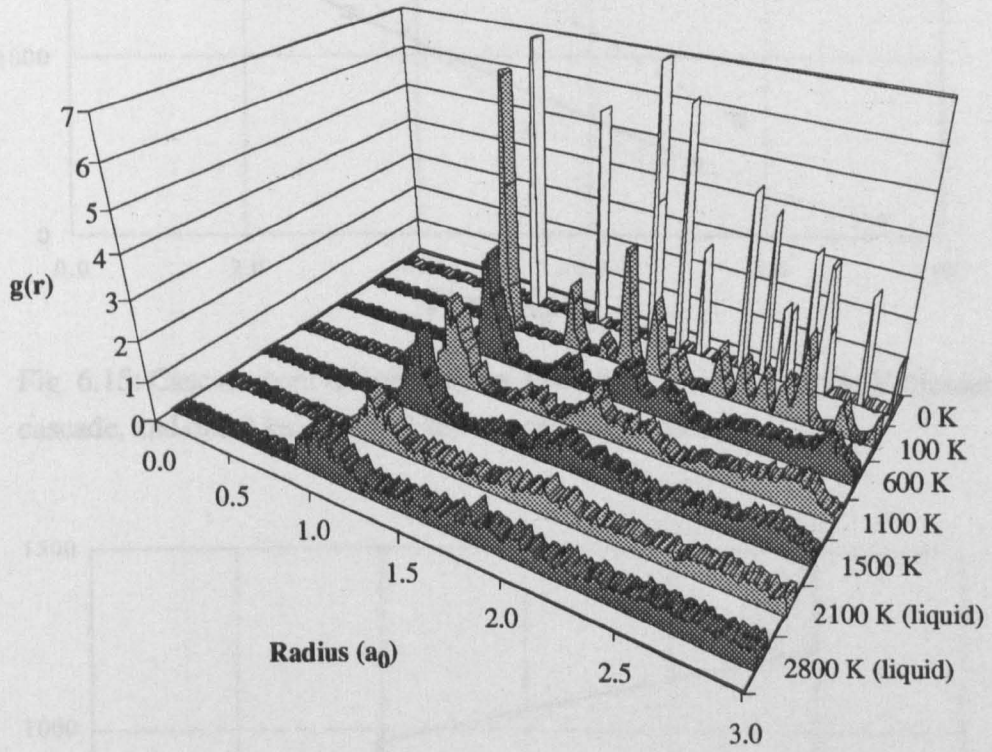

Fig. 6.14(d): The radial pair distribution function g(r) of a zirconium block at various temperatures, showing the gradual loss of crystalline order with increasing temperature. (The liquid state above T_m was verified by visual observation using AVS™.)

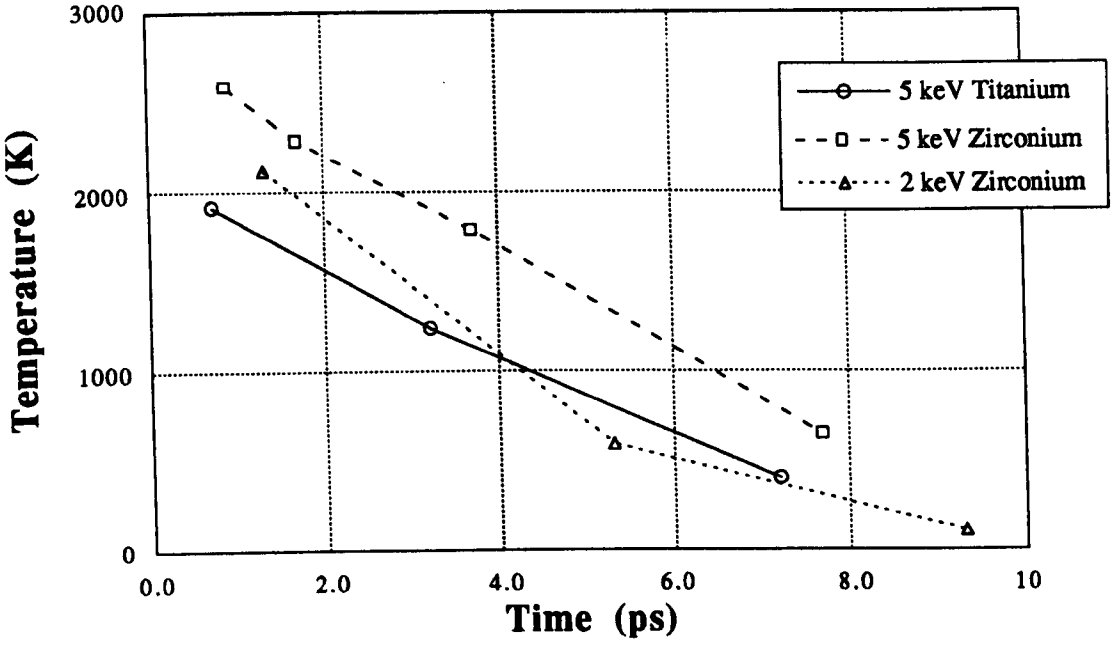

Fig. 6.15: Cascade core temperature vs. evolution time for one 5 keV titanium cascade, and one 2 keV and a 5 keV cascade in zirconium.

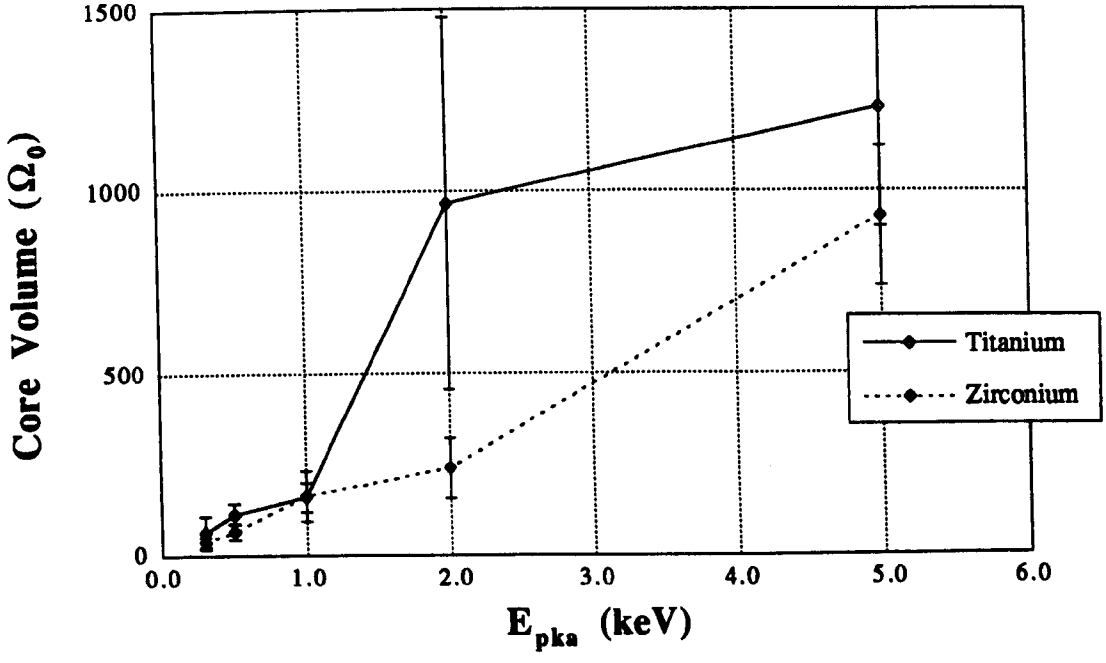

Fig. 6.16: Mean core volume vs. PKA energy for all cascades in both models. The error bars indicate the standard deviation from the mean.

VII

The Final Defect State

7.1 Introduction.

The 'final defect' or 'primary damage' state is of great importance in an engineering context, since it is from this damaged condition that the microstructure of the component, be it reactor core support, fuel cladding or semiconductor device, will subsequently evolve. It is now that the effects of the HCP structure will again come into play since the structure disordering effects of the cascade have passed. Having already established the existence of a strong preference for basal-plane SIA production and migration in the solid state during quasi-static simulations in chapter 4, comparison with the MD results will show whether these still apply for cascade-produced defects. The final numbers of SIAs and vacancies and their spatial configurations, including any clusters formed, have implications for the subsequent migration of defects, and hence the magnitude of any production biasing that might exist.

- § -

7.2 Results.

All the data presented in this chapter has been derived from the TV files. As mentioned in chapter 3, the method of flagging displaced atoms in MOLDY means that the final number of displaced atoms, N_f, is not equal to the actual number of true vacancies and SIAs that exist, N_v, since one SIA may be marked by two displaced atoms and a vacant site for the BS interstitial, or even three atoms and two vacancies for the BC case. Therefore the only accurate way to assess the final number of Frenkel pairs is to visually count the number of vacant sites with no associated displaced atom, giving N_v. The configurations and cluster sizes of the defects were also assessed visually using MacAtoms™ and Atom-TV™.

7.2.1 Defect Production.

As mentioned in section 6.3, the majority of the SIAs produced by a cascade are distributed around the periphery of the disordered zones, with a small proportion produced by RCSs, indicating that these are not as significant as thought in earlier theories. This is due, as pointed out in chapter 5, to the thermal de-focusing of RCSs, which increases the energy per displacement for the chain to continue, and therefore reduces their efficiency with temperature. Since cascade core temperature increases with PKA energy, RCSs become less and less probable, even though focused-collision chains increase in number with E_{pka}. Other SIAs, both single and clusters, are the result of 'lobes' of disorder protruding from the cascade core, similar to the ballistic ejection mechanism of English et al. (1991), which leave several SIAs in close proximity to one another, and separated from the core vacancies. These then cluster rapidly during the relaxation phase. Most defects are in, or very close to their final positions at around $t_{peak} + \tau_d$, the end of the athermal portion of the relaxation phase. The vacancies are scattered around the centres of the disordered zones and, although clustering has occurred to some small extent, nothing approaching cascade collapse has occurred since no very large vacancy clusters were seen , except in one case which will be discussed later.

The final number of vacancies, N_v, is shown for both models in fig. 7.1 and, as in the case of N_{peak}, is not linearly dependent on E_{pka}. Very recent analysis of MD results for a variety of metals (Bacon et al. 1994) have found that this relationship is in fact a power law, such that

$$N_v = A\left(E_{pka}\right)^m \qquad (7.1)$$

where A and m are constants which appear to be weakly dependent on mass. Plotting N_v vs. E_{pka} on a log-log scale, shown in fig 7.2, reveals this to be the case above 1 keV since all the N_v values for one metal give an extremely good fit to a straight line. (The values of A and m are for E_{pka} in units of keV.) This power-law fit is excellent for both models above 1 keV, and still extremely good even when all PKA energies are included. The dependence above 1 keV ties in again with the transitions seen in the parameters involved in cascade evolution as detailed in the previous chapter, and therefore with the onset of true cascade conditions.

Applying the same analysis to the N_{peak} results from section 6.4.1 demonstrates that this parameter too has such a dependence as shown in fig. 7.3, though the actual value of N_{peak} depends to some extent on r_{srch}. What is of note is that for N_v $m \approx 0.8$ above 1 keV for both models, i.e. $m < 1$, and hence the final number of defects shows a decreasing dependence on PKA energy as E_{pka} increases, whilst for N_{peak} m is between 1.2 and 1.3, i.e. $m > 1$, which shows an increasing dependence on E_{pka} as PKA energy increases. Thus the ratio of N_{peak}:N_v becomes larger with increasing PKA energy, and is mirrored in the increasing ratio of the NRT prediction to the actual number of defects produced.

7.2.2 Cascade Efficiency.

The effective efficiencies of all the cascades simulated in this work have been calculated such that

$$k' = \frac{2N_v\bar{E}_d}{E_{pka}} = 0.8\frac{N_v}{N_{NRT}} \qquad (7.2)$$

where k' is the effective efficiency and N_{NRT} is the final number of Frenkel pairs predicted by equation 2.5. Note that E_{dam} in equation 2.5 is equal to E_{pka} since no

electronic losses have been accounted for in these simulations. The results for both models are shown in figs. 7.4(a) and (b), using the values derived in chapter 5 for $\overline{E}_d$. Also included in these figures are the k' values when only the single and di-interstitials are taken into account, since these are believed to be the most mobile. In both cases the 'mobile defect' efficiency is only slightly less than the efficiency for all defects produced, indicating that single and di-interstitials are by far the most common SIA configurations. This will be discussed in more detail later.

For both Ti and Zr the same form of k' is exhibited as that seen for other metals, both in simulation (Diaz de la Rubia et al. 1994, Bacon et al. 1994) and experiment (Averback et al. 1978, Jung 1983, Rehn & Wiedersich 1992). The sudden drop in k' from ~0.6 at the lowest energies to ~0.3 at PKA energies of around 0.5 - 1 keV is now a well established phenomenon, first seen in simulations of W by Guinan & Kinney (1981). It is caused by both the disordering of the cascade core and the heating effect of the thermal spike enabling diffusive recombination within the most disordered regions, which were neglected in the Kinchin & Pease (1955) hard-sphere calculations. At low energies the absence of any definite core and the relatively diffuse nature of the relatively small number of displaced atoms mean these effects are minor, and k' is close to the NRT estimate of 0.8. However, as PKA energy increases the presence of a core and thus a significant subsequent thermal spike becomes more established, and their effects therefore increase, thereby reducing k'. At around 1 keV, for the Ti model at least, true cascade conditions have been reached, and the characteristic 'knee' is seen in k' as it levels off. Again, in the Zr model this effect is less pronounced and is more of a gradual curve, reflecting the same form as the results from the previous chapter. The increased presence of focused collision sequences at higher PKA energies, as discussed in the previous chapter, also has its effect on k' by dissipating energy in displacements which produce no defect, albeit at less energy per displacement, which would otherwise have been used to produce a permanent Frenkel pair. Because each of these low-energy displacements uses less

energy than a 'standard' displacement, more are generated and hence the increase in the N_{peak}:N_v ratio pointed out in the previous section.

7.2.3 Defect Configurations and Clustering.

This is also of great importance as far post-cascade microstructural evolution is concerned. It is generally thought that the larger a cluster of defects, the lower its mobility, which affects the migration of SIA clusters particularly since these play a major role in the production biasing effects. The cluster spectra for SIAs and vacancies for all cascades are shown in figs. 7.5(a) and (b) for the Ti and Zr models respectively. Note that the vertical axis depicts the mean number of defects per cascade, and not clusters per cascade. For these spectra a defect is counted as part of a cluster if it has at least one neighbour in that cluster and therefore clusters may be of quite irregular shape, especially the larger vacancy clusters. What is of note from the TV files is that the majority of the clusters, both SIA and vacancy, are present in or close to their final form at the end of the relaxation phase, and only a small fraction of SIAs are seen to cluster during the remainder of the thermal spike.

For the most part the cluster distributions for both models are qualitatively similar, with no great differences in cluster sizes seen at a particular PKA energy, though there is a slight difference in the vacancy cluster distributions in that the maximum cluster sizes are a little larger for the Ti model. However, this is probably due to the statistics rather than any real or significant effect. Quantitatively, the Ti model generally has more of each particular type of cluster, as would be expected given the larger N_v for Ti. There is therefore no appreciable difference in clustering, despite the factor of two in mass between the two metals.

The most prevalent form of both vacancies and interstitials is the single, isolated

defect, although di-vacancies and di-interstitials can occur even at the lowest PKA energies employed here. There is, in general, only a slight difference in the clustering of SIAs and vacancies in that there appears to be a tendency for vacancies to form larger clusters than SIAs. As PKA energy increases, so does the probability of a larger cluster being formed but even though N_v is higher for Ti, there is no significant difference in the maximum cluster size given the lower number of cascades at the higher energies.

The actual configurations of the final defects confirm those deduced in chapter 4. By far the most common SIAs are the BC and BS forms in both single and clustered interstitials, with the remainder in the metastable C or BO form, though these were quite rare. As suspected, and confirmed in chapter 5, the BS and BC sites are degenerate and single SIAs are often seen to switch from one form to the other. Fig. 7.6 shows the final state of a 5 keV cascade in Zr, with the various defects labelled. It is unfortunately difficult to appreciate the nature of each configuration from such a two-dimensional image, but the SIA clusters are nonetheless clearly visible, being made up of several neighbouring displaced atoms and vacant sites. Determination of vacancy cluster sizes, particularly di-vacancies is nigh on impossible from one picture, and requires the use of Atom-TV™ to allow viewing from a variety of angles to ascertain whether suspected clusters are, in fact, closely spaced single vacancies.

Di-interstitial clusters were formed by neighbouring BS and BC interstitials on adjacent <11$\bar{2}$0> rows, most commonly in the same basal plane, though sometimes in adjacent basal planes, i.e. the same prism plane. Both these forms are present in the main picture in fig. 7.6. Invariably one of the pair of SIAs is a BC and the other a BS, as this appears to cause minimum disturbance to the surrounding atoms. (When part of a cluster, the BC is depicted in fig. 7.6 as three displaced atoms and two vacant sites, with the central atom equidistant from and between the vacancies, and the BS by four displaced atoms and three vacant sites with the central vacancy

equidistant from, and almost between, the two neighbouring 'interstitials'. This is perhaps best shown in fig 7.6(c) for the tetra-interstitial, comprising two BC and two BS interstitials, with SIAs at opposite 'corners' of the loop having the same form.) This is also in agreement with the Mercer-Calder (1992) static study cited in chapter 4. The only exception to this case was a cluster of two C interstitials directly above one another in the same $\{10\bar{1}0\}$ plane, also investigated by Mercer-Calder, which has a slightly lower binding energy than the basal cluster. One other form of di-interstitial investigated in the above study was that of three atoms sharing one site, similar to the BS, but this configuration was never seen in the MD simulations, probably due to the large difference in binding energy with the other two forms.

The larger SIA clusters, i.e. tri-, tetra- and penta-interstitials, all consisted of the BS and BC forms, though the actual arrangement of the interstitials varied, from all SIAs next to each other within the same basal plane, to all SIAs stacked 'vertically' in a staggered manner in adjacent basal planes. Configurations extending within the same $\{\bar{2}202\}$ plane were not seen for clusters above three SIAs, since it is thought that the staggered $\{10\bar{1}0\}$ stacking pattern results in less net distortion to the surrounding structure. Generally, the most common configurations fell between these two extremes, with tri-interstitial clusters often forming triangular loops akin to inserting an extra L_4 lens into the structure (see fig. 5.6), such as depicted in fig. 7.6(b), and similarly tetra-interstitials often formed rectangular loops analogous to the insertion of an additional L_1 lens, such as shown in fig. 7.6(c). In all cases however, the larger loops formed stable prism plane loops with Burgers vector $\mathbf{b} = \frac{1}{3}\langle 11\bar{2}0\rangle$, again in complete agreement with the Mercer-Calder static study. This interstitial loop orientation also concurs with experiments on Zr (Griffiths 1988, 1991), where the majority of interstitial loops detected were of the $\mathbf{b} = \frac{1}{3}\langle 11\bar{2}0\rangle$ variety. On no occasion were any loops with $\mathbf{b} = \frac{1}{2}[0001]$ formed from during simulations, i.e. between the basal planes and consisting of O, C or T interstitials.

In the case of the vacancy clusters, the preference appears to be for closed loops where three or four vacancies are concerned, analogous to the removal of an L_3 or L_4 lens for a tri-vacancy, and an L_1 or two neighbouring L_3 lenses for tetra-vacancies. The tetra-vacancy loop shown in fig. 7.6 is of the L_1 type. No marked preference for orientation was observed, i.e. di-vacancies were equally probable in the in-plane and out-of-plane form, and the tri- and tetra-vacancies also showed approximately equal numbers of basal and prism plane clusters. This is, however, not surprising since the binding energy of the di-vacancy is approximately the same for both cases in both the models used here (Mercer-Calder 1992, Ackland et al. 1994). The penta- and hexa-vacancy clusters showed no regular shape, though very few of these were seen. Voids were not seen on the occasions where clusters of 4 or more vacancies were present, though the configuration of four vacancies in a tetrahedron with an atom in the O interstitial site within occurred several times in the higher energy cascades immediately after the relaxation phase. However, as the block cooled, the central atom moved to one of the vacancies, recombining with it and thus leaving a tri-vacancy. The one large cluster of nine vacancies referred to in section 7.1 was seen to form during a long simulation (~20 ps) of a 5 keV Ti cascade. This cascade was of the compact and high N_{peak} variety, and therefore the thermal spike energy was concentrated in one small volume. After the relaxation phase, the nine vacancies were quite close to one another but only a few constituted a cluster. As time progressed, the vacancies were seen to agglomerate into a more close-knit arrangement with six forming a prism plane loop and the remaining three tagged on one end. However, this was the only occurrence of anything resembling cascade collapse or vacancy loop formation in this work. Experiments involving ion irradiation of α-Ti show that the vacancy loop yield is almost zero for self-ions, even at PKA energies much higher than simulated here (Phythian et al. 1991), and loops are only formed by irradiation with heavier ions, which produce cascades with much higher energy densities. This also holds true for other metals (Calder et al. 1992). The reason that one cascade displayed partial clustering in the present work is probably due to its compact nature,

and therefore its high energy density. Definite collapse effects have been seen in simulations of Cu (Diaz de la Rubia & Guinan, 1992), but only at 25 keV, five time the upper limit of PKA energy in this study, so the absence of large vacancy loops in this work is not surprising, even for the Zr model.

When compared to cubic metals, the cluster spectra for interstitials show more similarity to that for Fe than for Cu (Bacon et al. 1994, Phythian et al. 1994), but still show lower probabilities for larger clusters. This may be explained by the difference in migration paths open to SIAs during the relaxation phase when clustering takes place. For the cubic systems, the closest-packed rows along which SIAs migrate exist in a three dimensional network, e.g. the <111> and <110> rows for the BCC and FCC cases respectively, aiding clustering. However, in the HCP system, the $<11\bar{2}0>$ close-packed rows lie in only two dimensions in 'unconnected' planes (in the sense that there are no between-plane migration routes with similar probabilities to those in-plane), which serves to restrict clustering. The SIA cluster spectra are, however, quite similar to those seen in Ni_3Al (Gao & Bacon 1994, Bacon et al. 1994), where it is thought that the presence of anti-site defects and the difference in sizes of the two alloy components hinders SIA agglomeration.

7.2.4 Defect Mobility.

The patterns of migration and movement of the defects have been assessed using Atom-TV™ to animate the TV files.

Typically, the vacancies are immobile in the ambient temperatures after the relaxation phase at the tail end of the thermal spike, though some small amount of rearrangement was seen in a few cascades in the time immediately following the relaxation phase. The interstitials, however, are very mobile indeed, though this is difficult to

appreciate without viewing the animations. (A video showing this has been prepared for conference presentations.)

Single SIAs are the most mobile, diffusing along the basal <11$\bar{2}$0> rows via the BS → BC → BS route in a caterpillar-like fashion as suggested in chapter 4. Often the single SIAs will come to a stop in the BS form, 'spin' around the shared vacant site and then move off along another basal row at 60° to the first. Single interstitials will also migrate between basal planes by the BS/BC → C → BC/BS route, again in agreement with the suggestions in chapter 4, but this is much less common and seems to occur mainly in the presence of another SIA or vacancy in the next plane, with which the SIA will cluster or recombine. Hence, single interstitial diffusion may be regarded as effectively two-dimensional.

For clusters of two or more SIAs, migration is confined to one dimension, i.e. along the <11$\bar{2}$0> cluster axis. This can be visualised as migration along the direction of the short string of displaced atoms making up the cluster, as shown in fig. 7.6. In agreement with Mikhin et al. (1994), di-interstitial migration is by an alternate shuffling mechanism such that one interstitial moves from the BS to BC form and its neighbour from BC to BS in the same direction, so moving $^1/_2$ a_0 along the row. When this is repeated, a full lattice parameter is traversed. Clusters of three or more move in a similar fashion, but mobility appears to reduce as the size of the cluster increases.

The movement of all SIA clusters appears to be diffusive in nature, i.e. the jumps are principally random. No coordinated movement towards or away from the cascade core was seen such as might be directed by thermal gradients, even by the single SIAs which are able to change direction, and little interaction between clusters was observed. What interaction was seen only took place when the random jumps took SIAs within a few lattice spacings of one another, and a larger cluster was formed.

Occasionally single and di-interstitials were seen to annihilate with vacancies but again, only when diffusion took the SIAs to within a few lattice parameters of the vacant sites, though SIA clusters of two or more can pass quite close to vacant sites without annihilation, and were also seen to pass over one another separated by a few basal planes without evidence of strong interaction. This presumably arises because they are hampered by their restriction to a single movement direction.

Quantifying the magnitude of the SIA cluster diffusion is difficult given the very small time scale of a single simulation. However, two longer simulations were made, one for each model at 5 keV, in an attempt to yield some comparative data between the two models. The number of whole lattice parameter jumps in a known number of time-steps (and hence time) was counted for all the defects remaining after these two cascades, and the results are presented in table 7.1, together with values for the effective diffusion coefficient D'. Fig. 7.7 shows D' against cluster size, and the fall in mobility as cluster size increases is clearly visible, with a marked drop for the tetra-interstitial clusters in Zr. The log-linear scale indicates an exponential decrease in cluster mobility as size increases. Although the decrease is more marked for the Ti model, D' for the same cluster size is of the same order for both models. This confirms that the single and di-interstitials are the most mobile, though the tri-interstitial clusters are also of similar mobility.

No explicit measurements of the migration energy of the SIAs have been made in the present work, as mentioned in chapter 4. However, a fair approximation may be deduced from the fact that

$$\nu_j = \nu_a \exp\left(\frac{-E_m}{k_B T}\right) \qquad (7.3)$$

where ν_j is the jump frequency, ν_a is the attempt frequency, E_m is the migration energy, k_B is Boltzmann's constant and T is the temperature. Assuming a jump

frequency of ~10^{12} Hz, a good approximation for both models from table 7.1, an attempt frequency of 10^{13} - 10^{14} Hz, and a temperature of 300 K, this gives a value of E_m^i, the interstitial migration energy, of ~0.1 eV. This is perhaps a little high in the light of other works showing the high basal-plane mobility of SIAs in the HCPs, such as Mikhin et al. (1994), where a basal E_m^i of 0.03 eV was found for a Zr model with similar c/a ratio to this work. This rough estimate of $E_m^i \approx 0.1$ eV corresponds to annealing at ~50 K, which falls into stages I_B - I_C on the annealing curve shown in fig 2.4. This is is in at least qualitative agreement with Mikhin et al. (1994), who suggest that, since the single and di-interstitials (and possibly the tri-interstitials) are all of very close mobility, stage I annealing, as described in chapter 2, can be explained by migration of SIAs and small clusters, rather than just single interstitials. They also speculated that the latter substages of stage I annealing may be due to the migration of larger interstitial clusters, but a much more in-depth specific investigation into the dependence of SIA and cluster mobility on temperature is required before any firm conclusions can be made as to which substages can be attributed to which configurations.

7.2.5 Cascade-Induced Mixing.

This effect has become increasingly studied in the last few years (e.g. Diaz de la Rubia et al. 1989, Diaz de la Rubia & Guinan 1992, Diaz de la Rubia et al. 1993, Bacon et al. 1994, Gao & Bacon 1994). Based on the calculation of the total mean square displacement (MSD) Δ^2 of the atoms in the simulation block at time t, such that

$$\Delta^2(t) = \sum_{i=1}^{N_j} |\mathbf{r}_i(t) - \mathbf{r}_i(0)|^2 \qquad (7.4)$$

where $\mathbf{r}_i$ is the position vector of the ith atom, and N_j is the number of atoms which have actually changed site (be it to another site or to an interstitial position), or

'jumped', during the cascade. Although of more significance for alloys, particularly of the ordered variety, this parameter is also relevant to pure materials in that is gives an indication of the amount of atomic movement taking place during a cascade. In the case of the HCP metals, by splitting Δ^2 into two components - movement in the basal plane (Δ_{xy}^2) and along the c-axis direction (Δ_z^2), any structurally induced differences in basal and c-axis mixing can be quantified. These are shown in fig 7.8(a) and (b) for both 2 and 5 keV cascades in Ti and Zr respectively. The lines are best fits through the data for several cascades, and N_j is the number of atoms which have changed site by the end of the cascade (± the standard deviation from the mean). Note that these are shown with respect to time even though here we are mainly concerned with the final defect state of the cascade, and it can be seen that mixing continues to some degree for several ps past the cascade peak, thus indicating the important role of the thermal spike in assisting the mixing process. However, the majority of the atomic movement has occurred within the collisional and relaxation phases, during the time of greatest core disorder.

Care must be taken in the interpretation of figs. 7.8(a) and (b) as, at first glance, it appears that there is significant anisotropy in the two components of Δ^2, with Δ_{xy}^2 for all cascades approximately twice Δ_z^2. This would be true if any out-of-plane jumps from one nearest-neighbour site to another were directly along the c-axis, as in the simple cubic lattice. However, this is not the case since out-of-plane jumps occur along <$\bar{2}$203> rows, and therefore also have a basal component. Thus, for a single <11$\bar{2}$0> jump, i.e. in-plane, $\Delta_{xy}^2 = a_0$ and $\Delta_z^2 = 0$, whereas for a single <$\bar{2}$203> jump, i.e. out-of-plane, $\Delta_{xy}^2 = (1/\sqrt{3}\, a_0)^2$ and $\Delta_z^2 = (1/2\, c_0)^2$. For a cascade in an ideal HCP metal, that is with $c_0 = \sqrt{(8/3)}\, a_0$, with one jump of each type, the total values of Δ_{xy}^2 and Δ_z^2 are such that $\Delta_{xy}^2 = 4/3\, a_0^2$ and $\Delta_z^2 = 2/3\, a_0^2$, and hence $\Delta_{xy}^2 = 2\Delta_z^2$ for a cascade with isotropic mixing, i.e. equal probabilities of in- and out-of-plane jumps. Since this is seen to be the case here, cascade mixing must be isotropic in these models, and therefore the HCP structure has no effect, despite the strong preference

for basal SIA migration. However, considering that the cascade core, and indeed the final defect state, shows a positive concentration of vacancies near its centre with SIAs ejected away from the core and given that vacancy migration is essentially isotropic in most HCP metals (Bacon 1993), it is possible that it is the vacancies which are primarily responsible for the isotropic nature of the intracascade mixing. In addition, the disordered, liquid-like state of the cascade core, which persists for some time past the displacement peak, could also be at least partially responsible for the atomic movements. This liquid mixing idea was used by Diaz de la Rubia et al. (1994) to explain their findings from simulations of Ni_3Al and Cu_3Au, in that the ratio of MSDs for each of the elements in the alloys closely matched their composition ratio. However, more recent work using another many-body potential (Gao & Bacon 1994, Bacon et al. 1994) for Ni_3Al has shown an elemental MSD ratio of between 4:1 and 5.5:1, i.e. greater than the 3:1 composition ratio, and therefore some other mechanism linked to solid state diffusion must be operating. These sets of findings are perhaps not as contradictory as they may first appear, however, as it is quite feasible that both mechanisms contribute to the overall total MSD, whether in an alloy such as those mentioned above, or in the HCP cases studied here.

For both models, Δ_{xy}^2 and Δ_z^2 at 5 keV are around 3 to 4 times their value at 2 keV, and this difference is greater than the factor of 2.5 in E_{pka}, indicating another non-linear relationship, this time between Δ^2 and E_{pka}. The same is also true of N_j, though with only two values of E_{pka} it is impossible to establish the exact nature of this relationship.

Comparing the degree of mixing in both models reveals a factor of approximately two in Δ^2 and N_j for the same values of E_{pka}. This must be attributable to the mass difference, and hence the $\overline{E}_d$ difference between the two metals, since the energy per displacement in Zr, and therefore energy per jump, is nearly twice that in Ti, and therefore approximately half as many jumps would be expected in the Zr model. In

comparison to other metals, the values of Δ^2 found for Ti are around 2.5 times greater than for Ni_3Al (Bacon et al. 1994), and 3 times those for Cu (Diaz de la Rubia et al. 1994) at the same PKA energies. While this may also be thought to be due to the mass difference between these materials, Δ^2 for Zr is still greater than in Cu and Ni_3Al by a factor of around 1.2 - 1.5, and therefore the extent of the intracascade mixing seems also to depend on structure. One possible reason for the lower mixing in Ni_3Al is the difference in size of the two constituents, which hinders atomic movement.

- § -

7.3 Discussion and Summary.

As in chapter 6, many features of the final defect state has been discussed concurrently with the results, so this section will deal mainly with a summary of the above results and expansion on any points needing further clarification.

The parameters characterising the final defect state, including the final number of Frenkel pairs and the defect production efficiency, show very similar form in relation to PKA energy to other metals (for examples, see Diaz de la Rubia et al. 1994, Bacon et al. 1994), thereby indicating that the underlying thermal spike processes affecting the final number of Frenkel pairs operate irrespective of structure, as is also the case for the basic mechanisms of cascade formation discussed in the previous chapter. As found in section 7.2.1, N_v shows a power-law dependence on E_{pka} for a variety of metals, not just the two HCP models in this work. What is of interest, however, is the quite small variation in the constants A and m in equation (7.1), not only for the two metals under study here, but also for Fe, Cu and Ni_3Al, all of which have atomic masses between those of Ti and Zr (Bacon et al. 1994). Despite the large variation in

mass, up to 100 % across the range mentioned above, A only changes by ~25 %, and m by less than ~6.5 %. It is not beyond the realms of possibility that this small percentage change in m is due to the statistical errors resulting from the relatively low numbers of cascades performed at higher PKA energies, and it therefore feasible that m is, in fact, an empirical constant with no dependence on mass or structure. A value for m of ~0.8 is not unreasonable given the results shown here. Unfortunately, most of the existing published works on MD simulations contain no specific data for the final number of Frenkel pairs in their calculations, and therefore further investigation is needed to establish whether m is a constant or not.

The value of A, however, cannot be a constant since N_v for a given PKA energy must vary with $\overline{E}_d$, and hence mass. The values obtained for A from this work (fitted to N_v values at $E_{pka} \geq 1$ keV) and the results in Bacon et al. (1994) for other metals (fitted to N_v values at $E_{pka} \geq 0.5$ keV) are plotted against $\overline{E}_d$ in fig. 7.9. (The $\overline{E}_d$ values are also from this work and Bacon et al. (1994). They differ slightly from the ASTM recommendation (standard E521, 1989), but are judged to be the more appropriate choice for consistency.) While this is hardly conclusive, given that only four metals are included in fig. 7.9, it is of great interest to notice that there is an excellent fit to a linear dependence of A on $\overline{E}_d$. Equation 7.1 can thus be modified to

$$N_v = \left(C - \alpha \overline{E}_d\right) E_{pka}^{\ m} \qquad (7.5)$$

where C is the intercept in fig. 7.9 as $\overline{E}_d$ tends to zero and α is the gradient of the straight line fit. Thus, N_v is zero if E_{pka} is zero or $(C - \alpha\overline{E}_d)$ is zero which, given the fitting parameters in fig. 7.9 occurs when $\overline{E}_d \approx 137$ eV. Using the fact that $\overline{E}_d$, for the metals plotted in fig. 7.9, is between 0.6 and 0.7 times the atomic mass in a.m.u., N_v would therefore be zero when the atomic mass of the element in question is well above 200 a.m.u. While this may not be physically reasonable, since it gives very low N_v values for heavy elements under self-ion irradiation, the empirical relationship

of equation 7.5 does hold very well for the lighter elements referred to above. Further investigation is needed to verify this relationship for other metals, and to provide a physical model to explain it.

The overall picture of the final defect state in the HCP metals emerges as a diffuse collection of vacancies, either singly or in very small clusters, surrounded by and separated from an even more disparate distribution of SIAs and small interstitial clusters. This is in common with the initial theories and the modelling of other metals. The magnitude of the mobility of the clusters is perhaps the most surprising result, since it has not been seen on this scale in MD simulations of other metals. (Visualisation using Atom-TV™ is of great value in observing this effect.) Simulations of four, five and six-interstitial clusters in Cu (Foreman et al. 1992) yielded a high, one-dimensional mobility and, in contrast to the results obtained here, they were much more mobile than single SIAs, though they migrated by the same coupled-crowdion mechanism. Moreover, this result fits an earlier theory by Foreman et al. (1974) explaining the formation of a regular lattice of gas bubbles in Cu during irradiation experiments. In simulations of Fe (Calder & Bacon 1993), SIAs only showed appreciable migration in the presence of the stress field of other clusters, which resulted in migration to increase the size of the clusters.

As pointed out in chapter 4, the preferred basal-plane migration of SIAs in Ti and Zr constitutes a diffusional anisotropy difference (DAD) (Woo 1988), which outweighs any elastic effects of sinks such grain boundaries and precipitates. The presence of this marked DAD in this work is by no means unique, since several earlier HCP studies, summarised by Bacon (1988), also found a lower migration energy for SIAs within the basal plane with their pair potential models. Other workers (Woo & Singh 1992, Singh & Foreman 1992) have proposed that the DAD and EID are only partially responsible for the biasing effect, since standard rate theory assumes that defects are produced singly and in a uniform distribution. While this is true for

defects produced by electron irradiation, is clearly not the case for those resulting from displacement cascades, and therefore the aforementioned authors suggested that the degree of defect clustering, particularly SIAs, serves to enhance the production biasing towards mobile vacancies at elevated temperatures, since large interstitial clusters are less mobile than single SIAs. Very large interstitial clusters ($\geq$ 10 SIAs) often collapse into faulted platelets (Ullmaier & Schilling 1980), at least in FCC metals, and are sessile and therefore begin to act as localised sinks, further reducing the number of mobile interstitials present.

The one-dimensional limitation on migration for SIA clusters holds marked implications for the behaviour of these defects in the presence of surfaces, grain boundaries and other extended defects such as precipitates in alloys, and under the influence of external stresses. From the results in this chapter, it can be deduced that SIAs will migrate preferentially to prism plane dislocations in the HCP metals. For clusters, the exact orientation of the dislocation is also important since they are locked into a single direction, though at higher temperatures it is probable that the single SIAs and smaller clusters will be able to migrate between planes as has occasionally been seen, allowing absorption at basal-plane sinks . Dislocations which run parallel to the migration direction of clusters, however, will be unnoticed unless within a few lattice parameters, as SIA clusters have not been seen to change direction within the basal plane, i.e. rotate by $\pm 60^{\circ}$. Vacancies, which are taken to have isotropic migration at high temperatures (not seen in these short simulations), will eventually migrate to sinks irrespective of orientation.

The implication of these results is that, since interstitials are highly mobile in both single and small clusters, they will readily leave the cascade site in the presence of favourably oriented dislocations or stresses, leaving a surplus of vacancies at the cascade site and, if trapped at solutes and grain boundaries or absorbed at surfaces and larger sessile clusters, effectively reduce the number of mobile interstitials in the

metal. Vacancies, on the other hand, remain immobile until the temperature is elevated to ~0.3 T_m, the temperature at which irradiation swelling becomes marked. The end result is that there will be an enhancement of the DAD-generated production bias at swelling temperatures in favour of vacancies caused by the rapid migration of SIAs and small interstitial clusters away from the cascade site, as also mentioned by Zinkle & Singh (1993).

None of the above effects has yet been studied in depth by simulation, though preliminary MD investigations of coherent Cu precipitates in α-Fe show that there is a very marked effect on point defects in the locality of the precipitate, with vacancies being absorbed within, and SIAs migrating under stress to the surface (Calder 1994). Unfortunately MD is a very compute-intensive methodology, and long simulations (i.e. of the scale of μs) of diffusional behaviour are beyond the scope of most computer systems, so extrapolations of the results of 10 - 100 ps simulations must be made. However, those studies which are in their early stages show great promise.

It is perhaps appropriate at this point to mention the limitations of the MD modelling used in this work, other than the small time-scale restrictions pointed out above. No account is made of loss of energy to the electronic system, either by inelastic losses of the initial particle causing the cascade (or indeed any of the atoms in the block), as mentioned in section 7.2.2, or during the thermal spike via electron-phonon coupling. This latter effect serves to remove heat from the ions during the thermal spike, thereby reducing its length and quenching the cascade faster. It was predicted by Finnis (1992) to have little effect for 5 keV cascades in Cu, but a more marked effect for Ni, a transition metal with partially filled d-electron bands. Since Ti and Zr fall into this category, it would perhaps be pertinent to include this phenomenon in the simulations. Its effect would only be seen at the limit of the PKA energies used in this work, and it has not been found possible to incorporate it appropriately in MD modelling. Thus, the majority of the MD investigations to date have not taken

electron-phonon coupling into account, and therefore the results detailed in this work are directly comparable with them. One other effect not included in this work is the removal of heat at the block boundaries, as pointed out in section 6.5.4. This is usually achieved by damping the atoms at the box faces to simulate conduction into an infinite heat sink at a fixed temperature (Diaz de la Rubia & Guinan 1990).

- § -

Table 7.1: Mobility data for single SIAs and small interstitial clusters in both models.

Cluster size	Ti		Zr	
	Jumps / Second	Diffusion Coefficient† ($m^2\ s^{-1}$)	Jumps / Second	Diffusion Coefficient† ($m^2\ s^{-1}$)
1	1.4×10^{12}	4.2×10^{-7}	9.4×10^{11}	2.8×10^{-7}
2	8.5×10^{11}	1.7×10^{-7}	7.8×10^{11}	2.1×10^{-7}
3	6.0×10^{11}	5.3×10^{-8}	6.7×10^{11}	1.4×10^{-7}
4	-	-	2.8×10^{11}	2.4×10^{-8}

† The term 'diffusion coefficient' is used with caution here, since the simulation blocks were not at constant temperature throughout the simulations with the Ti model falling from ~320 K to 172 K in 16 ps, and the Zr model falling from ~424 K to 383 K in 18 ps. Nonetheless, they are useful for comparative purposes, and have been calculated as $D=^1/_6(x^2/t)$, where x is the total distance moved by the cluster in time t.

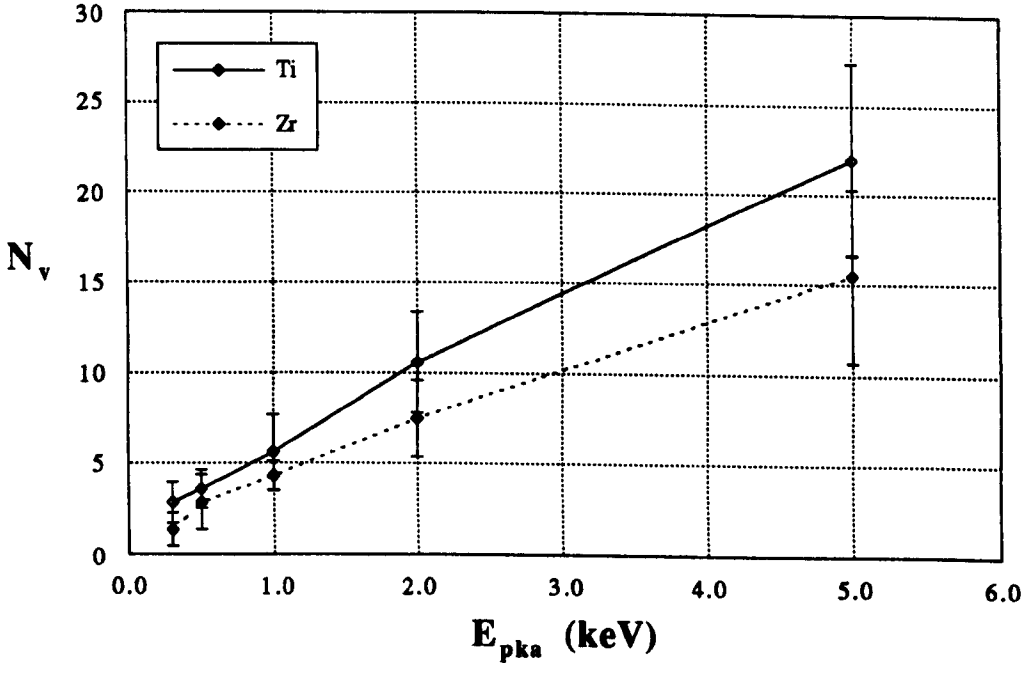

Fig. 7.1: Final number of vacancies (and hence Frenkel pairs) vs. PKA energy for both models. The error bars show the standard deviation from the mean.

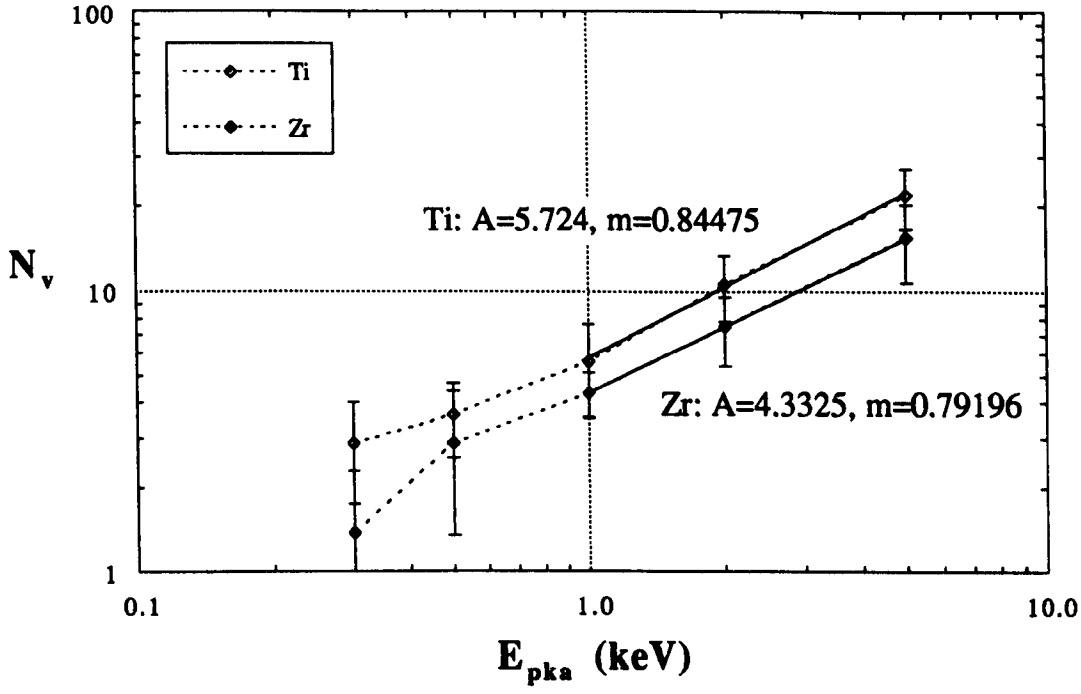

Fig. 7.2: Final number of vacancies vs. PKA energy for both models on a log-log scale, exposing an exceptionally good fit to the power-law relationship above 1 keV. The error bars show the standard deviation from the mean

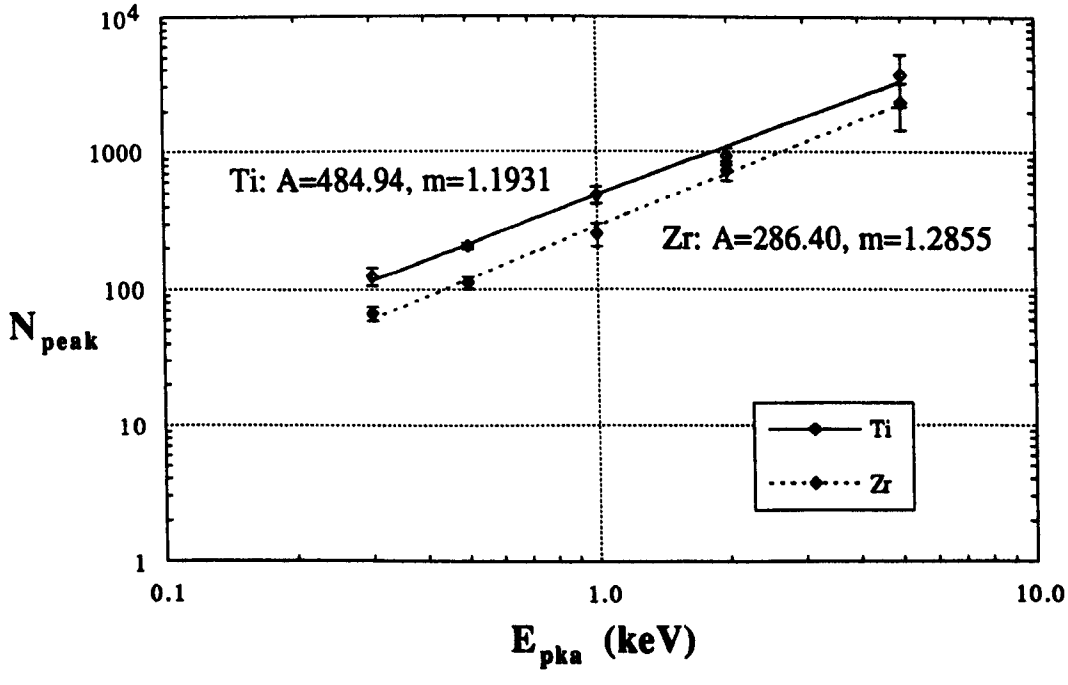

Fig. 7.3: N_{peak} vs. E_{pka} on a log-log scale, again showing a good fit to a power-law dependence. The error bars show the standard deviation from the mean.

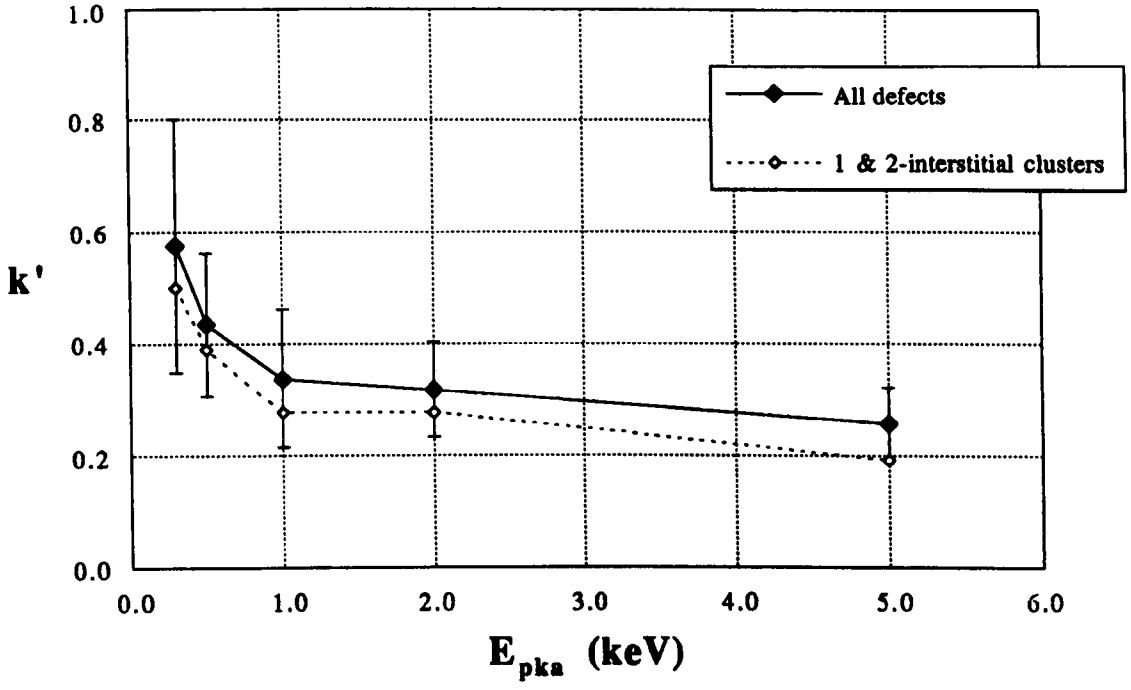

Fig. 7.4(a): Effective cascade efficiency for all cascades in the titanium model. The error bars show the standard deviation from the mean.

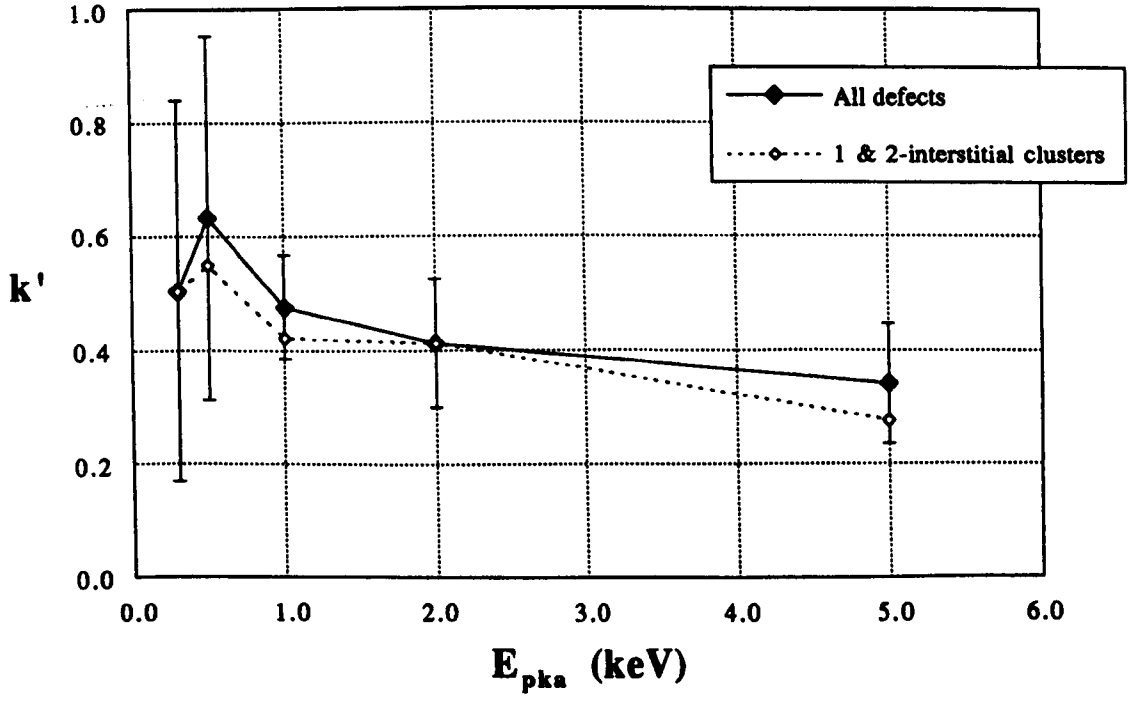

Fig. 7.4(b): Effective cascade efficiency for all cascades in the zirconium model. The error bars show the standard deviation from the mean.

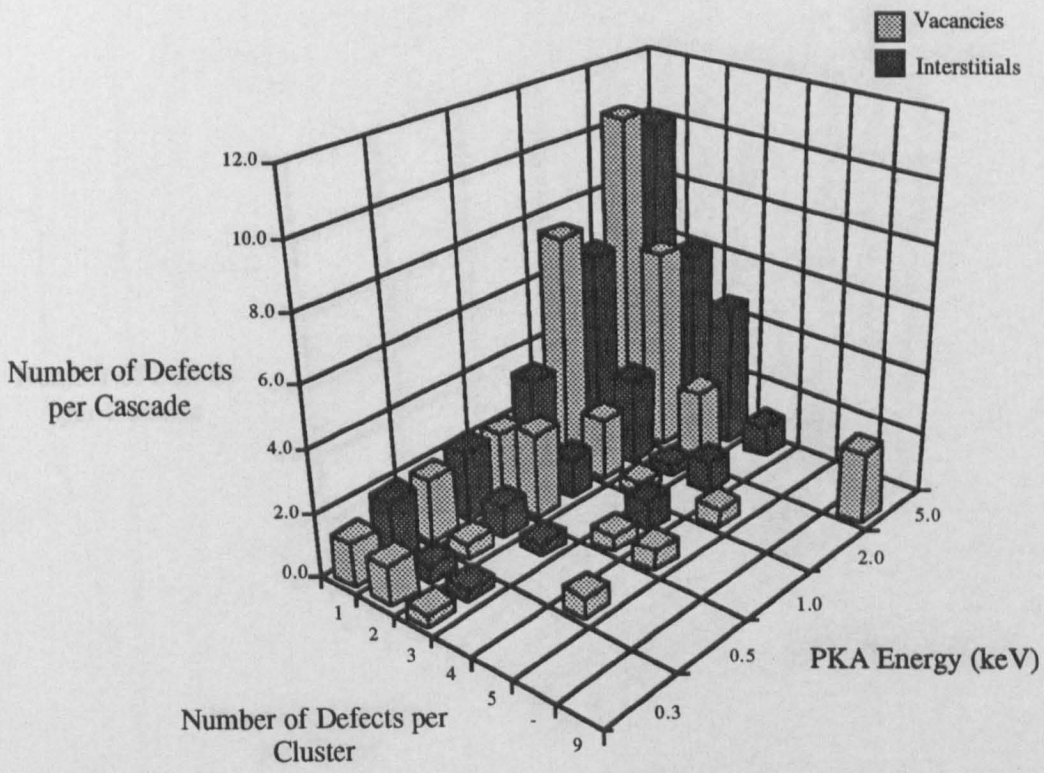

Fig. 7.5(a): Cluster spectra of SIAs and vacancies for the Ti model over all cascades simulated.

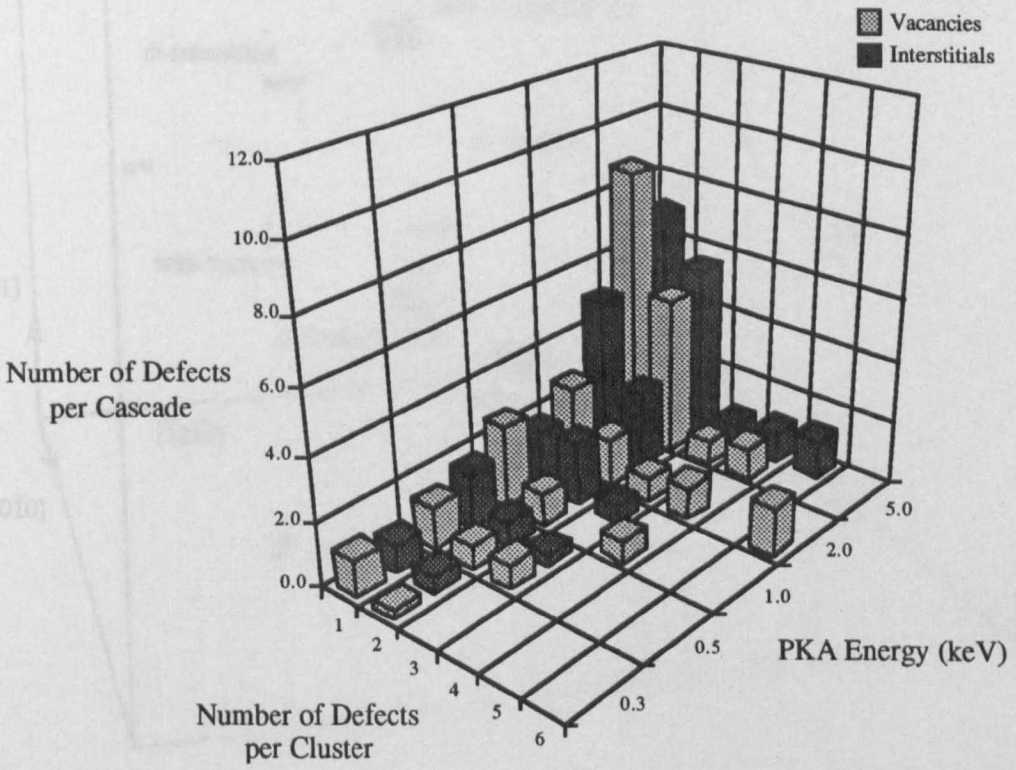

Fig. 7.5(b): Cluster spectra of SIAs and vacancies for the Zr model over all cascades simulated.

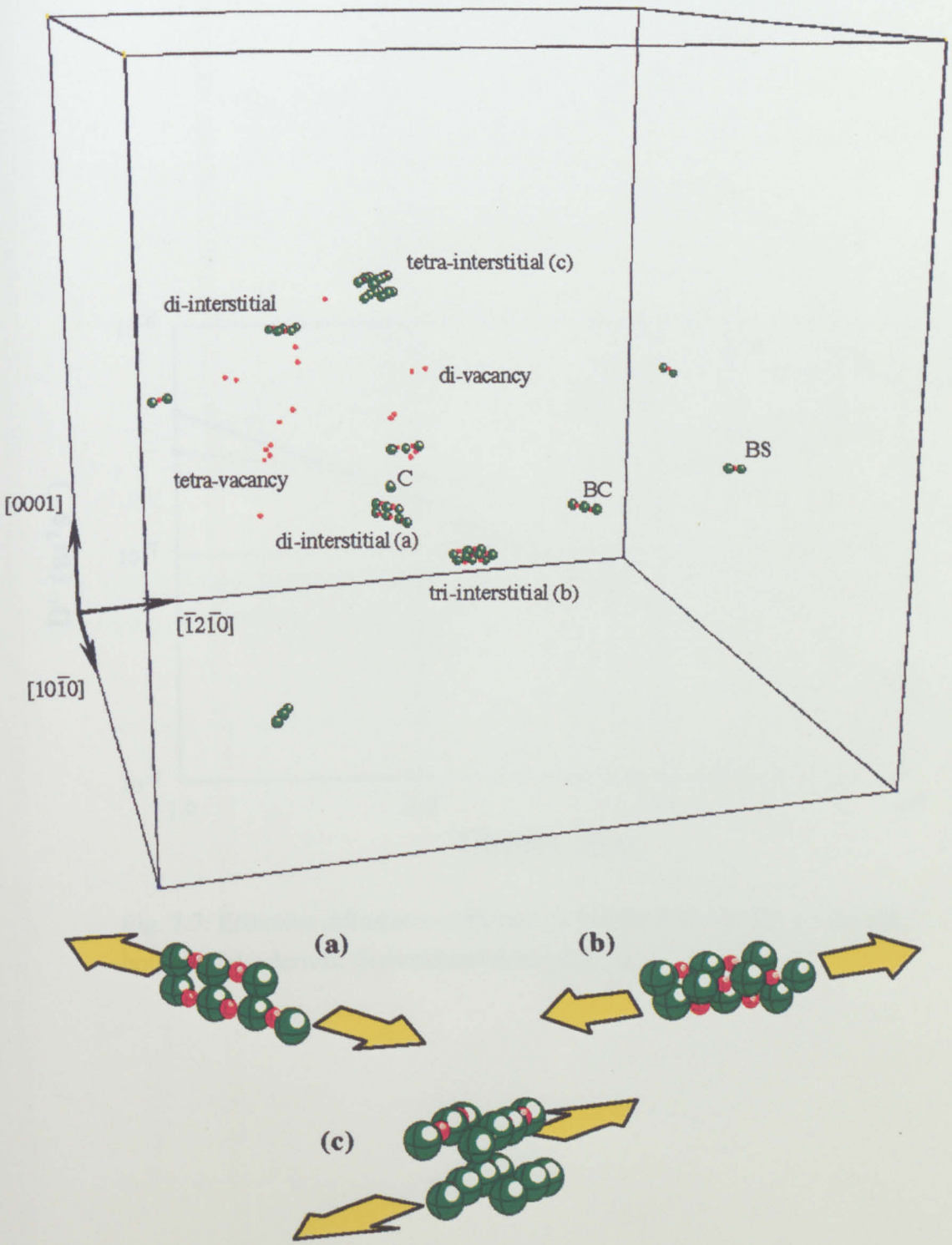

Fig. 7.6: Final state of a 5 keV Zr cascade. Labels show the various configurations of vacancies and interstitials. For the sake of clarity, only one defect of each type is labelled in most cases. Smaller figures (a), (b) and (c) show magnified views of di-, tri- and tetra-interstitials respectively, with their associated migration directions.

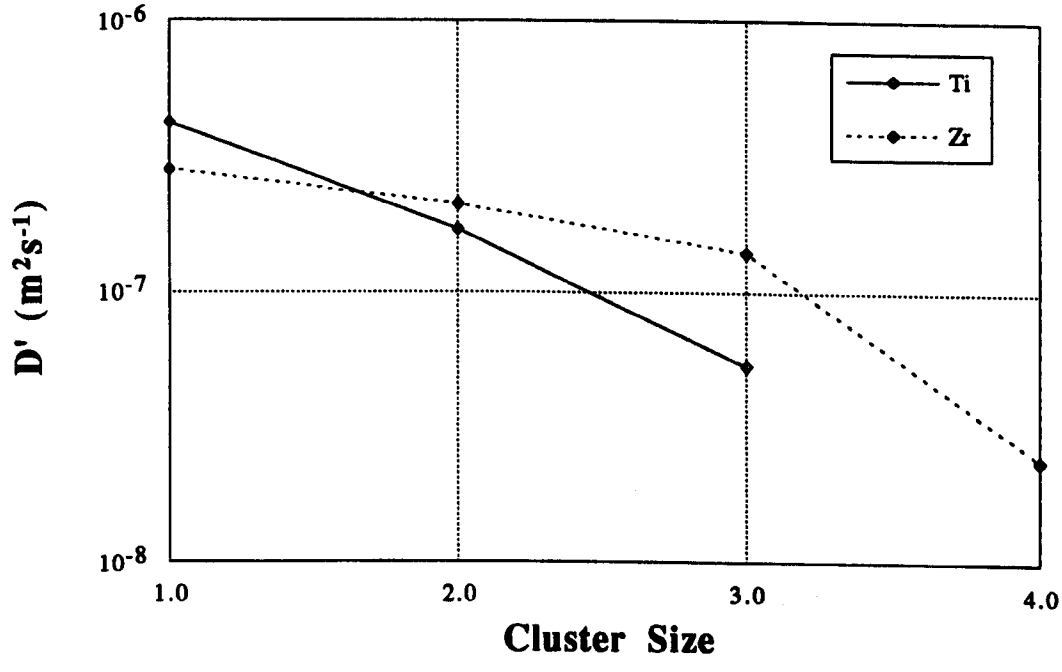

Fig. 7.7: Effective diffusion coefficient vs. cluster size for SIA clusters in both models, derived from extended simulations.

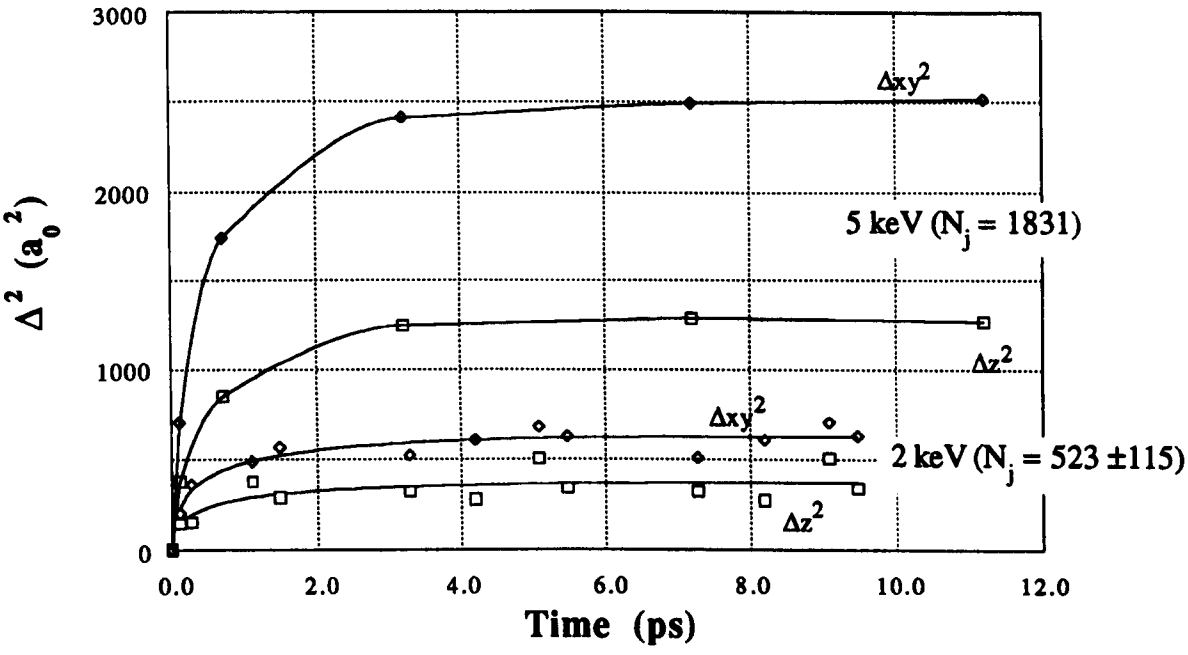

Fig. 7.8(a): Cascade-induced mixing parameter vs. time for all 2 keV cascades and one 5 keV cascade in the titanium model.

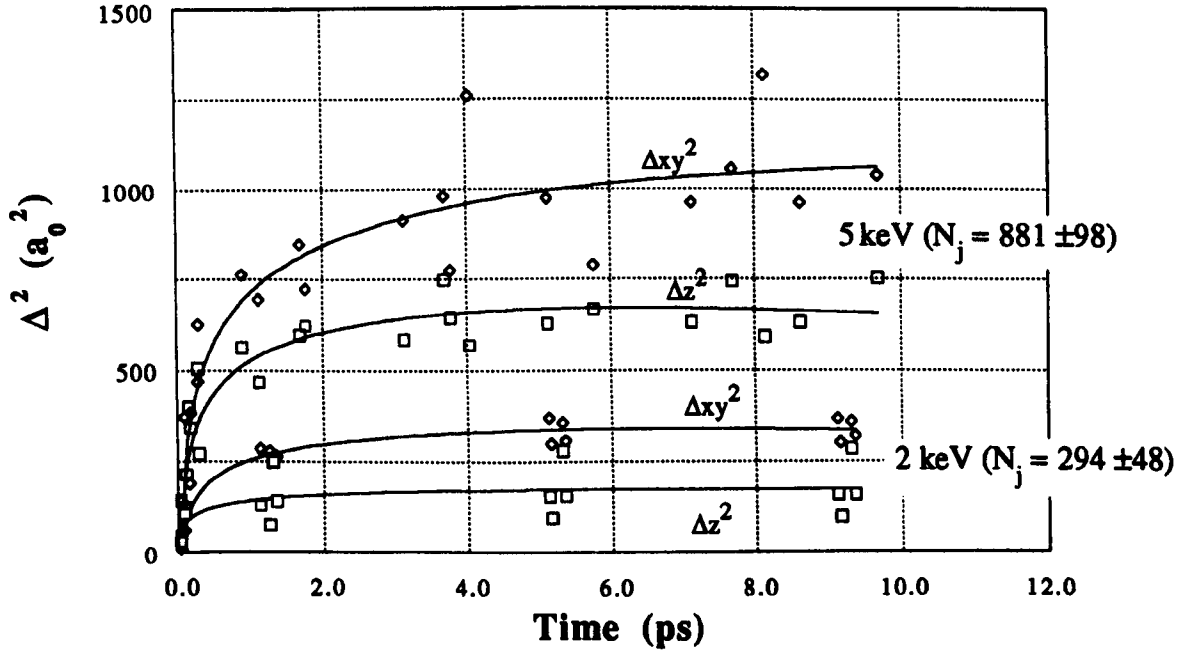

Fig. 7.8(b): Cascade-induced mixing parameter vs. time for all 2 keV and 5 keV cascades in the zirconium model.

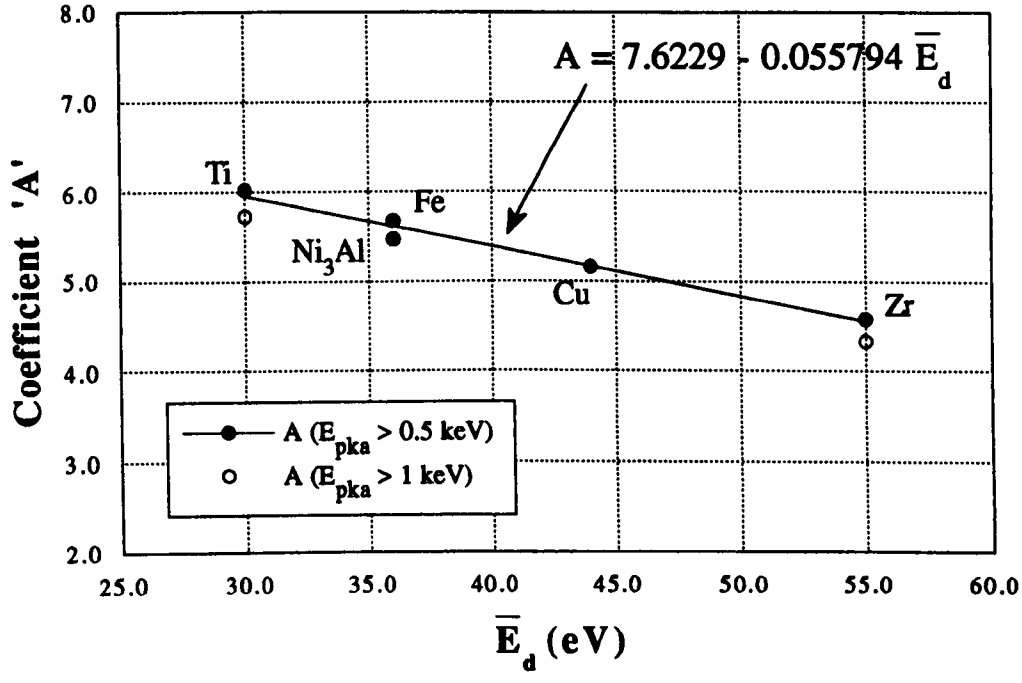

Fig. 7.9: Coefficient A in equation (7.1) vs. $\overline{E}_d$. (Data after this work and Bacon et al. 1994)

VIII

Conclusions, Closing Remarks and Suggestions for Further Work

8.1 Conclusions

- The two Ackland potentials for Ti and Zr, have been suitably modified for dynamic events, and closely follow experimental and theoretical predictions for the P-V response of these two models. Together with the necessary modifications to MOLDY, these constitute a foundation model for these two HCP metals.

- Of the eight possible single SIA configurations in the HCP structure, only four are found to be stable in the Ti and Zr models used here. In both cases, the BS and BC forms are degenerate and therefore, in terms of the two-interstitial model, together constitute the stable interstitial. The metastable sites are the BO and C sites for the Ti and Zr models respectively, though the BO form appears to reconfigure to either the BS or BC given thermal energy, leaving the C interstitial as the most likely candidate for the metastable form in the two-interstitial model.

- As a direct consequence of the preference for basal interstitials, and the degeneracy of the BS and BC forms, SIA migration shows a high preference for the BS $\rightarrow$ BC $\rightarrow$ BS basal plane route along the $<11\bar{2}0>$ rows and may therefore be regarded as effectively two-dimensional. Clusters also migrate via this route, though their mobility is reduced with size, and their migration restricted to one dimension.

- The displacement threshold energy shows a complex dependence on direction, explained in terms of the 'lenses' of atoms surrounding the PKA, and the arrangement of the atoms in the locality. This dependence is almost identical in form for the two models and is therefore determined predominantly by structure. The mean values of E_d for both models reflect the mass difference between the two. A broad agreement for E_d^{min} with experiment was found.

- Two distinct forms of cascade are seen at threshold energies, these being a fairly

compact variety with few RCSs and focused collision sequences and, conversely, a form in which the majority of the displaced atoms are contained in focused collision sequences. Both these forms have a characteristic value for the energy per displaced atom at the cascade peak, with more atoms displaced per eV for the latter variety than the former.

- Displacement cascades have been simulated at PKA energies of 0.3 to 5 keV in both models, with a variety of initial PKA trajectories. No discernible dependence of cascade form on PKA direction was seen, due to the structurally-disordering effects of the displacement cascade process.

- A marked change in the general cascade morphology is seen at PKA energies of around 1 keV, linked to the onset of 'true' cascade conditions, i.e. the establishment of a distinct, highly disordered cascade core. In terms of energy per displaced atom at the peak, this change in morphology correlates with the two forms seen at threshold, and indicates a significant increase in the number of temporarily displaced atoms contained in low-energy focused collision sequences.

- This change in cascade form is also reflected in the parameters used to characterise the cascades. These include the relaxation time τ_d, which becomes markedly less dependent on PKA energy as E_{pka} increases past ~1 keV. N_{peak} shows an increasing dependence on E_{pka} and N_v a decreasing dependence.

- The nature of the relationship of the final number of Frenkel pairs, N_v, to PKA energy is established as a power-law dependence, with mass-dependent coefficient and a fractional, possibly constant, exponent.

- The effect of increasing atomic mass is seen as spreading the change in cascade form over a larger energy range, i.e. the transformation mentioned above is more

gradual in the Zr model. It also has influence, by virtue of increasing $\bar{E}_d$, on N_{peak} and N_v, reducing both with increasing mass. However, the exact nature of this relationship is not simply a linear one due to other geometrical and thermal effects.

- The collisional phase of the cascade can be divided into two, according to the maximum KE of all atoms in the simulation block. During the primary stage, when $E_{max} \geq E_d^{min}$, all permanent displacements occur. The secondary stage, from the time E_{max} drops below E_d^{min} to the cascade peak, is comprised solely of temporary displacements, many of which are contained in collective radial focused collision chains at the higher PKA energies.

- The state of the disordered cascade core at the peak, and for some time afterwards, is best described as a non-equilibrium quasi-liquid. This would concur with the radial pair distribution functions, core densities, temperatures at the peak, and the isotropy of the intracascade mixing which takes place.

- The relaxation phase may also be divided into two. During the first, athermal stage, characterised by τ_d, displaced atoms recombine rapidly with nearby vacant sites, with little interaction or interference with neighbouring atoms. The second, thermally assisted stage, shows slower recombinations by diffusive mechanisms to vacant sites further away until the final defect state is reached.

- The effective defect production efficiency factor, k', shows the now classic rapid fall from near the NRT standard of 0.8 at low PKA energies, to around 0.4 as E_{pka} reaches ~1 keV. This corresponds to the change in cascade morphology mentioned above, and is associated with the increasing effect of the thermal spike assisting recombination. Again, increasing mass has the effect of changing the transition in k' from a marked 'knee' in Ti to a more gradual curve in Zr.

- No significant vacancy clustering occurred in the core during any simulations, again suggesting that the core cannot be a true liquid, at least at the cascade energies studied. The great majority of the vacancies are in their final configurations by the end of the relaxation phase.

- Most, but not all, of the SIAs are produced in their final configurations by the end of the relaxation phase. The main mechanism for SIA-vacancy separation is not the RCS, but incomplete relaxation of the periphery of the cascade core. However, RCSs do play a small role, though their significance is reduced with increasing PKA energy.

- The greater majority of SIAs remain as single defects. Some clustering takes place during the thermal spike, though most clusters are already present in their final form at the end of the relaxation phase. This is not the case in the cubic materials, where much more clustering occurs during the thermal spike. It is though that the limitations on SIA migration to the basal planes hinders this thermal spike clustering in the HCP metals.

- All the SIA clusters formed are of the $\mathbf{b} = {}^1/_3 \langle 11\bar{2}0 \rangle$ variety, i.e. perfect prism plane loops, in agreement with experiment. No discernible preference for vacancy loop orientation was found.

- The extent of clustering, both vacancy and interstitial, is increased with increasing PKA energy and is qualitatively similar in both models. Compared with cubic metals, the cluster spectra (for the SIAs at least) show most similarity to α-Fe, though the overall degree of clustering is still less in these HCP metals, especially at the higher PKA energies.

- Many of the fundamental aspects of cascade formation and the final defect state are

common to all MD simulations of a variety of metals, indicating a general application of the effects and mechanisms found in this work to all metals, irrespective of mass and structure.

- § -

8.2 Closing Remarks.

This work is the first in-depth investigation of the response of the HCP metals to radiation damage using MD and many-body potentials. As such, it is wide-ranging in content, encompassing events ranging from zero energy, such as point defect properties at 0 K, through the threshold regime and into the higher energy region, comparable with existing studies on other systems. It is hoped that this work will provide a broad and sound foundation for future research to build on.

The facilities and resources used to perform the calculations and modelling used in this work are as follows: Initial simulations were carried out on the IBM 3081 mainframe at Liverpool and the Amdahl VP1200 vector-processor at the Manchester Computing Centre (MCC). Unfortunately, both these services were withdrawn during the course of this study, and the remaining work was performed on the replacement Sun UNIX system at Liverpool and Fujitsu VPX240 at MCC. Other incidental work, such as the melting simulations, was carried out an a Silicon Graphics Indigo™ workstation in the Radiation Damage Group at Liverpool. Analysis of the results and production of this thesis were accomplished using MacAtoms™, Ball & Stick™, Kaleidagraph™, Microsoft Excel™, Adobe Photoshop™, MacDraw Pro™ and MacWrite Pro™ on the Apple Macintosh™, and AVS™ on the SGI™ workstation.

- § -

8.3 Suggestions for Further Work.

The most obvious next stage in this work is to continue the present study to higher PKA energies, since these arise in the spectrum for materials in fission-based power reactors. Some studies have already been undertaken for other metals, with PKA energies of up to 25 keV beginning to be studied. At the present state of the art, times of ~0.1 ms per atom per time-step are regularly achieved for α-Fe (Calder 1994), whereas for the work detailed here, approximately 0.2 ms per atom per time-step were required. This is to do with the close-packed nature of the HCP system, such that one atom has approximately twice as many neighbours within the range of the interatomic potential than in the BCC case. Such work would provide additional data for the verification (or otherwise) of the power-law relationship between E_{pka} and N_v, as well as extending the data for the parameters characterising cascade evolution and the final defect state.

Further to the discussion in section 7.3, it would be fruitful to carry out MD simulations of defect behaviour in the presence of grain boundaries and surfaces at various orientations to the <11$\bar{2}$0> directions since, on an engineering scale, real materials contain these and other extended defects. Surface effects on cascade processes, not just the final defect state, have recently been simulated (Ghaly & Averback 1994, Averback & Ghaly 1994) with respect to ions entering a surface to create a cascade. The results from these simulations show that, under some conditions, the presence of a surface markedly increases the number of defects the cascade produces by providing an 'escape route' for the material ejected from the disordered cascade core. This then leaves a reduced amount of material at the cascade site, which collapses either into a large vacancy loop or some more complex dislocation structure. Since such ion irradiation of surfaces is the chosen method for many reported radiation damage experiments on cascade collapse, this work casts

possible doubt on the results of these experiments, though the extent to which this is so has yet to be investigated.

Other effects meriting attention include electron-phonon coupling, which is thought to be quite important for transition metals such as Ti, cascade overlap, as would occur in 'real' situations, and alloying, though as yet no potentials have been developed for HCP alloys. This last point has great significance as far as reactor core components are concerned, since very few metals are used in their pure form for engineering purposes. The transitional nature of Ti and Zr also means that they will have some directional character to the atomic bonds. While this is not explicitly incorporated into the potentials used in this work, the pair term V(r) (for both models) has some inherent directionality in that the HCP structure is favoured over the FCC by careful use of the perturbation approximation. The many-body term, however, is completely isotropic. Several new potentials with direct inclusion of bond angularity have recently been developed for several structures (Nishitani et al. 1994, Baskes & Johnson 1994), which use a modification of the EAM (see chapter 3) such that specific bond types, corresponding to shared electron orbitals, are modelled rather than spherically symmetrical atoms. As such, these potentials are more complex than those used here, although in some cases the expected differentiation between structures with similar nearest-neighbour shells fails to emerge (Nishitani et al. 1994). However, the electron theory on which they are based has possibilities for predicting and modelling many experimentally observable effects such as phase transformations, binary phase diagrams in metallic and non-metallic alloys, and even magnetic properties, as described in 'Electron Theory in Alloy Design' (see Finnis 1992).

With reference to chapter 6, particularly section 6.4, MOLDY has recently been modified to compute stresses at atomic sites (Calder 1994), but additional modifications are possible to further investigate the thermodynamic processes accompanying the kinetics of cascade formation. These include dividing the

simulation block into cells, possibly using the existing link cells, and recording the temperature, pressure, kinetic and potential energies, total impulse, density, and SIA and vacancy concentration in each cell at each documented time-step. However, useful though this data is, it will slow down any MD simulations producing it, and will also require additional storage.

An increasing trend in the field of computer simulation is the development of hybrid models, combining the discrete nature of MD and Monte-Carlo codes with a continuum approach, particularly for seeking to link modelling and experimental results (Kapinos & Bacon 1994). The attractiveness of this approach over solely MD studies is that, for a full understanding of many aspects of radiation damage, statistically substantial numbers of cascades are required to confirm many of the possible trends identified in MD simulation to date. At present these can only be achieved by BCA codes. However, as pointed out in chapter 3, the BCA is extremely poor at modelling thermal processes or collisions of the order of a few eV, and therefore a mixture of BCA and MD simulations and continuum treatment of the results is advantageous.

It is clear, from this and other studies, that there is still some way to go before a full understanding of the underlying mechanisms of cascade generation and the effects of radiation damage is achieved, despite the wealth of experimental and simulation data generated to date. However, this is a relatively young field of research, coming to the fore with the availability of more powerful computing facilities and graphics techniques. It will continue to be investigated many years into the future, especially with the growing interest in fusion-based power, which will involve higher energy effects and new, possibly non-metallic materials.

Bibliography

Ackland G.J., Finnis M.W. & Vitek V.
(1988) *J. Phys. Forum*, **18**, p153.

Ackland G.J.
(1992) *Phil. Mag. A*, **66**, p917.

Ackland G.J., Wooding S.J. & Bacon D.J.
(1994) *Phil. Mag. A, Submitted for publication.*

Andersen H.C.
(1980) *J. Chem. Phys.*, **72**, p2394.

ASTM Standard E521.
(1989) *ASTM Annual Book of Standards.*

Averback R.S., Benedek R. & Merkle K.L.
(1978) *Phys. Rev. B*, **18**, p4156.

Averback R.S. & Ghaly M.
(1994) *Nucl. Instrum. & Methods B*, **90**, p191.

Bacon D.J. & Martin J.W.
(1981) *Phil. Mag. A*, **43**, p883.

Bacon D.J.
(1988) *J. Nucl. Mater.*, **159**, p176.

Bacon D.J., Calder A.F., Harder J.M. & Wooding S.J.
(1993) *J. Nucl. Mater.*, **205**, p52.

Bacon D.J.
(1993) *J. Nucl. Mater.*, **206**, p249.

Bacon D.J., Calder A.F., Gao F., Kapinos V.G. & Wooding S.J.
(1994) *Presented at COSIRES '94, Santa Barbara. Nucl. Instrum. & Methods. To be published.*

Baskes M.I. & Johnson R.A.
(1994) *Model. Simul. Mater. Sci. Eng.*, **2**, p147.

Beavan L.A., Scanlan R.M. & Seidman D.N.
(1971) *Acta Metallica*, **19**, p1339.

Beeler J. & Besco D.B.
(1964) *Phys. Rev. A*, **134**, p530.

Beeler J.
(1966) *Phys. Rev. A*, **150**, p470.

Berendsen H.J.C. & Van Gunsteren W.F.
(1985) *Proc. Int. School of Physics 'Enrico Fermi' (North-Holland)*, p43.

Biersack J.P & Ziegler J.F.
(1982) *Nucl. Instrum. & Methods*, **194**, p93.
Biget M., Maury F., Vajda P., Lucasson A. & Lucasson P.
(1971) *Rad. Eff.*, **7**, p223.
Born M. & Mayer J.E.
(1932) *Z. Phys.*, **75**, p1.
Brinkman J.A.
(1954) *J. App. Phys.*, **25**, p961.
Bullough T.J.
(1992) *Symposium on Materials Modelling: "From Theory to Technology." (IOP Publishing: Bristol 1992)*, p111.
Calder A.F., Bacon D.J., Phythian W.J. & English C.A.
(1992) *Mater.Sci. Forum*, **97-99**, p183.
Calder A.F. & Bacon D.J.
(1993) *J. Nucl. Mater.*, **207**, p25.
Calder A.F.
(1994) *Private Communication.*
Caro A. & Victoria M.
(1989) *Phys. Rev. A*, **40**, p2287.
Caro M., Ardelea A. & Caro A.
(1990) *J. Mater. Res.*, **5**, p2652.
Daw M.S. & Baskes. M.I.
(1984) *Phys. Rev. B*, **29**, p6443.
Deng H.F. & Bacon D.J.
(1994) *Presented at COSIRES '92 Berlin, Rad. Eff. & Def. in Solids*, **130-131**, p507.
Diaz de la Rubia T., Averback R.S., Hsieh H. & Benedek R.
(1989) *J. Mater. Res.*, **4**, p579.
Diaz de la Rubia T. & Guinan M.W.
(1990) *J. Nucl. Mater.*, **174**, p151.
Diaz de la Rubia T. & Guinan M.W.
(1990) *Rad. Eff. & Def. in Solids.*, **113**, p151.
Diaz de la Rubia T. & Guinan M.W.
(1992) *Mater.Sci. Forum*, **97-99**, p23.
Diaz de la Rubia T. & Phythian W.J.
(1992) *J. Nucl. Mater.*, **191-194**, p108.

Diaz de la Rubia T., Caro A., Spaczer M., Janauary G.A., Guinan M.W. & Victoria M.
(1993) *Nucl. Instrum. & Methods*, **80-81**, p86.

Diaz de la Rubia T., Guinan M.W., Caro A. & Scherrer P.
(1994) *Presented at COSIRES '92, Berlin. Rad Eff. & Def. in Solids.*, **130-131**, p39.

English C.A. & Jenkins M.L.
(1987) *Mater. Sci. Forum*, **15-18**, p1003.

English C.A., Eyre B.L. & Holmes S.M.
(1980) *J. Phys. F: Met. Phys.*, **10**, p1065.

English C.A., Foreman A.J.E., Phythian W.J., Bacon D.J. & Jenkins M.L.
(1992) *Mater. Sci. Forum*, **97-99**, p1.

Ercolessi F., Tossati E. & Parinello M.
(1986) *Phys. Rev. Lett.*, **57**, p719.

Ercolessi F., Tossati E. & Parinello M.
(1988) *Phil. Mag. A*, **58**, p213.

Erginsoy C, Vineyard G.M. & Englert A
(1984) *Phys. Rev. A*, **133**, p595.

Erginsoy C., Vineyard G.H. & Englert A.
(1964) *Phys. Rev. A*, **133**, p595.

Eyre B.L., Maher D.M. & Perrin R.C.
(1977) *J. Phys. F: Met. Phys.*, **7**, p1371.

Fincham D. & Heyes D.M.
(1985) *Adv. Chem. Phys.*, **63**, p493.

Finnis W.M. & Sachdev M.
(1976) *J. Phys. Forum.*, **6**, p965.

Finnis M.W.
(1988) *AERA Report No. R13182.*

Finnis M.W.
(1991) *Symposium on Materials Modelling: "From Theory to Technology." (IOP Publishing: Bristol 1992)*, p99.

Finnis M.W.
(1992) *"Electron Theory in Alloy Design", Ed: D.G. Pettifor & A.H. Cottrell (IOM Press).*

Foreman A.J.E.
(1974) *Rad. Eff.*, **21**, p81.

Foreman A.J.E., English C.A. & Phythian W.J.
(1991) *AEA Technology Harwell Report No. AEA-TRS-2029.*
Foreman A.J.E., Phythian W.J. & English C.A.
(1992) *Phil. Mag. A*, **66**, p671.
Foster A.H., Harder J.M & Bacon D.J.
(1987) *Mat. Sci. Forum*, **15-18**, p849.
Frank W.
(1988) *J. Nucl. Mater.*, **159**, p122.
Frank W. & Seeger A.
(1987) *Mater. Sci. Forum*, **15-18**, p57.
Fukumura A., Sekimura N. & Ishino S.
(1991) *J. Nucl. Mater.*, **179-181**, p897.
Fuse M.
(1985) *J. Nucl Mater.*, **136**, p250.
Gao F. & Bacon D.J.
(1993) *Phil. Mag. A*, **67**, p289.
Gao F. & Bacon D.J.
(1994) *Phil. Mag. A. In the press.*
Ghaly M. & Averback R.S.
(1994) *Phys. Rev. Lett.*, **72**, p3.
Gibson J.B., Goland A.N., Milgram M. & Vineyard G.H.
(1960) *Phys. Rev. A*, **120**, p1229.
Griffith M.
(1988) *J. Nucl. Mater.*, **159**, p190.
Griffith M.
(1989) *J. Nucl. Mater.*, **165**, p315.
Griffith M.
(1991) *Phil. Mag. A*, **63**, p835.
Harder J.M & Bacon D.J.
(1986) *Phil. Mag. A*, **54**, p651.
Heinish H.L. & Singh B.N.
(1992) *J. Nucl. Mater.*, **191-194**, p1083.
Heyes D.M. & Smith W.
(1987) *Information Quarterly for Computer Simulation of Condensed Phases (SERC Daresbury Labs.)*, **26**, p68.

Holmes S.M., Eyre B.L., English C.A. & Perrin R.C.
(1979) *J. Phys. F: Met. Phys.*, **9**, p2307.

Hood G.M., Laursen T., Jackman A., Belec R., Schultz R.J. & Whitton J.L.
(1991) *Phil. Mag. A*, **63**, p937.

Hood G.M.
(1993) *Defects & Diffusion Forum*, **95-98**, p755.

Howe L.M.
(1970) *Phil. Mag A.*, **22**, p965.

Igarashi M., Khantha M. & Vitek V.
(1991) *Phil. Mag. B*, **63**, p603.

Jenkins M.L. & Wilkins M.
(1976) *Phil. Mag. A*, **34**, p1155.

Johnson R.A. & Beeler J.R.
(1981) *"Interatomic Potentials & Crystalline Defects.", Ed: J.K. Lee (AIME)*, p165.

Johnson R.A.
(1991) *Phil. Mag. A*, **63**, p865.

Jung P.
(1983) *J. Nucl. Mater.*, **117**, p70.

Kapinos V.G. & Bacon D.J.
(1994) *Phil. Mag. A*, **68**, p1165.

Kapinos V.G. & Bacon D.J.
(1994) *Presented at COSIRES '94, Santa Barbara. Nucl. Instrum. & Methods. To be published.*

Kenik E.A. & Mitchell T.E.
(1975) *Phil. Mag. A*, **32**, p815.

Kinchin G.H & Pease R.S.
(1955) *Rep. Progr. Phys.*, **18**, p1.

Kirk M.A., Blewitt T.H. & Scott T.L.
(1977) *Phys. Rev. B*, **15**, p2914.

Kirk M.A. & Blewitt T.H.
(1978) *Metall. Trans. A*, **9A**, p1729.

Kirk M.A. & Blewitt T.H.
(1982) *J. Nucl. Mater.*, **108-109**, p124.

Kulp D., Ackland G.J., Sob M.M., Vitek V. & Egami T.
(1992) *Model. Simul. Mater. Sci. Eng.*, **1**, p315.

Lenard-Jones J.E.
(1924) *Proc. R. Soc. A*, **106**, p463.
Maury F., Roux G., Vajda P., Minier C., Lucasson A. & Lucasson P.
(1970) *Cryst. Latt. Def.*, **1**, p361.
Maury F., Vajda P., Lucasson A. & Lucasson P.
(1973) *Phys. Rev. B*, **8**, p5496 & 5506.
McQueen R.G., Marsh S.P., Taylor J.W., Fritz J.N. & Cater W.J.
(1970) *"High Velocity Impact Phenomena", Ed: R. Kinslow (Academic Press).*
Mercer-Calder E.M.
(1992) *Ph.D. Thesis, Liverpool University.*
Merkle K.L.
(1966) *Phys. Stat. Solidi*, **18**, p173.
Mikhin A.G., Osetsky Y.N. & Kapinos V.G.
(1994) *Phil. Mag. A*, **70**, p25.
Mitchell T.E., Das G. & Kenik E.A.
(1975) *Proc. 5th Int. Conf. on the Fundamental Aspects of Radiation Damage in Metals, Gatlinburg, Tenn. USERDA Conf. 751006-P1*, p73.
Monti A.M., Sarce A., Smetniansky-de Grande N., Savino E.J. & Tomé C.N.
(1991) *Phil. Mag. A*, **63**, p925.
Neely H.H.
(1970) *Rad. Eff.*, **3**, p189.
Nishitani S.R., Alingaghian P., Hausleitner C. & Pettifor D.G.
(1994) *Phil. Mag. Lett.*, **69**, p177.
Norgett M.J., Robinson M.T., Torrems I.M.
(1975) *Nucl. Eng. & Design*, **33**, p50.
Norskov J.K. & Lang N.D.
(1981) *Phys. Rev. B*, **21**, p2131.
O'Connor D.J. & Biersack J.P.
(1986) *Nucl. Instrum. & Methods*, **15**, p14.
Oh D.J. & Johnson R.A.
(1988) *J. Mater. Res.*, **3**, p471.
Oh D.J. & Johnson R.A.
(1989) *J. Nucl. Mater.*, **169**, p5.
Olander D.R.
(1976) *"Fundamental Aspects of Nuclear Fuel Elements." (Technical Information Centre, ERDA, USA)*, p373.

Parinello M. & Rahman A.
(1980) *Phys. Rev. Lett.*, **45**, p1196.

Pearson W.B.
(1967) *"A Handbook of Lattic Spacings & Structures of Metals & Alloys." (Pergamon Press).*

Phythian W.J., English C.A., Yellen D.H. & Bacon D.J.
(1991) *Phil. Mag. A*, **63**, p821.

Phythian W.J., Foreman A.J.E., Stoller R.E., Bacon D.J. & Calder A.F.
(1994) *Submitted for publication.*

Rehn. L.E. & Wiedersich H.
(1992) *Mater.Sci. Forum*, **97-99**, p43.

Robertson I., Heine V. & Payne M.C.
(1993) *Phys. Rev. Lett.*, **70**, p1944.

Robertson I.M., Tappin D.K. & Kirk M.A.
(1993) *Phil. Mag. A*, **68**, p843.

Robinson M.T. & Torrens I.M.
(1974) *Phys Rev. B*, **9**, p5008.

Rose J.H., Smith J.R., Guinea F. & Ferrante J.
(1984) *Phys. Rev. B*, **29**, p2963.

Schwartz D.L. & Schwartz D.M.
(1978) *Rad. Eff.*, **38**, p15.

Seeger A.
(1958) *Proc. 2nd. U.N. Int. Conf. on Peaceful Uses of Atomic Energy, Geneva (U.N. New York)*, **6**, p250.

Seitz F.
(1952) *Physics Today*, **5(6)**, p6.

Silsbee R.H.
(1957) *J. Applied Physics*, **28**, p1246.

Singh B.N. & Foreman A.J.E.
(1992) *Phil. Mag A.*, **65**, p975.

Smithells Metals Reference Book
(1985) 6th Edition, Butterworths.

Thompson M.W.
(1969) *"Defects and Radiation Damage in Metals." (Cambridge University Press).*

Tomé C.N., Monti A.M. & Savino E.J.
(1979) *Phys. Stat. Solidi*, **92**, p232.
Ullmaier H. & Schilling W.
(1980) *"Physics of Modern Materials." (International Atomic Energy Agency: Vienna)*, p301.
Vajda P.
(1977) *Rev. Mod. Phys.*, **49**, p481.
Vialaret P., Moreau F., Bessis A., Dimitrov C. & Dimitrov O.
(1975) *J. Nucl. Mater.*, **55**, p83.
Vineyard G.H. & Gibson J.B.
(1961) *Bull. Am. Phys. Soc.*, **6**, p158.
Voter A.F. & Chen S.P.
(1987) *M.R.S. Proceedings*, **82**, p175.
Wei C.Y. & Seidman D.N.
(1981) *Phil. Mag. A*, **43**, p1419.
Wilson K.L. & Seidman D.N.
(1975) *Rad. Eff.*, **27**, p67.
Wilson K.L., Baskes M.I. & Seidman D.N.
(1980) *Acta Metallica*, **28**, p89.
Woo C.H.
(1988) *J. Nucl. Mater.*, **159**, p237.
Woo C.H.
(1991) *Phil. Mag. A*, **63**, p915.
Woo C.H. & Singh B.N.
(1992) *Phil. Mag. A*, **65**, p889.
Ziegler J.F., Biersack J.P. & Littmark U.
(1985) *"The Stopping Range of Ions in Solids." (Oxford: Pergamon).*
Zinkle S.J. & Singh B.N.
(1993) *J. Nucl. Mater.*, **199**, p173.

APPENDIX A

MODLY as Modified for the HCP Metals.

This appendix is further to chapter 3, and contains a list of the main sections and routines within MOLDY, a brief description and the modifications made to them to convert the code to the HCP structure. Further details on the finer points of MOLDY can be found in the references cited in chapter 3.

MAIN: The central core of MOLDY. Modifications were extensive and included reading in the $^{c}/_{a}$ ratio as well as the lattice parameter, allowing input of the PKA direction in the HCP 4-index system, changing the data reading routines to read in the three part composite potential, and the addition of several arrays to store and output the data for the TV files during the simulation.

HCPLAT: A new routine to generate the HCP structure. The points making up the structure are stored in a unit cube, meaning the lattice is 'squashed' to fit the x, y and z coordinates in the -0.5 to +0.5 limits. The actual physical dimensions of the simulation box are stored in another 3 x 3 vector array and, when multiplied by the coordinates stored in the unit cube give the 'real' coordinates of each atom in three-dimensional space. The routine was also modified to allow the use of non-cubic simulation blocks when required, whilst ensuring an even number of atomic planes in each of the x, y and z directions to allow the periodic boundary conditions to function correctly.

PRTLAT: Short routine to print the atom indices and their coordinates to aid the

insertion of point defects for the work in chapter 4.

CEHCP: New routine to calculate the cohesive energy of the model lattice. Only the Ackland part of the potential need be taken into account for this calculation, since the structure is assumed to be in equilibrium at 0 K.

CORREC: This routine is called after each force calculation to apply the Gear 4-value algorithm corrector step to the dynamic variables assigned to each atom, such as position, velocity and acceleration.

IDENT: Used to check for vacant sites and displaced atoms and flag them accordingly. This routine was rewritten to search the HCP unit cell rather than a cubic cell.

INVERT: Short routine to find the inverse of a 3 x 3 matrix.

KINTEN: Evaluates the kinetic tensors of the box matrix after the force calculations for use in the Lagrangian equations of motion.

KRAVLC: Around 70 % of the run-time of a simulation is spent in this routine, which calculates the net force on each atom from its neighbours in the same link cell and the 26 surrounding link cells. The new composite potential was inserted.

LCSITE: Sets up the link cell map for the perfect lattice.

LINVLC: Readjusts the link cell map during the simulation before each force calculation, moving atoms from one link cell to the next as they cross the link cell boundaries.

MATPRO: Finds the product of two 3 x 3 matrices.

PREDIC: Applies the predictor step of the Gear 4-value algorithm to the dynamic variables before the force calculations.

QUENCH: Routine to remove heat by selective velocity reduction, such that if the velocity and acceleration of an atom are in the same direction, i.e. it is speeding up, it is ignored, but if the velocity and acceleration vectors are opposed, i.e. it is slowing, the atom is stopped. This routine is called every time-step during quasi-static simulations such as detailed in chapter 4 and mirrors the stepped relaxation procedure used in static modelling.

REJECT: Routine to remove atoms from the structure to create pre-simulation vacancies, again used for point defect investigations. Modified to remove atoms by index and not coordinates as in previous versions.

RHOVLC: Calculates the density function ρ_i for use in the many-body part of the force calculations. Modified to include the new many-body potential.

RUNAVS: Called at the end of a simulation to output summary and atom files, and to print some running averages, a leftover of fixed time-step calculations.

SCALEV: Scales the velocities of the atoms to the required kinetic temperature.

SETVEL: Initialises the atom velocities from a random distribution.

TEACUP: Important routine to alter the size of the time-step based on the largest predicted atom velocity and the predicted changes in atom positions.

All the routines were modified where necessary to allow differing numbers of atoms in the x, y and z directions, necessary to produce an approximately cubic simulation block in the HCP system.

APPENDIX B

Determination of the Model Melting Temperature.

This appendix is further to chapter 6, and contains a description of the method of determining T_m for the Ti and Zr models. The procedure used is, as stated in chapter 6, a simplification of that employed by Kapinos & Bacon (1993) to investigate vacancy clustering and loop formation in a model melted zone such as is possibly present in the cascade core. It is based on obtaining a temperature vs. time curve for the transition from melt to solid, and deducing T_m from the arrest temperature.

A long, thin 'sausage' of atoms of 150 basal planes, each containing 30 atoms and transverse to the long axis, was set up in MOLDY. The periodic boundary conditions were allowed to operate, but thermal expansion prevented by using constant volume conditions, and the time-step size set at a constant 5 fs. The block was treated as 101 layers (so there was a central layer), and a random distribution of vacancies set up throughout the block equivalent to a concentration of 3 % to reduce the amount of superheating required to produce a molten region. This is also consistent with the typical few % free volume change of metals on melting (Smithells Metals Reference Book). Each layer contained, on average, ~43 atoms from which the kinetic temperature of each layer was determined.

To melt the centre of the block, an initially random distribution of velocities was applied to the central 31 layers, scaled to a maximum temperature of 3500 K in the middle and reducing according to layer distance from the centre. The block was then allowed to develop for 1000 time-steps (~5 ps) to allow the distribution to become approximately Gaussian, and to smooth out any small zones of widely differing temperature.

To determine the melting temperature, both ends of the block were damped by applying a small viscous damping force to the 30 layers at either end of the block. This force is of the form $\mathbf{F}_i = -\mu \mathbf{v}_i$, after Caro & Victoria (1989), where μ is the damping coefficient and $\mathbf{v}_i$ is the velocity of the ith atom. In this case $\mu = 5.0 \times 10^{-14}$ N s m^{-1}, which yields an equilibrium temperature of ~10 K in the damped regions and is small enough to allow the central region to attain crystallinity during solidification - were μ too large the melted zone could be frozen as an amorphous solid. The simulation was run for 100 ps (20,000 time-steps) whilst recording the temperature in the central 5 layers of the block every 10 time-steps. These temperature profiles are shown in figs. 1 and 2. They have been mathematically smoothed by application of the local smoothing function in Kaleidagraph™, owing to the often quite variable temperature in one layer between time-steps. It can be seen that in both models at around 35 - 40 ps there is a short plateau and a marked coincidence of the five temperature traces, most obvious for the Zr model. It is during this time that solidification of the central layers takes place.

Checks were made on the progress of the simulation every 20 ps or so by outputting the atom coordinates and viewing them in three-dimensional form using AVS™. In this way the state of the centre of the block could be visually confirmed, and several snapshots at various times during the simulations are shown in fig. 3 for the Zr model. The inward advancement of the solid-liquid interface is clearly visible and, although perhaps not immediately obvious from fig. 3(c), the beginnings of planar order are evident in the centre section as solidification takes place between ~35 - 45 ps. (Viewing fig. 3(c) from the edge of the page along its long axis, i.e. along the [0001] direction, makes this a little more noticeable.) At 100 ps, as in fig. 3(d), the block is unmistakably crystalline solid and, even with the temperature around 1000 K in the central layers, there is very little thermal disruption to the structure.

The quoted value of T_m was made from the mean actual temperature (as opposed to the smoothed fits shown in figs. 1 and 2.) of all five central layers averaged over the length of the solidification plateau, with the error quoted being the standard deviation of the temperature values from the mean. As stated in chapter 6, the value for Zr gives a very good match to experiment, whilst that for Ti is ~550 K too low. Several different sets of simulation parameters were tried for this model, including concentrations of vacancies of 0 and 6 % and two different damping coefficients, but these did not affect the resulting T_m in any significant way. Therefore, the reason for this quite large discrepancy remains as yet undetermined, but could possibly be due to having too soft a core in the pair part of the Ti potential, since this would lower T_m. However, were this the case, the Zr model, which is based on the same potential formalism, would be expected to exhibit similar behaviour, and since it does not, this cannot be the only factor affecting the melting temperature.

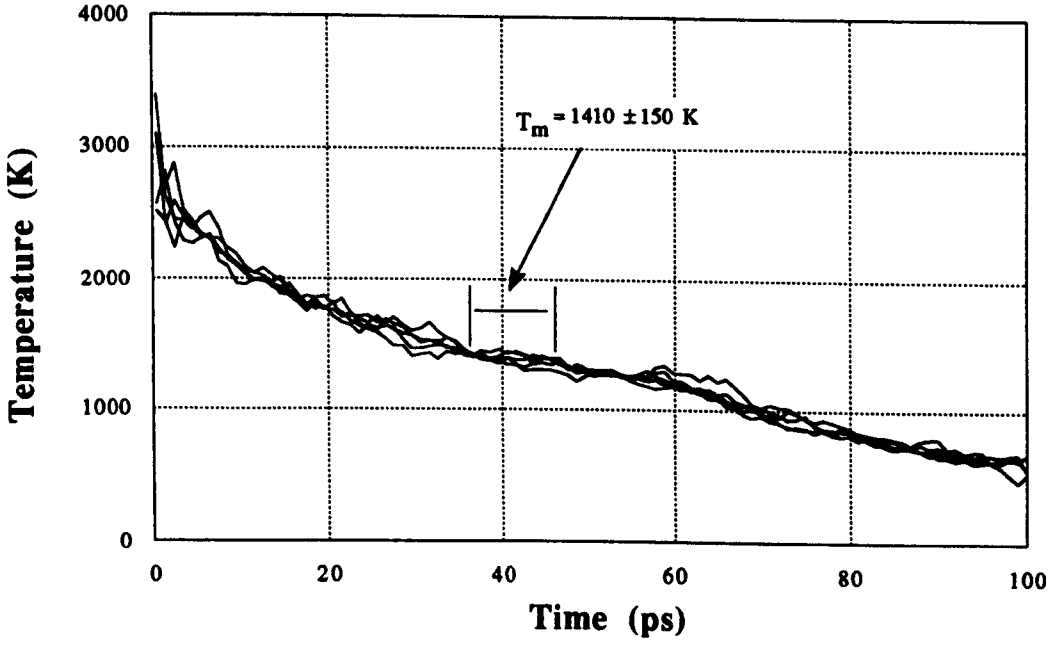

Fig. 1: Temperature vs. time for the five central layers of the Ti block.

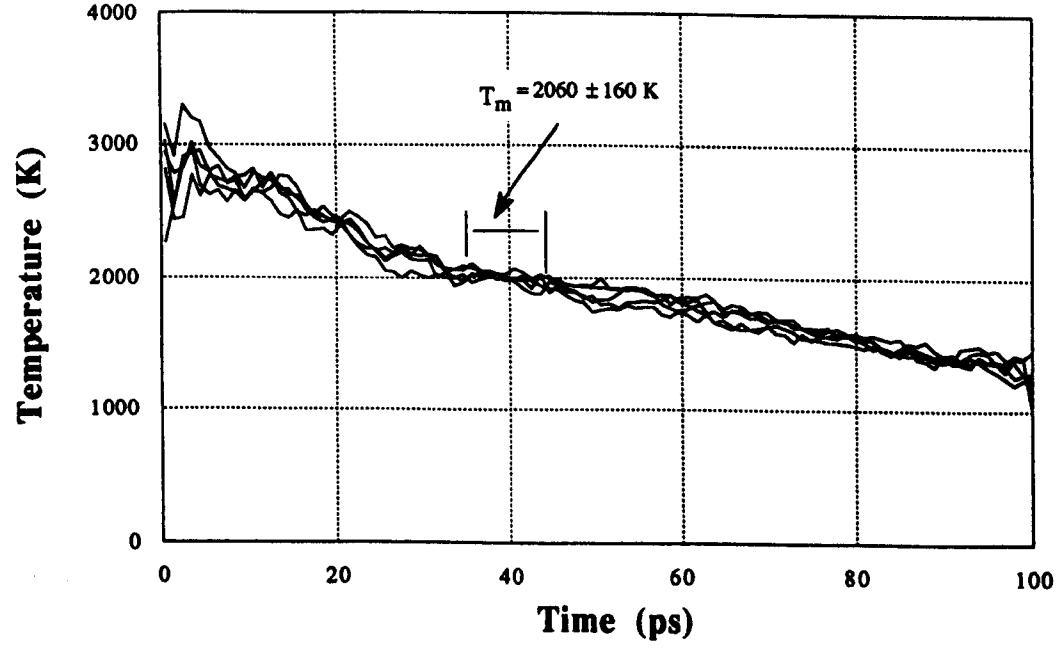

Fig. 2: Temperature vs. time for the five central layers of the Zr block.

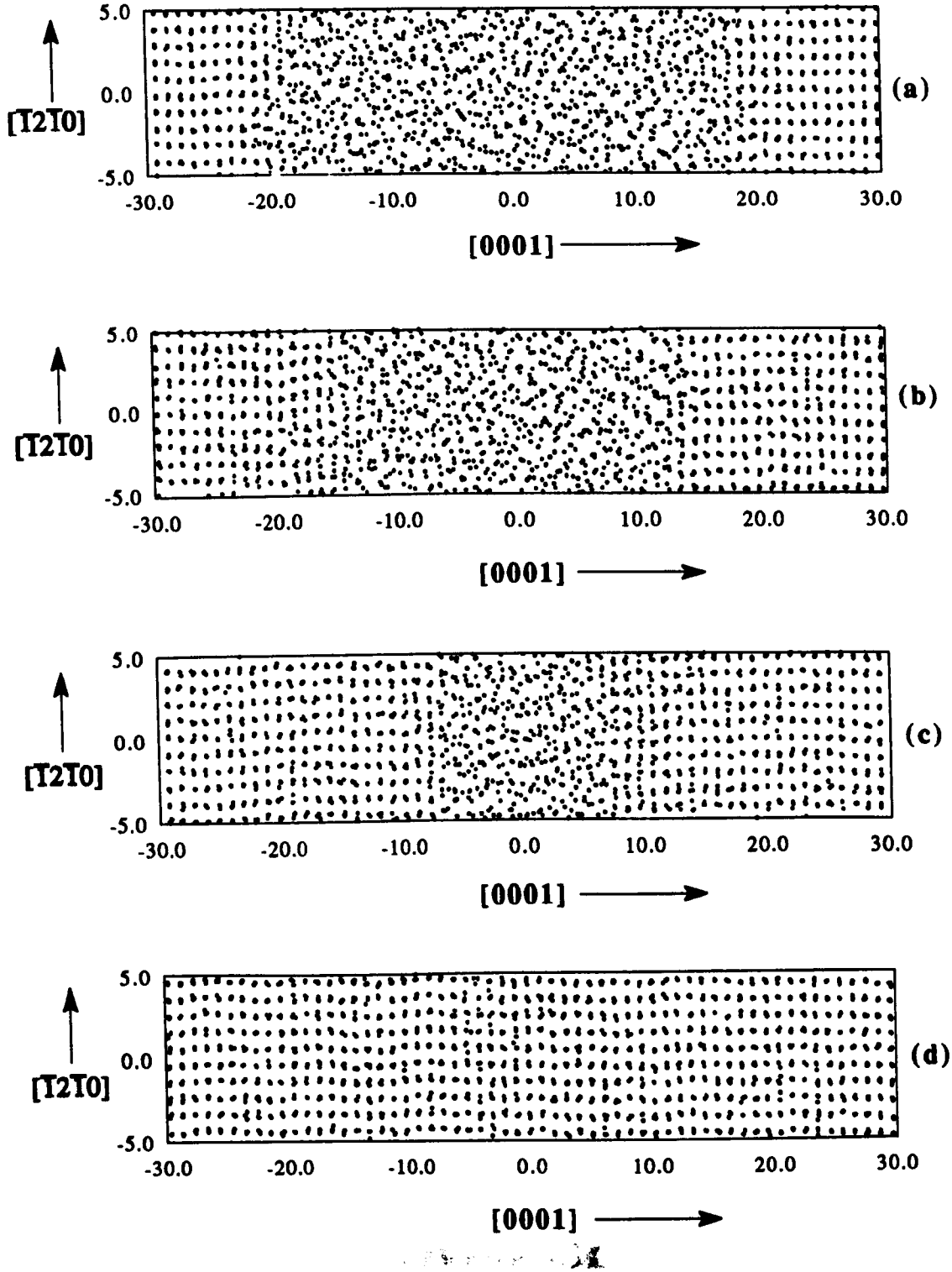

Fig. 3: Snapshots of the atom positions during solidification. Only the central 61 basal planes are shown for clarity, and the times for each frame are 0, 20, 40 and 100 ps respectively.